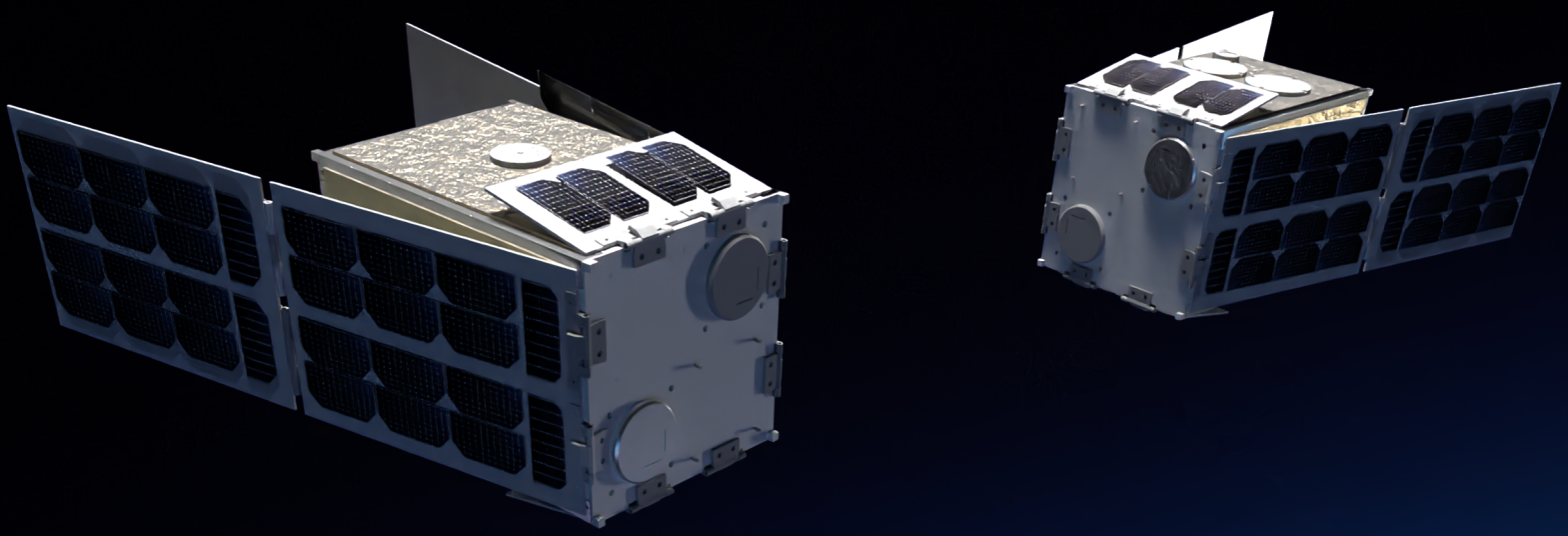

SCATTER: Final Report

Surface-gas Collision with Aerodynamic Twins for Thermospheric Experimental Research

AE3200 Design Synthesis Exercise - Group 17
Version 1.2

Group Members

Sabin-Viorel Anton	4996380
Killian Caignie	5013909
Daniel Calliess	4869710
Oscar Junius	5104556
Andrei Pârvulescu	5118344
Naishadha Perugu	4857631
Jort Roelofs	4645553
Oliver Ross	5008042
Srujan Vaidya	5072034
Ziqi Zhang	5087007

Principal tutor
Christian Siemes

Coaches
Thomas Hunter & Jingyi Liu

Completion Date
June 21, 2022

Faculty of Aerospace Engineering

TU Delft Delft University of Technology

Executive Overview

Current trajectory estimations for spacecraft travelling in Low Earth Orbit (LEO) have a significant limitation in their ability to quantify atmospheric drag and the resulting orbital decay. This is largely due to a lack of understanding in how thermospheric particles interact with satellite surfaces during flight. Depending on the number of particles, their temperature, the spacecraft surface, and parameters known as the energy, normal momentum, and tangential momentum accommodation coefficients, the manner in which particles scatter following impact with the spacecraft is affected. This affects the exchange in kinetic energy between the particles and the spacecraft, which is the cause of atmospheric drag. The nature of these so-called gas-surface interactions (GSI) is currently not well understood at altitudes where there is a significant particle number density of atomic helium, or equivalently, above about 450 km. As a result of this, current space missions must make use of mitigation strategies with respect to their satellite operations throughout the mission lifetime. This includes very large safety margins for collision probability estimations, as orbits cannot be predicted with enough accuracy. These margins lead to a very low threshold for when such a probability is considered a warning and requires corrective measures. In orbits which are becoming increasingly densely populated with new satellites, such mitigation strategies are costly in terms of time and financial resources, as the number of collision warnings over a certain period of time is becoming increasingly frequent. Therefore, a more permanent solution would be to develop higher fidelity trajectory estimations through improved atmospheric drag modelling, motivating the following mission need statement:
"To ensure safe satellite operations in ever more densely populated orbits, there is a need to improve the current atmospheric drag modelling for more accurate trajectory predictions at altitudes in the range 100 – 600 kilometres by 2035."

Project Surface-gas Collision with Aerodynamic Twins for Thermospheric Experimental Research (SCATTER) is a novel project aiming to resolve the uncertainty in atmospheric drag modelling through improved understanding of GSI. By taking measurements of atmospheric chemical composition, translational acceleration and other, the project would reveal more about the nature of GSI at various orbital altitudes. Based on a market analysis conducted on the space sector and the wider scientific community, the results and conclusions obtained from this project can be very attractive to satellite developers, launch providers and other researchers alike. Furthermore, there has been no mission that has characterized these GSI at altitudes as high as 600 km. Therefore, it was concluded that project SCATTER is a project with a low risk of being made redundant and with a high scientific value. As a result of this, several primary, secondary and tertiary objectives were created which best reflect the needs of the market and the overarching scientific aim. These are presented below:

1.1 Measure the drag of 2 satellites flying in the same atmospheric conditions with different tangential to normal surface area ratios, at altitudes between 150 km and 600 km
2.1 Measure the atmospheric temperature at altitudes between 150 km and 600 km
2.1 Measure the particle number density of helium and atomic oxygen at orbital altitudes between 150 km and 600 km
3.1 Use as high a percentage of off-the-shelf components in the satellites as possible

In addition to these main objectives, there are a number of fixed constraints to be taken into consideration. First, the launch date of this product shall take place no later than 2035. Furthermore, the development cost must be less than 10MEUR. To enable any future spacecraft design to measure meaningful results regarding GSI and its impact on atmospheric drag, first an analysis into the mission profile of the project was required. Using an in-house developed trajectory modelling tool which takes into effect atmospheric drag, solar activity and magnetic field effects, it was concluded that throughout the mission lifetime there will three distinct phases where scientific measurements will be taken. Phase 1 takes place at the highest altitude range of between 600 km and 400 km, while Phase 2 ranges from 400 km to 300 km and finally Phase III ranges from 300 km until re-entry. An overview of all mission phases can be seen in figure 1.

The Vega-C launch vehicle is chosen for this mission, as can be seen in figure 1. This is because this launcher offers frequent ride-sharing opportunities for smaller satellites to orbits of 600 km. As most ride sharing programs launch into sun-synchronous orbits, the inclination is expected to be around 97°. Throughout all three of these phases, the spacecraft will predominantly be in their science mode, which entails the measuring of scientific data and the transmission of the collected data when in range of the ground station. Given that the natural decay of the orbit is slow in phase 1, a propulsion system is needed to arrive at the target altitude for phase 2 before the end of the mission lifetime. Therefore, from phase 1 to phase 2 a sequence of propulsive burns are applied to reduce the altitude in steps of 10 km. During these manoeuvres, the spacecraft will not take measurements and instead will be in its orbit manoeuvre mode. Between these manoeuvres, the spacecraft will be in its science mode taking measurements and collecting data. By applying such an orbit control technique, Phase 1 is expected to last 189 days, with 20 scientific measurements of translational acceleration possible. From phase 2 onwards, the natural

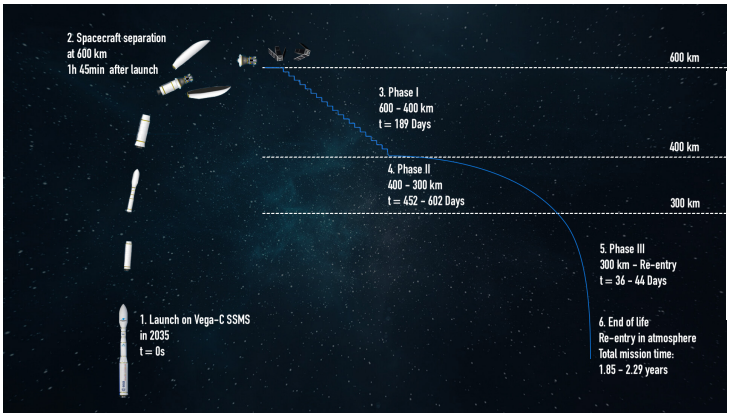

Figure 1: Overview of the mission of project SCATTER, with the three distinct science phases presented.

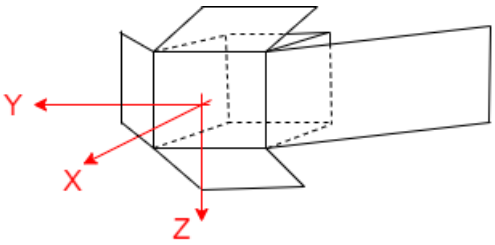

Figure 2: Preliminary shape sketch of the design, with the reference coordinate frame described.

decay of the orbital altitude due to drag is sufficient to decrease the altitude before reaching the maximum mission lifetime. Depending on the satellite mass and solar activity, the operational lifetime for phase 2 is estimated to be on average a duration of 595 days. In this period 255 measurements will be taken. Phase 3 is expected to last for one month, in which 98 measurements are taken. Upon re-entering, the spacecraft will configure itself into a re-entry mode for safe burn-up.

In order to satisfy the primary mission objectives as described earlier, it is necessary to have at least two satellites with distinctly different projected areas flying in proximity to each other, such that the difference in drag and resulting orbital decay is reflective of the nature of GSI. In order to achieve this drag sensitivity to GSI while maintaining a high reliability and low cost, it was found using Direct Simulation Monte Carlo simulations with a Cercignani-Lampis-Lord model that a CubeSat spacecraft geometry with long shallow angles is preferred, with one spacecraft travelling with these panels quasi-parallel to the flow while the other is travelling with these same panels perpendicular to the flow. These orientations are referred to as the low and high drag configurations, respectively. A basic sketch of the satellite shape can be seen in figure 2, with the body axis system drawn on top. In the high drag configuration the satellite travels in the y-direction, and in the low drag configuration it travels in the x-direction. The lengths of the side panels should be as long as possible, while the optimal angle for these panels is around 10°. This was the primary means of defining the external geometry of the spacecraft itself. The shallow angled panels of the spacecraft also serve as the solar arrays, which allow for the generation of electric power for the internal components. The satellite's main solar arrays are 2U wide by 6U long, and are deployed at an angle which matches the aerodynamic angle which is required for drag sensitivity. The smaller 2U by 1u panels are also covered in solar cells. These panels cannot be bought fully off-the-shelf due to the non-standard deployment angle. Whether only the hinges need to be modified, or all the panels is to be determined. By combining the in-house trajectory simulations with the position of the sun, the generated power could be determined. This was found to be approximately 20.8 W of orbital average power when the panels were tracking the Sun (this will be hereby referred to as the satellite "power mode"). This, in combination with a power storage system which can store up to 270 Wh means that scientific measurements to be taken consecutively over a duration of 122 hours before the batteries must be recharged. Therefore, the solar panels perform both the need of aerodynamics and power generation with ample safety margin.

In order for the spacecraft to experience differential drag forces and therefore different orbital decays, it is essential that the orientation of the spacecraft is maintained with respect to the oncoming flow. Furthermore, there is a need for an elaborate formation control scheme to ensure that the satellites do not drift too far apart from each other. This leads to a need for a high accuracy attitude determination and control system (ADCS) and orbit control system (OCS) subsystem, respectively. The ADCS subsystem consists of an attitude determination system which contains six Sun sensors, two magnetometers, and Pulse-40 inertial measurement units (IMU). The IMUs also serve as scientific instruments. For attitude control, an assembly of magnetorquers and reaction wheels was chosen. Because of how rapidly the spacecraft's attitude is subjected to change, the ADCS cannot be controlled manually. As such, the data returned from the magnetometer and/or Sun sensors are inputted into a proportional-derivative control scheme which uses the reaction wheels to generate the required control torque which needs to be applied to the body. This allows for a attitude determination accuracy of an average of 1° and a control accuracy of at least 5° for at least 99% of the total orbit. Besides, in order to deal with the initial tumbling after separation, a so-called "B-dot" algorithm which can use magnetometer measurements and magnetorquers is used, which can decrease the angular velocity of the spacecraft down to 0.01 rad/s in 6 hours with a 50 % safety margin. A formation flying control scheme based on a proportional-integral-derivative binary controller is implemented. Using this, the satellites can switch orientation to keep a specified target separation of 300 km in all phases. To manage the computations involved for the different required control schemes, the SatBus 3C2 On-Board Computer

(OBC) from NanoAvionics is selected, featuring an ARM Cortex M7 processor with a clock frequency of 400MHz.

The main objective of the mission is to measure the drag of two satellites with distinctly different surface area ratios, as well as the atmospheric temperature and the particle number density. To enable the spacecraft to accurately measure all required scientific data which reflects these objectives, the spacecraft carries an assembly of sophisticated payload instruments which is switched on while the spacecraft is in its dedicated science mode. This assembly consists mainly of two mass spectrometers, originally developed for the QB-50 mission, to measure the chemical composition of the thermosphere while in orbit, two Pulse-40 inertial measurement units (IMU), shared with ADCS, to measure the translational acceleration in Phase 3 and one Novatel OEM719 GNSS receiver to determine the orbit decay over time between the two spacecraft. Measurements from each of these payloads can be done at a sampling frequency 0.1 Hz in order to achieve a sufficiently high resolution along the orbit. This in turn leads to a total scientific data rate of approximately 356.8 bps. To ensure that none of this scientific information is lost, an on-board memory storage capacity of 468 Megabytes was added. This allows for the storing of scientific information over three days consecutively with no communication to the ground station, while maintaining a safety margin of two. In nominal spacecraft operations, there should be about 20 minutes of contact time with the ground station, which with a downlink data rate of 615kps will allow all stored data to be sent down to the ground within the communications window.

Throughout the complete lifetime of the mission, the spacecraft must be able to withstand the harsh environment of space. Therefore, a robust thermal control subsystem (TCS) and structural subsystem has to be designed which respects these challenges. By making use of the ESATAN-TMS software, it was concluded that passive thermal control mechanisms are sufficient to regulate the temperature of the spacecraft in low earth orbit. These passive mechanisms include a combination of white paint, Kapton film and other coatings with various absorptivity and emissivity in order to guarantee that the equilibrium internal temperature remains within the operating temperature range of the internal components. As it pertains to the structural element of the spacecraft, a standard CubeSat frame was initially selected, which was then heavily modified to accommodate the integration of all internal components. Through extensive simulation of the static and dynamic loads which can be expected during launch on-board the Vega-C rocket using ANSYS, it was found that the maximum stress to be experienced during launch is significantly lower than the yield stress of the chosen aluminium alloy 6061-T6. Furthermore, upon conducting vibrational analysis, it was found that the lowest natural frequency of 399 Hz is well above the resonant frequency of the launcher. Given that launch is the most structurally critical flight phase, it can be said with reasonable confidence that the structure of this spacecraft design is sound enough to for the mission profile at hand.

Throughout the design process, the subsystems must integrate with each other. This results in a compact shape, which can fit into the launcher and which does not offset the centre of gravity positioning away from the axis of symmetry of the body (which in turn would create perturbing moments that the ADCS subsystem must counteract). With these taken into account, the detailed integrated CubeSat (with the internal components exposed) can be seen in figure 3. The primary structural body of the CubeSat is a 2U by 2U by 3U shape, with the deployable solar panels clearly visible. The large, 6U long solar arrays have a hinge in the middle such that they can be stowed during launch into a compact, standard 12U CubeSat shape. Based on detailed analysis in computer aided design (CAD) software, it was found that the 12U CubeSat was found to have sufficient internal volume to accommodate all necessary internal components, with available margin for cabling and wiring, which was not yet taken into account in this stage of the design. Furthermore, as can be seen in the figure, the internal layout aims to be as axisymmetric as possible around the X axis to prevent any rotating moments. The feasibility of this internal layout will be reviewed in later stages of the design when detailed physical prototyping takes place.

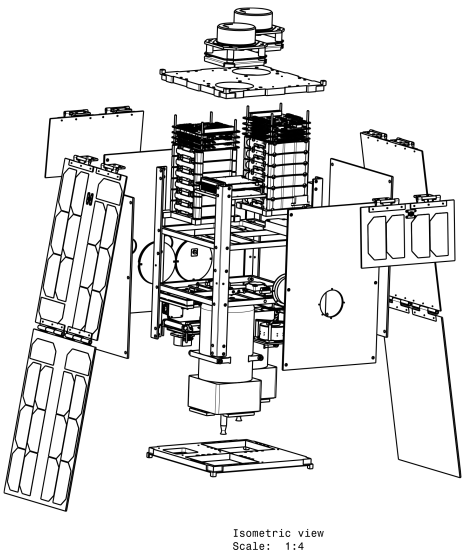

Figure 3: Exploded view of the SCATTER spacecraft, with body panels removed to expose the internal components.

In addition to the construction of the complete physical layout of the spacecraft, the system integration also allows for the creation of more detailed estimates for the mass, power and cost budgets for each of the subsystems, and for the system as a whole. These are presented in tabular form in table 1. As it can be seen here, the cost for one spacecraft is well below the constraint that was specified earlier. Furthermore, while there is no specific constraint on the mass of the spacecraft itself, the mass correlates with comparable spacecraft in the industry. This further suggests that this spacecraft is a feasible option for the mission objectives which were specified.

Throughout the design process, the sustainability and the risk of the design was assessed. Sustainability is included in many parts of the design, such as the use of a ridesharing launch, green propellants, and extensive debris mitigation strategies. A life cycle assessment was conducted for all aspects of the space mission, identifying

potential causes of environmental damage and future recommendations. Potential polluting processes include production of triple junction solar cells and lithium-ion batteries. Furthermore, technical risks were identified per subsystem and mitigation procedures specified, if required. These risks were continuously updated throughout the design process and quantified based on their likelihood and consequence.

Table 1: Detailed design budget allocation for single satellite.

Subsystem	**Component**	**Cost** $[EUR]$	**Mass** $[kg]$	**Dimensions for Single Component** $[mm^3]$	**Peak Power** $[W]$	**Idle Power** $[W]$	**Production**
Structure	Bulkheads (4 no.)	12262.00	2.729	224x224x18.5	0.000	0.000	Customised
	Panels (4 no.)	9112.00	2.028	303.2x207x3	0.000	0.000	Customised
	Rails (4 no.)	1779.00	0.396	18x18x340.5	0.000	0.000	Customised
	Counterweight	7.00	0.230	18x18x42	0.000	0.000	Customised
	Subsystem	23,160.00	5.383	-	0.000	0.000	Customised
TCS	-	66,153.25	0.330	-	0.000	0.000	Customised
OCS	Engines with propellant(2 no.)	577,467.50	5.200	200x100x100	42.000	0.600	Off-shelf
ADCS	Magnetorquer	9,750.00	0.196	95.9x90.1x17	1.200	0.175	Off-shelf
	Surface mounted Sun sensor (2 no.)	22,378.00	0.002	34x40x20	0.300	0.080	Off-shelf
	Solar panel mounted Sun sensor (4 no.)	38,092.00	0.070	20x10x5.7	0.026	0.007	Off-shelf
	Reaction wheels (4 no.)	100,688.00	0.740	50x50x40	7.200	1.200	Off-shelf
	Magnetometers (2 no.)	27,972.00	0.170	96x43x17	0.750	0.750	Off-shelf
	Subsystem	198,880.00	1.178	-	8.726	2.432	Off-shelf
EPS	Small solar panels (2 no.)	11,160.00	0.240	10x113.5x227	-	-	Customised
	Large solar arrays (2 no.)	78,120.00	1.120	10x681x227	-	-	Customised
	Battery Packs	39,600.00	2.212	80x80x135	-	-	Off-shelf
	PCU (2 no.)	4,000.00	0.116	80x80x20	2.118	0.132	Off-shelf
	PDU (2 no.)	4,000.00	0.115	80x80x18	-	0.132	Off-shelf
	BCU (4 no.)	8,000.00	1.008	80x80x19	-	0.195	Off-shelf
	Subsystem	144,880.00	4.811	170x10x10	-	0.393	-
TT&C	Patch Antenna (2 no.)	4,300.00	0.100	80x80x5	-	-	Off-shelf
	Transceiver (2 no.)	20,000.00	0.400	90x65x25.3	-	-	Off-shelf
	Cables	3,645.00	0.100	-	-	-	Off-shelf
	Subsystem	27,945.00	0.600	-	12.000	1.000	Off-shelf
C&DH	Main flight computer	18,364.21	0.124	95.5x90.17x6.57	-	1.000	Off-shelf
Payload	Mass spectrometer (2 no.)	200,000.00	0.400	98x98x64	0.880	0.000	Off-shelf
	GNSS receiver	19,965.00	0.109	96x90x18.1	0.000	1.500	Off-shelf
	GNSS patch antenna	250.00	0.070	61.2x61.2x16.2	1.500	0.000	Off-shelf
	IMU (2 no.)	46,000.00	0.024	30x28x14	0.600	0.600	Off-shelf
	Subsystem	266,215.00	0.603	-	2.980	2.100	Off-shelf
Total	System	1,323,064.96	18.229	-	-	7.524	-

In conclusion, the SCATTER mission aims to improve the accuracy of orbital drag models by measuring the drag coefficient of two satellites in low Earth orbit. Improving these models allows for more accurate orbital trajectory predictions, allowing for more accurate predictions of satellite collision probability. This will be achieved by launching two satellites, which will fly in high and low drag configurations. Due to the sensitivity of the satellites' drag coefficient to energy, normal momentum, and tangential momentum accommodation coefficients, as well as the on-board mass spectrometers, these coefficients can be determined. This sensitivity stems from the deployable panels. The mission consists of three phases: the first phase starts at 600 km, and ends at 400 km. In this phase, 20 measurements will be taken over a 189 day period, and the altitude will be reduced with the propulsion system after every measurement. The second phase is between 400 km and 300 km, and is expected to take 595 days, during which 255 measurements will be taken. Propulsion will only be used for formation maintenance, as the satellites must not drift to far away from each other. The third and final phase starts at 300 km, and ends when the satellites burn up. In this phase, it is expected that 98 measurements will be taken over a 1 month period. By implementing this strategy, it can be said with confidence that the mission need statement and objectives can be satisfied, and meaningful results can be obtained for the benefit of the wider space community.

Table of Contents

Nomenclature

Abbreviations

ADCS	Attitude Determination & Control Subsystem
AES	Advanced Encryption Standard
AISC	Application-Specific Integrated Circuit
BCU	Battery Control Unit
BER	Bit Error Rate
BPSK	Binary Phase Shift Keying
C&DH	Command & Data Handling
CoM	Centre of Mass
COTS	Commercial-Off-The-Shelf
CVCM	Collected Volatile Condensable Material
DM	Development Model
DoD	Depth of Discharge
DRAMA	Debris Risk Assessment and Mitigation Analysis
ECHA	European Chemicals Agency
ECSS	European Cooperation for Space Standardization
EPS	Electrical Power System
ESA	European Space Agency
FEC	Forward Error Coding
FM	Flight Model
FR4	Flame-Retardant 4
GNSS	Global Navigation Satellite System
IMU	Inertial Measurement Unit
INMS	Ion and Neutral Mass Spectrometer
ISO	International Organization for Standardisation
ITU	International Telecommunications Union
LCA	Life Cycle Assessment
LEO	Low-Earth-Orbit
MEPS	Modular Electrical Power System
MPPT	Maximum Power Point Tracker
MSAFE	The Marshall Solar Activity Future Estimates model
NASA	National Aeronautics and Space Administration
NOAA	National Oceanic and Atmospheric Administration
OAP	Orbital Average Power
OCS	Orbit Control Subsystem
PCB	Printed Circuit Board
PCU	Power Conditioning Unit
PDU	Power Distribution Unit
PEEK	Polyether ether ketone
PET	Polyethylenterephthalat
PID	Proportional-Derivative-Integral
POD	Precise Orbit Determination
PSD	Power Spectral Density
PTFE	Polytetrafluoroethylene, space-grade thermoplastic
QPSK	Quadrature Phase Shift Keying
REACH	European Parliament directive concerning the Registration, Evaluation, Authorisation and Restriction of Chemicals
RoHS	Restriction of Hazardous Substances in Electrical and Electronic Equipment
SM	Structural Model
SNR	Signal-to-Noise Ratio
SoC	state of charge
SSMS	Small Spacecraft Mission Service
SSO	Sun Synchronous Orbit
SVHC	Substances of Very High Concern
TCS	Thermal Control Subsystem
TML	Total Mass Loss
TT&C	Telemetry, Tracking and Command
UN COPUOS	United Nations Committee on the Peaceful Uses of Outer Space

1. Mission Introduction

In order to establish context for this report, section 1.1 will provide the background information of the mission, sections 1.2 to section 1.7 will provide the overview of the mission, system and report including the user requirements, the market analysis as well as the design and verification and validation philosophies.

1.1 Background

In the past decade, the number of satellites in Low-Earth-Orbit (LEO) (altitudes between 100 km and 1500 km) has risen by 180%, according to Boley et. al. [1]. This is primarily due to the increasing number of satellite constellations being deployed by large space-industry organizations. As shown in figure 1.1, this has also led to a growing number of payloads (as shown by the orange curve). In the future, this could lead to an increased number of debris, which, for several reasons, could decrease the rate of success of future space missions in that altitude range. From a design point of view, in the mission planning stage, collision avoidance strategies must be developed and additional delta-V budget must be assigned to spacecraft in order to account for collision avoidance scenarios with a margin. Furthermore, the options of orbital altitudes become limited, as to avoid high collision probabilities which would require such corrective measures. From an operational point of view, larger numbers of satellites and debris are leading to more frequent collision warnings, as well as a shorter time to react to such warnings [1], which, in turn, decrease mission life-time and affect mission success.

The sustainability of LEO space traffic management is directly linked to the uncertainty of orbital predictions, both in the short and long term. While the solutions to decrease this uncertainty adopted by most space missions currently are to avoid densely-populated orbits, intentionally de-orbit spacecraft in the end-of-life phase, or push them in "graveyard" orbits [1], these pose only short-term fixes to the problem. Pragmatically, the uncertainties themselves must be decreased, through the development of better orbit-propagation models that accurately predict external disturbances and therefore, decay. One of the most significant contributors to decay in LEO, which is also a source of uncertainty in these models, is **atmospheric drag** [2].

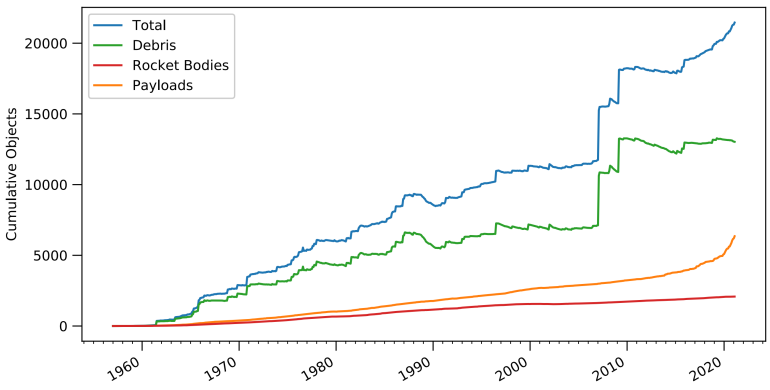

Figure 1.1: Cumulative on-orbit distribution functions (all orbits). Deorbited objects are not included. The 2007 and 2009 spikes are a Chinese anti-satellite test and the Iridium 33-Kosmos 2251 collision, respectively. The recent, rapid rise of the orange curve represents new-space satellite constellations [1].

The atmospheric drag of spacecraft in rarefied gas flows depends on two main aspects: the atmospheric conditions in the vicinity of the spacecraft (atmospheric composition, particle-number density, temperature, and the gas-surface-interaction (GSI) between the incoming flow particles), and the exposed areas of the spacecraft. Atmospheric properties are presently taken from empirical models derived from mass-spectrometer data collected in LEO, such as NRLMSISE-00 [3], and hence, have a limited accuracy. Furthermore, they require predictions of solar activity in the form of the F10.7 cm flux parameter, which strongly affects particle density [3]. As a result, these models show an error of up to 30% in their predictions of particle number density [3] and constitute one main source of error in predicting the drag force. GSI in drag models, on the other hand, is quantified by three parameters: the energy-accommodation coefficient, α, the normal momentum accommodation coefficient, σ_n and the tangential moment accommodation coefficient, σ_t. The physical meanings of these parameters are given in equation 1.1 [4]:

$$\alpha = \frac{T_{k_i} - T_{k_r}}{T_{k_i} - T_{wall}} \quad \sigma_n = \frac{p_{n_i} - p_{n_r}}{p_{n_i} - p_{n_s}} \quad \sigma_t = \frac{p_{t_i} - p_{t_r}}{p_{t_i} - p_{t_s}}, \tag{1.1}$$

where T_k is temperature in K, p_n is surface-normal momentum, p_t is surface-tangential momentum, and the i index indicates incident flow, while the r index indicates reflected flow, and s indicates surface-bound particles. Varying these parameters between their extreme values of 0 and 1 quantifies the type of particle scattering that occurs on a surface: for a value of 0, specular reflection is observed, while for a value of 1, diffuse reflection is observed. Any value in-between leads to quasi-specular reflection. These scenarios are shown in figure 1.2, figure 1.3 and figure 1.4:

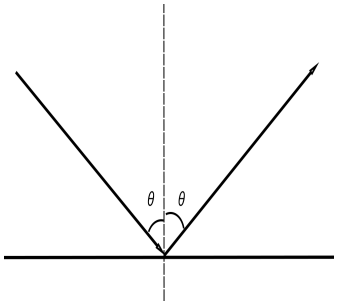

Figure 1.2: Specular reflection of gas particles on a surface.

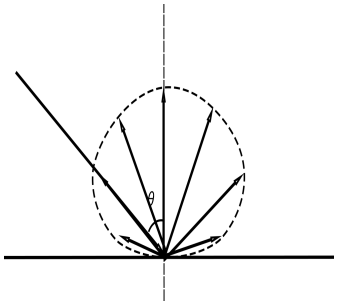

Figure 1.3: Diffuse reflection of gas particles on a surface.

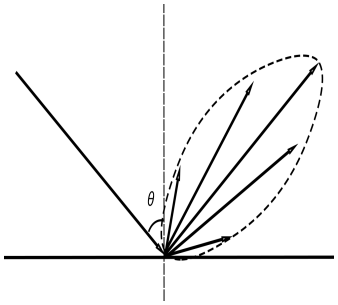

Figure 1.4: Quasi-specular reflection of gas particles on a surface.

The drag force experienced by spacecraft can vary up to 50% with these parameters [4], and therefore, they represent the largest source of uncertainty in drag modelling. Hence, to decrease this uncertainty, scientific missions must be planned to collect experimental data that can be used to determine the variation of these coefficients with altitude in LEO. Data collected from such missions can be used to validate and improve existing models, and hence allow for more accurate short and long-term orbit propagation predictions. To address the issues posed in section 1.1, a new mission is proposed in this report, namely **Project "Surface-gas Collision by Aerodynamic Twins for Theromspheric Experimental Research" (SCATTER)**. SCATTER has the following mission need statement:

Mission Need Statement: *"To ensure safe satellite operations in ever more densely populated orbits, there is a need to improve the current atmospheric drag modelling for more accurate trajectory predictions at altitudes in the range 100 – 600 kilometres by 2035."*

1.2 Mission and System Description

SCATTER plans to deploy by 2035, a pair of identical CubeSats into LEO, in the same orbit, at an altitude between 550 km and 600 km. In this orbital range, a significant change in the gas-surface interaction is expected, from more diffuse reflections with high energy accommodation at lower altitudes, to more specular reflections with less energy accommodation at higher altitudes. This, in turn, changes the drag coefficient significantly. Such a phenomenon is thought to occur due to varying oxygen concentration and temperature. The satellites shall decrease their altitude by means of propulsion as well as aerodynamic decay, and shall perform differential-drag formation flying at a given set of predetermined altitudes, by alternatively switching their orientations with 90° with respect to an axis perpendicular to the flow vector. For every scientific phase, the difference in drag force experienced by the satellites shall be recorded together with atmospheric composition, density and temperature, in order to compute the GSI accommodation coefficients specific to the altitude range of said phase. At the end of life, the satellites shall be de-orbited and burn up in Earth's atmosphere.

To perform this mission, the SCATTER system is composed of three elements: the space element, the ground element, and the launch element. Furthermore, direct interfaces with the Sun, for power generation, and a GNSS network, for orbit determination, shall exist with the space element. An overview of the elements constituting the SCATTER mission is given in figure 1.5.

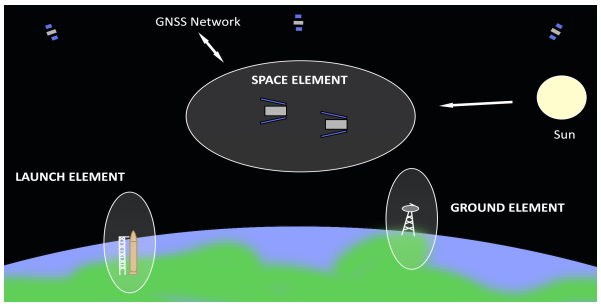

Figure 1.5: SCATTER Mission main elements and interactions.

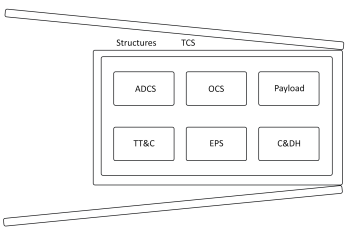

Figure 1.6: Overview of SCATTER space element and its subsystems.

As depicted in the figures, the SCATTER space element shall consist of the two satellites mentioned above. Each satellite is a system composed of several subsystems. These are the following:

- **The Structures Subsystem** - consisting of the spacecraft bus, it provides structural stability to the satellite and support to all other subsystems;

- **The Orbital Control Subsystem (OCS)** - consisting of the engines, the fuel tanks, radiators, controller and electronic components coming with these. Its main function is to control the orbit of the satellites;
- **The Attitude Determination and Control Subsystem (ADCS)** - consisting attitude determination sensors and attitude control actuators, it provides full control over the attitude and angular velocity of the satellites;
- **The Payload Subsystem** - consisting of mass spectrometers, GNSS receivers and accelerometers, it measures the satellite and atmospheric parameters enabling the on-ground computation of the drag coefficient throughout the mission;
- **The Telecommunication and Telecommand Subsystem (TT&C)** - consisting of transceivers and antennas, it ensures communication and data transfer between the space element and the ground element;
- **The Electrical Power Subsystem (EPS)** - consisting of photovoltaic panels and power storage units, it ensures the power required by all other subsystems is being generated, stored and provided;
- **The Command and Data Handling Subsystem (C&DH)** - consisting of the on-board flight computer, it sends commands and communicates with all the other subsystems;
- **The Thermal Control Subsystem (TCS)** - consisting of heat sinks, thermal blankets and heaters, it provides the necessary temperature ranges for nominal operation to all subsystems;

The solution SCATTER proposes to ensure a high sensitivity of its satellites to energy accommodation coefficient consists in the deployment of flat surfaces, in the form of solar panels, at shallow angles with respect to the incoming gas flow. These flat surfaces produce different drag for different levels of accommodation, due to the type of particle occurring. As portrayed in figure 4.8, figure 4.9 and figure 4.10, at a high level of accommodation, these surfaces shall experience mostly diffuse reflections which would lead to higher drag as compared to low accommodation levels. This design choice makes the satellites sensitive in the orientation having the solar panels pointed as shallow angles, and lacking sensitivity in any perpendicular orientation. The former is called a "low-drag" configuration, while the latter is called a "high drag" configuration. These are shown in figure 1.7. With the mission and system outlined, section 1.3 shall state the requirements given by the stakeholders of this mission.

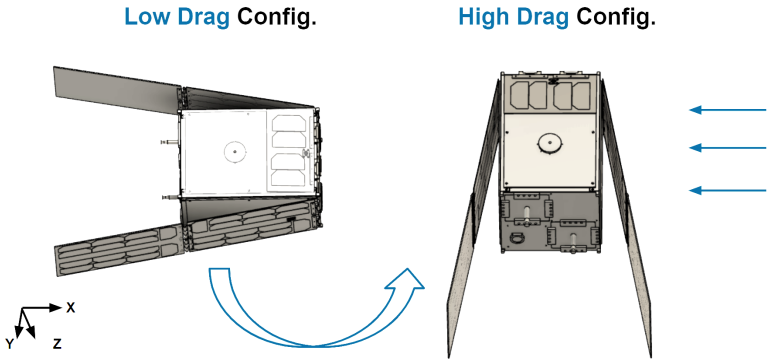

Figure 1.7: SCATTER satellite low and high drag configurations, in the body (B) frame.

1.3 User Requirements

In this section, the requirements coming from the stakeholders are outlined word-for-word. It should be noted that these requirements are not written in a "VALID" (Verifiable, Achievable, Logical, Identifiable and Definite) format, but shall be used instead to define mission and system-level requirements in chapter 3 and chapter 2. They are given below:

Table 1.1: Overview of User Requirements.

ID	Description
REQ-U-01	The mission shall be composed of at least two satellites
REQ-U-02	The shapes of the satellites shall be non-compact such that the contributions from pressure on the frontal surfaces and friction on the side surfaces change significantly for different satellite attitudes
REQ-U-03	The two satellites shall fly in the same orbit
REQ-U-04	The distance between the two satellites shall not exceed 500 km.
REQ-U-05	The satellites shall carry a multi-frequency GNSS receiver that allows on-ground orbit determination with an accuracy better than 10 cm for position
REQ-U-06	The satellites shall carry a mass spectrometer that is able to measure atomic oxygen (O) and helium (He) concentrations, and atmospheric temperature
REQ-U-07	The mission shall be composed of at least two satellites

REQ-U-08	The operational lifetime of the mission shall be at least one year
REQ-U-09	The mission shall consist of three distinct science phases.
REQ-U-10	In Phase I, science operations shall be performed at altitudes with helium concentration of at least 20 % in terms of number density.
REQ-U-11	In Phase II, science operations shall be performed between altitudes of 300 km to 400 km.
REQ-U-12	In Phase III, science operations shall be performed at altitudes below 300 km.
REQ-U-13	The satellites shall be able to perform 90° attitude changes in yaw and/or pitch.
REQ-U-14	The satellites shall be able to control their attitude within ±10° for at least one orbital revolution independent of their orientation with respect to the atmospheric flow.
REQ-U-15	Thrusters shall not be used for attitude control.
REQ-U-16	The satellites shall carry an attitude sensor with an average accuracy of 1° for the inertial attitude.
REQ-U-17	The satellites shall carry an attitude sensor with an accelerometer to measure the non-gravitational accelerations during the final science phase.
REQ-U-18	The mission shall withstand the radiation environment during the entire lifetime.
REQ-U-19	The required response collision avoidance between two satellites shall be analysed.
REQ-U-20	A procedure for collision avoidance between two satellites shall be implemented.
REQ-U-21	The overall mission's availability and reliability shall be estimated.
REQ-U-22	Radioactive materials shall not be used.
REQ-U-23	The satellites shall be de-orbited after maximum lifetime.
REQ-U-24	The satellites shall burn-up completely during re-entry.
REQ-U-25	The satellites shall be shaped such that the ratio of the areas of the surfaces perpendicular and parallel to the atmospheric flow changes by factor of three or more when changing the attitude by 90 ° in yaw or pitch.
REQ-U-26	The data rate of the downlink shall be sufficient to transmit measurements from all scientific instruments operating at a measurement rate of 0.1 Hz .
REQ-U-27	COTS options shall be included in the trade-off analysis whenever possible.
REQ-U-28	The satellites shall have a propulsion system for orbit and formation control.
REQ-U-29	The launch shall be no later than 2035.
REQ-U-30	The cost of the mission shall not exceed €10 million, excluding the costs of launch and operation.
REQ-U-31	An estimation of the costs for launch shall be provided.

With these requirements defined, a market analysis is now performed in section 1.4.

1.4 Market Analysis

Since 2009 to 2020, the global turnover of the space economy has grown from $216.6 billion a year to $446.88 billion a year when, in 2020, 50% of the turnover was accounted for by commercial space services and products. The global satellite industry revenue production has also grown from $106 billion in 2006 to $271 billion in 2020 [1]. The spacecraft market is also projected to have a compound annual growth rate (CAGR) of 8% in the period between 2022 and 2027 [2]. By the time of the mission's launch in 2034, the market can be expected to have grown even further. This rapid growth bodes well for the future interests of space missions due to the active market and potential for investment. However, to better understand the market, it is still necessary to conduct a market analysis, which will be done in this section. Derived from the market analysis were the market-based requirements, which are listed in table 1.2.

Table 1.2: Market-based requirements for the SCATTER Mission.

Identifier	Requirements	Rationale
REQ-MARK-01	The data from the mission shall be open source and FAIR (findable, accessible, interoperable and reusable)	Since it is a scientific mission, having an open source data would be beneficial to the scientific community and to the space traffic management globally.
REQ-MARK-02	The space element shall leave the TT&C active during re-entry to fulfil the potential opportunity to transmit data during this phase.	The TT&C may not necessarily be able to transmit usable data, but the subsystem can remain active in case it can to maximise altitude-diverse data gathered (passivation of the spacecraft is not necessary for satellites re-entering from LEO [3]).

[1] `https://www.statista.com/topics/5049/space-exploration/#topicHeader__wrapper`, retrieved on 29-04-2022
[2] `https://www.mordorintelligence.com/industry-reports/spacecraft-market`, retrieved on 29-04-2022
[3] `https://room.eu.com/article/Down_to_Earth_how_to_deorbit_satellites_and_save_money`, Retrieved on: 09-05-2022

1.4.1 Market Need

Many satellites are placed in LEO as less fuel is required to send satellites to a lower orbit compared to a higher one. Additionally, it allows for efficient communication and navigation due to the availability of high bandwidth and the low communication latency. And it allows for high resolution imaging of the Earth's surface and weather as well as recording data on the atmosphere, magnetosphere, etc. for scientific and commercial purposes [4]. This makes LEO very densely populated. One of the disadvantages of LEO is that satellites in this region experience high atmospheric drag which can lead to rapid orbital decay and uncertainty in orbital positioning.

Due to the large uncertainties in orbit prediction models, orbit prediction models are very conservative when calculating collision probabilities. As collision warnings that result from these probabilities are both costly in time and resources, the aerospace industry has interest in reducing orbital prediction uncertainties [5]. This can be done by better modelling of the atmospheric drag coefficient in LEO, which is the goal of this mission.

Thus, the primary driver of demand for this mission in the market is the need for improvement of gas-surface interaction (GSI) models. By finding a more accurate value of the aerodynamic drag coefficient C_D, this mission can improve the drag modelling aspect of orbital prediction models: a relation which is visualized in figure 1.8. Following these improvements, C_D could be determined more accurately for given spacecraft shapes and atmospheric conditions [5]. Based on the given driver of demand, the market can be divided into segments. Then, the target market for the product of this mission can be identified.

1.4.2 Target Market

In order to establish the product development plan and provide a market prediction, the target market for the designed satellites needs to be specified. This leads to figure 1.8, where three groups of potential customers are derived from the driver of demand, with the representative participants listed.

Firstly, an improved GSI model with high accuracy can be regarded as progress in applied physics research. Therefore, it is reasonable to identify scientific communities who are focusing on this area as potential customers. The most significant representative participant included in this group is the aeronomy community [6].

Moreover, the improvement of the accuracy of GSI model will further lead to more accurate orbit prediction, including orbit decay prediction. Customers with various characteristics could be seen as being possible to provide financial supports for the benefits of orbital prediction with higher accuracy. Space agencies such as the European Space Agency (ESA) and the National Aeronautics and Space Administration (NASA) can be recognized as the main potential customers. The primary reason is the improvement of orbit prediction models, which leads to a reduction in collision warnings. Too many warnings and avoidance manoeuvres may interrupt the normal mission operations of the satellites. A more efficient collision warning system, based on improved orbital prediction results, will help decrease the number of warnings. Moreover, improved orbit decay analysis can help perform delta-V budget analysis for orbital station-keeping. In addition to that, ESA had an annual budget of 6.4 billion EURO in year 2021 [7], while NASA has an annual budget of 23.2 billion US Dollar [8]. This means that space agencies have relatively high purchasing power. For the same reasons, commercial aerospace companies, such as SpaceX, MAXAR and SES, are also identified as potential customers.

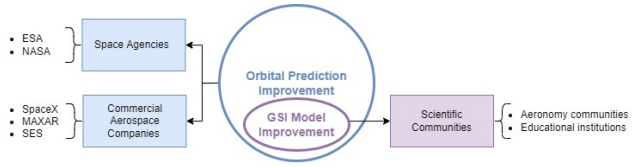

Figure 1.8: Target market segmentation showing the demand drivers in circles and the consequent market segments in boxes.

1.4.3 Competition Assessment

Apart from considering the market need and the target market, competition also has to be considered. Similar missions or upcoming advances in alternative methods endanger the need of the mission as the timeline between the development and the launch date is long.

The SOAR (Satellite for Orbital Aerodynamics) mission of the DISCOVERER project [9] was a fairly recent mission that specifically studied the GSI aspect of the VLEO orbit (less than 420 km of altitude as it was launched from ISS [10]). Even though the SOAR mission is similar to the later phase of the SCATTER mission where the altitude is low, the main benefit for SCATTER is the measurement of atmosphere drag above 450 km, as drag is a large contributor to the perturbing forces up to 600 km [6] and many active satellites fly in the range of 400 km to 600 km [7]. There do not seem to be any direct competitions in the market at the moment since this is a specific scientific

[4] `https://www.universetoday.com/85322/what-is-low-earth-orbit/`, retrieved on 29-04-2022
[5] `https://aerospace.org/Annual-Report-2018/creating-path-through-contested-space`, Retrieved on: 09-05-2022
[6] `https://gsil.engr.uky.edu/`, retrieved on 28-04-2022
[7] `https://www.esa.int/Newsroom/ESA_budget_2021`, retrieved on 29-04-2022.
[8] `https://www.planetary.org/space-policy/nasas-fy-2021-budget`, retrieved on 29-04-2022.
[9] `https://discoverer.space/soar-satellite-for-orbital-aerodynamics-research/`, retrieved on 29-04-2022.
[10] `https://www.heavens-above.com/orbit.aspx?satid=25544`, retrieved on 29-04-2022.

mission targeting few groups as shown in figure 1.8.

Market SWOT Analysis

In order to better capture the state of the market and assess the position of the SCATTER mission relative to it, a market SWOT (strengths, weaknesses, opportunities and threats) analysis has been made.

The most important strength would be the strong aerospace presence in Europe, from both commercial companies and also ESA. These usually fund and/or contribute to the development of scientific missions in space, making logistics easier and forming a knowledge hub in the region.

The most significant weaknesses would be the uncertainties that arise from the pandemic and the Russian invasion in Ukraine. These events hinder logistics on the continent, decrease the monetary resources available for space missions, increase the prices of components and transportation etc.

Figure 1.9: Market SWOT analysis diagram of the Small Satellite for Aerodynamics mission. Formatted according to [8].

The most important opportunity would be the potential impact of the scientific data. With more data about GSI and better aerodynamic prediction models, other future space missions might require smaller safety margins for collision avoidance propellant, making the operation cheaper, increasing the amount of missions that come to fruition and decreasing unnecessary warnings, which in turn reduces the operational costs. The most significant threat would be if a competitor implements the same mission before our team. If this happens, and the competitor decides to have the data open source, available to the public, the current mission would lose its main purpose and the resources would most probably be reallocated. This would lead to an end of the mission.

1.5 Design Philosophy

While the ability to fulfil the mission objectives with a considerable margin is naturally the primary goal of the design, this cannot be the only factor which drives engineering decisions on a system or subsystem level. This is because other practical constraints to the design could hinder its feasibility for manufacturing and launch. Therefore, to ensure that the design respects the interests of all stakeholders, the following factors will be considered throughout the complete design process from conceptual to detailed design: design performance, cost, reliability and safety, sustainability and cost. The relative importance of each and when they were considered throughout the design procedure will be addressed in the list below:

- **The performance of the engineering system** is naturally one of the primary factors to consider in the engineering process. If the engineering product does not satisfy the primary mission objectives set by the stakeholder then the mission has no reason for taking place. Therefore such objectives must held to the highest regard unless current technologies make the mission virtually impossible, or the consequence of cost and/or risk is too great.
- While **cost** is not a primary concern in comparison of performance of an engineering system, it must always be kept into consideration, especially when considering the selection of exact engineering products. If the project runs over-budget, there is a risk that key stakeholders stagnate progress by stopping the funding. However, in certain cases if the mission objectives require the development of novel technologies, then an increase in cost may be an inevitable consequence. Therefore, in the engineering process the team must determine whether the obtaining of certain mission objectives outweighs the downside of extra expenses.

- **Reliability and Safety** is an aspect that the team must hold to the highest regard if it impacts the well-being for human lives. With regard to the reliability of certain components, most components must have a probability of failure below a certain threshold in order to be certified for use in space. In the case that the probability of failure is violated, then redundancies may be needed.
- **Sustainability** follows a similar philosophy as that of cost. Unsustainable concepts may lead to authorities preventing the concept from being manufactured and operated. However, these sustainability requirements may need to be violated in the interest of increased performance.

1.6 Verification and Validation Philosophy

Throughout several stages of the detailed design of SCATTER, verification and validation procedures were needed for either the design itself, or for specific numerical tools developed to advance this design to higher levels of detail. These procedures are split into three categories in this report, which are discussed below:

- **Design Verification Procedures** - design verification can be done at a system or subsystem level, and it implies compliance with the outlined requirements for said system or subsystem. Compliance can be achieved through four methods: inspection, analysis, demonstration and testing [9]. If a requirement must be verified through testing or demonstration, due to lack of information, this report shall only provide a proposed procedure of verification. However, if analysis or inspection is used as a verification method, this shall be done by use of existing design information and calculations. For requirements that cannot be verified through analysis or inspection that are not satisfied by the current design, a mitigation strategy shall be added as a recommendation in chapter 19;
- **Design Validation Procedures** - design validation is done at a system level only, and implies the comparison of existing design parameters with those from designs of similar missions. The design is considered validated if the discrepancies between subsystem budgets (in terms of mass, power or cost) can be explained by different design decisions taken by SCATTER w.r.t. the comparison case;
- **Software Verification and Validation** - any software designed to size subsystems or the mission of SCATTER at a detailed level shall be validated with literature data. Similar scenarios to those simulated by the software, outlined in research papers, shall be recreated using the software and simulated. The results shall be compared against one another. They shall be considered similar if the following conditions apply. If the software to be validated uses a numerical solver of any kind, the results it produces shall be validated in a quantifiable way, using a minimum R^2 value of 0.85. This is chosen as to ensure proper correlation with reality for extreme cases simulated with said software. If a part of a software computing parameters is based on analytical equations, it is sufficient to validate it qualitatively, in case not enough data is published in said paper to completely describe the initial conditions of the simulation.

While arbitrary, the verification and validation philosophy outlined above is considered to ensure sufficient confidence in the predictions and estimations of parameters used in this report. As such, it will be applied throughout.

1.7 Report Outline

With all general aspects of the SCATTER project covered in the sections above, the structure of the report is summarized in this paragraph. The report begins in chapter 1 with a general overview of the mission, system, development philosophies and organizational matters. Next, in chapter 2, an overview of the system-level requirements, and procedures leading up to the preliminary design of SCATTER is summarized. Following this, an extensive overview of the SCATTER mission is given in chapter 3, including life-time, kinematic, aerodynamic and budget estimations for all science and operational phases, from launcher separation until de-orbiting. With the closure of this chapter, the different subsystems of SCATTER begin to be discussed and sized to a detailed level, starting with Aerodynamic design in chapter 4 up to chapter 12. After the latter chapter, the integration of all these subsystems is given in chapter 13, together with the integration of the space element with the chosen launcher, Vega-C. This chapter concludes the description of the detailed design, and it is followed by the system-wide verification and validation procedures performed on it in chapter 14, which concludes with a series of compliance matrices for all defined requirements. The report is concluded with several matters for future stages of the design, namely the manufacturing assembly and testing plan in chapter 15 and the project design and development logic in chapter 16, as well as a sustainability overview of the current design in chapter 17 and a technical risk assessment in chapter 18. The final chapter of the report, chapter 19, provides conclusion based on the current design and recommendations for future development.

2. System Overview

This chapter presents an extensive overview of the SCATTER system, and its evolution throughout the organizational stages of the project, from a series of design concepts up to the preliminary design. The chapter begins with a functional analysis of SCATTER in the form of a functional flow diagram (FFD) and a functional break-down structure (FBS). Next, the system-level requirements of SCATTER are given in section 2.2, together with the rationales behind them. Following this, an overview of the considered design concepts and their trade-off is shown in section 2.3. Finally, the preliminary design is presented in section 2.4.

2.1 System Functional Flow Diagram & Breakdown Structure

The functional flow diagram and the functional breakdown structure are presented for the SCATTER mission in figure A.1. These diagrams expand the 6 mission phases (Launch and Preparation, Launcher Separation, Phase I, Phase II, Phase III and End of Life) up to 3 levels of detail, and specifically describe the operational sequences in all science phases.

2.2 System Requirements

The requirements of the SCATTER system are outlined in this section and are split into 7 categories: functional requirements - flowing from the FFD and FBS, performance requirements - linked to functional requirements, design requirements, legal constraints, resource constraints, safety constraints and sustainability constraints. The functional requirements of SCATTER are given below:

Table 2.1: System Functional Requirements.

ID	Description	Rationale
REQ-SYS-F-01	~~From 30 minutes before launch onwards, the space element shall supply power to the C&DH and ADCS subsystems.~~	- Crossed out because there is no communication with launcher [10].
REQ-SYS-F-02	The space element shall withstand the structural static loads given in the Vega-C Launcher Vehicle Catalogue without permanent damage to any subsystem	Any permanent damage to any subsystem following launch will directly inhibit the satellite's ability to fulfil the scientific objectives in space. Derived from block 1.7 in FFD
REQ-SYS-F-03	The space element shall withstand the structural dynamic loads given in the Vega-C Launcher Catalogue without permanent damage to any subsystem	Any permanent damage to any subsystem following launch will directly inhibit the satellite's ability to fulfil the scientific objectives in space. Derived from block 1.7 in FFD.
REQ-SYS-F-04	The space element shall not exert structural loads which are beyond the limits stated in the Vega-C Launcher Catalogue	Any damage to the launch vehicle will negatively impact launcher performance, which can therefore jeopardize nominal orbital insertion and fairing separation. Derived from block 1.7 in FFD.
REQ-SYS-F-05	The space element shall not experience constructive mechanical oscillations during launch.	Constructive mechanical oscillations add an external force on the entire launch vehicle which can adversely impact the controllability and structural integrity of the launch vehicle. Derived from block 1.7 in FFD.
REQ-SYS-F-06	~~From 30 minutes before launch onward, the space element shall exchange housekeeping data with the launcher.~~	Crossed out because the launcher does not communicate with the satellites [10].
REQ-SYS-F-07	The space element shall separate from the Vega-C launcher fairing.	Derived from all the mission objectives in chapter 3 and block 2.1 in FFD.
REQ-SYS-F-08	The system shall initialize its subsystems following launcher separation	Derived from all mission objectives outlined in chapter 3. Derived from blocks 2.2, 2.3 and 2.4 in FFD.
REQ-SYS-F-09	~~During operational phase, the space element shall measure the helium and oxygen number densities in LEO, between 300 km and 550 km~~	Crossed out as it is a mission requirement
REQ-SYS-F-10	~~During operational phase, the space element shall measure the atmospheric temperature in LEO, between 300 km and 550 km~~	Crossed out as it is a mission requirement
REQ-SYS-F-11	~~The space element shall measure the translational acceleration in LEO, between 300 km and 550 km~~	Crossed out as it is a mission requirement
REQ-SYS-F-12	The space element shall store all measured scientific data onboard while out of range of the ground element	Data that is collected from the payload cannot be sent in real-time due to range constraints and shadowing from the Earth's surface (assuming one ground station) and should not be lost. Derived from block 3.2, 4.2 and 5.2 in FFD
REQ-SYS-F-13	The space element shall transmit all the measured scientific data to the ground element	Derived from functional flow diagram block 3.2 for acquisition of key scientific data. Derived from blocks 3.3, 4.3 and 5.2 in FFD.
REQ-SYS-F-14	The space element shall receive telecommands from the ground element.	Derived from FFD block 3.3, 4.3 and 5.3.
REQ-SYS-F-15	~~The space element shall execute the commands which are received from the ground element~~	Struck out as it is a duplicate requirement.
REQ-SYS-F-16	The space element shall operate in the temperature conditions experienced in Low Earth Orbit	Any environmental damage to the satellite can inhibit its ability to fulfil scientific objectives and acquire data. Derived from blocks 3.1, 4.1 and 5.1, as well as 3.4, 4.4 and 5.4.
REQ-SYS-F-17	The space element shall operate in the pressure conditions experienced in Low Earth Orbit	Any environmental damage to the satellite can inhibit its ability to fulfil scientific objectives and acquire data. Derived from blocks 3.1, 4.1 and 5.1, as well as 3.4, 4.4 and 5.4.
REQ-SYS-F-18	The space element shall operate in the radiation conditions experienced in Low Earth Orbit	Any environmental damage to the satellite can inhibit its ability to fulfil scientific objectives and acquire data. Derived from blocks 3.1, 4.1 and 5.1, as well as 3.4, 4.4 and 5.4.
REQ-SYS-F-19	The space element shall operate in the magnetic conditions experienced in Low Earth Orbit	Any environmental damage to the satellite can inhibit its ability to fulfill scientific objectives and acquire data. Derived from blocks 3.1, 4.1 and 5.1, as well as 3.4, 4.4 and 5.4.
REQ-SYS-F-20	The space element unit shall determine its attitude.	Derived from all the mission objectives stated in chapter 3. Derived from blocks 2.4, 3.1, 4.1 and 5.1 in FFD
REQ-SYS-F-21	The space element unit shall control its attitude	Derived from all the mission objectives stated in chapter 3. Derived from blocks 2.4, 3.1, 4.1 and 5.1 in FFD
REQ-SYS-F-22	The space element shall know its position and velocity following the de-tumbling phase	Derived from all the mission objectives stated in chapter 3. These parameters play a role in the drag coefficient computation, and the control of the space element. Derived from blocks 3.1, 4.1, 5.1 and 2.8 in FFD
REQ-SYS-F-23	The space element shall control its orbit	Derived from all the mission objectives stated in chapter 3. This ensures the science phases described in chapter 3 are performed. Derived from block 2.8 in FFD

REQ-SYS-F-24	The space element shall be able to change its projected area to the orbital path.	Derived from all the mission objectives stated in chapter 3. This ensures the science phases described in chapter 3 are performed. Derived from blocks 3.1, 4.1, 5.1, 4.5 and 5.5 in FFD.
REQ-SYS-F-25	~~The space element shall stow appendages when reentering the atmosphere.~~	Crossed out as the space element will burn up under any orientation. Derived from blocks 6.2.1 and 6.2.2 in FBS.
REQ-SYS-F-26	~~The space element shall deactivate the TCS, ODCS and ADCS when re-entering the atmosphere.~~	Crossed out as these operations are deemed unnecessary for fulfilling the mission.
REQ-SYS-F-27	Electronic components shall be protected against electrical overloads.	Derived from risk assessment and mitigation strategies in chapter 18. Derived from blocks 3.4, 4.4 and 5.4 in FFD
REQ-SYS-F-28	~~The space element shall initialize ODCS, GNSS and TT&C subsystems after detumbling.~~	Crossed out, as it is already covered by REQ-SYS-F-08.
REQ-SYS-F-29	During the final countdown and ascent phases of the mission, all electronic components of the space element shall be switched off.	Based on VEGA-C launcher constraints that apply to CubeSat integration [10]. Derived from block 2.1.3 in FBS
REQ-SYS-F-30	The space element shall not require external power from the launcher during the launch phase.	Based on VEGA-C launcher constraints that apply to CubeSat integration [10]. Derived from block 2.1.3 in FBS
REQ-SYS-F-31	All electronic components shall interface with the C&DH subsystem.	To receive and execute the telecommands without having antennas for each subsystem, the data will pass through C&DH, which is then passed on to all other subsystems. Interfacing is therefore necessary. Derived from block 2.2.3 in FBS

The performance requirements of SCATTER are given below:

Table 2.2: System Performance Requirements.

ID	Description	Rationale
REQ-SYS-P-01	~~From 30 minutes before launch onwards, the space element shall supply power to the C&DH and ADCS subsystems.~~	Crossed out as the Vega-C launcher does not provide power to the satellites [10]
REQ-SYS-P-02	The space element shall operate within a temperature range of at least 173 K to at most 373 K.	This was found to be the most critical temperature range using results from a thermal analysis on a flat plate of 6 CubeSat Units
REQ-SYS-P-03	The space element shall operate in space conditions within altitudes of 150 km to 600 km for at least 3 years.	Derived from the lifetime estimations of the mission in chapter 3
REQ-SYS-P-04	The space element shall operate nominally at a pressure range of 10 Pa to 105 Pa.	Derived from expected mission altitudes calculated in chapter 3 and the NRLMSISE-00 model data [3]
REQ-SYS-P-05	The space element shall operate nominally under a dynamic load range of 10 g in all body-axes	This dynamic load range is to be expected based on the dynamic load range of the Vega-C rocket for CubeSAT deployers. [3]
REQ-SYS-P-06	~~The space element units shall orient their antennas with a pointing accuracy of TBD deg~~	Crossed out as it is a subsystem requirement and constrains the design space
REQ-SYS-P-07	The space element units' orbital position shall be known with an accuracy of at least 10 cm in Euclidean distance	Derived from REQ-U-05
REQ-SYS-P-08	The space element unit shall be able to maintain its attitude around the x-axis with respect to the body axis frame with an accuracy of at least 5° for the duration of at least 48 hours.	Angle derived from the maximum error of existing drag models of 20 % [11], and duration estimated from science mode time estimates in chapter 3.
REQ-SYS-P-09	The space element unit shall be able to orient itself with a magnitude of at least 90° around the x-axis with respect to the body axis frame, within a time of 180 seconds.	Derived from REQ-U-13 regarding changes in roll and pitch. The time was chosen to allow for high momentum storage, while not affecting the science-mode-spent time in the mission given in chapter 3.
REQ-SYS-P-10	The space element shall measure the atmospheric temperature with an absolute error of at most 60 K.	This value was derived from a 10% error on the minimum expected temperature during the mission according to the NRLMSISE-00 model as current models have an uncertainty around 10% [3].
REQ-SYS-P-11	The space element shall measure the atmospheric temperature with a frequency of at least 0.1 Hz.	Derived from REQ-U-26.
REQ-SYS-P-12	The space element shall measure the helium particle concentration with an absolute error of at most 10^{11} m^{-3}.	Derived from the maximum allowed ΔC_{D_α} error of 20 % [11], the accuracy of NRLMSISE-00 density data [3] and the estimated orbital range of the mission from chapter 3.
REQ-SYS-P-13	The space element shall measure the helium particle concentration with a frequency of at least 0.1 Hz.	Derived from the REQ-U-26.
REQ-SYS-P-14	The space element shall measure the atomic oxygen particle concentration with an absolute error of at most 10^{10} m^{-3}	Derived from the maximum allowed ΔC_{D_α} error of 20 % [11], the accuracy of NRLMSISE-00 density data [3] and the estimated orbital range of the mission from chapter 3.
REQ-SYS-P-15	The space element shall measure the atomic oxygen particle concentration with a frequency of at least 0.1 Hz.	Derived from the REQ-U-26.
REQ-SYS-P-16	The space element shall measure its non-gravitational acceleration with an accuracy of at least $2 \cdot 10^{-7}$ m^2 s^{-1}.	Derived from the maximum allowed ΔC_{D_α} error of 20 % [11], the accuracy of NRLMSISE-00 density data [3] and the estimated orbital range of the mission from chapter 3.
REQ-SYS-P-17	The space element shall measure its acceleration with a frequency of 0.1 Hz.	Derived from REQ-U-26.
REQ-SYS-P-18	The satellite shall have a minimum Signal-to-Noise ratio of 3 dB for effective ground communication.	Derived from Space Mission Engineering: The New SMAD [12]
REQ-SYS-P-19	The satellite shall operate without communication with the ground station for at least 3 days.	Derived from de-tumbling simulations which take up to two days after which a safety margin of one day was applied
REQ-SYS-P-20	The space element unit shall be able to maintain its attitude around the y-axis with respect to the body axis frame with an accuracy of at least 5° for the duration of at least one orbital revolution.	Angle derived from the maximum error of existing drag models of 20 % [11], and duration estimated from science mode time estimates in chapter 3.
REQ-SYS-P-21	The space element unit shall be able to maintain its attitude around the z-axis with respect to the body axis frame with an accuracy of at least 5° for the duration of at least one orbital revolution.	Angle derived from the maximum error of existing drag models of 20 % [11], and duration estimated from science mode time estimates in chapter 3.
REQ-SYS-P-22	The space element unit shall be able to orient itself with a magnitude of at least 90° around the y-axis with respect to the body axis frame, within a time of 180 seconds.	Derived from REQ-U-13 regarding changes in roll and pitch. The time was chosen to allow for high momentum storage, while not affecting the science-mode-spent time in the mission given in chapter 3.
REQ-SYS-P-23	The space element unit shall be able to orient itself with a magnitude of at least 90° around the z-axis with respect to the body axis frame, within a time of 180 seconds.	Derived from REQ-U-13 regarding changes in roll and pitch. The time was chosen to allow for high momentum storage, while not affecting the science-mode-spent time in the mission given in chapter 3.
REQ-SYS-P-24	The data storage system of the space element shall be able to store at least 300 Megabytes of data.	Derived from the measurement frequency, an average ground contact time of 30 minutes [12], with a safety factor of 2.
REQ-SYS-P-25	The space element shall store all measured scientific data onboard while out of range of the ground element for at least 3 days.	Time range derived from estimated de-tumbling time computed in chapter 3

The design requirements of SCATTER are given below:

Table 2.3: System Design Requirements.

ID	Description	Rationale
REQ-SYS-D-01	The space element units shall have a natural frequency higher than 115 Hz, by a margin of 5 Hz.	Derived from the Vega-C SSMS specified launch natural frequencies [10].
REQ-SYS-D-02	The space element shall fit in the fairing of the launcher, with a minimum clearance of 1 mm.	Distance estimated with computed perpendicular elastic deflections of a standard 12U CubeSat under the Vega-C launch loads [10]
REQ-SYS-D-03	The space element shall have a launch mass below 35 kg per satellite.	This requirement is derived from the Vega-C SSMS maximum mass allowed for CubeSats [10].
REQ-SYS-D-04	~~The space element shall draw a maximum power of TBD W from the launcher during launch phase.~~	Crossed out as the space element doesn't draw power from launcher
REQ-SYS-D-05	~~The space element shall have a minimum Delta V budget of 150 m/s.~~	Crossed out because it is a fluid budget more than a hard requirement.
REQ-SYS-D-06	The space element shall have a shape such that the ratio of the areas of the surfaces perpendicular and parallel to the atmospheric flow changes by a factor of three or more when changing the attitude by 90° in yaw or pitch	Derived from REQ-U-25.
REQ-SYS-D-07	The space element shall fit inside a $390 \times 244 \times 244\,\mathrm{mm}^3$ volume	Derived from the Vega-C SSMS maximum volume for CubeSats [10].
REQ-SYS-D-08	The space element shall not contain materials that outgas with a Total Mass Loss greater than 1%	Derived from Vega-C SSMS outgassing criteria [10].
REQ-SYS-D-09	The space element shall not contain materials that outgas with a Collected Volatile Condensable Material greater than 0.1%.	Derived from Vega-C SSMS outgassing criteria [10].

The legal constraints of SCATTER are given below:

Table 2.4: System Legal Constraints.

ID	Description	Rationale
C-LEGAL-01	The space element shall comply with the International Telecommunications Union (ITU) standards while communicating with the ground element.	Derived from all mission objectives outlined in chapter 3 and the ITU regulations [1].
C-LEGAL-02	The space element operations shall comply with the national space legislation of the nations involved in construction and development of the mission.	Derived from all mission objectives outlined in chapter 3
C-LEGAL-03	The space element operations shall comply with the national space legislation of the country from which the space element is launched.	Derived from all mission objectives outlined in chapter 3
C-LEGAL-04	The space element shall comply to the regulations stipulated in the international space treaties to which the construction and development nations are bound.	Derived from all mission objectives outlined in chapter 3
C-LEGAL-05	The space element shall comply to the regulations stipulated in the international space treaties to which the launching nation is bound.	Derived from all mission objectives outlined in chapter 3
C-LEGAL-06	The system shall comply with the European Cooperation for Space Standardization (ESCC).	Derived from all mission objectives outlined in chapter 3
C-LEGAL-07	The space element shall be able to demonstrate its technical and programmatic innocuousness for the main passenger in case of a piggyback mission.	Derived from Vega-C SSMS specified main conditions for piggyback missions.
C-LEGAL-08	The space element shall in no case be entitled to affect the launch schedule in case of a piggyback mission.	Derived from Vega-C SSMS specified main conditions for piggyback missions.
C-LEGAL-09	A dummy payload shall be provided in case the space element is not ready for launch.	Derived from Vega-C SSMS specified main conditions for piggyback missions.

The resource constraints of SCATTER are given below:

Table 2.5: System Resource Constraints.

ID	Description	Rationale
C-RES-01	The mission cost shall not exceed 10 million euros (2022 inflation [2]), excluding the costs of launch and operations.	Derived based on REQ-U-30.
C-RES-02	The mission shall launch no later than January 1st, 2034.	Derived from REQ-U-29 and the risk mitigation strategies given in chapter 18.
C-RES-03	~~The upper bound of the mission launch costs shall be estimated with a maximum error of 3%.~~	Crossed out as requirement is impossible to verify with existing information
C-RES-04	~~The upper bound of the mission operations costs shall be estimated with a maximum error of 3%.~~	Crossed out as requirement is impossible to verify with existing information
C-RES-05	At least two suppliers should be considered for any mission-critical, externally-manufactured component in the system.	Derived from the risk mitigation strategies in chapter 18
C-RES-06	The space element of the mission shall be insured for launcher failure.	Derived from the risk mitigation strategies in chapter 18

The safety constraints of SCATTER are given below:

Table 2.6: System Safety Constraints.

ID	Description	Rationale
C-SAFE-01	~~The space element shall not use radio-active materials in an amount larger than 0.1 g.~~	Crossed out as it is replaced with C-SUS-01
C-SAFE-02	~~The space element shall burn-up during the de-orbiting phase~~	Struck out as it is replaced by C-SAFE-06
C-SAFE-03	~~The space element shall implement a collision avoidance strategy for other registered LEO satellites~~	Struck out as it is a sustainability requirement
C-SAFE-04	Safety factors of at least 1.25 shall be used when designing the system.	Derived from the risk analysis outlined in chapter 18
C-SAFE-05	The response time of the inter-satellite collision avoidance sequence shall be below 5 hours.	Derived from the risk analysis outlined in chapter 18 and an assumed collision probability of $1e-6$ [13]
C-SAFE-06	Upon burn-up, the space element shall not produce falling debris heavier than 100 g	Derived from the risk analysis outlined in chapter 18 and mass derived from an average mass of hail.

[1] `https://www.itu.int/pub/R-REG-RR`

[2] `https://www.officialdata.org/us/inflation/2018?endYear=2035&amount=7000000000000&future_pct=0.03`, retrieved on 21/06/2022.

The sustainability constraints of SCATTER are given below:

Table 2.7: System Sustainability Constraints.

ID	Description	Rationale
C-SUS-01	The satellites shall use non-toxic propellants which comply with the Regulation, Evaluation, Authorization and Restriction of Chemicals (REACH) agreement.	Derived from the sustainability strategy outlined in chapter 17
C-SUS-02	The space element shall implement a collision avoidance strategy for other registered LEO satellites	Derived from the sustainability strategy outlined in chapter 17

With all requirements outlined, section 2.3 provides a description of the conceptual designs and trade-off process performed to obtain the preliminary design of SCATTER.

2.3 Trade-Off Summary

In this section, the 5 design concepts considered for SCATTER, as well as the trade-off procedure and results are outlined. The 5 concepts take different approaches at solving the problem posed by the mission of formation flying using differential drag. Besides the performance aspect, reliability, cost and sustainability have also been considered when generating them. The five options are given below:

- **Concept 1 - CubeSat design with active aerodynamics via rotating panels**: Concept 1 aims to benefit from a standardized CubeSat frame for lower cost, but with active aerodynamics (through the usage of rotating panels) in order to increase its sensitivity to gas-surface interaction. The rotating panels themselves shall contain solar cells attached onto them, while also allowing for a larger surface area behind them, where additional solar arrays can be added for power generation. Due to the primary body being shaded from the sun by the panels, passive thermal control is likely to be sufficient.
- **Concept 2 - CubeSat based design with passive aerodynamics**: Concept 2 aims to benefit from its simplicity, which in turn translates into its high reliability and low development cost. In order for such a design to satisfy the aerodynamic requirements of the mission, it is likely that a non-standard shape is required, such as 1x2x6U design. In order to accommodate for the power requirements, all the long frontal faces are to be covered with solar cells. Throughout operation, a large amount of surface area will be exposed to sunlight, therefore this concept would likely require active thermal control.
- **Concept 3 - Prismatic aerodynamic design with passive aerodynamics** The prismatic aerodynamic design aims to maximize the possible aerodynamic features of a small satellite to accomplish the scientific objectives. Due to the diagonal faces, a larger surface area can be covered with solar cells as they will all be exposed to partial sunlight. This is also beneficial from a thermal design perspective as no face will be directly exposed to the sunlight, so passive thermal control is likely to be sufficient.
- **Concept 4 - CubeSat design with deployed solar panels and passive aerodynamics** Concept 4 has a similar principle to that of concept 1; however, the wings themselves are fixed to the body and are passive, thereby increasing reliability and decreasing cost in comparison while also having favourable aerodynamic properties. Furthermore, the large panel area allows for large solar panel array area, therefore increasing the amount of possible power which can be generated. However, this means that while generating power, the full solar array body will be exposed for heat absorption and emission, thereby requiring a combination of active and passive thermal control.
- **Concept 5 - CubeSat design with active aerodynamics via folding bus**: The folding bus is an active design aiming for radical shape change (therefore sensitivity to drag forces) while maintaining a compact shape. Reliability and cost are issues that need to be reviewed due to this not being implemented before on other missions. However, due to its small design, passive thermal control can be applied.

The concepts outlined above are shown in figure 2.1, figure 2.2, figure 2.3, figure 2.4 and figure 2.5.

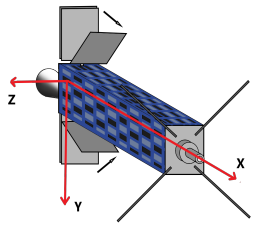

Figure 2.1: Concept 1 - CubeSat design with rotating panels.

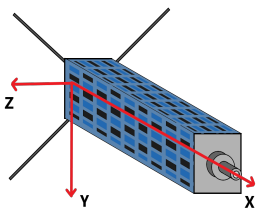

Figure 2.2: Concept 2 - Traditional CubeSat design.

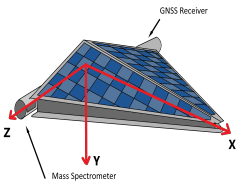

Figure 2.3: Concept 3 - Passive aeroshape design.

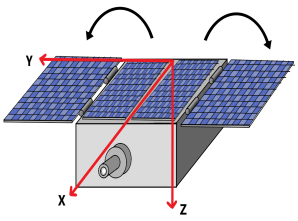

Figure 2.4: Concept 4 - Passive CubeSat design with enlarged panel.

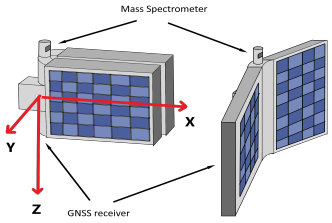

Figure 2.5: Concept 5 - Active aerodynamics folding body design.

With these concepts generated, the trade-off procedure is now defined. The general criteria used within it were derived from the primary and secondary project objectives listed in section 3.1. Weights were assigned to these criteria from 1 to 10, where 10 signifies the strongest correlation between a criterion and mission success. The scoring system is from 1 until 4, where 1 implies incorrectable deficiencies in the design, 2 suggests correctable deficiencies, 3 is awarded for good performance and 4 for excellent performance. These criteria are listed below:

1. **Drag sensitivity to gas-surface interaction** - this criterion is derived from the primary objective of the SCATTER mission in section 3.1, which is to measure the gas-surface-interaction particle energy, normal and tangential momentum accommodation coefficients of rarefied atmospheric gas, at a range of Low-Earth-Orbit altitudes between 150 km and 600 km, in order to improve existing high-altitude drag models. To achieve this, the SCATTER space element shape must be sensitive enough to changes in these accommodation coefficients, in order for the measured drag coefficient variation with altitude to capture them. Therefore, the difference in drag coefficient at different projected surface areas of the satellites, $\Delta C_D = C_{D_2} - C_{D_1}$, for energy accommodation coefficients of 0 and 1 yields ΔC_{D_α}, which is used as a design parameter describing the drag sensitivity to gas-surface interaction. This parameter is calculated with Eq. (2.1):

$$C_{D_\alpha} = (C_{D_2} - C_{D_1})_{\alpha=1} - (C_{D_2} - C_{D_1})_{\alpha=0}\,, \tag{2.1}$$

   where C_{D_2} denotes the drag coefficient of a satellite with the projected surface area S_{ref_1}, and C_{D_2} is the drag coefficient for S_{ref_2}. Given that this criterion is directly linked to the success of the mission, it is given **a maximum weight of 10**.
2. **Number of measurements** - this criterion was derived from the primary and secondary objective of SCATTER in section 3.1, and describes the number of data points collected from 600 km to de-orbiting, in all science phases. This criterion is related to two quantifiable properties of the satellite, namely the average power available and the average ballistic coefficient of the satellite. Having a large power available implies that more of the mission time can be used for science instead of charging, leading to more measurements. Furthermore, the absolute ballistic coefficient is inversely-proportional to the orbital decay time and mission lifetime. It becomes increasingly important in Phase III, where orbital decay occurs in weeks rather than years. As both of these aspects play an equal role in the possible total number of measurements, they were considered equally when scoring concepts. Given that a low number of measurements does not lead to mission failure according to the objectives in section 3.1, **this criterion is given a weight of 5**. Scoring of this criterion is done based on a default "worst design" which would combine the average power of concept 2 with the ballistic coefficient of concept 4. This was given a weight of 1. The other concepts were scored relative to this one, using a linear scaling. For the scoring of this criterion, it was assumed that the error of the drag coefficient measurement is < 0.1. Therefore, concept 2 gets a score of 2, as it is just above this threshold. Since, concept 4 is the best, it gets a score of 4. The other 3 concepts are scored using a linear scaling based on these extreme data points.
3. **Sustainability** - this criterion is linked to the overall goal of the project to design a sustainable space mission which would, in term, lead to a more sustainable usage of the LEO space and prevent future debris formation. Therefore, the main aspect influencing the sustainability of SCATTER and the one considered in this trade-off is the probability of inter-satellite collision. Collision between the satellites of the space element would lead to new debris in the orbit used by them, which would render said orbit unusable for future missions, and therefore, contribute to the aspect this mission is trying to prevent. Given all of this, **this criterion is given a weight of 5**. Scoring for this criterion is done based on the probability of collision computed for every design. As the probability of collision depends on the "characteristic length" of each shape, which is defined as the maximum distance between any two points inside the satellite shape, a default "worst design" was derived by placing the deployable solar panels of concept 4 on concept 5. This led to a probability of collision of 6.1e-5. Therefore, this was given a score of 1, and the others were scored relative to it using linear scaling.
4. **Reliability** - this criterion is related to the overall probability of failure of the mission due to a subsystem failure of the space element. Every subsystem plays a role into this probability to some extent, and therefore this criterion cannot be quantified at this stage. To that end, when scoring concepts based on this criterion, the overall complexity of the design was assessed. A simple design, with off-the-shelf components such as concept 2 is, therefore, considered more reliable than a complex design with cyclically-moving mechanisms, such as

concepts 1 or 5. Given that this criterion is directly related to the success of the mission, **it is given a weight of 7.** Scoring for this criterion is done based on the number of moving mechanisms in each design, and their use during the mission (cyclical or a one-time deployment). Concept 5 is assumed to be a default "worst design" in this category, as its entire body is linked by a cyclically-moving mechanism. Therefore, it is given a score of 1. Concepts 2 and 3, both, receive a maximum score of 4, as they are solid shapes, without deployables, while concept 3 is given a score of 3 due to its deployable solar panels. Finally, concept 1 gets a score of 2, due to its deployable, rotating panels.

5. **Cost** - this criterion flows from the development cost of every subsystem within the space element, including testing and certification. Given the cost user requirements mentioned in [14], choosing designs with custom components which require complex manufacturing processes and tests, increases the risk of going over-budget, and intrinsically, mission failure. Therefore, **this criterion is assigned a weight of 5**. Scoring for this criterion shall be made qualitatively, based on the manufacturing complexity of the structure, which is assumed to be the most expensive component of the design, and driving the cost of integration of other subsystems. Thus, relative scoring was used, based on a default "worst design", which would combine the intricate moving mechanisms of concept 1 with the complex, unconventional shape of concept 3. To that end, concept 2 is assigned maximum score of 4, as it resembles an off-the-shelf CubeSat design, while concept 4 gets a score of 3 due to the added complexity of deployable solar arrays. Concepts 1 and 5 get a score of 2, as they have one element each which would increase the costs of development significantly, namely cyclically-moving mechanisms or complex shapes.

The trade-off table itself is given in table 2.8, where the scores are given out of a total 128:

Table 2.8: Design Trade-off Table. The maximum score is 128.

Criterion	Weight	Concept 1	Concept 2	Concept 3	Concept 4	Concept 5
Drag Sensitivity to GSI	**10**	2	2	4	3	2
Number of Measurements	**5**	3	2	3	3	3
Sustainability	**5**	2	3	4	2	2
Reliability	**7**	2	4	4	3	1
Cost	**5**	2	4	2	3	2
Total Score:		**69**	**93**	**113**	**91**	**62**

As it can be seen in the trade-off total scores, concept 3 performs best, followed by a closely by concepts 2 and 4. Concept 3 seems to excel in drag sensitivity to GSI, which implies it would yield the most reliable data for the modelling of particle energy accommodation coefficient as a function of altitude. It performs fairly well in number of measurements as well, having a mid-range average power available of 17.28 W, with a relatively high ballistic coefficient. This implies that this concept will have less time to spend in the scientific Phase III, but it will dedicate more of that time to performing measurements, than most concepts. Finally, it seems to be the most sustainable and reliable option, as it is a set of only 2 solid bodies without any deployable or moving mechanisms. Its main disadvantage is its high development cost, due to the unconventional shape it employs, which would require complex, in-house manufacturing, and it would lead to a volume-inefficient structure. To mitigate concept 3's shortcomings, several aspects from other concepts can be borrowed. However, to know what aspects to be borrowed from which concept, a sensitivity analysis is performed on the entire trade-off, to determine the variation of the winner design with changing the weights of the criteria. This is done in below.

three sensitivity analyses are performed on the weights of the conceptual design trade-off shown in table 2.8. The first determines how changing the weights of the criteria will affect the winning concept. For this analysis, the criteria weights were varied between 0 and 10, in all combinations possible, leading to 100000 individual trade-offs. For each of them, the winning concept was calculated and recorded. Fig. 2.6 shows the amount of times each concept wins for varying weights. The second and third analyses vary the scores of all concepts for criteria 1 and 4: the drag sensitivity to GSI and reliability. These were chosen, as they are assigned the highest weights in the trade-off: of 10 and 7 respectively. The results are shown in Fig. 2.7 and Fig. 2.8.

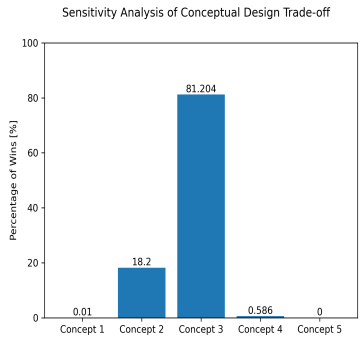

Figure 2.6: Sensitivity analysis of the number of trade-off wins for every combination of weights between 1 and 10.

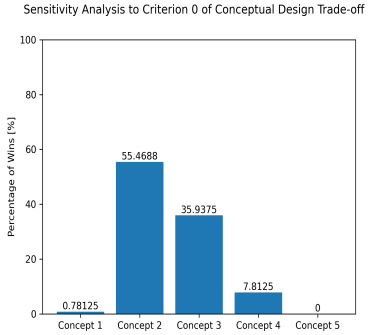

Figure 2.7: Sensitivity analysis of the number of trade-off wins for every combination of scores between 1 and 4 in criterion 1.

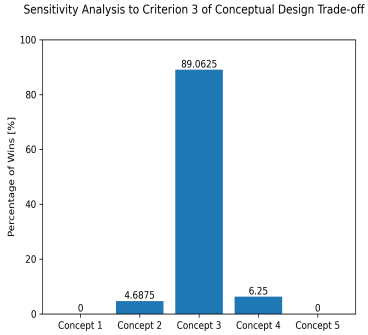

Figure 2.8: Sensitivity analysis of the number of trade-off wins for every combination of scores between 1 and 4 in criterion 4.

As it can be seen in the Fig. 2.6, concept 3 wins more than 80 % of the time, followed by the concept 2, which wins 18.2 % of the time. This confirms that concept 3 is indeed the best one, and furthermore, certain aspects from concept 2 could be used to improve 3. All other concepts win a negligible number of times, and therefore, are discarded as design choices. Fig. 2.7 shows that varying the scores of criterion 1 randomly results in concept 2 becoming the best design. This occurs because the high performance of concept 3 in this criterion is neglected. In Fig. 2.8, concept 3 wins 90 % of the times, when the relative reliability of all concepts is being neglected. It is therefore clear that concepts 2 and 3 have clearly-defined advantages over all other concepts. Concept 2 is very reliable and cost-effective, while showing a poor sensitivity to GSI. Concept 3 performs very well in the latter criterion, but requires high manufacturing costs. Therefore, in the next section, these advantages shall be analysed and incorporated into a singular design.

2.4 Preliminary Design of SCATTER

Following the results of the trade-off and sensitivity analysis, the winner is therefore a new design, which combines the advantages of an aerodynamic shape on the scientific data quality and the low inter-satellite collision probability, with the low cost and high reliability of a plain CubeSat design. This concept consists of a CubeSat body with two deployable solar panels. The novelty lies in the idea of deploying them at a shallow angle with respect to the flat plates upon which they lie. In figure 2.9, figure 2.11 and figure 2.10 front, side and isometric views of this concept are shown, where the solar panels are coloured in blue. Please note that the angle given in the graphs is not the one chosen for this preliminary design. Instead, 10 ° were chosen, as they were found to provide a high ΔC_{D_α}.

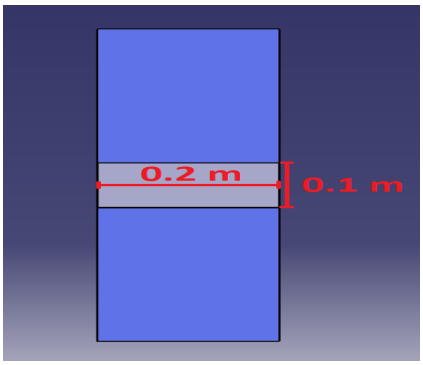

Figure 2.9: Front view of the SCATTER preliminary design.

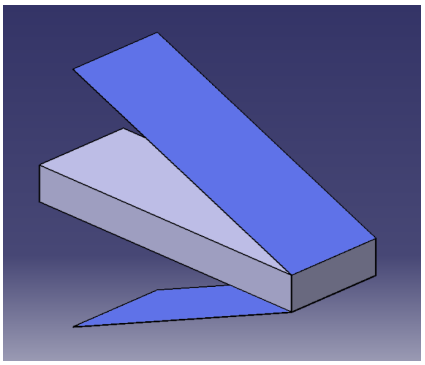

Figure 2.10: Isometric view of the SCATTER preliminary design.

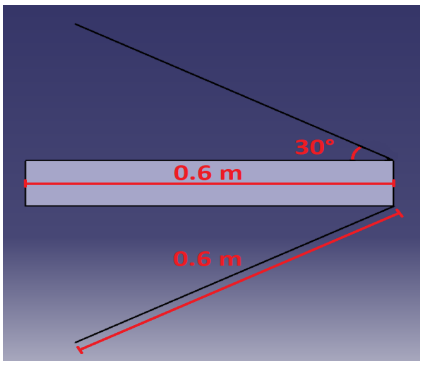

Figure 2.11: Side view of the SCATTER preliminary design.

As it can be seen in the figures above, the shape of the preliminary SCATTER design is a 1U x 2U x 6U, which is a non-standard CubeSat shape. This decision was made to maximize the sensitivity to gas-surface-interaction, and at the same time, allow for a simple spring mechanism to be used for the solar panel deployment. Furthermore, it allows for a large flat-plate surface area on the faces without solar panels to be used for the GNNS and TT&C patch antennas, as they have a large field of view and small multi-pass effects. An overview of the main parameters of the preliminary design is given in table 2.9. Two sets of parameters are given: values for the low drag configuration (small surface area) and high-drag configuration (large surface area). These values were computed only for science mode, as the remaining operational modes and duty cycles were implemented in the detailed design phase.

Table 2.9: Key design features of the new design choice for project SCATTER.

Design feature	Final Value Selection Large Surface Area	Final Value Selection Small Surface Area	Unit (if applicable)
$\mathbf{C_{D,\alpha=0}}$	3.791	3.54	[-]
$\mathbf{C_{D,\alpha=1}}$	2.27	3.63	[-]
$\Delta C_{D\alpha}$	1.109	1.109	[-]
$\mathbf{P_{available}}$	20.29	12.616	[W]
Mass	15.83	15.83	[kg]
Volume	0.012	0.012	$[m^3]$
Bus Cost	1.09	1.09	[€M]
Probability of Collision	$3.2894 \cdot 10^{-5}$	$3.2894 \cdot 10^{-5}$	[-]
TCS	Passive	Passive	[-]
OCS	Mono-propellant	Mono-propellant	[-]
ADS	1. Six sun sensors 2. Two magnetometers 3. Two gyroscopes	1. Six sun sensors 2. Two magnetometers 3. Two gyroscopes	[-]
ACS	1. Three magnetorquers 2. Four reaction wheels	1. Three magnetorquers 2. Four reaction wheels	[-]
TT&C	Patch Antenna	Patch Antenna	[-]
Payload	1. Mass spectrometer 2. Accelerometer 3. GNSS receiver	1. Mass spectrometer 2. Accelerometer 3. GNSS receiver	[-]

With the primary parameters of the preliminary design of SCATTER outlined in the table above, section 2.5 now breaks down the trade-able values pertaining to this design at a subsystem level, using statistics [12].

2.5 Preliminary Design Budgets

This section aims to present the preliminary budget allocation which is support by statistical analysis[12]. The results are shown in table 2.10.

Table 2.10: SCATTER preliminary design budgets table.

Source	Preliminary Design			Preliminary Design Fraction		
Subsystem	**Cost [EUR]**	**Mass [kg]**	**Average Power** $[W]$	**Cost [%]**	**Mass [%]**	**Average Power** [%]
Structures	€ 14,700.00	3.170	0.000	1.41%	20.03%	0.00%
TCS	€ 51,957.89	0.790	0.000	5.00%	4.99%	0.00%
ODCS	€ 129,000.00	3.960	1.328	12.41%	25.02%	10.53%
ADCS	€ 293,250.00	1.580	1.328	28.22%	9.98%	10.53%
EPS	€ 223,600.00	3.170	1.992	21.52%	20.03%	15.79%
TT&C	€ 20,000.00	0.790	2.656	1.92%	4.99%	21.05%
C&DH	€ 6,650.00	0.790	2.656	0.64%	4.99%	21.05%
Payload	€ 300,000.00	1.580	2.656	28.87%	9.98%	21.05%
Total	€ 1,039,157.89	15.830	12.616	100.00%	100.00%	100.00%

As shown in the table above, the most expensive subsystem is the Payload subsystem, followed closely by the ADCS and EPS. While the first value makes sense in the context of the mission, it was expected that the second value was expected to decrease due to the off-the-shelf nature of CubeSat components and the relatively low pointing accuracy required by REQ-P-08, REQ-P-20 and REQ-P-21. In terms of mass budgets, the mass of the EPS was expected to increase, together with the mass of ODCS due to the high ΔV required for Phase I of the mission, and the constraining power requirement. In general, these expectations were confirmed by the detailed design budgets outlined in section 14.2.

2.6 System Overview Closing Remarks

Based on the trade-off performed in this chapter, it was concluded that the aerodynamic drag sensitivity and reliability are the most relevant aspects of the design. The idea of combining concepts 2 and 3 into a shallow-angle CubeSat design proved to be an efficient solution at a preliminary level. However, parameters such as the number of solar panels, panel deployment mechanism and CubeSat shape may dampen these advantages. The reliability aspect is highly dependent on the number of deployables, as well as the amount of off-the-shelf components. Furthermore, the sensitivity to accommodation coefficient can be optimised with a sensitivity analysis on the ΔC_{D_α} with the number of panels, their angle and their length. Therefore, in the detailed design such aspects must be analysed further to determine their sensitivity advantage over other concepts, feasibility w.r.t. subsystem integration, launcher integration and power budgets.

3. Mission Overview

This chapter concerns the mission planning and operational concept to achieve the scientific objectives and satisfy all requirements. First, the mission objectives are presented in section 3.1 and mission requirements are presented in section 3.2. Orbit selection is discussed in section 3.3, the launch vehicle is selected in section 3.4. Next, an overview of the mission and its operational concept is given in section 3.6. Finally, a collision avoidance strategy is outlined in Section 3.7 and mission verification and validation is performed in section 3.8.

3.1 Mission Objectives

It is important to restate the goals of the overall project and the objectives which need to be achieved. The primary mission objective (with index one) outlines the most crucial goal which must be attained with this project. Without achieving this objective, this mission would not have a reason to be developed and operated. Secondary objectives (indicated with a two) are key to ensuring that all key scientific goals are met, though the result is not mission-critical if failure occurs. Finally, tertiary mission objectives (denoted with a three) allow for the project to realise its full potential, but would not impact the scientific performance of the mission in the event of failure.

1.1 **Measure the drag of 2 satellites flying in the same atmospheric conditions with different tangential to normal surface area ratios, at altitudes between 150 km and 600 km.**
2.1 **Measure the atmospheric temperature at altitudes between 150 km and 600 km.**
2.2 **Measure the particle number density of helium and atomic oxygen at orbital altitudes between 150 km and 600 km.**
3.1 **Use as high a percentage of off-the-shelf components in the satellites as possible.**

To comply with the primary mission objective outlined above, scientific measurements shall be made at several altitude steps within the given range of 150 km to 600 km. A scientific measurement is defined as the data collected throughout one science mode cycle. An altitude step is defined as an altitude range experienced by the satellites in science mode, for which the atmospheric density varies less than 5%, and can be assumed to be constant.

3.2 Mission Requirements

The requirements of the SCATTER mission are given in Table 3.1, together with the rationale behind them.

Table 3.1: SCATTER Mission Requirements.

ID	Description	Rationale
REQ-M-01	The mission shall consist of at least two satellites.	Derived from REQ-U-01 and the primary mission objective given in section 3.1.
REQ-M-02	The mission shall have an operational lifetime of at least 1 year.	Derived from REQ-U-08.
REQ-M-03	The space element of the mission shall be de-orbited after its predetermined lifetime has passed.	This is a requirement derived from sustainability needs outlined in chapter 17 and REQ-U-23.
REQ-M-04	The mission shall consist of three science phases.	Derived from REQ-U-09.
REQ-M-05	Phase 1 shall begin at an altitude where the helium particle number density is at least 20%.	Derived from REQ-U-10 and the primary mission objective given in section 3.1 as accommodation coefficient values are the least known at altitudes where helium particle number densities becomes significant.
REQ-M-06	In Phase 1, the space element shall collect scientific data points in circular orbital altitude steps of at most 10 km.	Derived from the mission operations analysis outlined in section 3.5
REQ-M-07	Phase 2 shall be performed at altitudes between 300 km and 400 km.	Derived from REQ-U-11.
REQ-M-08	In Phase 2, the space element shall collect at least 50 scientific measurements.	Derived from the mission operations analysis outlined in section 3.6.5, and power duty cycle estimates outlined in chapter 5. One scientific measurement is defined to be the duration of one science mode.
REQ-M-09	Phase 3 shall be performed at altitudes between the re-entry altitude and 300 km.	Derived from REQ-U-11.
REQ-M-10	In Phase 3, the space element shall collect at least 5 scientific measurements.	Derived from the mission operations analysis outlined in section 3.6.6, and power duty cycle estimates outlined in chapter 5.
REQ-M-11	An inter-satellite collision avoidance strategy shall be implemented throughout the operational lifetime of the mission, from space element commissioning phase to re-entry.	Derived from REQ-U-12.
REQ-M-12	~~The response time of the inter-satellite collision avoidance sequence shall be below 5 hours.~~	Crossed out as it became a system constraint.
REQ-M-13	The mission shall measure the helium (He) and atomic oxygen (O) particle number densities throughout all scientific phases.	Derived from all mission objectives outlined in section 3.1, and REQ-U-06.
REQ-M-14	The mission shall measure the atmospheric temperature throughout all scientific phases.	Derived from REQ-U-06.
REQ-M-15	The mission shall be able to derive the translational acceleration of the space element units using the position and velocity data from a GNSS receiver in science Phases I, II and III.	Derived from REQ-U-05.
REQ-M-16	The mission shall use an accelerometer to measure the translational acceleration in Phase III.	Derived from REQ-U-17.
REQ-M-17	The orbital in-plane distance between the satellites of a measuring unit shall not exceed 500 km throughout all scientific phases.	Derived from REQ-U-04 and the need to ensure constant atmospheric features between satellites for drag coefficient determination.
REQ-M-18	The testing procedures shall be documented to avoid errors during testing.	Requirement derived from strategies implemented to mitigate potential risk, see RISK-TECH-19 and RISK-TECH-20 in chapter 18.
REQ-M-19	The flight readiness of the satellite elements shall be verified prior to final integration with the launch vehicle.	Requirement derived from strategies implemented to mitigate potential risk, see RISK-TECH-19 and RISK-TECH-20 in chapter 18.
REQ-M-20	The satellites in a measuring unit shall be at least 50 km apart (Euclidean distance).	Requirement derived from strategies implemented to mitigate potential risk, see RISK-TECH-19 and RISK-TECH-20 in chapter 18.

REQ-M-21	The difference in orbital altitude between the satellites of a measuring unit shall not exceed 3 km.	3 km distance is the orbital altitude difference, which results in a 20 % change in atmospheric density according to the NRLMSISE-00 model. Given that this value is assumed to be constant in later scientific analysis, any higher percentage difference can lead to significant error in ΔC_{D_α}.
REQ-M-22	The mission shall have an operational lifetime of at most 3 years.	Reliability of low cost ($<$ € 10 Million) and low mass ($<$ 100 kg) satellite missions is limited [15], and thus the life time was derived to ensure a mission reliability of at least 70 % based on literature [16].
REQ-M-23	The spacecraft shall comply with the requirements outlined in "Small Spacecraft Mission Service VEGA-C User's Manual".	Based on the constraints imposed by the piggyback rules for the VEGA launcher [10].

3.3 Orbit Selection

The choice of orbit is strongly interconnected with the scientific objectives of this mission, which require a minimum helium number density of 20% in the initial science phase. As the chemical composition of the thermosphere varies with altitude, this sets a lower bound on the initial orbit altitude. An upper limit on the initial orbit altitude arises from the time until re-entry and related reliability of all systems. The time until re-entry increases exponentially with increasing altitude, thus a higher initial orbit requires either an increased overall system reliability, or a propulsion system to decrease the altitude.

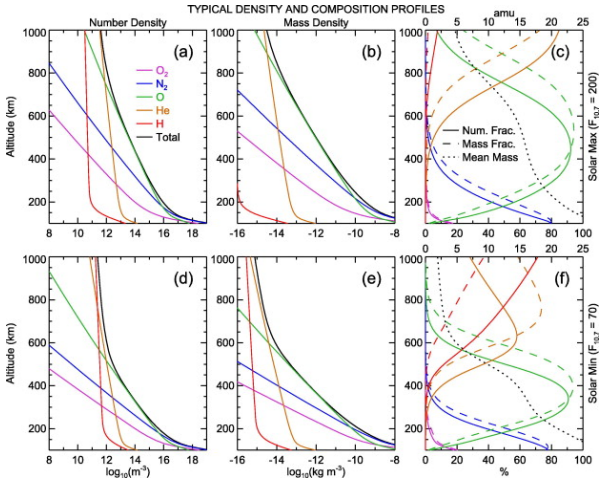

Figure 3.1: Thermosphere density and composition according to NRLMSISE-00 model for solar maximum and minimum [17].

Both atomic oxygen and helium will be measured in the first science phase, and their composition varies throughout the thermosphere. Figure 3.1 shows the number density and composition environment in the thermosphere for both high and low solar activity using the NRLMSISE-00 model[1]. At high solar activity, atomic oxygen is dominant between 200 and 760 km, and helium above 760 km. In low solar activity, the altitude of the oxygen-to-helium transition decreases from 760 to 520 km [17]. An updated model, NRLMSIS 2.0, exists, but except for lower nitrogen and oxygen densities, "the NRLMSISE-00 thermosphere is largely retained" [3] thus, the NRLMSISE-00 model can be used for orbit selection.

A number density of 20% helium is achieved at roughly 430 km in solar minimum and 620 km at solar maximum. Compared to larger satellites, the low budget and relatively lower quality of components in small satellites, results in an average operational lifetime in the range of 1 to 2 years[2]. With a higher initial orbit, a higher lifetime and thus higher reliability is required from all components, which is infeasible given the budget requirements for SCATTER. Therefore, a propulsion system capable enough to decrease the orbit to a point where it can naturally decay is needed. An orbit and operational concept is chosen to ensure that the time until re-entry is less than three years.

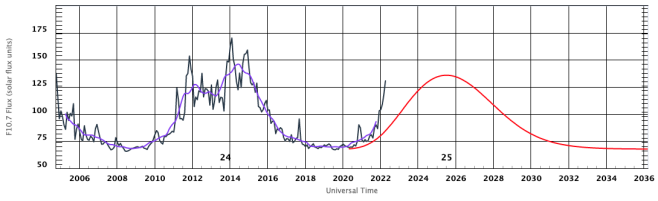

Figure 3.2: Solar Cycle F10.7cm Radio Flux Prediction:[3].

A preferred initial orbit altitude of 600 km is chosen to both satisfy the helium number density requirement in all solar cycle phases, but not impose too high system reliability or the need for a heavier propulsion system. This altitude also allows scientific measurements in the helium-oxygen transition phase, given medium to low solar activity. As seen in figure 3.2, the National Oceanic and Atmospheric Administration (NOAA), predicts the next solar maximum to occur in 2025 followed by a solar minimum in approximately 2034 [4]. As the mission is required to launch before 2035, this allows full launch schedule flexibility, as discussed in section 3.4.

[1] https://ccmc.gsfc.nasa.gov/modelweb/models/nrlmsise00.php, Retrieved 30-05-2022
[2] https://pure.tudelft.nl/ws/portalfiles/portal/10531886/art_3A10.1007_2Fs12567_016_0138_0.pdf, Retrieved: 09-05-2022
[3] https://www.swpc.noaa.gov/products/solar-cycle-progression, Retrieved 13-05-2022
[4] https://www.swpc.noaa.gov/products/solar-cycle-progression, Retrieved 09-05-2022

A circular orbit is chosen since for an elliptic orbit the density between the separated satellites would be too variable. Furthermore, an elliptic orbit tends to circularize itself over time. The inclination choice is further discussed in section 3.4.

3.4 Launch

The choice of launch vehicle is driven by the insertion orbit required, cost, launcher availability, sustainability and reliability. The preferred insertion orbit was determined in section 3.3 as a circular orbit with 600 km altitude and no importance of inclination. Although the atmosphere is more dynamic over the poles, the largest changes in atmospheric composition and temperature occur over altitude, due to the exponential decrease in density with altitude. Thus, for achieving the scientific objectives, there is no preference for any orbit inclination.

Given the small size of this mission and the low budget available, a launch as primary payload on a dedicated launch vehicle is not feasible in terms of cost, launch requirements and sustainability. Currently, available small launch vehicles like the Electron rocket with a sun-synchronous orbit (SSO) payload mass of 200 kg have a launch cost of 7.5 M$ [5]. Furthermore, given the circular low Earth orbit the satellites will operate in, there is no need for a special orbit trajectory justifying the use of a dedicated launch vehicle. Thus, this mission is considered as a small secondary payload.

Launching as a secondary payload allows ridesharing along a primary payload, given there is excess mass and volume available in the launcher. This reduces the launch cost substantially and decreases the environmental impact per payload as several payloads share the same launch vehicle. Since the orbit is determined by the main payload, flexibility in the insertion orbit and launch schedule is required.

Ridesharing options are available from commercial launch vehicle providers such as SpaceX, Arianespace, Spaceflight, Nanoracks, ISIS among other companies. These providers sell secondary payload places on regular scheduled launches with prices of about 1 M$ for a mass of 50 kg[6][7]. The most frequently used launch vehicles for ridesharing missions with proven reliability are given below:

- Antares/Mintoaur
- Atlas V
- Dnepr/Soyuz
- Falcon 9
- PSLV
- Vega/Vega-C

The majority of these vehicles launch into the common ISS orbit of 45 °inclination or into SSO. Other launch vehicles exist but have performed very limited ridesharing launches up to this day and have yet to prove their reliability against these established launchers. The Antares and Minotaur rockets are mainly used for direct launches from the ISS. A launch from the ISS has been considered as the cheapest option, but the deployment orbit of 400 km to 420 km is too low for this mission [8]. Both the Russian Dnepr rocket using old ballistic missile rockets[9] and the very established Soyuz rocket will not be considered as launch solution due to Russia's invasion of Ukraine and the sanctions enforced on it. Falcon 9 has its own independent rideshare program and launches frequently into 34.5 °inclination to 98 °inclination and 245 km to 580 km altitude orbits[10]. Atlas V is heavily used by the US government and launches into any orbit and inclination. The Indian PSLV rocket is frequently used for ridesharing missions into SSO and serves altitudes above 600 km regularly. The European Vega rocket started its first rideshare mission in 2020 and is now frequently operating into SSO and altitudes up to 700 km[11]. An upgraded version, Vega-C is tailored towards small payloads and will enter into service in 2023, offering places next to main payloads and fully dedicated ridesharing missions[12].

To achieve the desired insertion orbit, both the PSLV and Vega-C launchers were identified as the best options, with high availability of launches to altitudes of 600 km and proven reliability of performing rideshare missions successfully at low cost. Vega-C was selected as the first choice, due to all logistical operations taking place in Europe. This includes the European launch site in French Guiana. Since the development and design of SCATTER is carried out in Europe, reduced transportation routes and logistics result in a cheaper and more sustainable concept. The Indian PSLV rocket will be used as a backup choice in case of unexpected problems with the availability of Vega-C. The launch window was selected to be during 2035, to launch into the predicted solar minimum and have enough time for production and testing of the satellites. This is especially important, since some structural parts are non-standard and require additional testing and qualification. A one-year launch window was considered to account for waiting time until an appropriate launch opportunity opens up. Table 3.2 shows a summary of the selected launch vehicle and its most important constraints for the design.

[5] `https://www.rocketlabusa.com/launch/electron/`, Retrieved 11.05.2022
[6] `https://spaceflight.com/`, Retrieved 12-05-2022
[7] `https://preciouspayload.com/launch-schedule/`, Retrieved 12-05-2022
[8] `https://nanoracks.com/products/iss-launch/`, Retrieved 11-05-2022
[9] `http://www.russianspaceweb.com/dnepr.html`, Retrieved 12-05-2022
[10] `https://www.spacex.com/rideshare/`, Retrieved 12-05-2022
[11] `https://www.arianespace.com/vehicle/vega/`, Retrieved 12-05-2022
[12] `https://www.arianespace.com/vehicle/vega-c/`, Retrieved 12-05-2022

Table 3.2: Details of Vega-C SSMS [18].

Name	Vega-C SSMS
Launch Service Provider	Arianespace
Main Orbit Availability	SSO and LEO, 500 km to 700 km
Launch Availability	At least once per year, expected to increase
Launch Cost	1 M$ to 1.3 M$
CubeSat Mass Constraint	10 kg to 35 kg
CubeSat Volume Constraint	300x300x600mm
CubeSat Main Frequencies (Lat/Long)	>115 Hz
CubeSat Launch Loads (Lat/Long)	±10 g
Additional Requirements	S/C inert during launch and no electrical connections or monitoring possible.

Vega-C can accommodate multiple payload adapters, allowing it to launch single, dual or multiple payloads. The Small Spacecraft Mission Service (SSMS) dispenser is used for dedicated rideshare missions to space. Figure 3.3a shows the payload assembly inside the Vega-C fairing. Inside the fairing, the satellites will be located next to other CubeSats, cantilever mounted at the bottom of the fairing on the SSMS Hexa module. CubeSats cannot be directly mounted inside the fairing, but require a CubeSat deployer. These deployers act as an interface between the launch vehicle and satellite, protect the satellites during launch, and deploy the satellite via a spring mechanism. Arianespace as the launch service provider recommends a selection of deployers, out of which the 12U deployer by Tyvak was chosen due to its datasheet and internal dimensions being public [19]. Figure 3.3b shows this deployer. As required by Vega-C, each spacecraft will be inert (S/C OFF, no RF emission, no status changes) during launch and will be automatically powered on after separation detection by the deployer door opening [18].

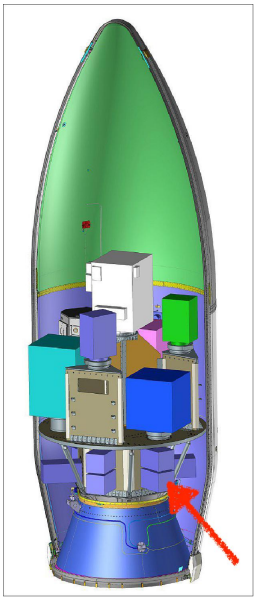

(a) SSMS payload assembly inside Vega-C fairing [18].

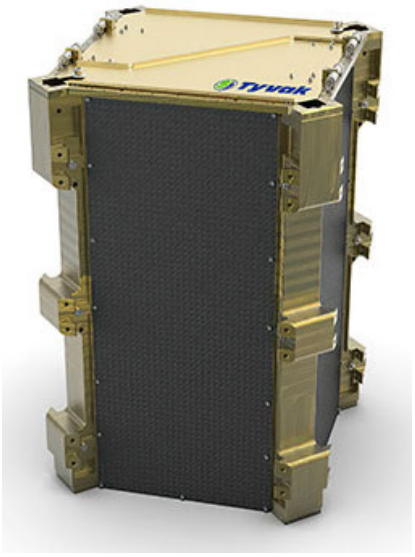

(b) Tyvak 12U deployer [19].

A summary of the desired initial orbit altitude, inclination and launch window is given in table 3.3. The orbit altitude tolerances specify the maximum acceptable deviations from the preferred initial orbit altitude during launch vehicle selection in the launch window.

Table 3.3: Orbit selection and launch date overview.

Altitude	Inclination	Launch Window
600 ± 5 km	no preference	2035

Vega-E (Evolution) is currently under development and is an updated version of Vega-C with a planned maiden flight in 2026. The third and fourth stage of Vega-C will be replaced by a new upper stage using green propellants. Furthermore, the use of additive manufacturing can reduce material waste. Vega-E has the potential to further reduce the environmental impact, compared to Vega-C, and is therefore recommended to be considered in future design phases. Next to using a rideshare launch on a European rocket, both these steps significantly improve environmental sustainability [13]

[13] `https://www.avio.com/vega-e`, Retrieved 13-06-2022

3.5 Mission Overview

The mission consists of two identical 12U satellites deployed in the same orbit, at 600 km, taking scientific measurements in three distinct science phases. The three science phases given by the user requirements are:

- Phase 1: Science operations at altitudes with helium (He) concentration of at least 20% in terms of number density
- Phase 2: Science operations between 300 – 400 km altitude
- Phase 3: Science operations below 300 km altitude until re-entry

Figure 3.4 provides a visual illustration of the mission and its procedure. After launch and 1h45min into the flight, the launcher sends a separation signal to the deployers containing the spacecraft. The satellites will be released via a spring mechanism and power up automatically upon receiving a door opening confirmation message [18]. The satellites then de-tumble, start up and test all systems to prepare for operation. After taking measurements in three scientific phases, they re-enter the atmosphere and burn up. To limit the total time until re-entry to less than three years, scientific measurements in phase 1 will be taken at altitude steps of at most 10 km and last 189 days. This results in 21 altitude steps from 600 km to 400 km as seen in Figure 3.4. The majority of mission time is spent in Phase 2 from 400 km to 300 km. The time taken in this phase is highly sensitive to solar activity and is expected to take between 452 days to 602 days. The sensitivity of time until re-entry to solar activity is further discussed in section 3.6.1. Phase 3 involves measurements from 300 km to re-entry and includes accelerometer measurements. This phase will take between 36 days to 44 days, depending on solar activity. This results in a total mission time of 1.85 years to 2.29 years. The functional flow of these steps is shown in more detail in section 2.1. Table 3.4 shows a detailed mission timeline with the time taken in each of these steps, the altitude, number of measurements taken per phase and number of manoeuvres performed. One measurement cycle is defined as one science mode, during which scientific measurements are taken. The time taken per phase, number of measurements and number of manoeuvres is derived and explained in section 3.6

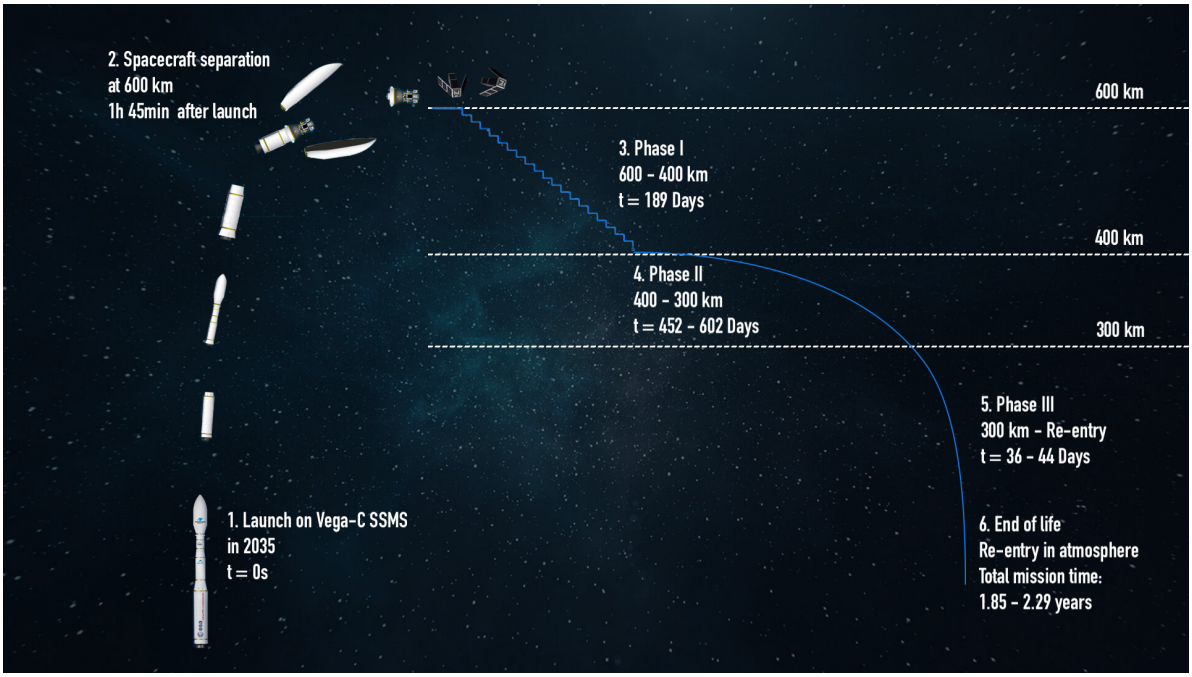

Figure 3.4: Mission Overview.

Table 3.4: Mission Timeline.

Event	Time			Altitude [km]	Measurements	Manoeuvres
	67.7 F10.7 flux	68 F10.7 flux	77 F10.7 flux			
Launch & Separation	-	1h 45min	-	0 to 600	0	0
De-tumbling	-	6 hours	-	600	0	0
Systems startup, tests and calibrations	-	1 Day	-	600	0	0
Phase 1	189 Days	189 Days	189 Days	600 to 400	84	21 for altitude decrease
Phase 2	602.27 Days	594.59 Days	451.71 Days	400 to 300	255	85 for formation maintenance
Phase 3	43.73 Days	45.39 Days	35.66 Days	300 to Re-entry	98	98 for formation maintenance
Total	**2.288 years**	**2.271 years**	**1.853 years**	**-**	**433**	**204**

3.6 Operational Concept

After describing the general mission layout in section 3.5, the operational concept for SCATTER is outlined in this section. First, the mission lifetime and sensitivity to solar activity is discussed in Section 3.6.1. Next, operational modes are defined in section 3.6.2 and the problem of satellite formation control is addresses in section 3.6.3. Finally, detailed operational plans are outlined for phase 1, phase 2 and phase 3, in section 3.6.4, section 3.6.5 and section 3.6.6 respectively.

3.6.1 Mission Lifetime

Estimating the time until re-entry is key for successful mission planning and developing the operational concept. The time until re-entry is mainly driven by natural decay in phase 2 and 3, whereas the time spent in phase 1 was chosen as 189 days over 21 altitude steps. This allows to limit the total time until re-entry, but have enough time for scientific measurements at each altitude step. The astrodynamics simulation discussed in section 3.8 was used to simulate the time spent in phase 1 and time until re-entry from 400 km in phase 2 and 3. The Marshall Solar Activity Future Estimates (MSAFE) model, uses past data of solar cycles 1 to 23 for future solar activity predictions [20]. The 50th percentile 13-month smoothed solar flux estimates during the launch window of 2035 are shown in table 3.5, including lower, predicted and upper bound during that launch window[14]. Figure 3.5a and figure 3.5b shows the orbit evolution over time for phase 1 and phase 2 until re-entry respectively. The end of phase 1 is predicted to occur at 404.5 km to 403.67 km after 189 days. Because only 9 days are spent at each altitude step, there is no significant effect of solar activity on phase 1.

Figure 3.5b shows the orbit evolution from 400 km until re-entry. Large differences in the time until re-entry are observed using the predicted values from the MSAFE model in 2035. Phase 2 is expected to last 594.59 days with a range of 451.71 days to 602.27 days, highlighting its sensitivity to solar activity. Phase 3 was simulated to last between 35.66 days to 43.73 days. These numbers are provided in Table 3.4 as a general overview. The total mission time is estimated between 1.853 years to 2.288 years, with an expected value of 2.271 years.

Table 3.5: Estimate of 50th percentile 13-month smoothed solar flux estimates during the launch window of 2035 [20].

Solar Activity in 2035	minimum	expected	maximum
F10.7cm flux	67.7	68	77

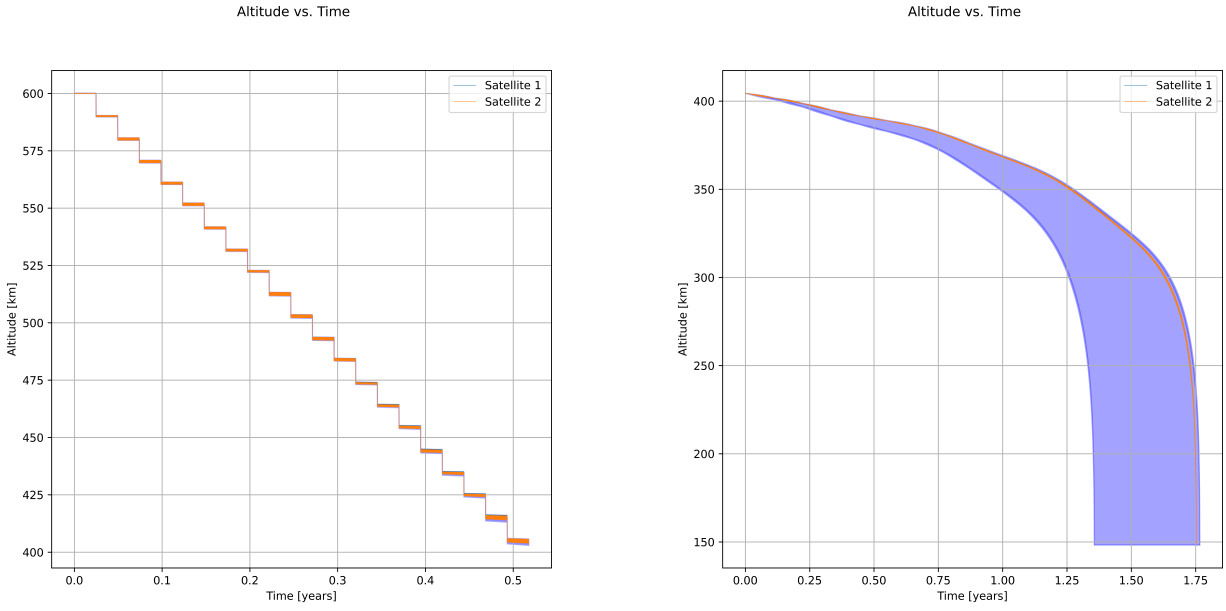

(a) Phase 1.

(b) Phase 2 and 3.

Figure 3.5: Orbit evolution under minimum, expected and maximum predicted solar conditions during 2035

3.6.2 Operational Modes

Due to the power demands and established duty cycles mentioned in table 5.8, scientific measurements can not be run continuously. The power system was designed to take 48h of measurements continuously before recharging the batteries, mentioned in section 5.2.2. Furthermore, each function performed, has different requirements on the satellite's attitude and power usage. Therefore, it was necessary to implement operational modes. These operational modes are described in table 3.6 and their attitude constraints are provided.

Table 3.6: Operational modes.

Mode	Satellite orientations	Description
Science	One satellite parallel and one perpendicular to the flow. Orientations are switched according to PD control input.	The satellites are in different orientations and perform scientific measurements. Data is stored and communication with ground station is done at each possible overpass. Reaction wheels are de-saturated if necessary.
Power	Both satellites in the same orientation, with one solar array pointing to the Sun.	The satellites are in the same orientation and recharge their batteries. Reaction wheels are de-saturated.
Propulsion	Both in same orientation, according to manoeuvre	The satellites perform an orbital manoeuvre and its correct implementation is checked at next ground station contact.
Safe	Both in low drag orientation	In case of emergency or failed ground contact in 2 consecutive, scheduled overpasses.
De-tumbling	Initially rotating after separation.	After spacecraft separation, the satellites stop their rotation induced by launch vehicle deployment.
Re-entry	Both in high drag orientation	Used for re-entry to ensure complete burn-up in the atmosphere.

Three modes (science, power and propulsion) are used for nominal operations and three modes (safe, de-tumbling and re-entry) are used in special circumstances. Science mode includes taking scientific measurements, storing data and communicating to the ground station at each scheduled overpass. During science mode, both satellites operate at different attitudes, making them drift apart over time. A control scheme was implemented in section 3.6.3 to keep the separation distance in a specified range. In power mode, the mass spectrometer shuts down, and the batteries are recharging. One of the main solar arrays is Sun-tracking, and both satellites go into low drag orientation to prevent a further increase in separation distance. The momentum wheels are primarily de-saturated during power mode and can be de-saturated during science mode if necessary, as explained in section 9.3. Propulsion mode is used for orbital corrections and manoeuvres, including collision avoidance manoeuvres. Re-entry mode ensures complete burn-up in the atmosphere. In De-tumbling mode, the induced angular rates from launcher separation are dampened. Finally, safe mode is used in case of an unresponsive satellite after 2 consecutive scheduled ground station passes. As the unresponsive satellite might not be able to rotate itself, in case one satellite is unresponsive, the operational satellite will adapt the orientation of the unresponsive one. As both satellites are always in the same operational mode, it is known in which orientation both satellites are. Further details on power requirements per operational mode are provided in table 5.6.

3.6.3 Satellite Formation Control

During the whole mission, the two satellites will fly in the same orbit, separated by a certain distance along the orbit. The maximum distance is 500 km as given by the user requirements. The challenging and unique aspect of this mission is that the two satellites will experience different accelerations due to their relative orientation in orbit. During science measurements, one satellite operates in a high drag orientation while the other is in a low drag orientation. They will slowly drift apart over time, and thus both have to switch orientations to keep the separation distance under 500 km. A differential-drag-based proportional-derivative-integral (PID) control scheme was implemented and used to simulate formation flying.

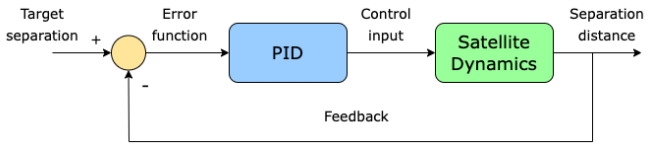

Figure 3.6: PID controller.

Figure 3.6 shows a block diagram of this control scheme. A desired separation distance of 300 km was chosen to reduce the collision risk between both satellites and to satisfy the requirement of a maximum of 500 km separation distance. The error function of actual separation distance compared to the desired value is continuously calculated by the astrodynamics simulation. Proportional, derivative and integral terms are used by the controller to calculate a control function, using adjustable control gains. The implementation of this PID controller into the astrodynamics software is discussed in section 3.8.1.

Since the control function outputs a continuous variable, both satellites switch orientation if the control function switches signs. This provides a binary output, which can be used to command the satellite orientation switches. The tuned controller gains are shown in table 3.7. A nominal mode has been implemented using only proportional gain, next to a transition mode with both differential and proportional gain. The nominal mode only takes the error in separation distance into account, while the differential term in transition mode also uses relative satellite velocity as input.

The nominal mode switches the satellites at the desired separation distance, resulting in an oscillation about the desired value. This oscillation is stable over short timescales, but diverges over time. As altitude decreases and the accelerations due to drag increase, these oscillations both increase in frequency, and diverge faster. The addition of a derivative term in the transition mode, leads to dampening of the separation oscillation about the desired

value. The dampening time is limited by the satellite dynamics and the magnitude of accelerations due to drag present at each altitude. The integral term was not found to be useful and therefore set to zero in both modes, resulting in a PD controller.

The transition mode was found to be especially useful in phase 2, where most of the operational lifetime is spent. The satellites drift apart over time, and need to be returned to their nominal separation state after a certain time of scientific measurements. Also, the orbits get increasingly elliptic over time when flying in different orientations, the density gets too variable between both satellites. Therefore, several propulsive manoeuvres are performed during the mission. Due to the diverging nature of the separation distance oscillations in nominal mode, these manoeuvres would need to cancel both along track separation and radial separation, leading to very high delta-V requirements as discussed in section 8.2. Using the transition mode before each manoeuvre in phase 2, allows reducing the relative velocity significantly, which in turn decreases the Delta-V requirements. The application and results of applying this formation control scheme are outlined in section 3.6.4, section 3.6.5 and section 3.6.6.

Table 3.7: PD controller gains.

PD mode	K_p	K_d	K_i
Nominal	1	0	0
Transition	1	0.2	0

3.6.4 Phase 1

Phase 1 starts at 600 km and ends at 400 km, lasting 189 days. Scientific measurements are taken at altitude steps of at most 10 km. The operational concept for one altitude step is shown in figure 3.7a for 600 km altitude. The satellites start at the nominal separation distance of 300 km and alternate between 48 hours of science mode and 6 hours of power mode. This results in 4 science modes per altitude step and 84 measurements done in phase 1. At this high altitude, the separation distance between both satellites reaches only 6 km after 9 days and therefore no input from the formation flying scheme is used. At the end of the 9 day period, a propulsive manoeuvre is performed to lower the orbit and decrease the separation distance back to 300 km. Figure 3.7b shows, that up to 12 m of radial separation is reached at the time of the manoeuvre, which needs to be accounted for in the manoeuvre. In total, 21 manoeuvres are performed in this phase.

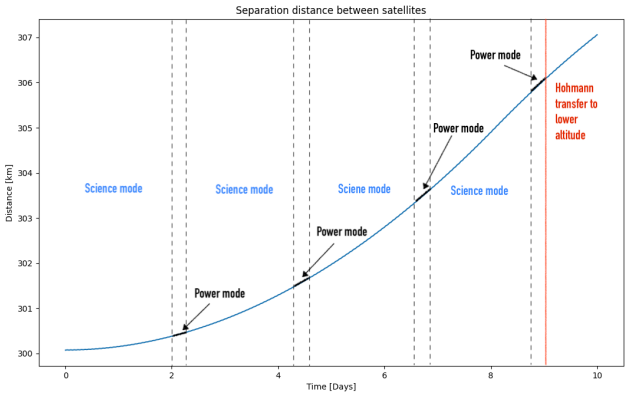

(a) Separation distance between satellites at 600 km simulated with AstroSIM.

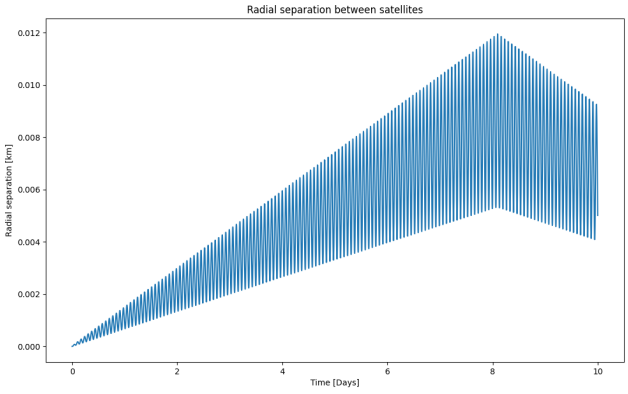

(b) Radial separation between satellites at 600 km simulated with AstroSIM.

Figure 3.7: Operational concept at 600 km.

3.6.5 Phase 2

From 400 km to 300 km, the satellites are in phase 2. In contrast to phase 1, the control scheme, outlined in section 3.6.3, is used to command the satellite orientations. In addition, power modes have been scheduled to not overlap orientation switches and thus, appear more often. Section 3.6.5 shows the separation distance over time at 400 km and the applied operational concept. The control scheme output is shown in green, indicating when orientation switches are made. As explained in section 3.6.3, the transition mode is applied to reduce the relative velocity and dampen the separation oscillations. As shown in figure 3.8b, the radial separation is then significantly reduced after 6 days. After this, a formation maintenance manoeuvre is performed to return the satellites to their nominal separation. In phase 2, 85 of these manoeuvres are done and 255 measurements are taken, where one measurement corresponds to one science mode.

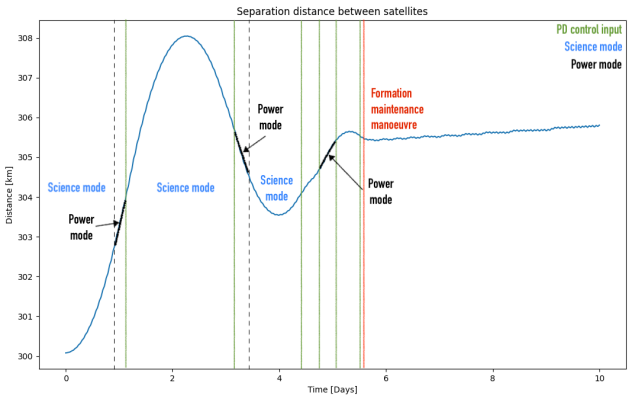

(a) Separation distance between satellites at 400 km simulated with AstroSIM.

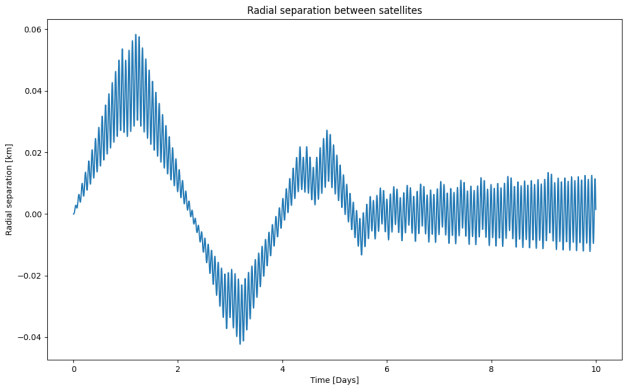

(b) Radial separation between satellites at 400 km simulated with AstroSIM.

Figure 3.8: Operational concept at 400 km.

3.6.6 Phase 3

Phase 3 begins at 300 km and involves accelerometer measurements in addition to the previously used instruments, as discussed in chapter 11. Section 3.6.6 shows the separation distance at 200 km and applied operational concept. In contrast to section 3.6.4, section 3.6.6 shows the last measurement cycles, after which the time until re-entry is in the order of hours. At these low altitudes, the science mode is very short, and the propulsive manoeuvre is applied after each science mode. At 200 km, 4.8 h of science are performed, followed by 1 h of power mode and a formation maintenance manoeuvre. The radial distance reaches up to 1 km after this time, as seen in figure 3.9b. The PD controller output is again shown in green and is used in nominal mode only during phase 3. This results in 98 measurements in total and 204 manoeuvres needed.

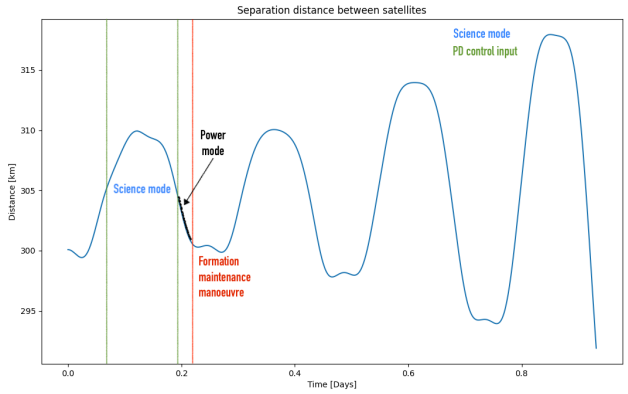

(a) Separation distance between satellites at 200 km simulated with AstroSIM.

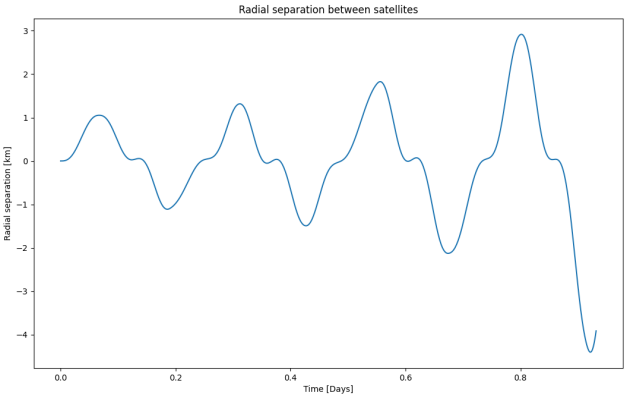

(b) Radial separation between satellites at 200 km simulated with AstroSIM.

Figure 3.9: Operational concept at 200 km.

3.7 Collision Avoidance Strategy

In this section, the software that was used to calculate the collision probability between the SCATTER satellites is explained, after which a preliminary verification is performed for its convergence.

3.7.1 ColCalc Software Description

While in operation, the satellites will fly relatively close (usually at a distance of around 300 km from each other). In order to calculate the expected number of collision avoidance manoeuvres needed throughout the mission lifetime, a Python Monte Carlo simulation tool named ColCalc was developed to calculate the probability of collision between the two satellites, in case one of them becomes non-operational and thus has certain position and velocity uncertainties.

The program is implemented in two dimensions as an equatorial orbit, using an inertial coordinate system centred on Earth. The exact direction of the x-axis does not matter for this analysis, as long as it is held constant and remains in an inertial frame. An orbit propagation algorithm is implemented, using an 8^{th} order Runge-Kutta scheme, which is explained in more detail in the next section. It implements the first-order term of the gravity force and a simplification of the drag force. There are two types of satellites used in the simulation: "rogue" and "target". There is only one target satellite, that is always initialised at the specified position and velocity to obtain a circular orbit. Multiple rogue satellites are used in the simulated, being initialised based on normal

distributions of the altitude, distance to the target, tangential and radial velocities. The simulation propagates their paths in time, and if any of the rogue satellites comes closer to the target satellite than a specified limit, it is considered a collision and the rogue satellite is eliminated from the simulation. The total number of collisions over the simulation time is then divided by the initial number of rogue satellites, the result being the collision probability. The case of one satellite crashing into Earth is also implemented, such that it is no longer considered in the simulation.

The following assumptions and simplifications are made:

AS-COL-01: *A spherical gravity field is used for the gravity force* - this assumption is made to reduce the runtime of the simulation. It is expected to hold, as the simulation is run over short periods of time and no significant effects are expected to accumulate;

AS-COL-02: *The density of the atmosphere for the drag force is assumed constant throughout the simulation* - this assumption is again made to reduce the runtime of the simulation. The density is computed at the beginning using the NRLMSISE-00 model, after which that value is used for the whole program. It is expected to hold, as the simulation is run over short periods of time at approximatively the same altitude, and as such the deviations in density are small;

AS-COL-03: *The drag coefficient of the target satellite can vary with a* $\sigma = \frac{C_{D_2} - C_{D_1}}{2}$ *standard deviation* - this assumption is made to model the uncertainty in drag coefficient during flight. This is in accordance with the lack of high-accuracy knowledge of the accommodation coefficient, which affects the drag coefficient. The most critical situation is when the satellites are at a 90°orientation difference, and thus makes the approaching velocity fastest. Any other orientation (including tumbling) would be less significant;

AS-COL-04: *All other assumptions regarding the propagation of the orbit made in AstroSIM are also valid here* - as the ColCalc software uses the same propagation but in 2 dimensions and a different inertial frame, the same assumptions and reasoning can be made;

AS-COL-05: *To check for a possible collision, the time-parametrised distance between two consecutive timestamps is considered* - this assumption is made such that also the possibility of close-encounter between timestamps is considered, especially for larger time steps. This is considered to hold for not too high time steps;

To calculate the actual probability of collision, the following initial conditions were set. Using these values, a collision probability between the satellites of $4.9 \cdot 10^{-6}$ was obtained.

- Altitude: $h_{target} = 200\,\text{km}$ and $h_{rogue} = 200 \pm 1\,\text{km}$ (2σ). The most critical case for collision probability is at the lowest simulated altitude (at 200 km), when the aerodynamic forces are the highest, and the satellites can get the fastest close to each other, due to the difference in drag. The 1 km 2σ variation is taken as the maximum altitude drift that can occur during Phase 3 at 200 km, as shown in figure 3.9b
- Distance between satellites: $d = 300 \pm 5\,\text{km}$ (2σ). The control scheme of the satellites keeps the distance between them at around 300 km. The highest variation during Phase 2 was simulated to be around 5 km 2σ, as shown in section 3.6.6.
- Tangential velocity: the tangential velocity for the target and the mean of the distribution for the rogue are calculated to be the exact orbital velocities to maintain a perfectly circular orbit at the altitude h_{target}. The 2σ deviation for the rogue distribution is 78.2 m/s, as this was the maximum relative tangential velocity between the satellites experienced during the simulation of Phase 3 at 200 km
- Radial velocity: the radial velocity for the target and the mean of the distribution for the rogue are set to zero, as ideally there would not be a tangential component of the velocity in-orbit. The 2σ deviation for the rogue distribution is 37.6 m/s, as this was the maximum relative radial velocity between the satellites experienced during the simulation of Phase 3 at 200 km
- Number of simulated rogue satellites: $N_1 = 10^7$. Because collision probability is expected to be between 10^{-5} and 10^{-4}, due to the limited available runtime at this design phase and because a histogram is not required, just the final probability, this number of satellites is considered sufficient for a preliminary Monte Carlo simulation.
- Timestamp: $dt = 50\,\text{s}$. As it will be shown in section 3.7.2, this is the largest timestamp that still provides accurate results for the probability.
- Simulation time: $t \approx 3.16\,\text{h}$ or two orbits. It is considered enough time for the satellite to perform a collision avoidance manoeuvre in 2 orbit revolutions, as a Hohmann transfer requires only half an orbit, thus maintaining a safety factor of 4. However, the time between malfunction and the first opportunity to command an avoidance manoeuvre should be taken into account, which currently is maximum in the range of half a day. Due to time constraints, the ColCalc simulation could not be run for so long; therefore, it is recommended for the next design iteration to run the simulation of at least half a day simulation time.

3.7.2 ColCalc Convergence Verification

In order to test the convergence of the software, the simulation was run using the following parameters, at different time steps: $h = 200\,\text{km}$, $d = 10\,\text{m}$, $N_1 = 10^5$, $t = 50\,000\,\text{s}$. The results are shown in figure 3.10. As it can be

seen, below and including a time step of 50 s, the value of the probability remains consistent. As such, the highest acceptable time step will be used, which is $dt = 50$ s.

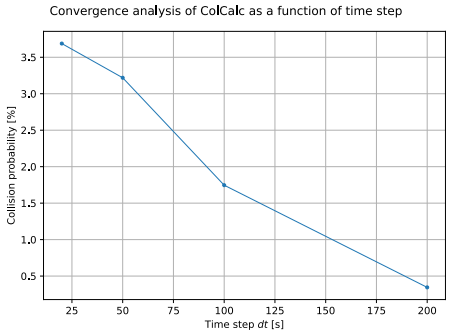

Figure 3.10: Convergence graph of the ColCalc software as a function of time step.

3.8 Mission Verification & Validation

To determine the mission profile of Project SCATTER and obtain accurate estimations of several orbital parameters such as mission lifetime and satellite position and attitude, numerical simulations were employed. This has been achieved using an in-house built non-linear 6 Degree-of-Freedom orbit propagation software written in Python 3.8. Furthermore, this software has been used to verify that the chosen mission profile satisfies all requirements outlined in section 3.2. An in-house software called "AstroSIM" was developed due to its high versatility and robustness, as it allows for the accurate prediction of several subsystem-specific design parameters on top of the resulting simulated orbits. In section 3.8.3, this software is validated using orbital data from two CubeSat missions [15]. Then, in section 3.8.3, the mission profile itself is verified and conclusions are drawn.

3.8.1 AstroSIM Software Description

AstroSIM consists of two solvers: a 3-degree-of-freedom solver allowing for large timescale orbit predictions, and a 6-degree-of-freedom solver aimed at the accurate simulation of a spacecraft's attitude for a limited number of orbits. **The main assumptions** used in these solvers are given in the list below:

AS-ASTRO-01: *The satellites are rigid bodies* - this assumption is made to neglect any elastic and thermal effects that could affect the moment of inertia of the satellites. As these would have a thermal subsystem to regulate their temperature, the assumption is expected to hold;

AS-ASTRO-02: *The NRLMSISE-00 model is used to model the atmosphere* - this assumption is made to derive in a robust way the atmospheric parameters needed for drag calculations. It will hold, given that this model is based on mass spectrometer atmospheric data;

AS-ASTRO-03: *The Earth is assumed to be a perfect sphere* - this assumption is made to keep the ground level constant for any latitude and longitude. Therefore, it is expected to introduce negligible errors in the prediction of the radius, R, especially around the poles and equator;

AS-ASTRO-04: *Tidal effects caused by the Moon are neglected* - this assumption is made as well to make the model more computationally-robust. Given that the effects caused by the Moon on LEO satellites is negligible, the assumption is valid;

AS-ASTRO-05: *Earth's magnetic field effect on the orbital decay is neglected* - this assumption is made to, again, make the Astrodynamics model more computationally robust. As the magnetic drag is an order of magnitude smaller than atmospheric drag for low altitudes (< 600 km), this assumption is valid;

AS-ASTRO-06: *Solar pressure drag effects are neglected* - this assumption is again made to make the software more computationally robust, as they are negligible in comparison to atmospheric drag effects at low altitudes (< 600 km).

AS-ASTRO-07: *For the 3-degree-of-freedom solver, all orbits are simulated around the equator* - this assumption is made to allow for the usage of large time steps in orbit simulations (> 600 s), and avoid numerical errors due to the singularity induced by Euler angles. For simulations spanning years, the errors introduced by this assumption are deemed acceptable.

The algorithm of AstroSIM is as follows. Three reference frames are used for different kinematic equations of the space element. These are: the Inertial Frame (I) - a fixed frame with its origin in the centre of the planet; the Earth-fixed, Earth-centered frame (C) - a frame rotating with the planet, with its centre in the centre of gravity of it, and its z-axis parallel to the axis of rotation, and the Vehicle-carried Earth frame (E) - a frame with its origin

[15] `https://directory.eoportal.org/web/eoportal/satellite-missions/c-missions/canx-7`

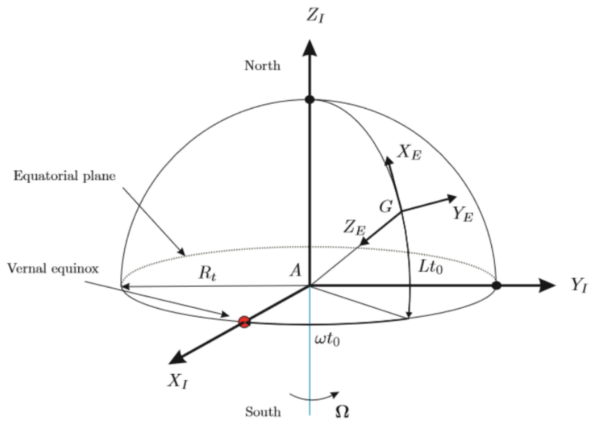

Figure 3.11: The reference frames used by AstroSIM [21].

in the Centre of Mass (CoM) of a satellite, its z-axis pointed towards the origin of the E-frame, and the x-axis pointed north. These are shown in Fig. 3.11:
The algorithm used is written in the E-frame, where the velocities V_N, V_E and V_D are defined along the x, y and z axes, while the angular rates of the satellite are defined as p, q and r along the same axes. The translational system of equations of motion is given in Eq. (3.1) [21]:

$$\begin{aligned}
\dot{V_N} &= \frac{F_x}{m} - 2\Omega_t V_E \sin\delta - \Omega_t^2 R \sin\delta\cos\delta - \frac{V_E^2 \tan\delta - V_N V_D}{R} \\
\dot{V_E} &= \frac{F_y}{m} + 2\Omega_t \left(V_D \cos\delta + V_N \sin\delta\right) + \frac{V_E}{R}\left(V_N \tan\delta + V_D\right) \\
\dot{V_D} &= \frac{F_z}{m} - 2\Omega_t V_E \cos\delta - \Omega_t^2 R \cos^2\delta - \frac{V_E^2 + V_N^2}{R},
\end{aligned} \tag{3.1}$$

where F_x, F_y and F_z are the external forces applied on the satellite, m is the mass of the satellite, δ and τ are the latitude and longitude of the satellite, Ω_T is the angular velocity of the Earth around the z-axis of the C-frame and R is the distance of the satellite to the center of gravity of the Earth. On top of these equations, the following kinematic insight is used [21] :

$$\dot{\delta} = \frac{V_N}{R}, \quad \dot{\tau} = \frac{V_E}{R\cos\delta}, \quad \dot{R} = -V_D. \tag{3.2}$$

These equations describe in full the translational motion of a satellite in orbit, with external forces applied to it. A disadvantage of them is a singularity that forms in polar orbits, when $\cos\delta \approx 0$. To counter this, a carefully chosen time step is used for these orbits in the 6 degree-of-freedom solver. For the 3-degree-of-freedom counterpart, orbits are simulated only at the equator, and errors are deemed acceptable. In a similar fashion, the equations of motion for the satellite's rotational motion in the 6-degree-of-freedom implementation are given by Eq.(3.3), in the E-frame [21]:

$$\begin{bmatrix} \dot{p} \\ \dot{q} \\ \dot{r} \end{bmatrix} = I_B^{-1} \cdot \left(\begin{bmatrix} M_x \\ M_y \\ M_z \end{bmatrix} - \begin{bmatrix} p \\ q \\ r \end{bmatrix} \times \left(I_B \cdot \begin{bmatrix} p \\ q \\ r \end{bmatrix} \right) \right) \tag{3.3}$$

Next, the intermediary angular rates of the satellite are given by [21]:

$$\begin{aligned}
\hat{p} &= p + \cos\theta \sin\Psi\dot{\delta} - \left(\cos\delta\cos\Psi\cos\theta + \sin\delta\sin\theta\right)\left(\dot{\tau} + \Omega_t\right) \\
\hat{q} &= q + \left(\sin\Psi\sin\theta\sin\Phi + \cos\Psi\cos\Phi\right)\dot{\delta} - \left(\cos\delta\left(\cos\Psi\sin\theta\sin\Phi - \sin\Psi\cos\Phi\right) - \sin\delta\cos\theta\sin\Phi\right)\left(\dot{\tau} - \Omega_t\right) \\
\hat{r} &= r + \left(\sin\Psi\cos\Phi\sin\theta - \cos\Psi\sin\Phi\right)\dot{\delta} - \left(\cos\delta\left(\sin\Psi\sin\Phi + \cos\Psi\sin\theta\cos\Phi\right) - \sin\delta\cos\theta\cos\Phi\right)\left(\dot{\tau} + \Omega_t\right).
\end{aligned} \tag{3.4}$$

Finally, the roll, pitch and yaw rates of the satellite (in the E-frame) are given by Eq. (3.5) [21]:

$$\begin{aligned}
\dot{\Phi} &= \hat{p} + \sin\Phi\tan\theta\hat{q} + \cos\Phi\tan\theta\hat{r} \\
\dot{\theta} &= \cos\Phi\hat{q} - \sin\Phi\hat{r} \\
\dot{\Psi} &= \frac{\sin\Phi}{\cos\theta}\hat{q} + \frac{\cos\Phi}{\cos\theta}\hat{r},
\end{aligned} \tag{3.5}$$

where $\dot{\Phi}$, $\dot{\theta}$ and $\dot{\Psi}$ are the roll, pitch and yaw angular rates of the spacecraft with respect to the E-frame. Because the above equations form a non-linear system of differential equations, an accurate, 8^{th} order Runge-Kutta scheme is employed to solve it for very large time steps (> 600 s), in order to get mission life-time predictions in reasonable computational times. This scheme is given by Eq (3.6):

$$\begin{aligned}
\mathbf{k_0} &= \mathbf{f}\left(\mathbf{P}, t\right) \\
\mathbf{k_1} &= \mathbf{f}\left(\mathbf{P} + \frac{4}{27}\cdot\Delta t\cdot\mathbf{k_0}, t\right) \\
\mathbf{k_2} &= \mathbf{f}\left(\mathbf{P} + \frac{1}{18}\Delta t\left(\mathbf{k_0} + 3\mathbf{k_1}\right), t\right) \\
\mathbf{k_3} &= \mathbf{f}\left(\mathbf{P} + \frac{1}{12}\Delta t\left(\mathbf{k_0} + 3\mathbf{k_2}\right), t\right) \\
\mathbf{k_4} &= \mathbf{f}\left(\mathbf{P} + \frac{1}{8}\Delta t\left(\mathbf{k_0} + 3\mathbf{k_3}\right), t\right) \\
\mathbf{k_5} &= \mathbf{f}\left(\mathbf{P} + \frac{1}{54}\Delta t\left(13\mathbf{k_0} - 27\mathbf{k_2} + 42\mathbf{k_3} + 8\mathbf{k_4}\right), t\right) \\
\mathbf{k_6} &= \mathbf{f}\left(\mathbf{P} + \frac{1}{4320}\Delta t\left(389\mathbf{k_0} - 54\mathbf{k_2} + 966\mathbf{k_3} - 824\mathbf{k_4} + 243\mathbf{k_5}\right), t\right) \\
\mathbf{k_7} &= \mathbf{f}\left(\mathbf{P} + \frac{1}{20}\Delta t\left(-231\mathbf{k_0} + 81\mathbf{k_2} - 1164\mathbf{k_3} + 656\mathbf{k_4} - 122\mathbf{k_5} + 800\mathbf{k_6}\right), t\right) \\
\mathbf{k_8} &= \mathbf{f}\left(\mathbf{P} + \frac{1}{288}\Delta t\left(-127\mathbf{k_0} + 18\mathbf{k_2} - 678\mathbf{k_3} + 456\mathbf{k_4} - 9\mathbf{k_5} + 576\mathbf{k_6} + 4\mathbf{k_7}\right), t\right) \\
\mathbf{k_9} &= \mathbf{f}\left(\mathbf{P} + \frac{1}{820}\Delta t\left(1481\mathbf{k_0} - 81\mathbf{k_2} + 7104\mathbf{k_3} - 3376\mathbf{k_4} + 72\mathbf{k_5} - 5040\mathbf{k_6} - 60\mathbf{k_7} + 720\mathbf{k_8}\right), t\right) \\
\mathbf{P^{t+\Delta t}} &= \mathbf{P} + \frac{1}{840}\Delta t\left(41\mathbf{k_0} + 27\mathbf{k_3} + 272\mathbf{k_4} + 27\mathbf{k_5} + 216\mathbf{k_6} + 216\mathbf{k_8} + 41\mathbf{k_9}\right),
\end{aligned} \tag{3.6}$$

where $\mathbf{f}$ is a vector function yielding the translational and rotational accelerations of the satellite, $\mathbf{P}$ is the position and attitude vector of the satellite at time t and $\mathbf{P^{t+\Delta t}}$ is the same vector at time $t + \Delta t$. The algorithm thus integrates the trajectory of multiple satellites through time. The drag force imposed on the satellites is computed using the DSMC Python software, and then applied as an external force here. The computed orbital decays are then plotted as functions of time.

With AstroSIM's orbit and attitude propagation models covered, the spacecraft control schemes implemented within the software, for mission and subsystem design, are now covered. These are the following: a differential-drag-based proportional-differential-integral (PID) binary control scheme to simulate formation flying between two satellites, a B-dot attitude control scheme used for satellite magnetorquer-based de-tumbling simulations, and an attitude proportional-differential (PD) scheme for reaction-wheel-based attitude control.

The PID formation flying scheme is as follows. Each satellite is assigned one of two possible drag coefficients C_{D_0} and $C_{D_{90}}$, $C_{D_0} \neq C_{D_{90}}$ which capture their drag forces at 0 ° and 90 °. A nominal (Euclidean) distance, d_{nom}, is also defined between the two satellites. The control scheme attempts to minimize the error function $e = e(t)$, defined as shown in Eq. (3.7):

$$e(t) = \frac{|\mathbf{X_2} - \mathbf{X_1}|}{d_{nom}} - 1, \quad \mathbf{X_i} = \begin{bmatrix} R_i\cos\tau_i\cos\delta_i \\ R_i\sin\tau_i\cos\delta_i \\ R_i\sin\delta_i \end{bmatrix}, \tag{3.7}$$

where $\mathbf{X_i}$ is the position vector of satellite i. The derivative of this error function is given in Eq. (3.8):

$$\frac{de}{dt}(t) = \frac{1}{d_{nom}}\frac{\partial\left|\mathbf{X_2} - \mathbf{X_1}\right|}{\partial t} \approx \frac{1}{\Delta t\cdot d_{nom}}\left(\left|\mathbf{X_2^{t+\Delta t}} - \mathbf{X_1^{t+\Delta t}}\right| - \left|\mathbf{X_2^t} - \mathbf{X_1^t}\right|\right), \tag{3.8}$$

where $\mathbf{X_i^t}$ is the position of satellite i at time t, and Δt is the simulation time step. The integral of the error function is consequently given by:

$$\int_{t_0}^{t} e(s)ds \approx \sum_{i=0}^{N_t} e(t_i)\cdot dt, \tag{3.9}$$

where N_t is the number of time steps simulated until a given time, t. A control function, u(t) is thus defined, as follows:

$$u(t) = K_p\cdot e(t) + K_d\cdot\frac{de}{dt} + K_i\cdot\int_{t_0}^{t} eds, \tag{3.10}$$

where K_p is the proportional gain, K_d is the differential gain and K_i is the integral gain of the scheme. Using this function, the drag coefficient configuration of the two satellites is given by the following law:

$$C_{D_1} = \begin{cases} C_{D_{90}}, u < 0 \\ C_{D_0}, u \geq 0 \end{cases} \quad , \quad C_{D_2} = \begin{cases} C_{D_0}, u < 0 \\ C_{D_{90}}, u \geq 0 \end{cases} \quad . \tag{3.11}$$

The B-dot scheme for magnetorquer de-tumbling is adapted from Sharma et al. [22], and is as follows. The magnetic field of Earth, B, is used to create a differential-only controller which is meant to cancel the angular velocity of the spacecraft. The magnetic dipole moment to be provided by the magnetorquer is therefore:

$$\mu_{\mathbf{M}} = -k\frac{\dot{\mathbf{B}}}{||\mathbf{B}||} \approx -\frac{k}{||\mathbf{B}||} \cdot \left(\mathbf{B} \times \mathbf{\Omega}_{\mathbf{B}}^{\mathbf{B}}\right), \tag{3.12}$$

where k is the control gain, and $\mathbf{\Omega}_{\mathbf{B}}^{\mathbf{B}}$ is the angular velocity of the satellite expressed in the body frame. The magnetic field of Earth, $\mathbf{B}$ is modelled in the E-frame using the following simplified laws:

$$\begin{bmatrix} B_N \\ B_E \\ B_D \end{bmatrix} = \begin{bmatrix} -B_0 \left(\frac{R_E}{R}\right)^3 \cos(i + \alpha_m) \\ 0 \\ -2 \cdot B_0 \left(\frac{R_E}{R}\right)^3 \sin(i + \alpha_m) \end{bmatrix}, \tag{3.13}$$

where $B_0 = 3.12$ μT is the magnitude of the field at the equator, and $\alpha_i = 9.6°$ is the inclination of Earth's magnetic pole. This model introduces significant error in the transient behaviour of the attitude, as it does not capture the dynamic behaviour of the Earth's magnetic field. However, for investigating de-tumbling time, it serves as a sufficient, conservative solution. The gain, k, is determined automatically, as shown in [22], according to:

$$k = 2 \cdot \sqrt{\frac{GM}{a^3}} \cdot (1 + \sin(\xi)) \cdot \min\left(\mathbf{I_B}\right), \tag{3.14}$$

where a is the semi-major axis of the satellites orbit, GM is the Earth gravitational parameter, ξ is the Geomagnetic inclination of the orbit and $\mathbf{I_B}$ is the diagonal moment of inertia matrix of the satellite. The control torque, in Body frame, from the magnetorquer is therefore:

$$\mathbf{T_B} = \max\left(\min\left(\mu_M, -\mu_{\mathbf{max}}\right), \mu_{\mathbf{max}}\right) \times \mathbf{B}, \tag{3.15}$$

where $\mu_{\mathbf{max}}$ is the maximum dipole moment that can be provided by the magnetorquer.
The attitude PD scheme for reaction wheel is as follows. An error function, $e(t)$ is defined as the cross product between the satellite's pointing vector $\mathbf{p}$, and its desired pointing vector, $\mathbf{s}$: $e(t) = \mathbf{p} \times \mathbf{s}$. The derivative of this error function is approximated as: $\frac{de}{dt}(t) = \frac{\partial(\mathbf{p} \times \mathbf{s})}{\partial t} \approx \mathbf{\Omega}_{\mathbf{B}}^{\mathbf{B}}$. The control function, $\mathbf{u(t)}$, is therefore defined as:

$$\mathbf{u(t)} = K_p \cdot (\mathbf{p} \times \mathbf{s}) + K_d \cdot \mathbf{\Omega}_{\mathbf{B}}^{\mathbf{B}}. \tag{3.16}$$

This function is directly applied to the 6 degree-of-freedom solver as an external torque.

3.8.2 AstroSIM Verification and Validation

AstroSIM's 3 degree-of-freedom solver has been verified and validated using data available in literature from a mission similar in scope to SCATTER, namely CanX7 [16]. The purpose of this mission is to investigate orbital decay using a sail CubeSat design. To do this, the space element (one satellite) was deployed from an altitude of 681.25 km into a circular orbit, and its decay was observed. The same decay has now been simulated using the proposed code, and the results were compared. These are shown in Fig. 3.12, and the mission parameters used in the simulation are given in Table 3.13 [17]:

[16] `https://directory.eoportal.org/web/eoportal/satellite-missions/c-missions/canx-7`
[17] `https://directory.eoportal.org/web/eoportal/satellite-missions/c-missions/canx-7`

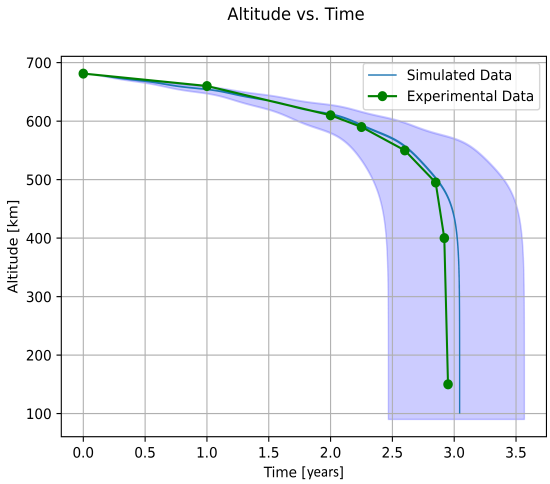

Figure 3.12: The simulated and recorded orbital decay of the CanX7 mission.

Figure 3.13: Table of spacecraft and mission properties of the CanX-7 mission.

Parameter	Value	Parameter	Value
Satellite Mass	7.5 kg	Orbital Altitude	681.25 km
Projected Surface Area	4 m^2	Expected F10.7	90
Drag Coefficient	2.2	Minimum F10.7	84
Orbital Velocity	7514 m/s	Expected F10.7	97

As it can be seen in the figure, the experimental and simulated orbital decays show a strong correlation for the given mission parameters. The simulation has also computed the predicted orbital decay range based on the 2σ estimations of the minimum and maximum F10.7 cm solar activity values from 2017, when the mission took place. The expected and experimental curves match with a $R^2 = 0.978$ value, thus validating the software for missions similar to CanX7.

AstroSIM's 6 degree-of-freedom solver and control schemes have been validated using one paper written by Sharma et. al [22], and verified with a system test of a reaction wheel actuation to enter the science mode outlined in section 3.6.2. In [22], a CubeSat is given an initial angular velocity vector, and magnetorquers using the B-dot algorithm are used to bring this velocity to zero. The following simulation inputs have been used:

Table 3.8: De-tumbling simulations initial parameters used in [22].

Parameter Name	Value	Parameter Name	Value	Parameter Name	Value
Diagonal Inertia	(0.33, 0,37, 0,35) kg m^2	Semi-major axis	6978 km	Initial Angular Velocity	(0.6, -0.5, -0.4) rad/s
Max. Dipole Moment	2 Am^2	Eccentricity	0	Ascending Node	0 rad
Initial Attitude (Body)	(0, 0, 0) rad	Inclination	56°	Argument of Periapsis	0 rad

The results of the de-tumbling simulations using both the method in [22] and AstroSIM are shown in Fig. 3.15 and Fig. 3.14:

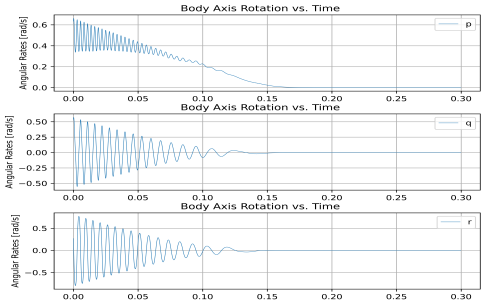

Figure 3.14: De-tumbling simulation of the CubeSat presented in [22] using AstroSIM and an in-house built B-dot algorithm.

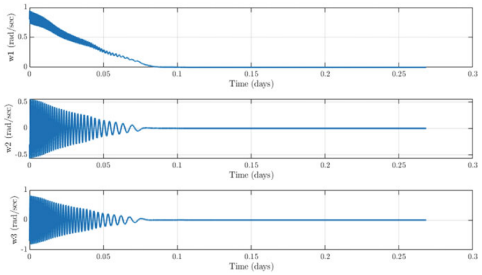

Figure 3.15: De-tumbling simulation of the CubeSat presented in [22] as shown in the publication.

As it can be seen in the figure, the AstroSIM de-tumbling simulation shows a very similar behaviour to the one shown in [22] for the given initial conditions. The body x-axis angular velocity remains positive for both simulations, while the other two oscillate around 0. It can be observed that the de-tumbling time computed by AstroSIM ($\approx$ 0.14 days) is significantly higher than the one observed in the paper ($\approx$ 0.09 days). This happens for two reasons: the magnetic field model used by AstroSIM is dipolar, and therefore, results in far less variation in $\mathbf{B}$ which decreases $\dot{\mathbf{B}}$. Furthermore, the control gains used in the paper remain unknown, and therefore, a better matching between the results could be achieved if the gains computed from Eq. (3.14) are tuned further. Given that the estimation is conservative, AstroSIM is considered validated for de-tumbling, as per the philosophy explained in section 1.6.

Validating the control scheme used for reaction wheels has proven difficult as no studies implementing such a scheme were found in literature. Therefore, a verification procedure is employed where a CubeSat satellite is actuated to enter "Science mode" as described in section 3.6.2. The angle of attack α and angle of sideslip β are being plotted as a result. It is expected that both of them converge towards 0 when the mode is entered. The simulation inputs used in this simulation are given in table 3.9:

Table 3.9: Reaction wheel system test initial parameters.

Parameter Name	Value	Parameter Name	Value	Parameter Name	Value
Diagonal Inertia	(0.0056, 0.026, 0.0026) kg m^2	Semi-major axis	6978 km	Initial Angular Velocity	(0, 0, 0) rad/s
Max. Wheel Torque	2 mNm	Eccentricity	0	Ascending Node	0 rad
Initial Attitude (Body)	(40, 20, 60)°	Inclination	56°	Argument of Periapsis	0 rad

The results of the reaction wheel actuation simulations for the system verification of the PD control scheme are shown in Fig. 3.16 and Fig. 3.17:

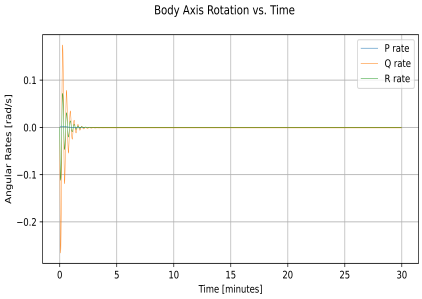

Figure 3.16: Satellite body angular rates under reaction wheel actuation for science mode simulated with AstroSIM.

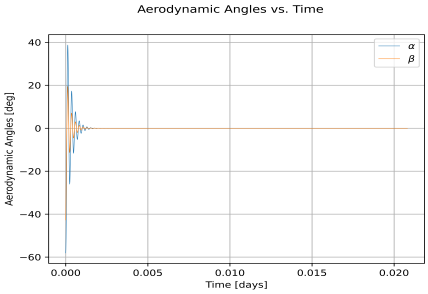

Figure 3.17: Satellite aerodynamic angles under reaction wheel actuation for science mode simulated with AstroSIM.

As it can clearly be seen in the figures above, the reaction wheel control scheme converges the angle of attack and side-slip angle to 0 ° as the angular rates of the spacecraft with respect to the E-frame are reduced to 0 by the reaction wheels, which is the expected result. Provided that the 6 degree-of-freedom solver itself has already been validated and given the philosophy outlined in section 1.6, the PD scheme is considered verified and validated.

3.8.3 Mission Requirement Verification

REQ-M-01: - this requirement is verified through inspection of section 1.2 and section 3.5, where all lifetime and mission profile calculations assume two satellites are being used;

REQ-M-02: - this requirement is verified through analysis of the mission lifetime in this phase of the project. In section 3.6.1, the lifetime of the mission is estimated to lie between 1.853 years and 2.288 years for minimum and maximum assumed solar cycles. As both estimations are larger than 1 year, the requirement is verified;

REQ-M-03: - this requirement is verified through analysis of the orbital altitude of the mission throughout its lifetime. As shown in figure 3.5, both satellites reach an altitude below 150 km, at which de-orbiting is certain to occur without any propulsive manoeuvres performed;

REQ-M-04: - this requirement is verified through the analysis of the mission profile performed in section 3.5, through table 3.4, where phase I is defined between altitudes of 400 km and 600 km, phase II between 300 km and 400 km, and phase III from 300 km down to de-orbiting. As all phases allow for the collection of scientific measurements, the requirement is verified;

REQ-M-05: - this requirement is verified through analysis using table 3.4 and the NRLMSISE-00 atmospheric model [3]. As it can be seen in figure 3.18, the helium concentration exceeds 20% beyond 385 km, which lies in a part of phase II and all of phase I. Therefore, the requirement is verified.

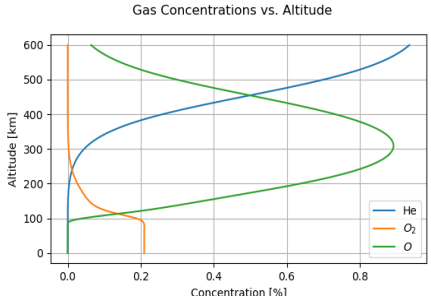

Figure 3.18: NRLMSISE-00 atmospheric gas concentrations with altitude for F10.7 = 68.

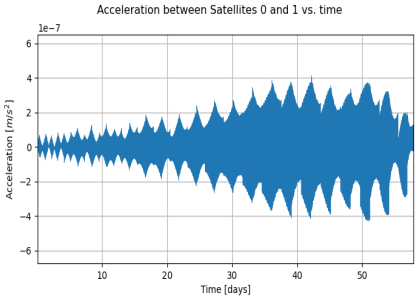

Figure 3.19: Simulated relative acceleration between satellites in Phase III, from 300 km to 100 km, using AstroSIM.

REQ-M-06: - this requirement is verified through analysis using table 3.4 and figure 3.5a, where 80 measurements are taken at 20 equidistant altitudes, between 400 km and 600 km;

REQ-M-07: - this requirement is verified through analysis using table 3.4 where phase II is simulated to last between 451.71 days and 602.27 days at altitudes between 300 km and 400 km;

REQ-M-08: - this requirement is verified through analysis using table 3.4 where in phase II, 255 measurements are planned and estimated possible;

REQ-M-09: - this requirement is verified through analysis using table 3.4 where phase III is simulated to last between 35.66 days and 45.39 days at altitudes between de-orbiting and 300 km;

REQ-M-10: - this requirement is verified through analysis using table 3.4 where phase III is simulated to last between 35.66 days and 45.39 days at altitudes between de-orbiting and 300 km;

REQ-M-11: - this requirement is verified through analysis in section 3.7.1, where the probability of collision is estimated and additional ΔV is added to the OCS subsystem in chapter 8 for this scenario;

REQ-M-13: - this requirement is verified through inspection of the payload subsystem, which is equipped with QB-50 mission mass spectrometers as shown in chapter 11 [23];

REQ-M-14: - this requirement is verified through inspection of the payload subsystem, which is equipped with QB-50 mission mass spectrometers as shown in chapter 11 [23];

REQ-M-15: - this requirement is verified by analysis of the mission profile, where differential-drag formation flying is simulated for all science phases in section 3.6.3, and inspection of the payload subsystem in chapter 11, where a GNSS receiver and patch antenna are added to the satellites;

REQ-M-16: - this requirement is verified through analysis, by simulating the relative satellite accelerations experienced in phase II of the mission. The resulting plot is shown in figure 3.19. As shown in chapter 11, the Pulse-40 IMU [18] has a bias instability of 6 μm/s^2, while the highest relative acceleration is 10 μm/s^2. Therefore, the requirement is not satisfied;

REQ-M-17: - this requirement is verified by analysis in section 3.6.3, where the in-plane orbital distance between the satellites is simulated in all phases. As the largest expected distance is 330 km, the requirement is verified;

REQ-M-18: - this requirement shall be verified through inspection in the testing and qualification stages of the project. Testing procedures and results shall be documented electronically and stored digitally;

REQ-M-19: - this requirement shall be verified through an inspection of the system verification procedures outlined in this report;

REQ-M-20: - this requirement is verified through analysis of the mission profile in the form of formation flying simulations using AstroSIM, in section 3.6.3. As the smallest expected distance is 290 km, the requirement is verified;

REQ-M-21: - this requirement is verified through analysis of the mission profile in the form of formation flying simulations using AstroSIM, in section 3.6.3. As the largest predicted altitude difference is 2.6 km, the requirement is verified;

REQ-M-22: - this requirement is verified through analysis of the mission profile in the form of lifetime simulations using AstroSIM in section 3.6.1. As the largest expected lifetime is 2.29 years, the requirement is verified;

REQ-M-23: - this requirement is verified partially in this report through inspection. In section 3.5, the mission is designed for the orbit imposed by Vega-C [10], by choosing an orbit inclination of 97 °. Furthermore, the CubeSat deployer size constraints are accounted for in chapter 13. The remaining requirements from the Launcher manual shall be verified through demonstration with mock-ups of the design, or ground-based qualification and acceptance tests.

[18] `https://www.sbg-systems.com/products/pulse-imu-sensor/`

3.9 Mission Overview Concluding Remarks

In future design phases, it is recommended to consider Vega-E as a more sustainable launch vehicle. In the operational concept, each phase was assessed separately at one altitude, however the operations change constantly with altitude. Thus, it is recommended to perform more extensive analysis on the operational concept and the formation flying over the complete altitude range. Finally, in the mission lifetime analysis, the 95th percentile of solar flux predictions could be included, and the initial orbit altitude could be varied. This would include launcher uncertainty and higher confidence in mission lifetime due to solar activity. A further recommendation that can be made about the collision avoidance strategy would be to have the satellites in quasi-parallel orbits, with a separation in the longitude of the ascending node. Such a separation would significantly decrease the risk of collision. However, due to the fact that the launcher will deploy the two satellites in the same orbit, an "inclination" change burn would need to be made somewhere near the poles. It is recommended for the next design iteration to analyse this option and see if it would decrease or increase the delta-V budget.

4. Aerodynamic Design

This chapter addresses the detailed aerodynamic design of the spacecraft for project SCATTER. This entails refining and optimizing the chosen preliminary shape which was selected in section 2.3 and providing a detailed aerodynamic profile for the design of other subsystems. This chapter is organized in the following order: first, the aerodynamic subsystem requirements will be presented in section 4.1. Following from this, an overview of the detailed aerodynamic design will be provided in section 4.2. This includes a brief description of the selected preliminary design and the reasons for its aerodynamic effectiveness. Following from this, the detailed design as described earlier can take place. Upon completion of the full aerodynamic analysis, the numerical software which is used in the aerodynamics design is verified against tried and tested software from industry standards, and is validated against experimental data from previous missions. Finally, to conclude this chapter, the aerodynamics subsystem is verified by demonstrating compliance with the subsystem requirements. These elements are presented in section 4.3.

4.1 Aerodynamic Requirements

Before any detailed aerodynamic analysis may begin, first the requirements for this particular subsystem must be outlined. This will drive the design process which will take place in the subsequent sections in this chapter. In order to ease the readability of the requirements, the reader is encouraged to review the criteria used in the trade-off of the preliminary designs, as described in section 2.3 (especially to get an understanding of the term "drag sensitivity to GSI", otherwise denoted as $\Delta C_{D\alpha}$). For reference, the ballistic coefficient is a measure of how easily an object can overcome air resistance. Mathematically, this is quantified as the equation

$$C_B = \frac{m}{C_D \cdot S} \tag{4.1}$$

Where C_B is the ballistic coefficient, m is the spacecraft mass, C_D is the drag coefficient and S is the projected surface area. With this information clarified, the aerodynamic requirements are presented in table 4.1.

Table 4.1: Aerodynamic shape subsystem requirements.

ID	Description	Parent Requirement	Rationale
REQ-AER-01	The shape shall have sensitivity to GSI parameters of at least 1.1	REQ-M-15	Errors in drag coefficient modelling (depending on selection of GSI Model and modelling of particle to particle collisions) ranges at approximately 20%. Assuming a satellite drag coefficient of 2.2 (which is standard according to SMAD [12]) and a safety factor of 1.25, then the difference in drag coefficient which could be omitted due to error is given as twice the absolute error of the drag coefficient of one satellite. This is given as $2 \cdot 0.2 \cdot 2.2 \cdot 1.25 = 1.1$
~~REQ-AER-02~~	~~The aerodynamic shape of the spacecraft shall have an average ballistic coefficient of at least 60 kg/m^2 over its two flying configurations and over altitudes between 100kilometre and 300 kilometre~~	~~REQ-M-22~~	Struck out on the basis that mission lifetime in phase 3 is a performance requirement which is affected by more than just aerodynamic shape. For example, a change in spacecraft mass can change the whole requirement here
REQ-AER-03	The structure of the space element shall be designed such that the ratio of the areas of the surfaces perpendicular and parallel to the atmospheric flow changes by a factor of three or more when changing the attitude by 90° in yaw or pitch	REQ-SYS-D-06	This requirement is given in the project description and high level requirements
REQ-AER-04	The difference in ballistic coefficient between the high and low drag configurations of the satellite at an altitude of 400 km shall be at least 30.257	REQ-M-22	The mission requires that one science mode segment is at most 72 hours due to the risk of the satellite power depleting. Therefore, the satellite drift between satellites must occur before that time period.

4.2 Aerodynamic Design Overview & Detailed Design

With the subsystem requirements clearly defined, the detailed design phase of the aerodynamic shape may take place. This will first begin with a description of the preliminary aerodynamic shape, which was found to be the most promising design following the trade-off described in section 2.3. As it can be seen in figure 4.1, the main body consists of a standardized CubeSat frame with dimensions of 0.228 m by 0.228 m by 0.340 m. These dimensions were primarily selected to have sufficient internal volume for all the internal components, and to be able to be compatible with standard satellite deployers for CubeSats and nanosatellites (see chapter 13). Along the side, top and bottom faces of the primary body, there are panels lying at shallow angles to the oncoming flow. During nominal operations, the first spacecraft travels along the x-axis towards the flow (so-called "low drag configuration"), while the second spacecraft is rotated along the z-axis and travels in the y-axis ("high drag configuration"). This shape is extremely effective for maximizing the drag sensitivity to GSI parameters, as when the collisions with oncoming air particles were mainly specular (in other words, the normal, tangential and energy accommodation coefficients are zero), the shallow angled panels contribute very little to the drag force as they are nearly parallel to the flow. However, as soon as there is a diffuse reflection of particles upon collision with the spacecraft surface (increase in normal, tangential and energy accommodation coefficients), the contribution

of the panels in frictional drag quickly becomes the predominant source of atmospheric drag due to their vast length. The small angles on the panel allows for an increased number of particles to collide with the spacecraft in comparison to a body with perpendicular straight edges, leading to an even higher sensitivity to GSI parameters. In the high-drag configuration, the large frontal surface area leads to a high drag at low normal, tangential and energy accommodation coefficients. However, the lack of side panel area means that there will be no drag caused by diffuse reflection of particles, resulting in a sharp decrease in drag coefficient with increasing normal, tangential and energy accommodation coefficients. For these reasons, this design was found to be very sensitive to GSI parameters and was chosen to be carried forward into detailed design.

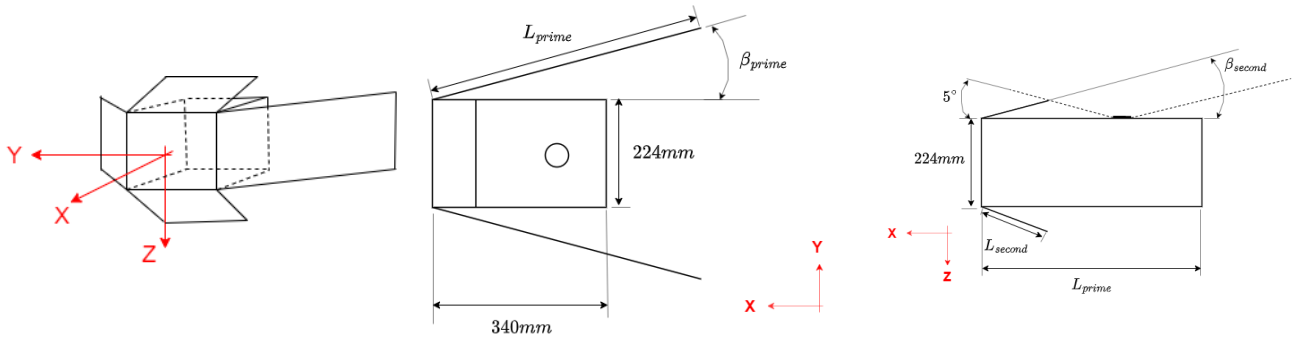

Figure 4.1: Isometric, xy plane view and xz plane view of the preliminary shape design. If the flow is travelling from the left to the right of the page, the low drag configuration corresponds to the xy and xz plane configuration. The high drag configuration corresponds to a rotation about the z-axis by 90 degrees with respect to the on-coming flow.

4.2.1 Optimization of the Aerodynamic Shape - Detailed Design

Although the findings from the trade-off were very revealing, there remains many open questions regarding the exact aerodynamic geometry that the satellite should have. While the importance of shallow body panel angles cannot be overlooked for drag sensitivity to GSI parameters, there are practical limits to this concept. Disproportionally long panels may require multiple hinges to deploy them in orbit, which in turn could hinder reliability. Furthermore, at the top and bottom faces of the spacecraft, long shallow-angled panels can block out the field of view of key payload and TT&C equipment. Finally, it is not yet understood which is the optimum angle that maximizes the drag sensitivity to GSI parameters. As a result of these factors, the optimisation procedure of the spacecraft aerodynamics consists mainly of quantifying the effect of panel length and angle on the drag sensitivity to GSI parameters, and determining an optimal shape which fulfils the requirements with the highest margin while respecting the practical constraints. These sensitivity analyses will be conducted here.

First, the large, shallow-angled panels which reside on the side of the spacecraft body will be considered. These panels are likely going to be the primary driver in the aerodynamic features of the spacecraft, due to their large surface area. Therefore, the influence of L_{prime} and β_{prime} should be immediately evident when they are modified. Asides from the reliability and mass concerns discussed in the previous paragraph, there is no concrete limit to the values which β_{prime} and L_{prime} can take. Therefore, in order to get an assessment of how L_{prime} and β_{prime} impact the overall aerodynamic performance of the spacecraft, first the length of the panel will be kept fixed while the angle of the panel is adjusted. Then, based on these results, the panel is kept fixed at the optimum angle and the length of the panel is adjusted. For each combination of panel angle and length, the projected area is calculated for both the high and low drag configurations using equation 4.2 and equation 4.3:

$$A_{projectedlarge} = 0.224 \cdot L_{prime} \cdot \cos(\beta_{prime}) \tag{4.2}$$

$$A_{projectedsmall} = 0.224 \cdot 0.224 + 2 \cdot (0.224 \cdot L_{prime} \sin(\beta_{prime})) + 2 \cdot (0.224 \cdot L_{second} \sin(\beta_{second})) \tag{4.3}$$

Then, with this information available, the drag coefficient can be simulated using the in-house developed DSMC-SIM tool (see section 4.3 for the verification of the software) with a normal, tangential and energy accommodation coefficient of 0 and then of 1. Using the simulated values, the drag sensitivity to GSI parameters can be determined using the equation as described in equation 2.1. Note that for these simulations, an altitude of 600 km is taken into consideration, as the sensitivity to GSI is most important at altitudes where the particle number density of helium is significant and the number density of oxygen is low. Furthermore, for the panels on the top and bottom faces of the spacecraft body, a length and angle of 100 mm and 5° is selected, respectively. This is mainly done to keep the effects of these panels constant, though the exact value does not matter for the time being.

The numerical results for the variation of β_{prime} are presented in figure 4.2 for a constant L_{prime} of 600 mm. In order to get a better visual of the nature of the trend, the data is also plotted in figure 4.3. As it can be clearly seen, the drag sensitivity to GSI parameters varies according to a shallow parabola where the most negative values indicate a higher sensitivity to normal, tangential and energy accommodation coefficients. However, while the

function is clearly even, the decrease in $\Delta C_{D\alpha}$ towards a β_{prime} value of zero is far more pronounced than for when the panel angle becomes very large. Therefore, a fourth order polynomial of the form shown in equation 4.4 is found to best represent the physical phenomena.

$$\Delta C_{D\alpha} = (3 \cdot 10^{-06})\beta_{prime}^4 - 0.0003\beta_{prime}^3 + 0.0159\beta_{prime}^2 - 0.2432\beta_{prime} - 0.5092 \tag{4.4}$$

This lead to a R^2 value of 0.9996 which demonstrates that the correlation is clear. Now, the optimum angle for the long panels is given by the largest number in magnitude (i.e. the most positive or most negative number) in the equation. To determine this, elementary calculus is used, where the derivative of the function is taken and then set to zero. This leads to a minimum point at an angle of β_{prime} of 10.18°. Therefore, in theory, this angle should perform best with respect to drag sensitivity to GSI parameters, and is the chosen angle which will be selected for the shallow-angled side panels.

Figure 4.2: Drag sensitivity to GSI parameters for various angles of the long, shallow-angled panels on the sides of the spacecraft body simulated with DSMC-SIM.

β_{prime} **[deg]**	**Projected Surface Area High Drag Configuration** $[m^2]$	**Projected Surface Area Low Drag Configuration** $[m^2]$	$\Delta C_{D\alpha=0}$ [-]	$\Delta C_{D\alpha=1.0}$ [-]	$\Delta C_{D\alpha}$ [-]
0	0.15232	0.05408	0.47445	-0.04072	-0.51517
5	0.15174	0.08063	1.43742	0.09177	-1.34566
10	0.15001	0.10698	1.94694	0.26112	-1.68582
15	0.14713	0.13293	1.80843	0.23442	-1.57401
20	0.14313	0.15827	1.63432	0.37090	-1.26342
30	0.13191	0.20640	0.98221	0.54416	-0.43805
40	0.11668	0.24990	-0.43661	-0.05374	0.38287

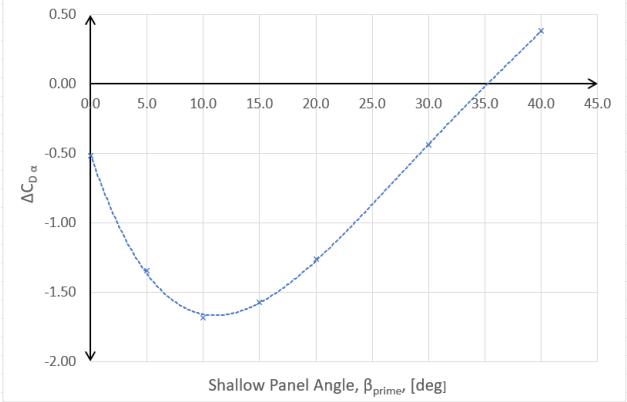

Figure 4.3: $\Delta C_{D\alpha}$ as a function of β_{prime} simulated with DSMC-SIM.

Now that the optimal angle has been set, the effect of the panel length can now be assessed using the procedure described earlier. The results of this analysis are shown in figure 4.4 and illustrated in figure 4.5. Here, the conclusions to be drawn are much more straightforward than for the optimal angle, as the drag sensitivity to GSI parameters is directly correlated to the length of the panel. Therefore, the longer the panel, the better the aerodynamic performance. Therefore, the selection of panel length will take the interests of other subsystems into account. Based off the analysis from chapter 5, there exists solar arrays which are of a dimension of 2U in width and 6U in length. These solar arrays can therefore serve as a means of power generation while also serving as the aerodynamic, shallow angled panels. Furthermore, these panels can fold in half which means that during launch, the panels can be very easily stowed into the launch vehicle, as discussed in section 13.6. Given that 6U (680 mm) is sufficient to fulfil REQ-AER-01, this panel length for the side panels is found to be sufficient.

Figure 4.4: Drag and ballistic coefficient values for the satellite high and low drag configurations for various orbital altitudes.

Panel Length, L_{prime}**, [mm]**	$\Delta C_{D\alpha}$
0	-0.36641
200	-0.95059
400	-1.19109
600	-1.68582

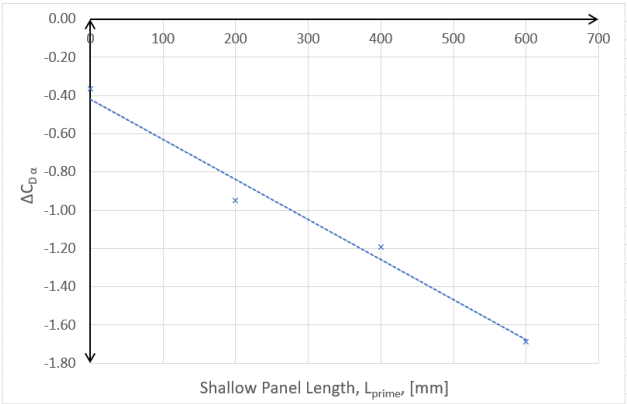

Figure 4.5: Drag coefficient sensitivity as a function of panel length for the shallow angled panels on the side of the spacecraft body simulated with DSMC-SIM.

With the sizing of the large shallow-angle panels selected, the impact of the panels on the top and bottom of the spacecraft can be directly examined. In order to do this, a similar aerodynamic sensitivity analysis can be made as previously. However, this time around, there is a concrete constraint on the length that the panels can have. This is due to the presence of the GNSS receiver, which is fitted onto the flat surface of the spacecraft body. This receiver is placed 119 mm (1U) away from the edge of the body to avoid the effects of multipath, which could affect

its performance. In order for the GNSS receiver to have a complete view of the GNSS satellites, an elevation angle of at most 5° is allowed and therefore, the shallow angle panels cannot obscure this field of view requirement. This introduces a constraint on the possible combinations of panel length (L_{second}) and angle (β_{second}) which are possible. The larger the length of the panel, the smaller the possible angle which can be used. By making use of trigonometric angles, the largest length of L_{second} can be found for incremental increases of β_{second}. Assuming that, just like in the case of the large shallow angle panels, larger panel lengths have a positive effect on drag coefficient sensitivity, only the longest possible panel lengths will be simulated for the given value of β_{second}. This yields the results shown in section 4.2.1.

Table 4.2: Drag sensitivity to GSI parameters for various combinations of panel length and angle for the short panels on the top and bottom surface of the spacecraft body simulated with DSMC-SIM.

β_{second} **[deg]**	L_{second} **[mm]**	**Projected Surface Area High Drag Configuration** $[m^2]$	**Projected Surface Area Low Drag Configuration** $[m^2]$	$\Delta C_{D\alpha=0}$ [-]	$\Delta C_{D\alpha=1.0}$ [-]	$\Delta C_{D\alpha}$ [-]
5	113.76	0.15001	0.10752	1.95616	0.30837	-1.69779
10	76.32	0.15001	0.10901	1.86470	0.31232	-1.55238
15	57.76	0.15001	0.10977	1.87182	0.31754	-1.55248
20	46.74	0.15001	0.11039	1.82584	0.29383	-1.53201
30	34.44	0.15001	0.11078	1.83940	0.36911	-1.47029

There are a number of key conclusions that can be taken from this analysis. Firstly, for these panels, the variations in $\Delta C_{D\alpha}$ is much less significant than for the side panels. While the $\Delta C_{D\alpha}$ was changing by a value of approximately two when changing the side panels, here the $\Delta C_{D\alpha}$ variation is about an order of magnitude less. The cause of this is simply due to the difference in panel length, which therefore highlights it as being the driving factor in the drag sensitivity to GSI. The current contribution of the short panels adds about 15% of drag sensitivity to the overall spacecraft configuration. While the requirement is satisfied without their presence, it is recommended to maintain them and elongate them as much as possible to add as much margin as possible, considering how this directly impacts the primary mission objective. With this in consideration, the second conclusion that could be made is that the most optimal configuration for the short panels corresponds to an β_{second} of 5°. This may seem counterintuitive, as results from the large side panels suggest that an angle of around twelve degrees is optimal. However, in this case, the decrease in allowed panel length which results from transitioning from 5° to 10° does not seem to be sufficiently counteracted by the increase in angle. For this reason, a shallower, longer panel is preferred in this particular case. With this analysis completed, the external aerodynamic shape of the spacecraft has been finalized.

4.2.2 Detailed Aerodynamic Profile of SCATTER

The optimised aerodynamic shape now allows for the simulation of its complete features throughout the various stages of the mission. This includes information on the drag and ballistic coefficient of the satellite at various orbital altitudes in both the high and low drag configurations, the lift and drag coefficient as a function of the spacecraft angle of attack and sideslip combinations. The benefits of this are two-fold: first, the outputted by this detailed analysis will serve as a useful tool for mission planning and lifetime assessments, as discussed in chapter 3 and second, the detailed shape analysis has been very focussed towards REQ-AER-01 due to how closely linked it is to the primary mission objective. However, the other requirements described in table 4.1 cannot be ignored, and this analysis will provide the sufficient information to ensure their compliance, as discussed in section 4.3.3.

Drag Coefficient as a function of orbital altitude. The drag coefficient that the spacecraft experiences is continuously varying due to the particle number density and the nature of the chemical composition of the atmosphere. Therefore, it is important to simulate the behaviour of this drag coefficient variation such that there is an accurate estimate of the drag force acting on the spacecraft at different altitudes, and how this impacts the orbital decay in the different mission phases. To determine the trend, the in-house DSMC-SIM simulator was used, and the spacecraft was simulated in the high and low drag configurations with incremental altitudes varying from 100 km to 1000 km. Throughout each simulation, an accommodation coefficient of 0.5 is selected as it this is an average value for this parameter, and there is very limited information on the actual expected value of this parameter at high altitudes. Using the drag coefficient, projected area ($0.10752m^2$ for low drag configuration, while $0.15001m^2$ for high drag configuration), and a total system mass of 18.2976 kg (see section 13.3), the ballistic coefficients are also calculated as this is the measure of the orbital decay of the two satellite flying configurations, and is used in the descriptions of requirements REQ-AER-02, REQ-AER-04, REQ-AER-05, and REQ-AER-06. The results of this analysis are presented in section 4.2.2, and the drag coefficients are visualized in figure 4.7. As it can be seen, the general trend of the drag coefficient in both the high and low drag configurations match the trend corresponding to a square-root curve. There is an initial sharp increase in drag coefficient, and then the curve flattens out at very high altitudes. Because the spacecraft geometric features and the accommodation coefficient are held constant, this trend must be due to the change in chemical composition of the atmosphere, leading to a variation in the number of particle to surface collisions. It is important to remember that particle number density does not mean atmospheric mass density (given in kg/m^3) as while the mass density of the atmosphere

may decrease with altitude, the particles are switching from heavier oxygen to lighter helium, so more particles may be present for the same mass density.

Figure 4.6: Drag and ballistic coefficient values for the satellite high and low drag configurations for various orbital altitudes simulated with DSMC-SIM.

Orbital Altitude, h, [km]	Drag Coefficient High Drag Configuration [-]	Drag Coefficient Low Drag Configuration [-]	Ballistic Coefficient High Drag Configuration [-]	Ballistic Coefficient Low Drag Configuration [-]
100	1.317	1.874	129.821	64.344
200	1.553	2.186	110.071	55.149
300	1.994	2.621	87.066	45.993
400	1.988	2.725	86.029	44.257
500	2.043	2.840	83.684	43.270
600	1.888	2.972	87.209	43.270
700	1.942	2.906	88.069	41.493
1000	1.966	2.837	86.968	42.502

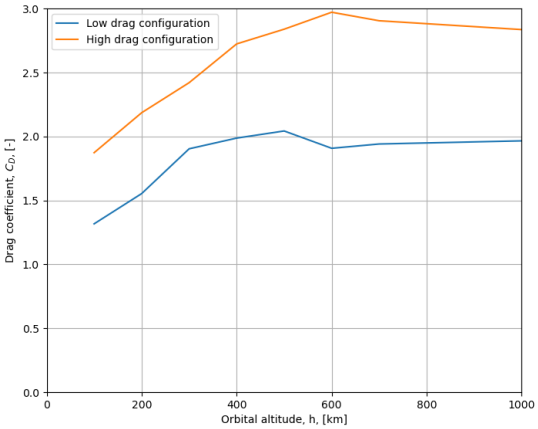

Figure 4.7: Drag coefficient as a function of orbital altitude for the high and low drag configurations of the spacecraft simulated with DSMC-SIM.

Lift, drag and moment coefficient as a function of spacecraft attitude. The second element of the detailed aerodynamic profile which must be completed is the computation of the translational forces and moments for various attitudes of the spacecraft. Similarly to the analysis for a change in altitude, this analysis is conducted using the DSMC-Sim tool. As the concept of projected surface area becomes quite obscure when rotating the spacecraft at non-right angles, for this analysis the aerodynamic coefficients will be provided with respect to a reference surface area of $0.04m^2$. For each value, an average altitude value of 400 km was considered, with an energy, normal and tangential momentum accommodation coefficient of 0.5. Using these parameters, the lift, drag and sideslip coefficients for different combinations of angle of attack and sideslip coefficient are given in table 4.3, table 4.4 and table 4.5.

Table 4.3: Lift coefficient for the finalized detail design for various combinations of angle of attack α and sideslip angle β simulated with DSMC-SIM.

α/β, [deg]	**0**	**45**	**90**	**135**	**180**
0	-0.045	0.00	0.072	0.00	0.00
45	-0.440	-0.235	0.677	0.378	-0.431
90	-0.0332	-0.391	1.126	0.386	-0.568
135	-0.739	-0.394	0.74421	0.226	-0.544
180	0.044	0.000	0.000	0.000	0.000

Table 4.4: Drag coefficient for the finalized detail design for various combinations of angle of attack α and sideslip angle β simulated with DSMC-SIM.

α/β, [deg]	**0**	**45**	**90**	**135**	**180**
0	5.243	9.316	10.337	7.587	7.039
45	5.596	10.444	10.187	10.042	6.240
90	5.519	11.346	10.082	11.297	6.990
135	5.439	10.009	10.125	10.197	5.953
180	5.252	7.693	10.444	9.247	5.315

Table 4.5: Sideslip coefficient for the finalized detail design for various combinations of angle of attack and sideslip angle simulated with DSMC-SIM.

α/β, [deg]	**0**	**45**	**90**	**135**	**180**
0	0.000	1.666	-0.93957	-1.814	0.000
45	0.000	3.228	-0.77152	-3.614	0.000
90	0.000	2.646	0.000	-2.735	0.000
135	0.000	3.612	0.735	-3.135	0.000
180	0.000	1.889	0.96381	-1.607	0.000

Firstly, for a constant angle of sideslip, the lift and the sideslip coefficients are odd functions, while the drag is an even function. This makes sense as when the angle of attack is rotated, the amount of projected surface area is the same and as the drag force is in the horizontal direction, the rotation of the body due to α should not affect the drag values. In the case of sideslip and lift coefficient, the exposed surface area is the same but mirrored, therefore, the resulting force is equal in magnitude but opposite in direction. Secondly, the two configurations in which the spacecraft is expected to spend most of its time, there is no expected lift force, but there could be a significant sideslip force (see table 4.5, $\beta = 90°, \alpha = 0°$). This may cause the satellites to drift prematurely and should be taken into account in mission planning. Following this analysis, the moments across all three axes are also computed using the in-house DSMC simulation. This is done for right angles only, as these are the orientations in which the spacecraft is more likely to travel during science mode. This is presented in the table 4.6, table 4.7 and table 4.8. Note that the axis system used matches the one shown in figure 4.1.

Table 4.6: Moment coefficient about the x-axis for the finalized detail design for various combinations of angle of attack α and sideslip angle β simulated with DSMC-SIM.

α/β, [deg]	-180	-90	0	90	180
-180	0.000	0.000	0.000	0.000	0.000
-90	0.000	0.000	0.000	0.000	0.000
0	0.000	0.000	0.000	0.000	0.000
90	0.000	0.000	0.000	0.000	0.000
180	0.000	0.000	0.000	0.000	0.000

Table 4.7: Moment coefficient about the y-axis for the finalized detail design for various combinations of angle of attack α and sideslip angle β simulated with DSMC-SIM.

α/β, [deg]	-180	-90	0	90	180
-180	0.000	0.000	0.000	0.000	0.000
-90	0.537	19.724	-0.537	-20.109	0.538
0	0.000	0.000	0.000	0.000	0.000
90	-0.539	-20.090	0.538	20.529	-0.537
180	0.000	0.000	0.0000	0.000	0.000

Table 4.8: Moment coefficient about the z-axis for the finalized detail design for various combinations of angle of attack and sideslip angle simulated with DSMC-SIM.

α/β, [deg]	-180	-90	0	90	180
-180	0.000	20.449	0.000	-19.694	0.000
-90	0.000	0.000	0.000	0.000	0.000
0	0.000	-20.434	0.000	20.547	0.000
90	0.000	0.000	0.000	0.000	0.000
180	0.000	20.634	0.000	-20.425	0.000

The most evident observation to make note of here is that there will be no roll in any right angle orientation (i.e, the values for the moment coefficient in the x-direction, shown in table 4.6 are all zero), which makes sense as in each angle here, the orientation of the spacecraft is symmetric across the x-axis, so no rolling moment is to be expected. Depending on the configuration and the angle which is 90°, either the yaw or the pitching moment will be non-negative. With this analysis completed, the detailed aerodynamic profile of the spacecraft has been fully outlined. Therefore, it is now appropriate to proceed further with the verification and validation procedures of this subsystem. This will take place in the next section of the chapter.

4.3 Aerodynamic Design Verification & Validation

Firstly, throughout the full detailed aerodynamic design, the in-house DSMC simulating tool has been used. Therefore, it is imperative that this simulation is properly verified and validated to ensure that the outputted results are consistent with reality. This will be done in section 4.3.1. Following from this, the spacecraft will demonstrate compliance with the subsystem requirements to ensure that this product satisfies the key objectives of the mission in section 4.3.3.

4.3.1 DSMC-SIM Software Description

As rarefied gas aerodynamics is at the core of SCATTER, numerous aerodynamic coefficients for different orbital conditions were required in the design presented in section 4.2. Therefore, a versatile and fast software was needed. While off-the-shelf codes such as SPARTA [24] provide accurate results, they are computationally expensive, and require post-processing. DSMC-SIM was then developed to circumvent these issues, and allow for large numbers of Direct-Simulation-Monte-Carlo simulations to be run. The code follows the VHS (Very-Hard-Sphere) model in [25]. The main assumptions of the DSMC model used are given in the list below:

AS-DSMC-01: *The gas flow is formed of a number of particles representing an arbitrary number of gas particles* - this assumption is derived from the statistical Brownian motion of the gas molecules, which follow the Maxwell-Boltzmann probability distribution function.It is valid for Knudsen numbers $K_n > 0.05$ [25]. Such a distribution can therefore also be represented by a lesser number of larger particles, each accounting for a given number of molecules travelling in the same direction and at the same speed;

AS-DSMC-02: *The particles constitute fully-elastic, perfect spheres* - this assumption is valid for perfect, rarefied gasses, at high temperatures and velocities, where the collisions between molecules are instantaneous and without energy loss. This is much like the atmospheric gasses at altitudes between 150 km and 600 km;

AS-DSMC-03: *The simulated fluid is assumed to be a perfect gas, following the Ideal Gas Law ($pV = \frac{\mu}{m}RT$)* - this assumption is valid for gasses that do not experience state changes, and for which intra-molecular collisions are negligible in comparison to collisions with external surfaces. This is indeed the case for the rarefied atmospheric gas found at high altitudes;

AS-DSMC-04: *The gas molecules are scattered according to a quasi-specular Maxwellian probability density function* - this assumption is valid for flows in the lower and middle parts of the Low Earth Orbit (altitudes $<$ 400 km), where the energy accommodation coefficient has a value between 0 and 1;

AS-DSMC-05: *The gas molecules are scattered according to a fully diffuse Maxwellian probability density function* - this assumption is valid for high altitudes in LEO (above 400 km), where the Helium concentration is significant;

AS-DSMC-06: *The gas molecules have a negligible volume, compared to the volume they occupy* - this assumption is valid for low-pressure, low-density gasses, such as the atmospheric rarefied flow experienced in LEO;

The algorithm for the DSMC-SIM model works as follows. N particles are defined in positions (x_i, y_i, z_i) on a rectangular domain, Ω, where $\Omega = \left\{(x, y, z) \in R^3 |, L_x \leq x < R_x; L_y \leq y \leq R_y; L_z \leq z \leq R_z\right\}$. Each particle represents $N_e = \frac{pV}{k_b TN}$ molecules of gas, where p and T are the atmospheric pressure and temperature, $V = (R_x - L_x) \cdot (R_y - L_y) \cdot (R_z - L_z)$, and $k_b = 1.382 \cdot 10^{-23}$ is the Boltzmann constant. The domain Ω is split into m volumetric cells of dimensions $(l_x \times l_y \times l_z)$.

The N particles in the domain are initialized with the following initial velocities given in Eq. (4.5) [25]:

$$V_{x_0} = U + f\left(m, T\right), \quad V_{y_0} = f\left(m, T\right), \quad V_{z_0} = f\left(m, T\right), \tag{4.5}$$

where U is the velocity of the object relative to the flow, and the $f(m,T)$ is a random velocity described by the Maxwell-Boltzmann probability distribution function [25]:

$$f(m,T) = \left(\int_{-\infty}^{v} 4\pi v^2 \left(\frac{m}{2\pi k_b T} \right)^{\frac{3}{2}} e^{-\frac{mv^2}{2k_b T}} dv \right)^{-1}, \tag{4.6}$$

with m being the mass of a molecule and v being its velocity component in one axis. The particles are drifted for every time step of the simulation according to a simple Euler time integration scheme [25]:

$$\begin{bmatrix} X' \\ Y' \\ Z' \end{bmatrix} = \begin{bmatrix} X \\ Y \\ Z \end{bmatrix} + \begin{bmatrix} V_x \\ V_y \\ V_z \end{bmatrix} \Delta t, \tag{4.7}$$

$[XYZ]^T$ is the position of the particle at time t, while $[X'Y'Z']^T$ is the position of the particle at time $t + \Delta t$. Next, two types of particle collisions are modelled by the algorithm: particle-particle collisions and particle-surface collisions. Particle-particle collisions are checked between particles in the same volumetric cell. For each cell, a fixed number of particles, M_{col} are assumed to collide, given by Eq. (4.8) [25]:

$$M_{col} = \frac{N_c^2 \pi \sigma^2 v_{r_{max}} N_e \Delta t}{2V_c}, \tag{4.8}$$

where N_c is the number of particles in one cell, σ is the effective diameter of the gas molecules, $v_{r_{max}}$ is the maximum relative velocity magnitude between two particles in the cell and V_c is the volume of the cell. For this number of particles in the cell, a collision is assumed to occur between two particles with absolute velocities $\mathbf{v_1}$ and $\mathbf{v_2}$ if [25]:

$$|\mathbf{v_2} - \mathbf{v_1}| > \epsilon v_{r_{max}}, \tag{4.9}$$

where ϵ is a stochastic random variable modelled by a uniform distribution probability density function. The collision occurring between these particles is modelled as perfectly elastic, with the new particle velocity vector components being described by Eq. (4.10) [25]:

$$\begin{bmatrix} V'_{1_x} \\ V'_{1_y} \\ V'_{1_z} \end{bmatrix} = \frac{1}{2} \begin{bmatrix} V_{1_x} + V_{2_x} \\ V_{1_y} + V_{2_y} \\ V_{1_z} + V_{2_z} \end{bmatrix} + \frac{1}{2} ||\mathbf{V_2} - \mathbf{V_1}|| \begin{bmatrix} \sin(\theta)\cos(\phi) \\ \sin(\theta)\sin(\phi) \\ \cos(\theta) \end{bmatrix}$$
$$\begin{bmatrix} V'_{2_x} \\ V'_{2_y} \\ V'_{2_z} \end{bmatrix} = \frac{1}{2} \begin{bmatrix} V_{1_x} + V_{2_x} \\ V_{1_y} + V_{2_y} \\ V_{1_z} + V_{2_z} \end{bmatrix} - \frac{1}{2} ||\mathbf{V_2} - \mathbf{V_1}|| \begin{bmatrix} \sin(\theta)\cos(\phi) \\ \sin(\theta)\sin(\phi) \\ \cos(\theta), \end{bmatrix} \tag{4.10}$$

where $\mathbf{V_1}$ and $\mathbf{V_2}$ are the velocity vectors of the 2 particles before the collision and $\mathbf{V'_1}$ and $\mathbf{V'_2}$ are the velocity vectors after the collision. The angles θ and ϕ are given by Gaussian distributions as follows [25]:

$$\cos(\theta) = 2 \cdot N(0,1) - 1 \qquad \sin(\theta) = \sqrt{1 - \cos^2(\theta)} \tag{4.11}$$

$$\phi = 2\pi \cdot N(0,1), \tag{4.12}$$

with $N(0,1)$ being the standard Gaussian distribution. Next, the particle-surface interactions are being modelled. Three types of collisions are accounted for by the algorithm: specular collisions, diffuse collisions and quasi-specular collisions. These are shown in Fig. 4.8, Fig. 4.9 and Fig. 4.10:

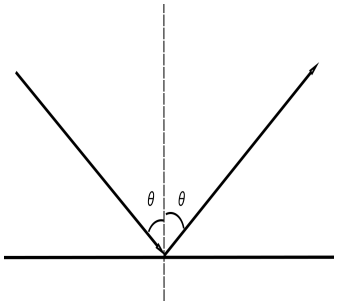

Figure 4.8: Specular reflection of gas particles on a surface.

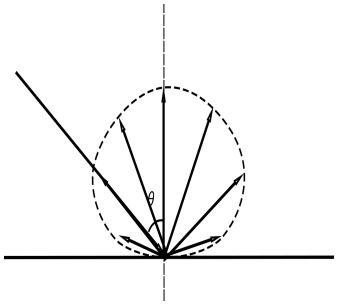

Figure 4.9: Diffuse reflection of gas particles on a surface.

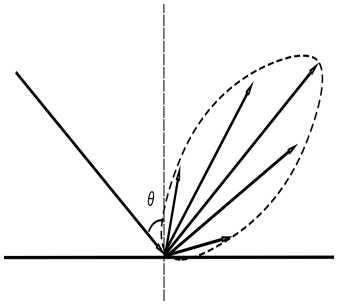

Figure 4.10: Quasi-specular reflection of gas particles on a surface.

Mathematically, specular reflection of particles are defined by reversing the orientation of the component of the velocity vector of the particles normal to the surface, as shown in Eq. (4.13) [25]:

$$\mathbf{V}'_{\mathbf{spec}} = \mathbf{V} - 2 \cdot \mathbf{V} \cdot \mathbf{n}, \tag{4.13}$$

where $\mathbf{n}$ is the normal unit vector to the object surface. For a diffuse reflection, the particle is reflected by the surface in a random direction, described by the Maxwell-Boltzmann probability density function [25]:

$$\mathbf{V}'_{\mathbf{diff}} = \mathbf{V} - \mathbf{V} \cdot \mathbf{n} \cdot (1 + f(m, T_s)) - (\mathbf{V} - \mathbf{V} \cdot \mathbf{n}) (1 - f(m, T_s)), \tag{4.14}$$

where $f(m, T_s)$ is given by Eq. (4.6), and T_s is the temperature of the surface. To define quasi-specular reflection, two coefficients are used: σ_n and σ_t, which model the normal and tangential momentum accommodation of the gas molecules to the surface. The quasi-specular collisions are described by [25]:

$$\mathbf{V}'_{\mathbf{quas}} = \mathbf{V} - ((1 - \sigma_n) \cdot 2 + \sigma_n \cdot (1 + f(m, T_s))) \cdot \mathbf{V} \cdot \mathbf{n} - (1 - \sigma_t) (\mathbf{V} - \mathbf{V} \cdot \mathbf{n}) (1 - f(m, T_s)). \tag{4.15}$$

To compute the drag and lift coefficients of an object in the flow of particles, an arbitrary time step Δt is used, in which the change in momentum in all axes is observed. The drag and lift coefficients is given by Eq (4.16) [25]:

$$C_D = \frac{\overline{\sum_{i=1}^{N} m_i \Delta V_{x_i}}}{\frac{1}{2} \rho U^2 S_{ref} \Delta t} \qquad C_L = \frac{\overline{\sum_{i=1}^{N} m_i \Delta V_{z_i}}}{\frac{1}{2} \rho U^2 S_{ref} \Delta t} \tag{4.16}$$

The algorithm is implemented in Python 3.9, using atmospheric properties from the NRLMSISE-00 atmospheric model.

4.3.2 DSMC-SIM Software Verification & Validation

The DSMC model proposed above has been verified using the SPARTA software, for the different concepts described in section 2.3. The simulations were performed at the atmospheric conditions of a 600 km altitude, using the momentum accommodation coefficients of $\sigma_t = \sigma_n = 1$, and a velocity of $v = 7010\ m/s$. For each concept, both projected reference areas were simulated to verify the DSMC software. The results are shown in Fig. 4.11 and Fig. 4.12:

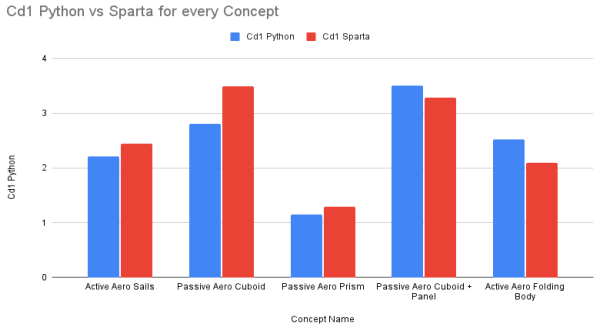

Figure 4.11: Drag coefficients with Python and SPARTA for reference area 1.

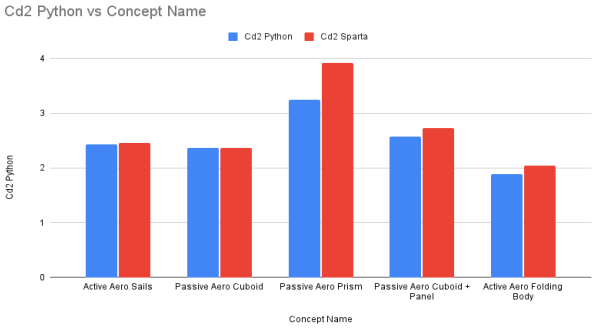

Figure 4.12: Drag coefficients with Python and SPARTA for reference area 2.

The R^2 value between the Python and Sparta results for the drag coefficient of reference surface area 1 is $R^2 = 0.87$. For the reference surface area 2, it is $R^2 = 0.92$. These results indicate a large correlation between the two pieces of software, for a wide range of complex shapes. The difference in results can be explained by stochastic errors due to insufficient averaging in the Python code, as well as the neglecting of particle-particle collisions in the latter. This assumption was made due to the rarefied nature of the gas at the altitude of 600 km. Therefore, the errors observed above are considered acceptable.

For the validation of the in-house DSMC software proposed, a case study is performed on a flat plate, at different altitudes and angles of attack. This case has also been studied in literature [26]. Firstly, the behaviour of the flow around the plate was investigated for different altitudes, to check where the atmosphere starts behaving as a rarefied gas instead of a continuum flow. The plate was simulated at an angle of attack of 50 °, at altitudes of 100 km, 120 km and 150 km. A cross-section of the simulated flow particles in each scenario is shown in Fig. 4.13, Fig. 4.14 and Fig. 4.15:

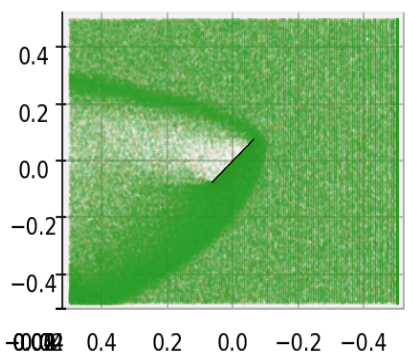

Figure 4.13: Flat plate at 100 km.

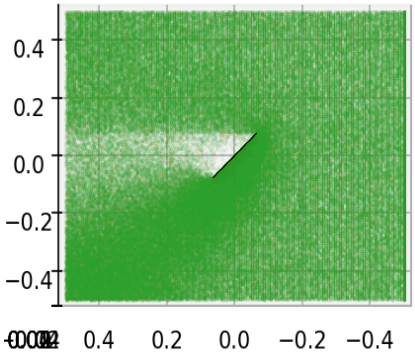

Figure 4.14: Flat plate at 120 km.

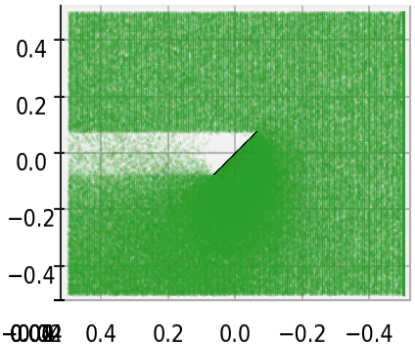

Figure 4.15: Flat plate at 150 km.

As it can be seen in the figures, a bow shock is observed at 100 km, where the continuum flow assumption is still valid for the atmosphere. This effect dims down with increasing altitude, and at 150 km it completely disappears. Next, the drag behaviour of the flat plate was investigated in rarefied flow conditions, for different angles of attack. For this investigation, the DSMC code was compared with data available from literature [27], for two situations: in the first, it was assumed that no particle-particle collisions occur, while in the second, there were not neglected. The results are shown in figure 4.16 and figure 4.17:

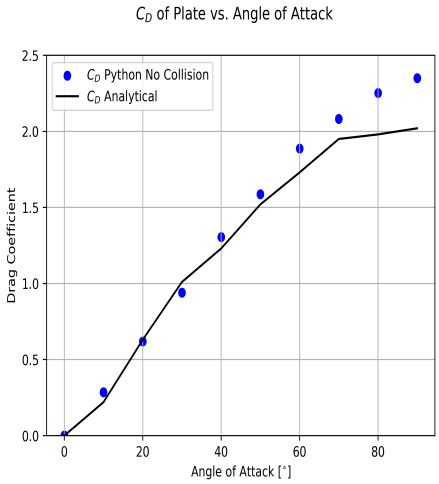

Figure 4.16: Comparison of flat plate drag coefficients with no particle-particle collisions [27].

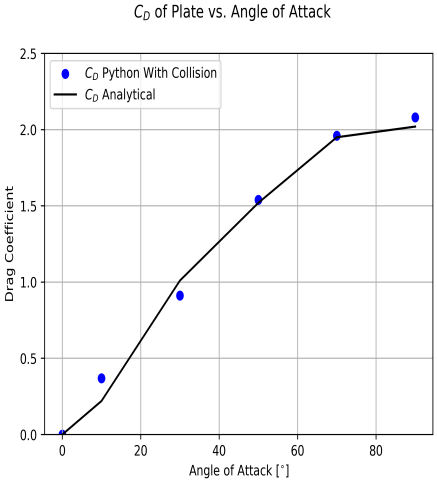

Figure 4.17: Comparison of flat plate drag coefficients with particle-particle collisions accounted for [27].

As it can be seen in the figures, there is a strong correlation between the analytical drag coefficient and the simulated one for both cases. When particle-particle collisions are neglected, the DSMC code overestimates the drag coefficient by 15 %, for high angles of attack. This error, however, seems to be corrected by accounting for these collisions. The plot on the left has an $R^2 = 0.961$, while the second plot has $R^2 = 0.99$. Given these results, it is concluded that the DSMC code provides results accurate to an acceptable level.

4.3.3 Aerodynamics Subsystem Requirements Verification

With the software verified, the aerodynamics subsystem can now be verified against the requirements which were defined at the start of the chapter. This is done below.

REQ-AER-01: - this requirement is verified an analysis of the drag coefficient sensitivity to tangential and normal momentum accommodation coefficients in section 4.2.2. Using DSMC-SIM, for $\sigma_n = 0, \sigma_t = 0$, $\Delta C_{D_{\alpha=0}} = 1.9469$, while for $\sigma_n = 1, \sigma_t = 1$, $\Delta C_{D_{\alpha=1}} = 0.2611$. Therefore, $\Delta C_{D_\alpha} = -1.68$, which satisfies the requirement;

REQ-AER-03: - this requirement is verified by exposing the amount of exposed surface area in both the normal and tangential directions. In the low-drag configuration, the amount of normal and tangential surface area is $0.221m^2$ and $0.818m^2$, respectively. In the high drag configuration, these values are $0.767m^2$ and $0.417m^2$, respectively. Therefore, taking the ratio of the ratios of surface areas in two directions yields: $0.270/1.841 = 6.820$. Therefore, this requirement is satisfied.

REQ-AER-04: - this requirement is verified through analysis of the ballistic coefficient of the satellite configurations at different orbital altitudes. As can be seen in section 4.2.2, the difference in ballistic coefficient at

400 km is 44.4, which is larger than the required difference. Therefore, this requirement is satisfied

4.3.4 Aerodynamic Design Concluding Remarks

The detailed aerodynamics design was able to satisfy the two out of the three key requirements attributed to this subsystem. While REQ-AER-03 was not satisfied, this is deemed to be an acceptable failure of the requirements, as the drag sensitivity to GSI parameters was found to be satisfied with a more compact shape than required. Therefore, this increased efficiency in the overall aerodynamic shape means that this requirement can be violated while continuing to satisfy the primary mission objectives. For future stages of development, it is recommended to simulate the aerodynamic performance with more particles in the simulation in order to reduce the numerical uncertainty, and to use a more CAD geometry for the simulations as currently only a smooth external STL file is used. This does not take into effect the impact that other extrusions such as thrusters and payloads may have.

5. Electrical Power Subsystem

This chapter covers the design of the electrical power system (EPS). First, the requirements of the subsystem are presented in section 5.1. After this, section 5.2 provides an overview of the subsystem, as well as analyses on both the power consumption and the systems sensitivity to power consumption, generation, and storage capabilities, followed by section 5.3, which presents the validation of the tool used to compute the power available, as well as the verification of the subsystem. Finally, section 5.3.3 presents some concluding remarks regarding the EPS, and recommendations for future design stages.

an overview of the system itself is provided in

5.1 EPS Subsystem Requirements

Table 5.1: Electrical power subsystem requirements

ID	Description	Parent Requirement	Rationale
REQ-EPS-01	The EPS shall be activated upon separation from the launch vehicle	REQ-SYS-F-08	Spacecraft must be shut down before deployment per launcher requirements.
REQ-EPS-02	The EPS shall provide at least 5.9 W OAP to the spacecraft subsystems during de-tumbling after separation..	REQ-SYS-F-30	Power figure based on all standby except for magnetorquers and sensors. Time based on simulations.
REQ-EPS-03	The EPS shall provide at least 9.7 W OAP to the spacecraft subsystems during science operations for at least 48 h.	REQ-SYS-F-30	Power as required by all systems in science mode. Time based on simulations.
REQ-EPS-04	The EPS shall provide at least 51 W peak power for at least 1 min.	REQ-SYS-F-30	Power figure based on peak OCS power draw and all standby. Time based on maximum burn time of 47.1 s.
REQ-EPS-05	The EPS shall provide at least 7.5 W OAP in safe mode.	REQ-SYS-F-30	Power figure based on all standby and ADCS de-tumbling power.
REQ-EPS-06	~~The EPS shall provide at least 50.1 W during orbital manoeuvres.~~	REQ-SYS-F-30	Struck out, fulfilled by REQ-EPS-04
REQ-EPS-07	The EPS shall provide at least 9.9 W in re-entry mode.	REQ-SYS-F-30	Power figure based on science mode.
REQ-EPS-08	~~The EPS shall satisfy requirements REQ-EPS-02 through REQ-EPS-06 during eclipse conditions.~~	REQ-SYS-F-30	Struck out as eclipse functionality is implied.
REQ-EPS-09	~~The EPS shall satisfy requirements REQ-EPS-02 through REQ-EPS-06 during sunlight conditions.~~	REQ-SYS-F-30	Struck out as sun-light functionality is implied.
REQ-EPS-10	All EPS components shall function in the LEO magnetic environment.	REQ-SYS-F-19	The spacecraft operates in LEO, so it must withstand the environment.
REQ-EPS-11	All EPS components shall function in the LEO radiation environment.	REQ-SYS-F-18	The spacecraft operates in LEO, so it must withstand the environment.
REQ-EPS-12	All EPS components shall function in pressures between 100 KPa to 0 KPa.	REQ-SYS-F-17	The spacecraft operates in LEO, so it must withstand the environment.
REQ-EPS-13	~~The EPS components inside the bus shall function in −40 °C to 70 °C temperature range.~~	REQ-SYS-F-16	Moved to TCS subsystem requirement REQ-TCS-15.
REQ-EPS-14	~~The EPS components outside the bus shall function in −40 °C to 80 °C temperature range.~~	REQ-SYS-F-17	Struck out because temperature ranges changed.
REQ-EPS-15	The EPS shall be ready for separation 45 days before launch.	REQ-SYS-F-30	Derived from launcher requirement.
REQ-EPS-16	The battery pack shall be at no less than55 % effective state of charge (SoC) upon deployment	REQ-SYS-F-30	Computed using 0.7 days de-tumbling time, assuming all standby power except for TT&C and ADCS.
REQ-EPS-17	The battery pack shall be able to supply no less than 205 Wh at EOL.	REQ-SYS-F-30	Computed using worst case orbit and preliminary sizing method.
REQ-EPS-18	~~The battery pack shall be capable of supplying~~ 50.1 W at EOL.	REQ-SYS-F-30	Struck out as it is already covered by REQ-EPS-04.
REQ-EPS-19	~~The internal components shall have a maximum volume of 0.03 m^3.~~	REQ-SYS-F-30	Struck out as volume is a trade-able budget and not a requirement.
REQ-EPS-20	The battery shall comply with IATA rules on passenger aircraft.	REQ-M-23	Launcher requirement per 5.5.1.2 of VEGA manual.
REQ-EPS-21	~~The internal components shall have a maximum mass of 3 kg.~~	REQ-SYS-F-30	Struck out as the volume of the subsystem is a trade-able parameter and not a constraint.
REQ-EPS-22	~~The solar arrays shall have a mass no more than 1.3 kg.~~	REQ-SYS-F-30	Struck out as the mass of the solar panels is a trade-able parameter.
REQ-EPS-23	The main solar arrays shall generate at least 30 W peak at EOL.	REQ-SYS-F-30	Number based on what it achievable and rounded down. Only peak is considered as it directly relates to OAP.
REQ-EPS-24	The main solar arrays shall deploy at an angle of 10° ±0.5°.	Mission Objective	Determined by aerodynamics.
REQ-EPS-25	~~The solar arrays shall be fail-safe.~~	N/a	Struck out as requirement does not follow from any other.
REQ-EPS-26	The solar arrays shall fit in the satellite deployment device.	REQ-SYS-D-07	We have to fit the deployment device.

5.2 EPS Detailed Design

The EPS serves to supply the satellite's subsystems with electrical power from deployment to reentry, without shutting down at any point during nominal operation. This is achieved by having both batteries and solar panels. The solar panels generate energy, which is either directly used by other subsystems, or used to charge the batteries. In eclipse conditions, or if extra power is required, the batteries will provide the satellite with power. Next to batteries and solar panels, other components are also required: These are battery control units (BCUs), power conditioning units (PCUs), and power distribution units (PDUs). The BCUs manage the batteries, ensuring that they will not be over- or undercharged. PCUs are the interface between the solar panels and the rest of the EPS, and PDUs distribute the power to other components in the satellite at the appropriate voltage.

This section is split into four subsections: The first, section 5.2.1, presents the chosen solution, starting with the internals, followed by the electric block diagram and an overview of the solar arrays. After this, section 5.2.2 presents the method used to analyse the power consumption, and the duty cycles and maximum times spent in science mode for a range of orbital altitudes. This is followed by section 5.2.3, which presents a sensistivity

analysis, analysing the effects of changing the electrical power required, the number of solar cells, and the number of battery packs.

5.2.1 EPS Design Overview

For the internal components of the EPS, the ISISPACE Modular Electrical Power System[1] is used. This system was chosen for its modularity, making design iterations, integration, and scaling easier. All components are daisy chained together, allowing for one main power rail as well as one communication point for the on-board computer to connect to. The chosen configuration will use 12 battery packs, evenly distributed over 4 BCUs, and 2 PCUs and 2 PDUs. One of these PDUs will act as a master, and the main interface with the on-board computer. Together, the PDUs power all the subsystems, and offer a high degree of redundancy. Two PCUs are installed as each carries only four maximum power point trackers (MPPT's), and six are required. Twelve battery packs are evenly distributed over the four BCUs, offering redundancy in power storage. To guarantee a 48 h science cycle, only 9 batteries are required. The 12 pack option was chosen for added redundancy, as well as ballast; the satellites would otherwise deorbit too quickly in the third phase of the mission, and this time cannot be guaranteed if their mass is too low. Each battery pack has a capacity of 45 Wh[1], giving the satellite a total capacity of 540 Wh. Only 270 Wh is used, as a depth of discharge (DoD) of 50 % is assumed [28]. This number is based on roughly 18000 battery cycles, or 16.5 orbits per day, for 3 years. The internal layout of the EPS can be seen in figure 13.4. The system consists of 2 PDUs, 2 PCUs, 4 BCUs, and 12 battery packs.

The PDUs are connected to the internal components as presented in figure 5.2. Each PDU has 4 voltage domains, VD0, VD1, VD2, and a sonboard mounted VD3. VD1 through VD3 can be set to any voltage below the rail voltage, which VD0 is set to. All systems except for the solar array deployment devices have are connected to multiple channels. The deployment devices were omitted from this, as they consist of heating elements and burn wires. Two 12 V regulators are required for the propulsion systems, as no 12 V bus is available on the PDUs with the current layout. The 4 solar arrays are connected to the 2 PDUs, with two redundant connections, as detailed in figure 5.2.

The solar panels are mounted on Y and Z faces of the satellite. Two big arrays, each with an area of 12U, are mounted to the Y faces, and two 2U panels are mounted to the Z faces. This can be seen in figure 5.1. In total the satellite has 64 solar cells, 4 on each 2U panel, and 28 on each 12U array. The 12U arrays consist of two 6U panels, which are connected with a 180° hinge. Both the 12U and the 2U arrays are connected to the satellite with a 10° hinge. Due to this non-standard deployment angle, either a modified or completely custom set of panels will be required. At the time of writing, a modified version of the EnduroSat 6U deployable panels[2] was considered.

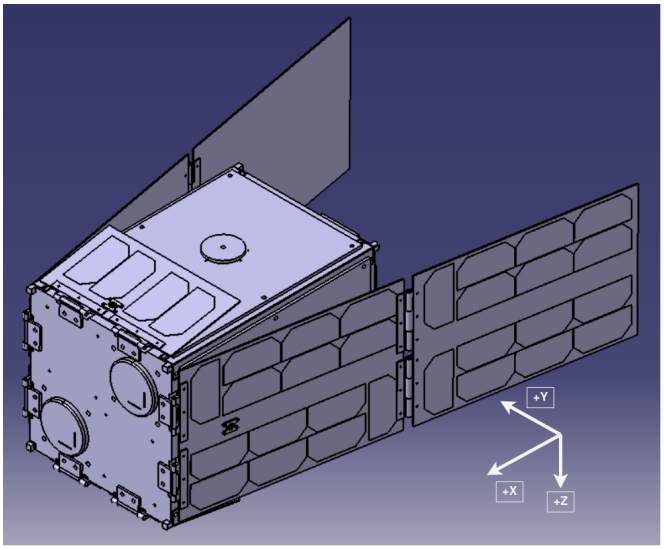

Figure 5.1: Deployed configuration of the solar panels.

[1] https://www.isispace.nl/product/modular-electrical-power-system/ , retrieved 15/06/2022
[2] https://www.endurosat.com/cubesat-store/cubesat-solar-panels/6u-deployable-solar-array/, retrieved 15/06/2022

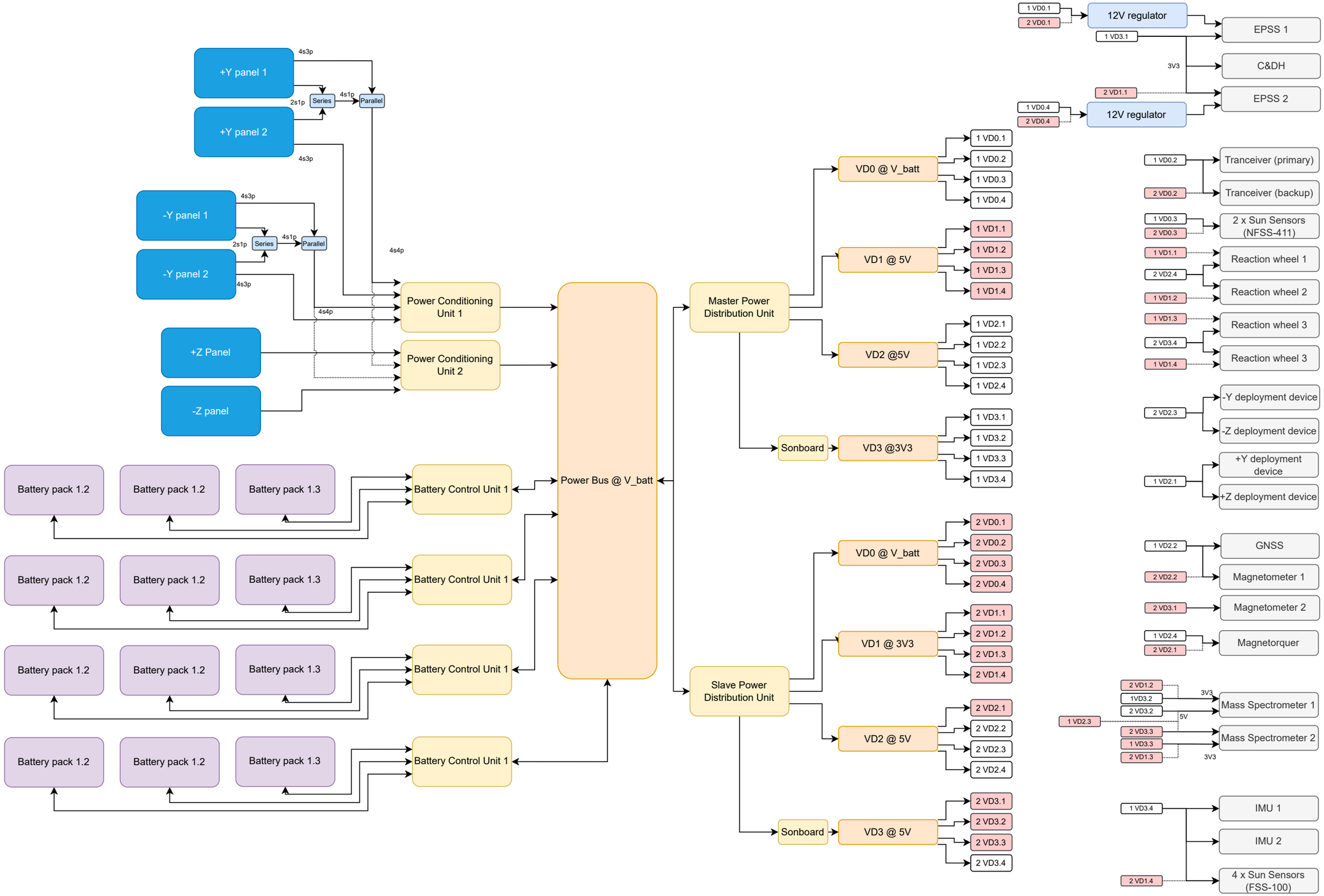

Figure 5.2: Block diagram of the electrical power subsystem. Dashed lines indicate backups, and red channel tags indicate that the channel is turned off under nominal science mode operation.

5.2.2 EPS Subsystem Power Consumption Analysis

The high-level method used to assess the design the EPS is based on orbital average power (OAP). This number is an electrical power consumption or generation, averaged out over an entire orbit, allowing easy computation of the satellite's energy balance.

1. Compute the generated OAP from the available solar panel area.
2. Compute the required OAP from the operational mode and subsystem power consumption.
3. Compute the power balance.
4. Compute the extra energy required if the balance is negative. Alternatively, compute how long operations can be sustained using extra battery power.

Before any of these computations can be done, efficiency factors, component power consumptions, and solar cell properties must be known first. The efficiencies and component power consumptions can be found in table 5.2, and the solar cell properties in table 5.3. The battery efficiency factor relates the input energy to the output energy.

Table 5.2: Efficiency factors, and idle and active power consumptions of internal components. Each PCU has 4 maximum power point trackers. Not all values are from the ISISPACE system, as these were not available.

Component	Efficiency [-]	Idle Power Consumption [W]	Active Power consumption [W]
PDU	0.96 [3]	0.066 [4]	N/a
PCU	0.96 [3]	0.066 [4]	0.331 per MPPT [4]
BCU	N/a	0.0487 [4]	N/a
Battery pack	0.95[5]	N/a	N/a

Table 5.3: Solar cell area and end-of-life efficiency factor.

Cell Area [m^2]	Cell End-Of-Life Efficiency [-]
0.003018 [6]	0.29 [7]

It was assumed that in sunlight conditions, all power is consumed directly from the solar panels, and during eclipse, all power comes from the batteries. This means that separate sunlight and eclipse efficiencies must be computed. An EPS layout as shown in figure 5.3 was assumed. This is different from figure 5.2, as solar energy used to charge the batteries also goes through the PDU. This was not changed, as it adds an inherent safety margin.

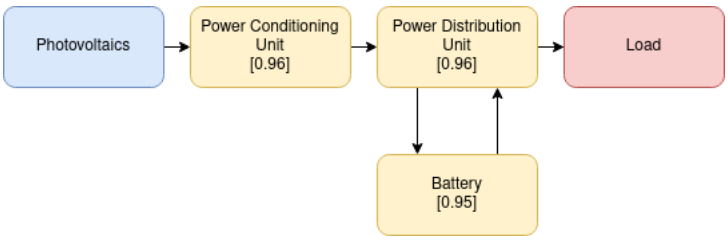

Figure 5.3: Simplified schematic of the EPS, illustrating the flow of energy. Sunlight and eclipse efficiencies of 0.9216 and 0.8405 are obtained.

The sunlight and eclipse efficiencies are 0.9216 and 0.8405, respectively. They do not change with altitude. These numbers are averaged into a single efficiency factor, based on the eclipse fraction of a circular orbit. For this, a the Sun, Earth, and satellite were assumed to be in the same plane. The averaged efficiency factors for the considered circular orbits can be found in table 5.4. These factors encompass the efficiency of the PCUs, PDUs and batteries, and were applied to the electrical power required by the other subsystems of the satellite.

Table 5.4: Weighted orbital average EPS efficiency. The Earth, Sun, and satellite were assumed to be in the same plane.

Orbital Altitude [KM]	Average efficiency [-]
200	0.8874
300	0.8888
400	0.8900
600	0.8918

[3] `https://nanoavionics.com/cubesat-components/cubesat-electrical-power-system-eps`, retrieved 15/06/2022
[4] `https://www.isispace.nl/product/modular-electrical-power-system/`, retrieved 15/06/2022
[5] `https://batterytestcentre.com.au/project/lithium-ion/`, retrieved 14/06/2022
[6] Obtained from `http://www.azurspace.com/images/products/0003401-01-01_DB_3G30A.pdf` following email message from Dr. Anja Nakarada Pečujlić, both on 31/05/2022
[7] `https://www.endurosat.com/cubesat-store/cubesat-solar-panels/6u-deployable-solar-array/`, retrieved 15/06/2022

With the efficiencies known, the power required from the solar arrays can be computed. For this, the subsystem power consumption must be known. Gathering the average operational times per orbit, as well as the peak and standby power consumptions of each subsystem, table 5.5 can be generated.

Table 5.5: Peak power, peak power orbit fraction, and standby power.

Subsystem	Peak power [W]	Peak Power Orbit Fraction [-]	Standby Power [W]
ODCS	42 (1645.1)[8]	0.0001379	0.6
ADCS	8.7	0.1	2.4
EPS	0.39 [1.99][9]	0.578 to 0.633	0.39
TT&C	12	0.0138	1
C&DH	N/a	N/a	1
Payload	2.98	N/a	2.1

These numbers can be then be used to compute the required power of the various modes. They can be found in table 5.6. The efficiency factors and MPPT power consumptions are not added to these numbers yet, as they depend on the orbit.

Table 5.6: Power required by subsystems per operational mode, and the minimum time the spacecraft must sustain them for.

Operational Mode	Power Required [W]	Time required [h]	Explanation
Science mode	9.2	48	All standby + All peak
Power mode	8.6	0.5 to 9 (altitude dependent)	All standby + ADCS
Propulsion mode	50.6	0.017	All standby + OCS peak
Safe mode	7.5	Indefinetely	All standby + ADCS in safe mode
De-tumbling	5.9	5	ADS, Magnetorquer, EPS, CMDH, GNSS, IMU
Re-entry	9.2	48	All standby + All peak

With the required OAP known, only the available OAP needs to be computed. This is done using AstroSim, as explained in section 5.3. For this, the solar panel geometry from section 5.2.1, and the values from table 5.3 were used. The results can be found in table 5.7. An inclination of 97° was assumed, and the numbers were averaged over a 24 hour period, starting on 20/03/2035, 12:00 UTC. Multiple values between 0° and 90° were tried for the right ascension of the ascending node, but no major differences were observed.

Table 5.7: OAP generated by the solar arrays in both science attitude, and the sun tracking power mode. An inclination of 97° and a right ascension of 0° were used, and the numbers were averaged over a 24 hour period, starting on 20/03/2035, 12:00 UTC.

Orbital Altitude [KM]	OAP Science Mode Low [W	OAP Science Mode High [W]	OAP Power Mode[W]
200	11.2	14	20.8
300	11.7	14.5	21.6
400	12.1	15.4	22.8
600	12.8	16.3	24

There are two limiting cases that must be sized for: Science, and de-tumbling. It was assumed that the satellites must function in science mode for at least 48 h(see chapter 3. Dividing the science mode power from table 5.6 by an altitude appropriate efficiency factor from table 5.4, and adding the OAP consumed by the MPPTs, yields the OAP required from the solar panels. This number is multiplied by 1.15, to add a safety margin. Subtracting it from the altitude appropriate low OAP from table 5.7 yields the limiting power balance. If this number is negative, more power is consumed than generated. The limiting available science times, corresponding charge times, and science duty cycles are shown in table 5.8.

Table 5.8: Maximum available science time and duty cycle, for various orbital altitudes assuming a safety factor of 1.15. Maximum duration computed assuming the full 270 Wh in the batteries is consumed. OAP required is OAP required from the solar arrays.

Orbital Altitude [km]	Mode	OAP required [W]	OAP generated [W]	Balance [w]	Maximum Duration [h]	Duty cycle
200	Science	13.41	11.2	-2.21	122.2	0.800
	Power	11.98	20.8	0.59	30.6	0.200
300	Science	13.42	11.7	-1.72	157.3	0.848
	Power	11.99	21.6	9.61	28.1	0.152
400	Science	13.42	12.1	-1.32	204.25	0.891
	Power	11.99	22.8	10.81	24.98	0.109
600	Science	13.43	12.8	-0.63	428.02	0.95
	Power	12.01	24	11.99	22.51	0.05

[8] 1645.1 W is not a real energy consumption, it is only used to budget for heating in energy calculations, see chapter 8
[9] 1.99 W is consumed from the solar arrays directly

5.2.3 Sensitivity Analysis

The sensitivity analysis for the EPS was conducted in for three variables: Power consumption, the number of solar cells, and number of battery packs. The changes are shown only for the 200 km orbit, as it is the most critical case.

Power Consumption

A constant load of varying magnitude was added to or subtracted from the existing power consumptions. The results can be found in table 5.9. The results clearly show that the duty cycles are highly sensitive to changing power consumptions, with the duty cycles and available science times dropping rapidly with increasing power consumption; the opposite is true with a decrease in consumption. This shows that a 10 % increase in OAP required has a large impact on available science, decreasing it by around 45 h, while the same increase adds around 170 h to the science time. Increasing consumption by 3 W causes the system not satisfy the science time requirement, while decreasing it by 2 W means that no duty cycles are required.

Table 5.9: Effect of changing the overall power consumption, at an altitude of 200 km. Base consumption is 9.7 W.

Change in power consumption [W]	-2	-1	0	1	2	3
Science mode OAP required [W]	10.82	12.11	13.41	14.71	16.00	17.30
Power mode OAP required [W	9.39	10.68	11.98	13.27	14.57	15.86
Maximum science time [h]	N/a	295.37	122.2	77.0	56.2	44.3
Science duty cycle [-]	1	0.917	0.800	0.682	0.565	0.447

Number of Solar Cells

To simplify the analysis of the sensitivity of the EPS to the number of solar cells, all power is assumed to be generated by the two main arrays, and the change in number of solar cells is split over the two arrays. The power generated scales linearly with the number of cells. Only half of this increase is applied to the power mode OAP generated, as only one array is exposed to sun light. Increasing the amount of power generated, increases both the maximum time available in science mode, as well as the science duty cycle. This can be seen in table 5.10. As with the power consumption changes, only slight changes in power production yield large changes in maximum continuous science operations, and science duty cycles. This means that losing more than 4 strings can already significantly affect the mission. Hence, reliable components must be used to in the EPS, particularly regarding power generation.

Table 5.10: Effect of changing the number of solar cells on power generation, available science time, and science duty cycle at an altitude of 200 km. Base number of cells is 56, as only the main arrays are considered.

Change in number of solar cells [-]	-24	-16	-8	-4	0	4	8
OAP generated, science low [W]	6.4	8.0	9.6	10.4	11.2	12	12.8
OAP generated, power mode [W]	16.3	17.8	19.3	20.1	20.8	21.5	22.3
Maximum science time [h]	38.5	49.9	70.9	89.7	122.2	191.5	442.6
Science duty cycle [-]	0.384	0.520	0.65	0.729	0.800	0.872	0.944

Number of Battery Packs

The number of battery packs primarily affects the maximum science time, as this was the limiting case for the power storage. Table 5.11 shows how changing the number of batteries affects the maximum science time. The duty cycle also changes, as the changing mass affects the burn time required for manoeuvres. An increase in burn time increases the amount of energy required for the manoeuvre, which is budgeted for in the science mode. Regarding the current design, this means that there is a high degree of redundancy in the power delivery, with the science mode time requirement still being satisfied with only 5 operational battery packs.

Table 5.11: Effect of changing the number of battery packs on available science time, and science duty cycle, at an atltitude of 200 km.

Change in number of battery packs [-]	-6	-3	0	3	6
Maximum science time [h]	64.8	94.3	122.2	148.5	173.3
Science duty cycle [-]	0.811	0.805	0.800	0.794	0.788

5.3 Electrical Power Subsystem Verification & Validation

The Electrical Power Subsystem was designed using a combination of analytical equations and numerical simulations. For the latter part of the design process, the AstroSIM tool outlined in section 3.8.1 was used, and coupled with an available solar power estimation equation based on the sun position in the C-frame at any given point in time. This tool is validated in section 5.3.1, while the design itself is verified in section 5.3.2.

5.3.1 AstroSIM Power Simulator Description & Validation

To estimate the avaliable power of the satellites of SCATTER at any given point in time, and for any orientation, AstroSIM's 6 degree-of-freedom solver was used. To model all N solar panels of each satellite in 3 dimensions, the normal unit vectors to their surfaces are defined as $\mathbf{n_i}, i \in \{0, N-1\}$, and their respective surface areas $A_i, i \in \{0, N-1\}$. The sun vector is defined as the vector pointing from the satellite CoM to the sun position, in the C-frame, $\mathbf{s_C}$, and it is computed using the AstroPy library [10]. The power of one panel, i, is therefore defined as:

$$P_i = \eta \cdot S_{sun} \cdot I_d \cdot A_i \cdot \min\left(\mathbf{n_i} \cdot \mathbf{s_C^B}, 0\right), \tag{5.1}$$

where η is the efficiency of the solar cells, $S_{sun} = 1362\,\mathrm{W^2\,m^{-1}}$ is the solar flux near Earth, I_d is the inherent degradation and $\mathbf{s_C^B}$ is the sun vector in the B-frame. For all panels, accounting for the effect of umbra, the total solar power is given by:

$$P_{total} = \begin{cases} \sum_{i=0}^{N-1} \eta S_{sun} I_d A_i \max\left(\mathbf{n_i} \cdot \mathbf{s_C^B}, 0\right), & \arccos\left(\mathbf{s_C^E} \cdot \begin{bmatrix}0\\0\\1\end{bmatrix}\right) > \arcsin\left(\frac{R_E}{R}\right) \\ 0, & \arccos\left(\mathbf{s_C^E} \cdot \begin{bmatrix}0\\0\\1\end{bmatrix}\right) \leq \arcsin\left(\frac{R_E}{R}\right) \end{cases}, \tag{5.2}$$

where $\mathbf{s_E^C}$ is the sun unit vector in the E-frame, R_E is the Earth radius and R is the current orbital radius.

To validate the power tool integrated in AstroSIM, the simulations performed in [29] are used. A CubeSat design in a circular Earth-bound orbit has been simulated both in the paper, as well as with AstroSIM, and the results were compared for one singular solar panel. The simulation inputs used in these simulations are given in table 5.12:

Table 5.12: Power simulation validation initial parameters.

Parameter Name	Value	Parameter Name	Value	Parameter Name	Value
RAAN	0 °	Semi-major axis	6782 km	Initial Angular Velocity	(0, 0, 0) rad/s
Inclination	52 °	Eccentricity	0	Ascending Node	0 rad

The results of the simulations using the parameters above are given in figure 5.4 and figure 5.5 for an arbitrary solar panel for simulation time practicality. Hence, for the +ve X solar panel:

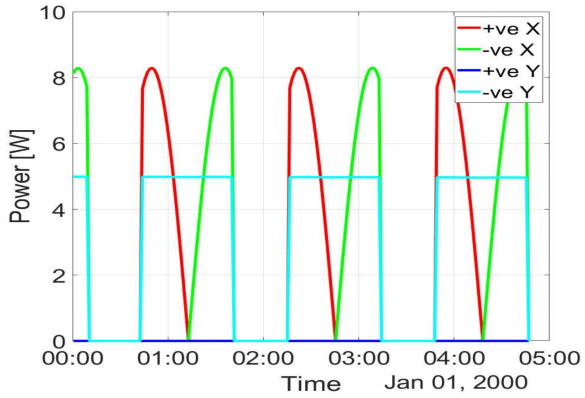

Figure 5.4: Available power simulation performed in [29].

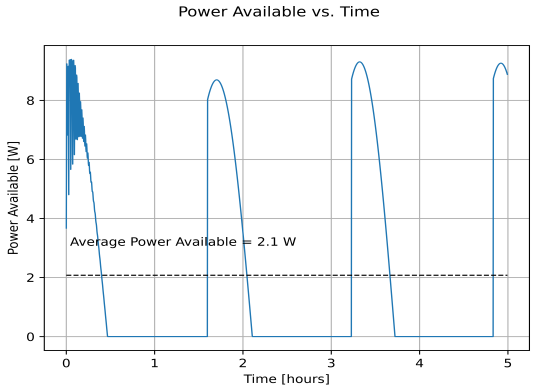

Figure 5.5: Available power simulation performed using AstroSIM, with the same initial parameters as in [29], for panel +X.

As it can be seen in the figures, AstroSIM closely resembles the simulation performed in [29], both in peaks of 8.2 W, and in eclipse time. The initial high-frequency oscillations observed in AstroSIM are due to the science mode transition, which is not simulated in [29]. Furthermore, the variation in peaks observed in AstroSIM is due to the disturbance torques affecting the satellite orientation throughout the orbit, which are not modelled in the paper. Based on these results and the philosophy outline in section 1.6, the power tool is considered validated.

5.3.2 Electrical Power Subsystem Requirements Verification

The verification of the Electrical Power Subsystem by compliance with requirements is given below:

[10] `https://docs.astropy.org/en/stable/index.html`, retrieved 26/05/2022

REQ-EPS-01: - this requirement shall be verified through qualification testing using a qualification model;

REQ-EPS-02: - this requirement is verified through analysis in section 5.2. The EPS is equipped with 12 ISISPACE battery packs [11], providing 270 Wh of energy with a DoD of 50 %. As the de-tumbling time estimated in chapter 9 is 6 hours, the energy required is predicted to be 30 Wh. Therefore, the requirement is satisfied;

REQ-EPS-03: - this requirement is verified through analysis of the OAP and duty cycles at different altitudes in table 5.7 in section 5.2. The most critical case at 200 km yields an available OAP of 11.2 W which is repurposed for science mode with a duty cycle of 84.6 %. Therefore, the requirement is satisfied;

REQ-EPS-04: - this requirement is verified through analysis of the peak power in section 5.2, where the peak power produced is estimated to be 153 W. Therefore the requirement is satisfied;

REQ-EPS-05: - this requirement is verified through analysis in section 5.2.2, where the safe-mode estimated OAP required by the subsystems is 7.5 W, which has a net positive energy balance;

REQ-EPS-07: - this requirement is verified through analysis in section 5.2.2, where the re-entry OAP required designed for is 9.9 W for a time of 48 hours at 200 km;

REQ-EPS-10: - this requirement shall be verified through ground-based qualification testing of the ISISPACE Modular EPS under simulated magnetic fields resembling Earth's;

REQ-EPS-11: - this requirement shall be verified through ground-based qualification testing of the ISISPACE Modular EPS under simulated radiation resembling low Earth orbit;

REQ-EPS-12: - this requirement shall be verified through ground-based vacuum testing in the qualification phase of the design;

REQ-EPS-15: - this requirement shall be verified through demonstration, by writing detailed timelines of the testing and qualification phases of the design, up until launch;

REQ-EPS-16: - this requirement shall be verified through sensor data after deployment of the satellites.

REQ-EPS-17: - this requirement is verified through inspection of the ISISPACE modular EPS declared a capacity of 45 Wh per battery pack [12], which results in a 270 Wh for the 12 battery packs used by SCATTER and a DoD of 50 %;

REQ-EPS-20: - this requirement shall be verified through qualification testing in later stages of the design;

REQ-EPS-24: - this requirement is satisfied through inspection of the current design of SCATTER, which has maximum solar panel angles of 10° and 5° according to chapter 13;

REQ-EPS-26: - this requirement is satisfied through inspection of the current design of SCATTER, as the large solar panels are 2 x 3 U in area and 10 mm in thickness, while the small solar panels are 2 x 1 U in area and less than 5 mm in thickness. These satisfy the CubeSat deployer constraints outlined in the Vega-C manual [10];

5.3.3 EPS Design Concluding Remarks

With this design cycle of the EPS now complete, a few notes must be made. Firstly, the modelling of power consumptions and efficiencies over an extended period of time is simplified. While using OAPs makes analysis easy, it does not provide detailed insight into the battery cycles, charge and discharge rates, or the instantaneous power consumption. The current work is sufficient for this design stage, but more in-depth analysis must be performed, both to improve confidence in the design, and to increase the accuracy of the mission planning. This would also allow for more accurate modelling of the efficiencies of the EPS, as they would no longer be averaged. The OAP generated, and hence the duty cycle and maximum science times, change constantly with orbital altitude. Secondly, ISISpace must be contacted in order to verify that the proposed layout for the MEPS works. While the system is modular, and should allow for this configuration, this must be confirmed with the supplier. Finally, the EnduroSat must be contacted about a modified version of their solar panels. It might be beneficial to contact multiple companies simultaneously, Pumpkin[13] and GOMspace[14] have completely custom and reasonably easy modifiable offerings, respectively.

[11] https://www.isispace.nl/product/modular-electrical-power-system/

[12] https://www.isispace.nl/wp-content/uploads/2019/12/ISIS-iMEPSv2-DS-00001-iEPS_Datasheet_v0.2-.pdf

[13] https://www.pumpkinspace.com/store/p166/Custom_PMDSAS_panel%2C_deployable%2C_per_cell.html, retrieved 15/06/2022

[14] https://gomspace.com/shop/subsystems/power/nanopower-tsp.aspx, retrieved 15/06/2022

6. Structures Subsystem

This chapter details the design and analysis of the custom structural frame. First, all the requirements to be satisfied are laid out in section 6.1. Next, the design is presented in section 6.2. Based upon this, a finite-element stress analysis is performed in section 6.3, which also includes a sensitivity analysis on body panel thickness. Finally, the verification and validation of the structural requirements is presented

6.1 Structures Subsystem Design Requirements

Table 6.1: Subsystem requirements.

ID	Description	Parent Requirement	Rationale
REQ-SM-01	The structure of the space element shall survive a static lateral load of +/- 10 g with a qualification factor of 1.25	REQ-SYS-P-05	Derived from Vega-C SSMS specified static loads
REQ-SM-02	The structure of the space element shall survive a static longitudinal load of +/- 10 g with a qualification factor of 1.25	REQ-SYS-P-05	Derived from Vega-C SSMS specified static loads
REQ-SM-03	The structure of the space element shall survive a sine sweep in the lateral direction with an amplitude of 2.5 g throughout the frequency band of 5 to 70 Hz at a rate of 2 oct/min with a qualification factor of 1.25	REQ-SYS-F-03	Derived from Vega-C SSMS specified sine vibrations
REQ-SM-04	The structure of the space element shall survive a sine sweep in the lateral direction with an amplitude of 1.25 g throughout the frequency band of 70 to 125 Hz at a rate of 2 oct/min with a qualification factor of 1.25	REQ-SYS-F-03	Derived from Vega-C SSMS specified sine vibrations
REQ-SM-05	The structure of the space element shall survive a sine sweep in the longitudinal direction with an amplitude of 2.5 g throughout the frequency band of 5 to 70 Hz5-70 Hz at a rate of 2 oct/min with a qualification factor of 1.25	REQ-SYS-F-03	Derived from Vega-C SSMS specified sine vibrations
REQ-SM-06	The structure of the space element shall survive a sine sweep in the longitudinal direction with an amplitude of 1.25 g throughout the frequency band of 70 to 125 Hz at a rate of 2 oct/min with a qualification factor of 1.25	REQ-SYS-F-03	Derived from Vega-C SSMS specified sine vibrations
REQ-SM-07	The structure of the space element shall survive random vibrations with a G_{RMS} of 5.9 g per axis for a duration of 120 s with a qualification factor of 2.25	REQ-SYS-F-03	Derived from Vega-C SSMS specified random vibrations
~~REQ-SM-08~~	~~The structure of the space element shall survive acoustic vibrations~~	~~The structure of the space element shall survive acoustic vibrations~~	Not required for CubeSat deployer if random vibration test is performed
REQ-SM-09	The structure of the space element shall survive shocks with a frequency of 100 Hz at a flight limit level of 30 dB	REQ-SYS-D-01	Derived from Vega-C SSMS specified shock levels
REQ-SM-10	The structure of the space element shall survive shocks with a frequency of 2000 Hz at a flight limit level of 1500 dB	REQ-SYS-D-01	Derived from Vega-C SSMS specified shock levels
REQ-SM-11	The structure of the space element shall survive shocks with a frequency of 10 000 Hz at a flight limit level of 1500 dB	REQ-SYS-F-03	Derived from Vega-C SSMS specified shock levels
REQ-SM-12	The deployer of the space element shall survive thermal loads with a thermal impingement of 1500 W/m^2 for a duration of 115 s	REQ-SYS-F-03	Derived from Vega-C SSMS specified thermal loads
REQ-SM-13	The structure of the space element shall have a structural stiffness such that the lateral natural frequency is higher than 115 Hz	REQ-SYS-F-05	Derived from Vega-C SSMS specified natural frequencies
REQ-SM-14	The structure of the space element shall have a structural stiffness such that the longitudinal natural frequency is higher than 115 Hz	REQ-SYS-F-05	Derived from Vega-C SSMS specified natural frequencies
REQ-SM-15	The structure of the space element shall be designed to fit its deployer	REQ-SYS-F-07	CubeSat must be launched within a dedicated deployer
REQ-SM-16	The structure of the space element shall be designed such that it does not obstruct the deployment mechanism of its deployer	REQ-SYS-F-07	Obstructed deployment leads to mission failure
REQ-SM-17	The materials of the structure of the space element shall endure a temperature range of 250 K to 450 K of for the duration of the mission	REQ-SYS-P-02	Material failure should not jeopardize mission outcome
REQ-SM-18	The materials of the structure of the space element shall endure a radiation of at most 1095 Sv for the duration of the mission	REQ-SYS-P-03	Material failure should not jeopardize mission outcome
REQ-SM-19	The materials of the structure of the space element shall endure the vacuum conditions for the duration of the mission	REQ-SYS-P-04	Material failure should not jeopardize mission outcome
~~REQ-SM-20~~	~~The structure of the space element shall be designed such that the ratio of the areas of the surfaces perpendicular and parallel to the atmospheric flow changes by factor of three or more when changing the attitude by 90 ° in yaw or pitch~~	~~REQ-SYS-D-06~~	This requirement is given in the project description and high level requirements

6.2 SCATTER Structural Design

The primary structure of the spacecraft is there for the purpose of providing the overall structural integrity as the main load path and serve as a platform for all other subsystems [30]. The dimensions of the primary structure adhere to a standard 12U CubeSat, while being able to fit in a Commercial-Off-The-Shelf (COTS) CubeSat deployer manufactured by Tyvak Nano-Satellite Systems [1]. A complete view of the structure can be seen in figure 6.1 and the internal layout can be seen in figure 6.2.

To satisfy REQ-OCS-05 on the CoM, a counterweight was added to the structural frame, as shown by the red circle in figure 6.2. Because of the tight packing of the subsystems, the size of the counterweight was kept minimal by assuming its material to be tungsten, which has a density of 19.28 g/cm^3. This resulted in a counterweight of 0.23 kg, which shifts the CoM to the required position, i.e. within less than 0.697 mm. All following components are fabricated from aluminium, which has a density of 2.7 g/cm^3.The other properties of the aluminium alloy used are further discussed in section 6.3.1.

[1] `https://www.tyvak.eu/launch-services/`

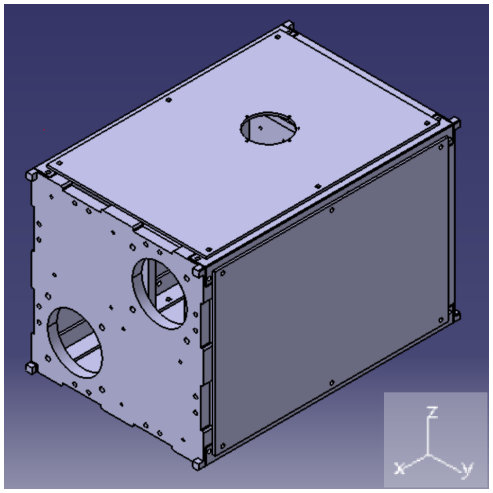

Figure 6.1: SCATTER frame.

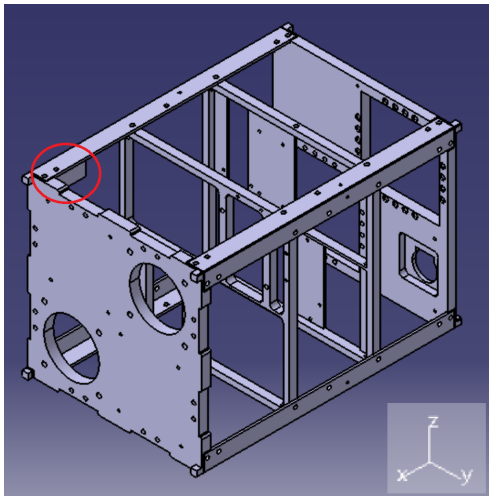

Figure 6.2: SCATTER frame internal view.

The front and end bulkhead are identical in size, and the corners are designed to accommodate the connecting rails and to facilitate the integration into the CubeSat deployer. The surface features of the front and end bulkhead do differ according to the subsystems that are connected to them, as shown in figure 6.3 and 6.4. The front bulkhead has two holes to place the mass spectrometers and pockets on the side for solar panel attachment. It further has holes for bolts to connect the mass spectrometer, the solar panels and the battery packs.

The main purpose of the end bulkhead is to provide part of the support for the propulsion system, for which it has two square cutouts, surrounded by the appropriate mounting holes. It further provides a mounting location for one of the sun sensors, which includes a pocket as to fit the sensor such that no other subsystems are obstructed. Mounting holes for the magnetorquer board are positioned around the sun sensor pocket, while the mounting holes for the reaction wheels are positioned in the opposite corner.

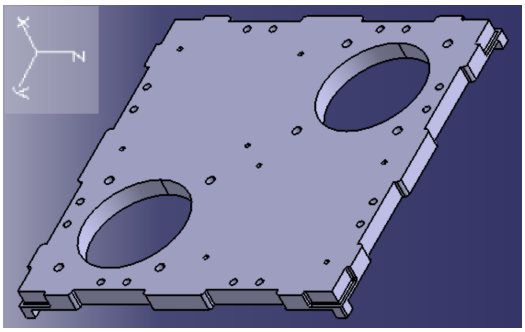

Figure 6.3: Front bulkhead.

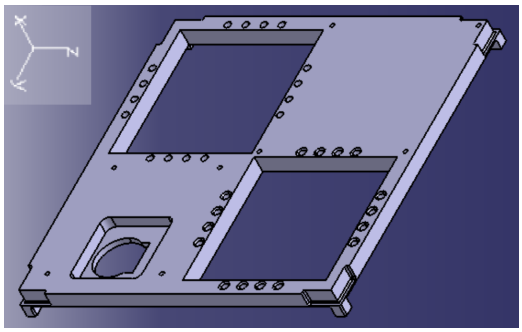

Figure 6.4: End bulkhead.

To section the internal space into three sections, two internal bulkheads were designed. Both of them started off as identical square frames, and their design was then iterated upon according to the internal layout of the subsystems. The engine bulkhead, shown in figure 6.5, provides support halfway of the propulsion system by means of mounting holes for the tanks. It further has plates to mount the IMU's and magnetometers. The centre bulkhead, as shown in figure 6.6, separates the compartment with the propulsion system from the front section containing the main payload, i.e. the mass spectrometers. It does this by providing mounting positions for the upper part of the fuel tanks.

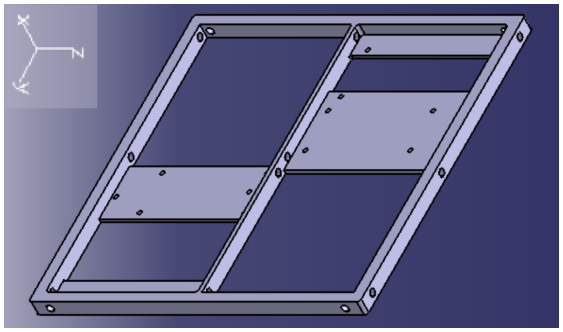

Figure 6.5: Engine bulkhead.

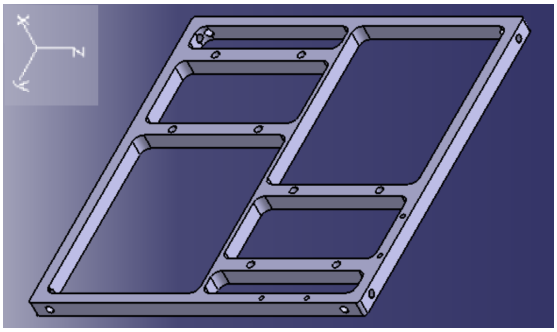

Figure 6.6: Centre bulkhead.

Apart from providing support to the other subsystems, it is also the function of the structural frame to provide protection against the hostile environment. The frame is therefore closed off with four body panels. Similar to the internal bulkheads, all body panels were initially identical in size with six mounting holes along the sides, but were then iterated upon to facilitate the subsystem integration. A regular body panel can be seen in figure 6.9. Two of these panels are mounted to the frame where no external equipment is present, i.e. the sides where the large solar panels are positioned. The body panel that will be facing zenith, i.e. into space, must facilitate the GNSS receivers. Therefore, a round cutout with the necessary mounting holes is present, as can be seen in figure 6.7. As discussed in chapter 7, the thruster section of the propulsion unit can be become quite hot at times and therefore this panel serves as an additional heat sink by providing a connection point to the engine, a so-called thermal strap. This is modelled with a cylindrical slab welded to the panel.

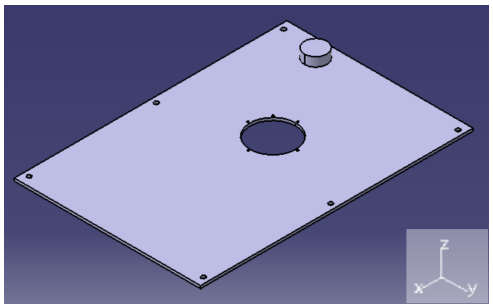

Figure 6.7: Body Panel accommodating GNSS antenna.

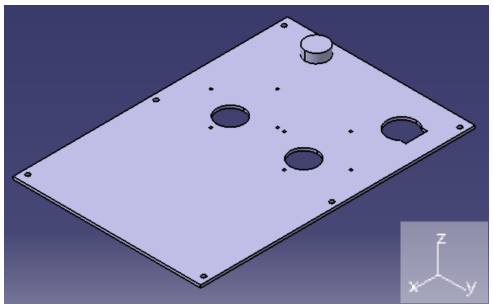

Figure 6.8: Body Panel accommodating TTC antenna.

On the opposite side of the spacecraft, i.e. the nadir side, the body panel has to accommodate two patch antennas for TT&C and another sun sensor, as shown in figure 6.8. The antennas are mounted on the surface, while circular holes allow for them to be connected to the internal receiver. The cutout for the sun sensor can be recognized from its distinctive shape, identical to the one in the end bulkhead. The TT&C panel also contains a slab acting as a thermal strap, similar to the one on the GNSS panel.

Table 6.2: Component breakdown

Component	Mass [kg]	Amount
Front bulkhead	1.293	1
End bulkhead	0.884	1
Engine bulkhead	0.272	1
Centre bulkhead	0.280	1
GNSS panel	0.506	1
TT&C panel	0.504	1
Regular panel	0.509	2
Rail	0.099	4
Counterweight	0.230	1
Structure	5.383	

To connect all the parts discussed above, a rail was designed to serve as the corner parts of the CubeSat. These L-shaped rails, as depicted in figure 6.10, provide mounting holes for all bulkheads, body panels and the battery stacks. A summary of all component masses and amounts can be found in table 6.2

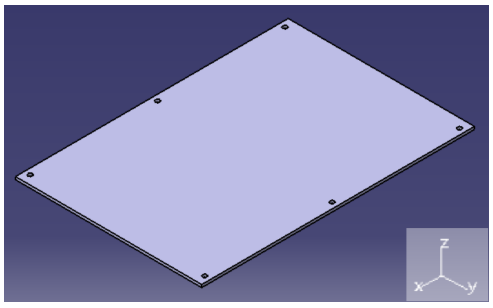

Figure 6.9: Regular body panel.

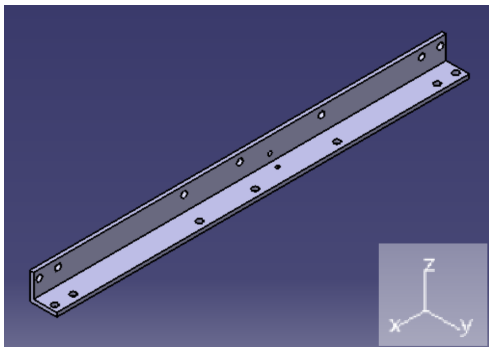

Figure 6.10: Connecting rail.

6.3 SCATTER Structural Analysis

Based upon requirements set by Arianespace in the SSMS Vega-C user's manual, a structural analysis was performed upon the structure discussed above. The software used for this purpose is ANSYS, a finite-element method software to solve mechanical problems numerically [31]. To use this software, the CAD file constructed in Catia V5 was imported, and an automated mesh was initially generated with the default settings. This was not deemed fit for the thin body panels, whereupon the mesh was locally refined, as shown in figure 6.12. Next, a fixed support was introduced at the end bulkhead, to simulate the cantilever mounting onboard the Vega-C. With this setup, static, dynamic and modal analyses were performed.

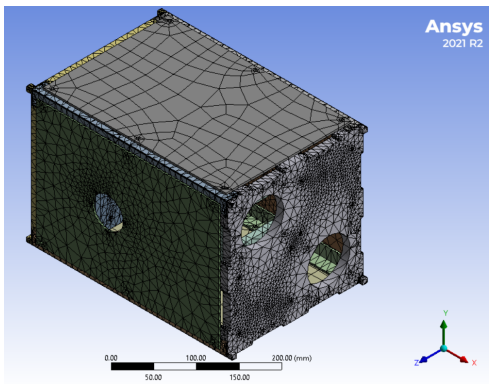

Figure 6.11: Meshing of the model with the according axis system.

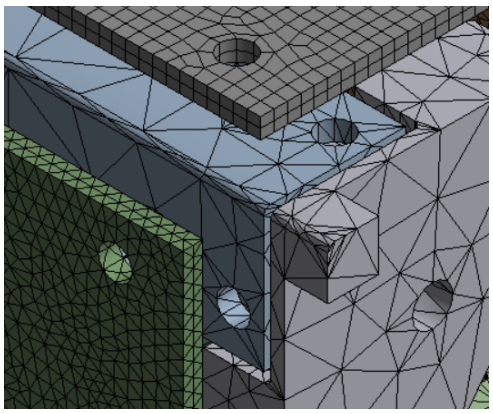

Figure 6.12: Locally refined panel mesh.

6.3.1 Structural Material Analysis

Inspecting the available COTS CubeSat frames, it was shown that the aluminium alloy Al 6061 T6 is a common space-grade metal used [32]. Therefore, it was decided to use the same material for the custom frame to be analysed and constructed. The 6061 aluminium alloy series contains silicon and magnesium as their main alloying elements. The T6 label indicates it has been heat treated, giving it the highest yield strength among the 6061 alloys, even surpassing some stainless steel types [2]. The alloy material properties are lined out in table 6.3.

Table 6.3: Material properties of Al 6061 T6.

Property	Value	Unit
Density	2700	kg/m^3
Tensile yield strength	276	MPa
Ultimate tensile strength	310	MPa
Young's modulus	68.9	GPa
Shear modulus	26	GPa
Shear strength	207	MPa
Poisson's ratio	0.33	/
Melting point	582 to 652	°Celsius

6.3.2 Structural Static Load Analysis

During launch, the spacecraft is subject to accelerations up to 10 g in all axis [33]. In order not to damage any internal subsystem, it is the task of the structure to transmit these loads through its base into the launch adapter. Before a CubeSat is allowed to fly on the Vega C rocket, numerous testing is involved. The most stringent one is the qualification testing, for which the highest safety factors apply. Therefore, if the structure is designed to withstand these tests, one can with confidence assume that all tests should be passed. For the analysis performed, the end bulkhead was constrained as a fixed support, as the CubeSats are cantilevered mounted onto the launch vehicle. For the loads, accelerations of 12.5 g were superimposed, as the qualification factor for static loads is 1.25 [33]. The results for the static load analysis are depicted in figure 6.13 and table 6.4. The maximum deflection occurs in the middle of the panels at the free moving side. The equivalent stress is based upon the Von-Mises criteria, which combines all three principal stresses such that it can be compared to the material's yield strength. The maximum equivalent stress of 22.9 MPa occurs at the panel edges. Comparing this result to the yield strength listed in table 6.3, shows that the material does not fail with quite a large margin.

[2] https://asm.matweb.com/search/SpecificMaterial.asp?bassnum=ma6061t6

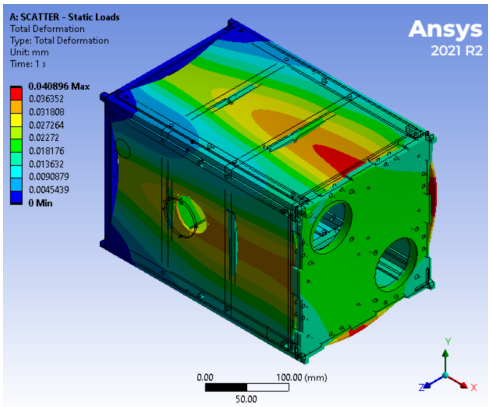

Figure 6.13: Scaled deformations due to launch acceleration.

Table 6.4: Static analysis results.

Parameter	Value	Unit
Maximum deformation	0.0407	mm
Maximum equivalent stress	22.9	MPa

6.3.3 Structural Modal Analysis

To avoid coupling during launch, the spacecraft should have natural frequencies that are at least higher than the vibrating frequency of the launch vehicle. Therefore, the natural frequencies of the spacecraft structure were analysed. There should be at least one octave separation between the vibrating frequency of the launcher and the first mode of the spacecraft, in order to mitigate dynamic coupling [34]. An octave increase in frequency is defined as the higher frequency being twice the lower frequency [34]. Following this rule and knowing that the launch vehicle vibrates at a frequency of 115 Hz, the aim was to have the lowest mode at least at a frequency of 230 Hz. An analysis of the modes was performed multiple times during the detailed design phase to check the structure's performance. As mentioned in section 6.2, the initial engine and centre bulkhead were mere square frames. With this initial design, the first modes of the frame were too low, causing a risk of resonance. To overcome this, structural elements had to be made stiffer in the direction of the exciting axis. As the integration process ran in parallel with the structural design, the frame was not merely adjusted to satisfy the natural frequencies, but the analysis was iterated each time the frame was altered to harbour a certain subsystem. This turned out to be a successful approach, as can be seen from the modes in table 6.5. Table 6.5 also includes the axes along which a force is most likely to trigger the respective mode. These axes can also be observed in the mode shapes depicted in figure 6.14 to 6.19. Note that due to a cantilever mounting, the launch direction is either Y or Z.

Table 6.5: The first six modes of the frame.

Mode	Value	Unit	Exciting axis
First	400	Hz	Y
Second	409	Hz	Z
Third	426	Hz	Z
Fourth	459	Hz	Y, Z
Fifth	464	Hz	Y
Sixth	467	Hz	Y

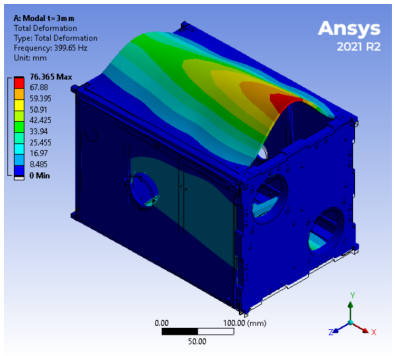

Figure 6.14: First mode.

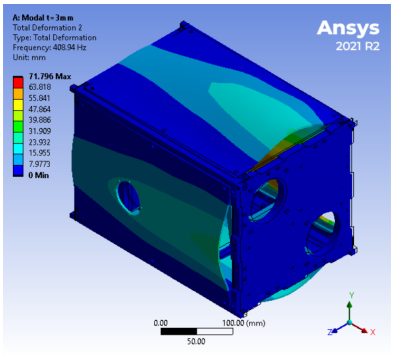

Figure 6.15: Second mode.

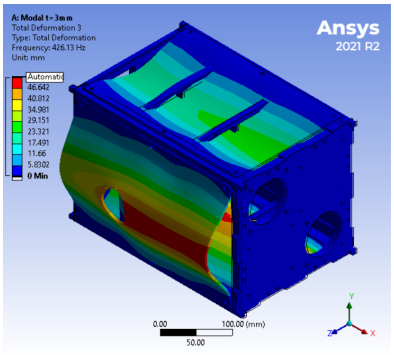

Figure 6.16: Third mode.

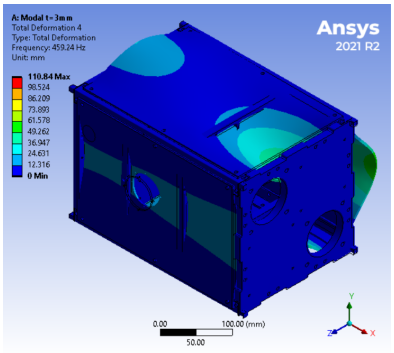

Figure 6.17: Fourth mode.

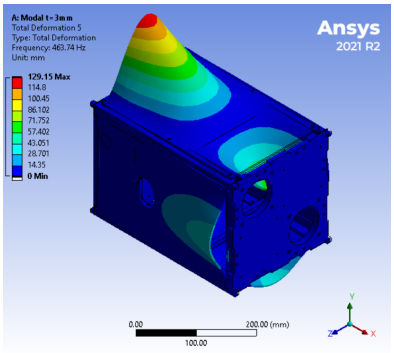

Figure 6.18: Fifth mode.

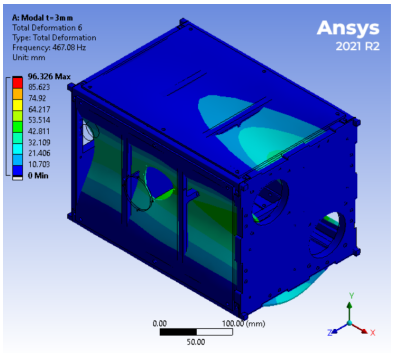

Figure 6.19: Sixth mode.

6.3.4 Structural Dynamic Loads Analysis - Random Vibrations

During launch, a spacecraft will be subject to random vibrations that are both mechanical and acoustic, and are caused by the launcher-spacecraft interface, engine combustion and turbulent boundary layers [35]. Because of the stochastic nature of these vibrations, they are described by a power spectral density (PSD) in terms of g^2/Hz, as shown in figure 6.20 and table 6.6. Analysis on random vibrations are often performed upon PCBs, to ensure that the rather thin structures do not collapse into each other when stacked [36]. Because the structural frame contains thin elements as well, the effects of random vibrations were analysed.

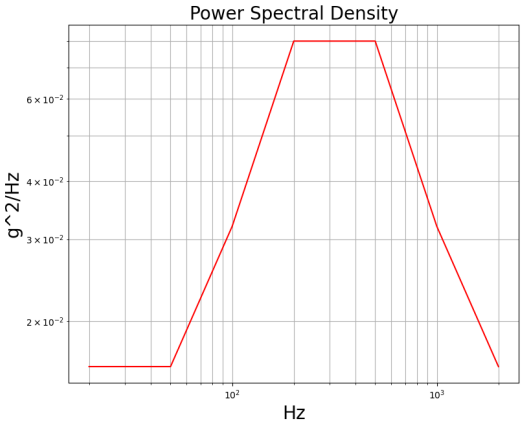

Figure 6.20: PSD characterizing the random vibrations.

Table 6.6: PSD data as specified in [33].

Frequency [Hz]	Power $[g^2/Hz]$
20	1.60×10^{-2}
50	1.60×10^{-2}
100	3.20×10^{-2}
200	7.99×10^{-2}
500	7.99×10^{-2}
1000	3.20×10^{-2}
2000	1.60×10^{-2}

To determine the equivalent load corresponding to this spectrum, several approaches exist [35]. One of the more conservative ones assumes that all modes up to 2000 Hz contribute to the random loads by calculating the peak load as follows [35]:

$$\begin{aligned} g_{peak} &= 3G_{rms} \\ &= 3\sqrt{\int_{20}^{2000} PSD df} \end{aligned} \tag{6.1}$$

Using equation 6.1 and integrating the log-log curve shown in figure 6.20, gave a peak load of 26.5 g when taking into account a qualification factor of 2.25 [33]. This approach would, however, lead to a very heavy design. Therefore, the mere PSD multiplied with the qualification factor was used as input for the numerical analysis, leading to results displayed in table 6.7 and figure 6.22 to 6.24. Note that due to the statistical nature of random vibrations, the results are statistical as well. The displacements in table 6.7 are the maximum displacements with a 2 σ probability. The maximum equivalent stress with the same probability was found to be 131 MPa, mainly occurring at the corners and front edge of the top panel, as depicted in figure 6.21.

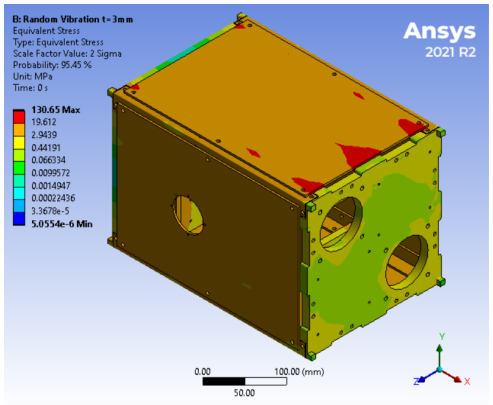

Figure 6.21: Stress distribution due to random vibrations.

Table 6.7: Maximum displacements due to random vibrations.

Displacement	Value [mm]
δ_x	0.202
δ_y	0.552
δ_z	0.356

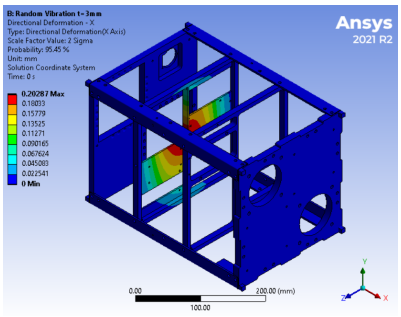

Figure 6.22: Displacement along the x-axis.

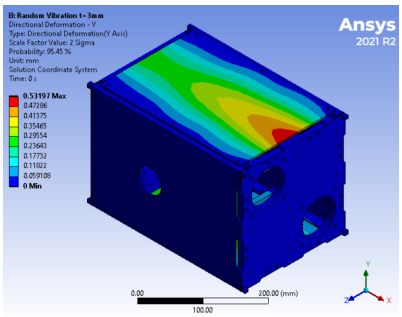

Figure 6.23: Displacement along the y-axis.

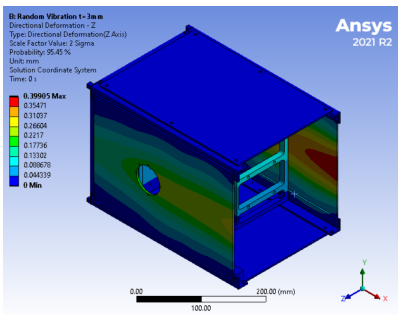

Figure 6.24: Displacement along the z-axis.

6.3.5 Structural Dynamic Loads Analysis - Sine Vibrations & Shock Loads

Aside from the primary structure, a spacecraft also contains secondary structures, including elements like solar arrays, antennas and pressure vessels [30]. On an even more detailed level, one can also identify tertiary structures: bolts, mounting brackets, component housings and electronic boxes [30]. Failure of secondary and tertiary elements does not immediately lead to mission failure, but important impacts on the mission might arise. These structural elements are mainly impacted by dynamic loads, such as sine vibrations and shock loads. Sine vibrations during launch arise due to the launcher-vehicle interface, engine combustion and during stage burn-out, the so-called pogo vibrations [37]. Shock loads are caused by engine ignition and shutdown, staging and separation from the launch vehicle and are a major concern for mountings and electronic boxes [37], [38]. So-called shaker tests are performed on structural models and flight models to ensure the overall integrity of the complete spacecraft [3]. As no detailed secondary and tertiary elements were designed, no numerical models could be built, and thus the relevant requirements are not satisfied by analysis but rather by testing.

6.3.6 Structures Subsystem Sensitivity Analysis

Observing the results of the structural analysis, it can be seen that the body panels often display the highest deformations and are the main contributors to the natural frequencies. As to prevent damage to both the internal subsystems and the external CubeSat deployer, the initial thickness of 3 mm of the body panels was varied to investigate its effect on the structure's performance in terms of natural frequency and the deformations due to static loads and random vibrations. Analyses for static loads, natural frequency and random vibrations were performed for thicknesses of 2 mm and 4 mm.

Static Loads

Increasing the plate thicknesses resulted in lower deformations of the body panels and vice versa, which is an expected result. The deformations changed by $+59\,\%$ and $-24\,\%$ for thicknesses of 2 mm and 4 mm respectively, as show in table 6.8 and 6.9. For the maximum equivalent stress, no significant variations were observed.

Table 6.8: Static analysis results, panel thickness 2 mm.

Parameter	Value	Unit
Maximum deformation	0.0646	mm
Maximum equivalent stress	21.7	MPa

Table 6.9: Static analysis results, panel thickness 4 mm.

Parameter	Value	Unit
Maximum deformation	0.0311	mm
Maximum equivalent stress	22.6	MPa

[3] https://www.esa.int/Enabling_Support/Space_Engineering_Technology/Test_centre/Electrodynamic_shakers

Natural Frequencies

As expected from observing the mode shapes in section 6.3.3, the panel thicknesses have a large influence on the modes of the frame. An incremental change of 1 mm resulted in changes of +11 % and −13 % for thicknesses of 2 mm and 4 mm respectively, as shown in table 6.10 and 6.11. While the effect is significant, REQ-SM-13 and REQ-SM-14 can still be satisfied with thinner panels, due to the stiffness of the other structural elements.

Table 6.10: The first six modes of the frame, panel thickness 2 mm.

Mode	Value	Unit	Exciting axis
First	356	Hz	Y
Second	365	Hz	Z
Third	380	Hz	Z
Fourth	404	Hz	Y, Z
Fifth	407	Hz	Y
Sixth	438	Hz	Y

Table 6.11: The first six modes of the frame, panel thickness 4 mm.

Mode	Value	Unit	Exciting axis
First	452	Hz	Y
Second	464	Hz	Z
Third	495	Hz	Z
Fourth	501	Hz	Y, Z
Fifth	564	Hz	Y
Sixth	569	Hz	Y

Random Vibrations

In line with the results of the sensitivity analysis on the static load, thinner plates are subjected to larger deformations and vice versa. With regard to the structural integrity of other subsystems and the CubeSat deployer, thinner panels pose an increased risk of colliding elements. Looking at the effect on the maximum equivalent stress, the magnitude for thinner plates was observed to be lower, i.e. 83 MPa, but it had a wider spread over the panels, as depicted in figure 6.25. The opposite was observed for thicker panels, yielding a local maximum equivalent stress of 163 MPa on the panel corners, as show in figure 6.26.

Table 6.12: Maximum displacements due to random vibrations, panel thickness 2 mm.

Displacement	Value [mm]
δ_x	0.203
δ_y	0.752
δ_z	0.603

Table 6.13: Maximum displacements due to random vibrations, panel thickness 4 mm.

Displacement	Value [mm]
δ_x	0.202
δ_y	0.387
δ_z	0.374

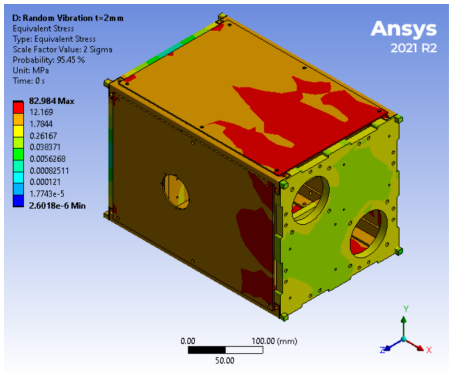

Figure 6.25: Stress distribution due to random vibrations, panel thickness 2 mm.

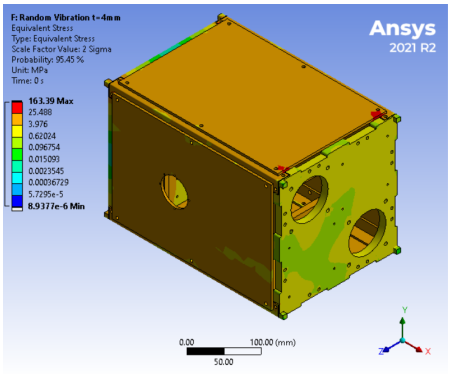

Figure 6.26: Stress distribution due to random vibrations, panel thickness 4 mm.

6.4 Structures Subsystem Requirements Verification

The verification of the Structures Subsystem by compliance with requirements is given below:

REQ-SM-01: - this requirement is verified through analysis in section 6.3.2. Lateral and longitudinal loads were superimposed, resulting in a maximum equivalent stress of 22.9 MPa, well below the aluminium yield strength of 276 MPa. Therefore, the requirement is satisfied.

REQ-SM-02: - this requirement is verified through analysis in section 6.3.2. Lateral and longitudinal loads were superimposed, resulting in a maximum equivalent stress of 22.9 MPa, well below the aluminium yield strength of 276 MPa. Therefore, the requirement is satisfied.

REQ-SM-03: - this requirement shall be verified through qualification and acceptance testing of the entire spacecraft with a shaker to ensure structural integrity of primary, secondary and tertiary structural elements.

REQ-SM-04: - this requirement shall be verified through qualification and acceptance testing of the entire spacecraft with a shaker to ensure structural integrity of primary, secondary and tertiary structural elements.

REQ-SM-05: - this requirement shall be verified through qualification and acceptance testing of the entire spacecraft with a shaker to ensure structural integrity of primary, secondary and tertiary structural elements.

REQ-SM-06: - this requirement shall be verified through qualification and acceptance testing of the entire spacecraft with a shaker to ensure structural integrity of primary, secondary and tertiary structural elements.

REQ-SM-07: - this requirement is verified through analysis in section 6.3.4. The maximum equivalent stress was computed to be 131 MPa with a 2 σ probability, which is lower than the aluminium yield strength of 276 MPa. Therefore, the requirement is satisfied.

REQ-SM-09: - this requirement shall be verified through qualification and acceptance testing of the entire spacecraft with a shaker to ensure structural integrity of primary, secondary and tertiary structural elements.

REQ-SM-10: - this requirement shall be verified through qualification and acceptance testing of the entire spacecraft with a shaker to ensure structural integrity of primary, secondary and tertiary structural elements.

REQ-SM-11: - this requirement shall be verified through qualification and acceptance testing of the entire spacecraft with a shaker to ensure structural integrity of primary, secondary and tertiary structural elements.

REQ-SM-12: - this requirement is verified through the purchase of a COTS CubeSat deployer with flight heritage.

REQ-SM-13: - this requirement is verified through analysis in section 6.3.3. The lowest mode is 400 Hz , well above the required 115 Hz. Therefore, the requirement is satisfied.

REQ-SM-14: - this requirement is verified through analysis in section 6.3.3. The lowest mode is 400 Hz , well above the required 115 Hz. Therefore, the requirement is satisfied.

REQ-SM-15: - this requirement is verified through designing the CubeSat frame based upon the available payload envelope in the COTS deployer

REQ-SM-16: - this requirement is verified through designing the CubeSat frame based upon the available payload envelope in the COTS deployer

REQ-SM-17: - this requirement is verified through the use of the space-grade aluminium alloy 6061-T6.

REQ-SM-18: - this requirement is verified through the use of the space-grade aluminium alloy 6061-T6.

REQ-SM-19: - this requirement is verified through the use of the space-grade aluminium alloy 6061-T6.

6.4.1 Structures Subsystem Design Concluding Remarks

Taking the resulting design of the frame and the analyses performed, a few remarks can be made. Firstly, although the custom frame can withstand the launch loads, compared to COTS frames, it is relatively heavy, considering some optimized 12U frames are as light as 1.5 kg [32]. This is mainly due to the front and end bulkhead. Because of the low stresses observed in these elements, their design could be iterated upon to lower the mass but keep their stiffness, e.g. by machining an isogrid structure. This iteration was not performed in this design stage due to its adverse effect on the mission planning: lowering the satellite mass lowers the mission time, jeopardizing the number of measurements to be taken. Secondly, more supports for the body panels and internal bulkheads could lower the deformations due to random vibrations significantly, decreasing the chance of colliding elements. Perhaps the additional support mass could offset the weight reduction suggested for the front and end bulkheads, thereby not affecting the mission planning. Thirdly, more analysis of the body panels could be required to investigate protection against radiation and debris shielding, two aspects that are also tied to the panel thickness. Finally, when further designing the secondary and tertiary structural elements, numerical analyses could be performed upon more complete models of the spacecraft, aiding the verification of dynamic load requirements.

7. Thermal Control Subsystem

This chapter describes the design of the spacecrafts Thermal Control Subsystem. Section 7.1 shows the requirements. Section 7.2 provides an overview of the design, followed by section 7.3 which provides the thermal analysis of the spacecraft. Finally, section 7.4 verifies and validates the requirements concerning the subsystem.

7.1 Thermal Control Subsystem Requirements

Table 7.1: Thermal control subsystem requirements.

ID	Description	Parent Requirement	Rationale
~~REQ-TCS-01~~	~~The thermal subsystem shall have a mass of 0.79 kg~~	~~REQ-SYS-D-03~~	This concerns mass budget.
REQ-TCS-02	The thermal sensors shall provide a temperature data to C&DH.	REQ-TCS-01	The temperature has to be reported to assess the thermal performance of the spacecraft.
~~REQ-TCS-03~~	~~The thermal subsystem shall consume at most 0.5 W.~~	~~REQ-TCS-01~~	This concerns power budget.
REQ-TCS-04	The thermal subsystem shall provide a temperature range of 283 K to 313 K to the propulsion system during its operation.	REQ-SYS-P-02	Operating temperature range of the module.
REQ-TCS-05	The thermal subsystem shall provide a temperature range of 243 K to 333 K to the propulsion system when it is non-operational.	REQ-SYS-P-02	Non-operational temperature range of the module.
REQ-TCS-06	The thermal subsystem shall provide a temperature range of 253 K to 323 K to the TT&C subsystem.	REQ-SYS-P-02	Operating temperature range of the module.
REQ-TCS-07	The thermal subsystem shall provide a temperature range of 248 K to 343 K to the Sun sensors.	REQ-SYS-P-02	Operating temperature range of the module.
REQ-TCS-08	The thermal subsystem shall provide a temperature range of 233 K to 343 K to the reaction wheels.	REQ-SYS-P-02	Operating temperature range of the module.
REQ-TCS-09	The thermal subsystem shall provide a temperature range of 248 K to 343 K to the magnetometer.	REQ-SYS-P-02	Operating temperature range of the module.
REQ-TCS-10	The thermal subsystem shall provide a temperature range of 233 K to 343 K to the magnetorquer.	REQ-SYS-P-02	Operating temperature range of the module.
REQ-TCS-11	The thermal subsystem shall provide a temperature range of 233 K to 358 K to the IMU.	REQ-SYS-P-02	Operating temperature range of the module.
REQ-TCS-12	The thermal subsystem shall provide a temperature range of 233 K to 358 K to the GNSS receiver.	REQ-SYS-P-02	Operating temperature range of the module.
REQ-TCS-13	The thermal subsystem shall provide a temperature range of 253 K to 313 K to the mass spectrometer.	REQ-SYS-P-02	Operating temperature range of the module.
REQ-TCS-14	The thermal subsystem shall provide a temperature range of 248 K to 338 K to C&DH.	REQ-SYS-P-02	Operating temperature range of the module.
REQ-TCS-15	The thermal subsystem shall provide a temperature range of 233 K to 343 K to the EPS module.	REQ-SYS-P-02	Operating temperature range of the module.
REQ-TCS-16	The thermal subsystem shall provide a temperature range of 123 K to 383 K to the solar panels.	REQ-SYS-P-02	The datasheet of the solar panel does not provide a temperature range, so a value from literature is taken[12].

7.2 Thermal Design Overview

The spacecraft has a passive thermal system to control the temperature in order to reduce the power required. Although the propulsion system and the EPS batteries do have heaters integrated with them, the heaters are considered as a part of those subsystems and the Thermal Control Subsystem does not introduce additional active components. The top and bottom panels of the spacecraft are painted white, whereas the body panels are covered with a variety of coatings. Two of the panels are covered with a 1 mil Kapton film, one panels is painted white, and the last panel is covered with a bare Aluminium coat.

The goal of the thermal analysis is to determine if the spacecraft can operate in the harsh environment of space. The general approach to a thermal system sizing is as follows:

1. Determine the operational/non-operational temperature ranges of the different subsystems on board.
2. Analyse the environment the spacecraft experiences and determine the hottest and coldest case.
3. Perform thermal analysis to determine if the passive thermal options are enough or an active system is required.
4. Perform laboratory tests to ensure the system is performing up to the expectations.

7.2.1 Subsystem Operating Temperature Range Analysis

The operational temperature ranges of all the components in the spacecraft is shown in table 7.2. It is evident that the propulsion system has the strictest temperature requirement during its operation and would be the area of interest during the thermal analysis. It is not favourable to determine a specific operational range of the whole spacecraft system, as it will restrict the design considerably and may eventually lead to inefficient or unfeasible solutions. Components such as solar panels have large temperature variations since they have a low thermal inertia and are disconnected from the body. Therefore, it is better to analyse the temperature of each component in the analysis and ensure all have acceptable temperatures.

Table 7.2: Operating temperature ranges of the components.

Component	Operating temperature range	Component	Operating temperature range
Solar panels[12]	123 K to 383 K	ADCS magnetometer	248 K to 343 K
EPS	233 K to 343 K	ADCS magnetorquer	233 K to 343 K
Propulsion (Operational range)	283 K to 313 K	ADCS sun sensor	248 K to 343 K
Propulsion (Non-operational range)	243 K to 333 K	ADCS reaction wheels	253 K to 323 K
C&DH	233 K to 358 K	GNSS receiver	233 K to 358 K
TT&C receiver	253 K to 323 K	IMU	233 K to 358 K
TT&C antenna	253 K to 323 K	Mass spectrometer	253 K to 313 K

7.2.2 Analysis of Interaction with External Environment.

The spacecraft would have three incoming radiation sources of heat energy, namely, the solar radiation from the sun, albedo radiation due to the sunlight reflecting off the surface of Earth, and the infrared radiation from the Earth itself. Apart from this, due to the high inclination and a non-SSO orbit, the spacecraft would experience two extreme cases, a hot case in which the satellite does not experience eclipse and a cold case in which it has the highest eclipse time. Designing the thermal system to withstand these two extreme cases would qualify the spacecraft for all the other thermal scenarios.

7.3 SCATTER Thermal Analysis

The representative thermal model was made in the ESATAN program to perform a multi nodal analysis of the spacecraft, as shown in figure 7.1. A simple geometry is created with 2D shapes, since conductive and radiative couplings have to be defined on each surface. Therefore, the thickness of different parts is not shown in the representation, but it is taken into account during the thermal calculations. Also, the GNSS and TT&C antennas are assumed to take the same temperature as the body panels they are mounted on. Each surface is divided into a mesh with nodes. The thermal model further assumes a lumped model estimation where the thermal properties of the mesh element are same as the node.

The next step is defining the material of all the components which would be used for conductive and radiative analysis. At this stage of the design, it is difficult to obtain the exact material properties of all the components from the manufacturers, therefore it is assumed that all the PCBs in the spacecraft are made up of FR4 material and all the metallic casings are made of Al 6061 T6, same as the structure.The bulk material of the component with the coating on the both the front and back surface of the components is listed in table 7.3. The material properties of the bulk material and the optical properties of the coating are listed in table 7.4 and table 7.5.

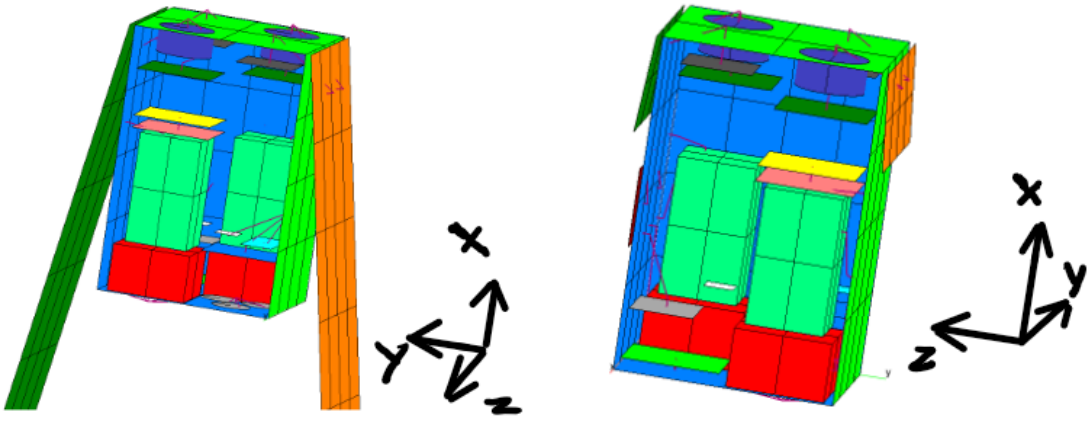

Figure 7.1: Representative Model for thermal analysis with properties in table 7.3.

Table 7.3: Material assigned to each component in ESATAN.

Component	Colour	Bulk Material	Optical set on surface 1	Optical set on surface 2
Top panel	Light green	Al 6061 T6	White paint	Hard anodised Al
Bottom panel	Blue cyan (inside surface)	Al 6061 T6	White paint	Hard anodised Al
TT&C antenna panel (+Z)	Blue cyan (inside surface)	Al 6061 T6	White Paint	Hard anodised Al
GNSS antenna panel (-Z)	Light green	Al 6061 T6	Bare Al coat	Hard anodised Al
+Y panel	Blue cyan (inside surface)	Al 6061 T6	Kapton film	Hard anodised Al
-Y panel	light green (outside)	Al 6061 T6	Kapton film	Hard anodised Al
EPS module	Grey square near the top	FR4	FR4 coat	FR4 coat
Solar Panels	Orange panels	FR4	Solar cell	FR4 coat
TT&C	Grey square at the bottom	FR4	FR4 coat	FR4 coat
C&DH	Yellow square	FR4	FR4 coat	FR4 coat
Engine	Red blocks	Al 6061 T6	chromic Al	inactive
Fuel tank	Turquoise green	Al 6061 T6	Kapton film	inactive
Reaction wheels	Grey circles at the bottom	Al 6061 T6	Black paint	Black paint
Magnetometer	Light blue rectangle beside tanks	Al 6061 T6	chromic Al	chromic Al
Magnetorquer	Green square at the bottom	FR4	FR4 coat	FR4 coat
Mass spectrometer base	Lavender	Al 6061 T6	ms_base_coat	inactive
Mass spectrometer	Lavender	Al 6061 T6	ms_head_coat	inactive
Mass spectrometer head	Lavender	Al 6061 T6	bare Al coat	inactive
IMU	White square beside tanks	FR4	FR4 coat	FR4 coat
GNSS receiver	Blue cyan square beside tanks	FR4	FR4 coat	FR4 coat

Table 7.4: Material properties of the bulk material.

Material	Conductivity $[W/mk]$	Density $[kg/m^3]$
Al 6061 T6 [1]	167	2700
FR4[39] [2]	17.62 along the plane, 0.32 through the plane	1850

Table 7.5: Optical properties of the coatings.

Coating	Absorptivity α (Sun)	Emissivity ϵ (IR)
White paint (GSFC NS44-B)[40]	0.34	0.91
Black paint (Anodise black)[40]	0.88	0.88
Kapton film 1 mm (Al-Al oxide overcoating)[40]	0.12	0.20
Bare Al coat [41]	0.17	0.1
FR4 coat [42]	0.6	0.7
Solar Cell [40]	0.8	0.85
Hard Anodised Al [40]	0.9	0.86

The conduction in the structural frame is automatically calculated by the software based on the material assigned to it as seen in figure 7.2. But the conductive coupling of the subsystems to the structure and the link between the solar panels and the structure via the hinges is defined manually in the model. For simplicity of the calculations, it is assumed that all the conductive links are made of Al 6061 T6, except the connection points of tanks and the engine of the propulsion system which are assumed to be made of Polyether ether ketone (PEEK) with a thermal conductivity[3] of 0.25 W/mK. The conductive heat flow is given by equation 7.1, where C is the conductive coupling which depends on the conductivity k [W/mK] of the material, the cross-sectional area A and the length L of the material.

$$Q = C\Delta T = \frac{kA}{L}\Delta T \tag{7.1}$$

The heat transfer between components, whose surfaces are in contact to each other, is given by equation 7.2. The contact conductance h_c is difficult to determine as it depends on the variety of factors such as the load applied, the surface roughness, material hardness [43]. Therefore, for sizing, a value of 1556 W/m^2K is taken from the literature [44]

$$Q = h_c \cdot A \cdot \Delta T \tag{7.2}$$

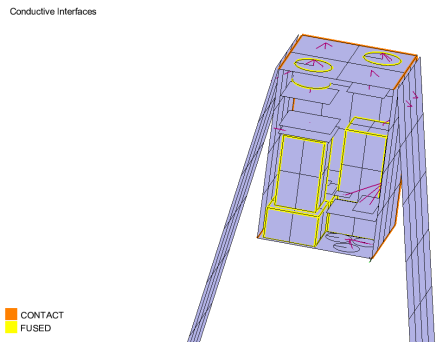

Figure 7.2: Conductive interfaces of the model.

The basis for all numerical simulation for thermal analysis is given by heat balance of a node, as shown in equation 7.3 [45].

$$(mc_p)_i \frac{dT_i}{dt} = Q_i + (\alpha(A_s J_s + A_{alb} J_{alb}) + \epsilon A_{IR} J_{IR}) - \Sigma_j R_{ij}\sigma(T_i^4 - T_j^4) - \Sigma_j C_{ij}(T_i - T_j) \tag{7.3}$$

Here $(mc_p)_i$ is the thermal mass of the node, with T_i, the temperature of the node at time t. Q_i the internal heat dissipation of the components, A_s, A_{alb}, A_{IR} the area of the surfaces facing the solar, albedo and the Earth IR radiation given by J_s, J_{alb} and J_{IR}, respectively. The terms R_{ij} and C_{ij} is the radiative and conductive coupling between the nodes. Finally, σ is the Stefan-Boltzmann constant.

[1] https://asm.matweb.com/search/SpecificMaterial.asp?bassnum=ma6061t6
[2] http://www.newlytrend.com/126-fr4-epoxy-sheet.html
[3] https://designerdata.nl/materials/plastics/thermo-plastics/polyetheretherketone

7.3.1 Thermal Subsystem Temperature Sensors Placement

Most of the onboard subsystems contain integrated temperature sensors to monitor their health. The EPS module has two temperatures per battery package, therefore 24 sensors in total. The propulsion system has one sensor to monitor the temperature of the tanks in order to heat them to the required temperature. Each mass spectrometer unit has and the magnetorquer has one too. Furthermore, the solar panels come with 6 integrated temperature sensors, with one per panel.

The mass spectrometer unit has additional 5 sensors which could be placed anywhere in the spacecraft to monitor specific areas of interests.

- TMP sensor 1: The first one would be placed on the C&DH board. This is the brain of the satellite, and it is imperative to monitor its own temperature and regulate the load accordingly in case extreme temperatures are reached.
- TMP sensor 2: The transceiver is a power demanding system and therefore will emit a lot of heat during downlink. Also, it is placed beside the propulsion system, which is already a high power dissipating system when active, therefore a sensor is required on the transceiver
- TMP sensor 3 and 4: Temperature sensors can be placed on the body panels near the location where the TT&C antenna and the GNSS antenna are placed.
- TMP sensor 5: The last sensor can be placed near the centre of the body where the magnetometer and IMU are placed, as this is the last location where the temperature of the system is not monitored.

7.3.2 SCATTER Thermal Analysis Results

The thermal model was simulated at altitudes of 600 km and 150 km in the aerodynamic and drag configuration in both cold and hot cases. This leads to eight different scenarios, for which the results of the interesting subsystems are provided below:

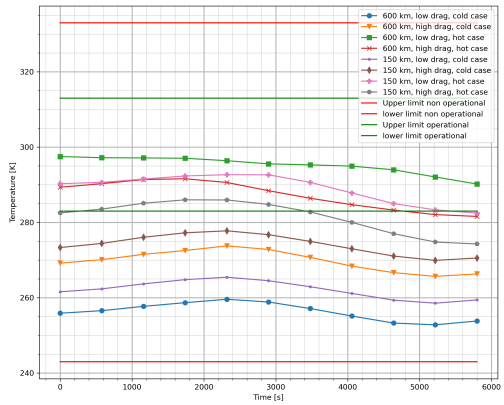

Figure 7.3: Temperature fluctuation of propulsion system.

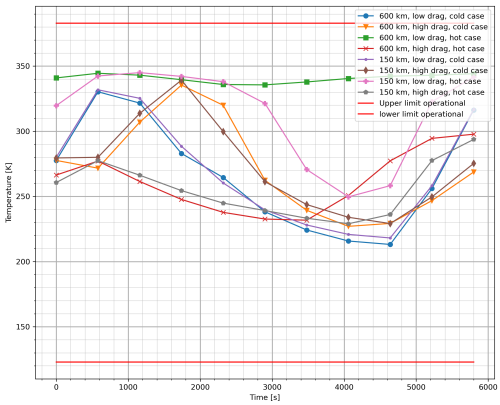

Figure 7.4: Temperature fluctuation of +Y solar panel.

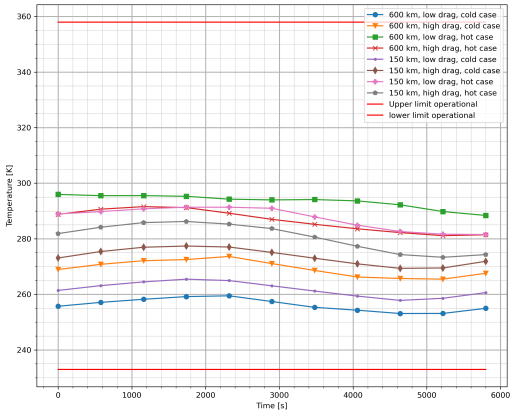

Figure 7.5: Temperature fluctuation of the -Z panel housing the GNSS antenna.

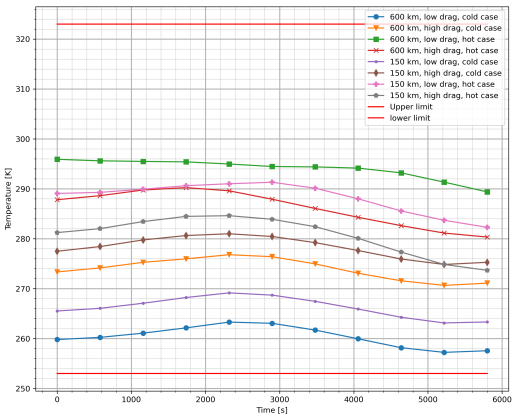

Figure 7.6: Temperature fluctuation of transceiver.

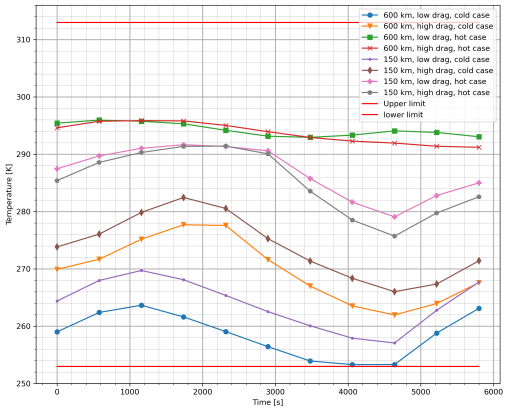

Figure 7.7: Temperature fluctuation of mass spectrometer.

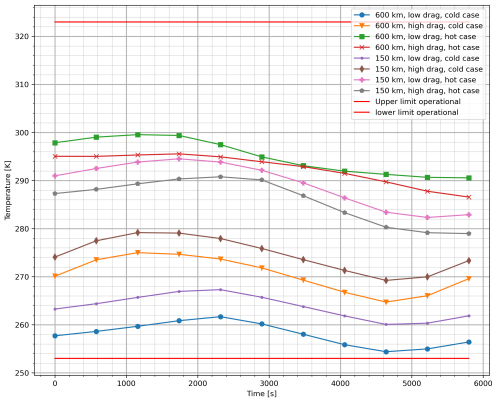

Figure 7.8: Temperature fluctuation of the +Z panel housing the TT&C antennas.

As seen in figure 7.3 the propulsion subsystem has the lowest operational range of any other subsystem. It has inbuilt heaters which will be used before a burn in cold cases or when it is below 283 K, whereas for the majority of hot cases it stays above the operational limit, where the heaters may be used to just maintain the optimal temperature.

The mass spectrometer and the TT&C antenna are an area of concern as they are just above the minimum operating limit as seen in figure 7.7 and figure 7.8. Even though those components may not be used all the time, it is important to keep them in the operational range instead of the survival range since they are imperative for the mission. They are at a potential risk and need to be monitored specifically and analysed more in detail. Furthermore, the solar panels experience the greatest temperature swings in due to them being detached from the body of the spacecraft as seen in figure 7.4. The maximum and minimum temperature of the all the other components can be found in table 7.6. Additionally, the temperature of the sun sensors needs to be monitored as well, as the margin is not big. It is also assumed that the sun sensors on the solar panel come as an integrated part and different from the ones on the body panels, which should be rated to experience the extreme conditions. However, this is not known for sure and should be monitored too. The remaining components are well within their temperature range, with large margins of $\geq$10 K.

Table 7.6: Temperature of the remaining subsystems.

Component	Temperature Range	Component	Temperature Range
Sun sensors	253 K to 302 K	IMU	255 K to 297 K
Reaction wheels	255 K to 300 K	GNSS receiver	259 K to 305 K
Magnetometer	256 K to 303 K	C&DH	257 K to 298 K
Magnetorquer	255 K to 300 K	EPS	256 K to 297 K

7.3.3 Thermal Control Subsystem Sensitivity Analysis

Thermal analysis showed that the mass spectrometer, transceiver and the TT&C antenna were close to the lower operational limit, and thus will be the focus of the sensitivity analysis. The optical property of surface 1 of the top plate housing the mass spectrometer is changed from white paint to bare Al coating, and the +Z and -Z panel coatings housing the TT&C and GNSS antennas are replaced with a Kapton film. The results are shown in table 7.7. The results are much better on the lower end for all these, but again for the mass spectrometer, it is quite close to the upper operating limit. Also, there is still is a lot of uncertainty with the optical coating of the antenna. Furthermore, the Kapton film on the +Z panel would need to have cuts to house the antenna. This would introduce discontinuity in the insulating material and reduce the performance of the insulating film.

Table 7.7: Sensitivity analysis results.

Component	New Temperature range	Operational Range
Mass spectrometer	264 K to 310 K	253 K to 313 K
Transceiver	268 K to 308 K	253 K to 323 K
TT&C antenna	264 K to 309 K	253 K to 323 K

Furthermore, as mentioned in section 6.2, there are metallic slabs which act as thermal straps attached to the +Z and -Z panels from the engine. This is done to keep the temperature of the engine in check during the burn, as they tend to get hot. Even if these panels face the sun directly, it is not an issue because the Kapton film has low values of α and ϵ, thus not much heat is absorbed, but still effectively take enough heat away from the engines.

7.4 Thermal Control Subsystem Requirements Verification

The verification of the Thermal Control Subsystem by compliance with requirements is given below:

REQ-TCS-02: - this requirement is verified through inspection of the SCATTER design, which is equipped with 5 temperature sensors placed as shown in section 7.3.1. Therefore, the requirement is satisfied;

REQ-TCS-04: - this requirement is verified through a thermal analysis performed in section 7.3.2 which yields a minimum temperature of 285 K and a maximum temperature of 297 during operation, therefore the requirement is satisfied;

REQ-TCS-05: - this requirement is verified through a thermal analysis performed in section 7.3.2 which yields a minimum temperature of 254 K and a maximum temperature of 298 K, therefore the requirement is satisfied;

REQ-TCS-06: - this requirement is verified through a thermal analysis performed in section 7.3.2 which yields a minimum temperature of 254 K and a maximum temperature of 298 K, therefore the requirement is satisfied;

REQ-TCS-07: - this requirement is verified through a thermal analysis performed in section 7.3.2 which yields a minimum temperature of 253 K and a maximum temperature of 302 K, therefore the requirement is satisfied;

REQ-TCS-08: - this requirement is verified through a thermal analysis performed in section 7.3.2 which yields a minimum temperature of 255 K and a maximum temperature of 300 K, therefore the requirement is satisfied;

REQ-TCS-09: - this requirement is verified through a thermal analysis performed in section 7.3.2 which yields a minimum temperature of 256 K and a maximum temperature of 303 K, therefore the requirement is satisfied;

REQ-TCS-10: - this requirement is verified through a thermal analysis performed in section 7.3.2 which yields a minimum temperature of 255 K and a maximum temperature of 300 K, therefore the requirement is satisfied;

REQ-TCS-11: - this requirement is verified through a thermal analysis performed in section 7.3.2 which yields a minimum temperature of 255 K and a maximum temperature of 297 K, therefore the requirement is satisfied;

REQ-TCS-12: - this requirement is verified through a thermal analysis performed in section 7.3.2 which yields a minimum temperature of 259 K and a maximum temperature of 305 K, therefore the requirement is satisfied;

REQ-TCS-13: - this requirement is verified through a thermal analysis performed in section 7.3.2 which yields a minimum temperature of 253.3 K and a maximum temperature of 296 K, therefore the requirement is satisfied;

REQ-TCS-14: - this requirement is verified through a thermal analysis performed in section 7.3.2 which yields a minimum temperature of 257 K and a maximum temperature of 298 K, therefore the requirement is satisfied;

REQ-TCS-15: - this requirement is verified through a thermal analysis performed in section 7.3.2 which yields a minimum temperature of 256 K and a maximum temperature of 297 K, therefore the requirement is satisfied;

REQ-TCS-16: - this requirement is verified through a thermal analysis performed in section 7.3.2 which yields a minimum temperature of 210 K and a maximum temperature of 350 K, therefore the requirement is satisfied;

7.4.1 Thermal Control Subsystem Concluding Remarks

Based on the results of the thermal analysis and the sensitivity analysis, it can be concluded that the temperature of the spacecraft can be maintained by just using simple passive systems. There are no mechanical parts involved, thus greatly increasing the reliability of the system. The spacecraft does have an active heating system, but it is considered as a part of the propulsion unit as it is an integral part of that system. Furthermore, the spacecraft has numerous temperature sensors integrated as part of subsystems to help monitor the temperature. These temperature sensors will greatly help to improve the thermal model in future to accurately represent the temperature of the spacecraft. The analysis showed that even though the subsystems were within their operational/non-operational range, there are uncertainties in the model due to the simplifications made. Thus, the bigger the margin, the bigger the confidence in the model to account for the uncertainties, however the mass spectrometer, TT&C antenna and the sun sensors were quite close to their limit and thus cannot be said with confidence if their temperature stays within the limits. Therefore, these components shall be monitored closely in the next design phases. Better performing options of these components should be looked into as well. Furthermore, the optical properties of the coatings needs to be further investigated on their specular and diffuse reflectivity, so that the radiation pressure can be modelled. This is important because GNSS receiver allows us to derive non-gravitational acceleration, which is a sum of aerodynamic and radiation pressure accelerations. Finally, only two bulk materials are used in the model and similar optical coating for the components due to the lack of information from the suppliers, which should be improved in the future as well.

8. Orbit Control Subsystem Design

In this chapter, the Orbital Control Subsystem (OCS) will be presented and analysed, including the delta-V budget. In section 8.1, the requirements of the OCS are listed. In section 8.2, the delta-V budget of the mission is derived and explained. In section 8.3, the OCS design is presented and analysed, including the sensitivity analysis. Lastly, in section 8.4 the verification and validation of the subsystem is performed.

8.1 OCS Subsystem Requirements

Table 8.1: Subsystem requirements.

ID	Description	Parent Requirement	Rationale
REQ-OCS-01	The propulsion subsystem shall provide at least 3 m/s of continuous delta-V burn.	REQ-M-06	Maximum delta-V needed per burn to lower orbit in phase 1. Calculated using Python.
REQ-OCS-02	The propulsion subsystem shall sustain at least 240 start-stop sequences.	REQ-M-06, REQ-M-08, REQ-M-10, REQ-M-11, REQ-M-22	20 Hohmann transfers per orbit in Phase 1 * 2 burns/orbit + 50 * 2 burns/man. / 2 sat in Phase 2 + 5 measurements in Phase 3 * 4 burns/meas. / 2 sat + 20 collision avoidance manoeuvres/year * 3 years + 50% contingency = 240
REQ-OCS-03	The propulsion subsystem shall be able to deorbit the satellite from insertion orbit to 400 km in less than 2 months.	REQ-M-22	To limit the total mission lifetime to less than 3 years, since most of the mission is spent in phase 2
REQ-OCS-04	The minimum needed total impulse burst for manoeuvres shall be bigger than 5 mNs.	REQ-M-10, REQ-M-11	Assuming value from another monopropellant system, as no other data is available. [5]
REQ-OCS-05	The thrust vector of the propulsion subsystem shall be pointing along an axis that passes at a maximum distance of 0.697 mm from the CoM of the satellite.	REQ-SYS-F-23	The burn time per phase 1 manoeuvre at nominal 1 N thrust was estimated at 45.9 s. With a 25% margin, it is 57.4 s. The reaction wheels can provide 0.04 Nms momentum without dumping. This results in a maximum 0.697 mNm torque. This results in a maximum 0.697 mm off-centre tolerance.
REQ-OCS-06	The thrust plume shall not affect the nominal operations of other external components of the satellite	REQ-SYS-F-16	If it does, it decreases either the component's lifetime, duty cycle, or even destroys it. Depending on the component, this might lead to a mission failure.
~~REQ-OCS-07~~	~~The propulsion subsystem shall have a size of maximum 4 U.~~	~~REQ-SYS-D-07~~	The requirement has been reversed and moved to S&M requirements
~~REQ-OCS-08~~	~~The propulsion subsystem shall have a wet mass of maximum 6 kg.~~	~~REQ-SYS-D-03~~	This is an issue for the budget. A requirement would only constrain the design space.
~~REQ-OCS-09~~	~~The propulsion subsystem shall use maximum 51 W peak power during burns.~~	~~REQ-EPS-06~~	The requirement overlaps in function with REQ-EPS-06
~~REQ-OCS-10~~	~~The propulsion subsystem shall use maximum 0.6 W power during stand-by.~~	~~REQ-SYS-F-23~~	Derived from the datasheet of the propulsion system choice
~~REQ-OCS-11~~	~~The propulsion subsystem shall be operational between 10 and 40 °C.~~	~~REQ-SYS-P-02~~	Moved to TCS requirements
REQ-OCS-12	The propulsion subsystem shall have enough delta-V capability to perform phase 1, 2 and 3 burns, and collision avoidance manoeuvres.	REQ-SYS-F-23	Without enough fuel / delta-V, the satellite cannot perform the necessary manoeuvres to control its orbit.

8.2 SCATTER Mission Delta-V budget

Delta-V relates to the amount of propellant the spacecraft needs to preform the required manoeuvres. However, in contrast to propellant mass, the required delta-V does not dependent on the mass of the spacecraft and is thus preferred. There are four main sources for the delta-V requirements of the SCATTER mission:

1. Hohmann transfers during Phase 1, required to decrease the altitude of the satellites in steps
2. Formation maintenance manoeuvres in Phases 2 & 3 and to cancel the along-track and radial position differences between the satellites after their scientific modes
3. Collision avoidance between the two satellites
4. Collision avoidance from other space objects

These will be analysed one by one in the coming subsections.

8.2.1 Altitude-Lowering Hohmann Transfers Analysis

During the first phase, the satellite will descend in steps of at most 10 km, as explained in section 3.5, from an initial altitude of 600 km to 400 km. This is done using Hohmann transfers for every step, as shown in figure 8.2 for one step. The sequence of manoeuvres was simulated using the Astrodynamics Simulator, as shown in figure 3.5a. In this simulation, the satellite starts with 1.6 kg of propellant and ends up with 0.788 kg, having consumed 0.812 kg of propellant. Transforming this into delta-V using Tsiolkovsky's rocket equation, it is obtained that a delta-V of 106.624 m/s is needed.

8.2.2 Analysis of Formation Maintenance Manoeuvres in Phases 2 & 3

During science mode in Phases 2 and 3, the satellites alternate between the two orientations (low and high drag configurations) in order to limit the difference in position between themselves, as compared to the standard 300 km along-track. This is not needed in Phase 1, as the separation never increases significantly enough to require a correction before an altitude step burn is done anyway. Because of these alternations in Phases 2 and 3, when

they finally exit the science and power modes, along-track and radial position differences must be cancelled out through formation maintenance manoeuvres. In phase 2 a transition ADCS control scheme is employed, which brings the satellites to circular orbits. The radial position difference in this phase is negligible (less than 25 m), leaving only the in-track position difference to be cancelled through a phase shift manoeuvre. In Phase 3 near the 200 km altitude, such a control scheme is not employed, as it would take up a significant amount of time from the science mode. Due to this, the satellites end up in a configuration similar to the one in figure 8.3, along the dashed line in the red and black orbits. A half-Hohmann manoeuvre will be employed, followed by a phase shift to cancel the remaining in-track position difference.

A phase shift manoeuvre consists of a prograde burn of the satellite further in front in the orbit (satellite 1), which raises its apogee, as shown in figure 8.1a. This eccentric transfer orbit has a larger orbital period than the original orbit; this means that satellite 1 will take longer to arrive back to its original position, effectively decreasing its orbital phase relative to satellite 2, as shown in figure 8.1b. When satellite 1 arrives back to its original position, it performs a retrograde burn to come back to its original orbit, finishing the transfer. In the above-mentioned figures, only one period is spent in the transfer orbit; however, multiple periods could be spent in that orbit, effectively lowering the delta-V requirement for the burns, as a lower semi-major axis change is needed. However, this also prolongs the time of the transfer.

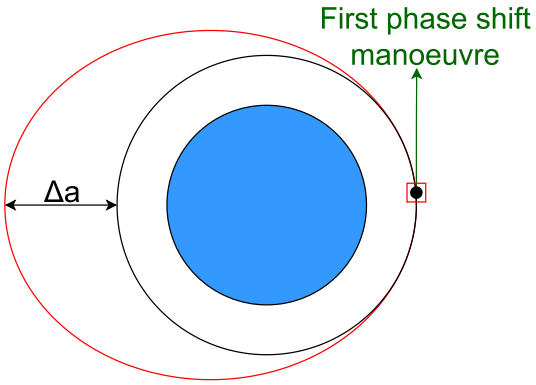

(a) First burn of the phase shift manoeuvre. The two satellites start at the same orbital position in the black orbit, and the red square satellite performs a prograde burn to move into the red orbit with a larger orbital period. The satellites move counterclockwise.

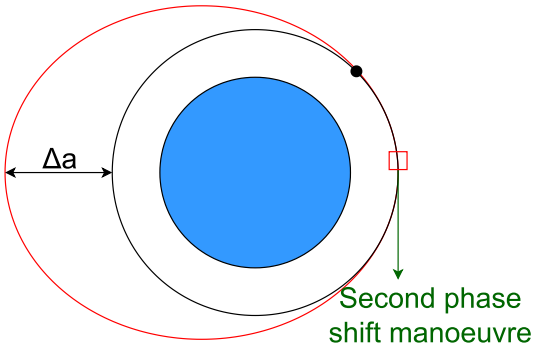

(b) Second burn of the phase shift manoeuvre. After spending a revolution in the transfer orbit, the red square satellite is now behind the black dot satellite, due to the difference in the orbital periods of the two orbits. The red square satellite performs a retrograde burn to return to the initial circular orbit.

To calculate the required transfer orbit and resulting delta-V requirements, a linearisation of the orbital period formula is employed, from which the change of the semi-major axis is calculated based on the chosen number of periods to be spent in the transfer orbit. This is summarised in equation 8.1, where a is the semi-major axis of the initial orbit (i.e. the radius for a circular orbit), N is the number of revolutions spent in the transfer orbit, Δpos is the required change in orbital phase in radians, and Δa is the resulting change in semi-major axis for the transfer orbit. From this, the required delta-V (two burns) is calculated according to equation 8.2, where $\mu = 398\,600.44\,\mathrm{km}^3/\mathrm{s}^2$ is the standard gravitational parameter of Earth, $r = a$ is the radius of the initial circular orbit, $a_T = a + \Delta a$ is the semi-major axis of the transfer orbit, and ΔV is the required delta-V for this manoeuvre (2 burns). The derivation of these equations can be found in [46], slides 69 - 70.

$$\Delta a = \frac{\Delta pos \cdot a}{3\pi} \cdot \frac{1}{N} \tag{8.1}$$

$$\Delta V = 2\left[\sqrt{\mu\left(\frac{2}{r} - \frac{1}{a_T}\right)} - \sqrt{\frac{\mu}{r}}\right] \tag{8.2}$$

In Phase 3, there are two cases: when the satellites are close to the 300 km altitude, due to the ADCS control scheme, a normal Hohmann transfer needs to be performed first, followed by a phase shift manoeuvre. However, when the satellites are close to the 200 km altitude, they will end up as shown in figure 8.3, along the dashed line, in the red and black orbit respectively, as mentioned earlier. For the satellite on the red orbit to return to the black orbit, it will first have to wait half a revolution, then perform a "half-Hohmann" prograde burn, which will recircularise the orbit. Afterwards, a phase shift manoeuvre is needed for cancelling the remaining along-track position difference.

In table 8.2, the initial parameters, assumptions and final results are shown for the phase shift manoeuvres in Phases 2 and 3. The final delta-V and time requirements are calculated as an average between the 400 km and 300 km altitude cases for Phase 2, and between the 300 km and 200 km altitude cases for Phase 3. The 300 km case is included twice to take into account the difference in revolutions spent in transfer orbit in Phase 2 versus Phase 3.

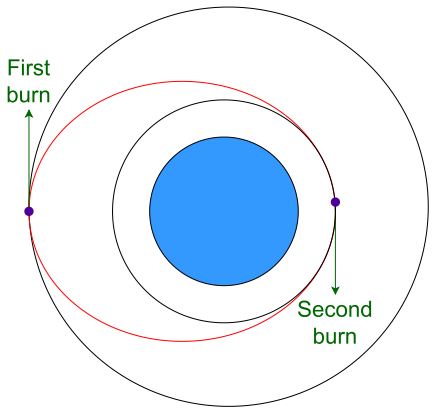

Figure 8.2: Orbit-lowering Hohmann manoeuvre. The satellite is shown with a purple dot and is moving counterclockwise. It starts in the outer circular orbit, performs a retrograde burn to bring it into the red transfer orbit, and after half revolution another retrograde burn to bring it into the inner circular orbit.

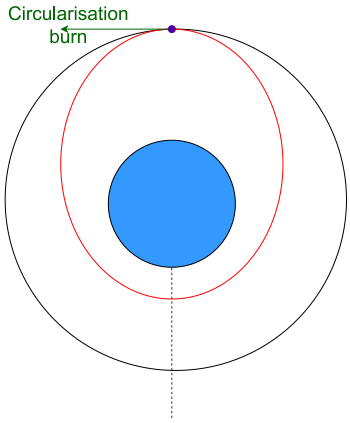

Figure 8.3: Orbit-lowering half-Hohmann manoeuvre. The satellite is shown with a purple dot and is moving counterclockwise. It starts in the outer circular orbit, performs a retrograde burn to bring it into the red transfer orbit, and after half revolution another retrograde burn to bring it into the inner circular orbit.

Table 8.2: Parameters and results for the phase shifts in Phases 2 and 3. The final two columns contain the averages for these phases, calculated from the Delta-V and Manoeuvre time columns. "Pos. diff." means position difference.

Radial pos. diff. [km]	Along-track pos. diff. [km]	No. of revolutions (N)	Delta-V [m/s]	Period [h]	Manoeuvre time [h]	Average delta-V [m/s]	Average manoeuvre time [h]
400	5.5	5	0.066	1.54	7.71	**Phase 2**	
300	3.8	5	0.047	1.51	7.54	0.056	7.63
300	3.8	3	0.078	1.51	4.53	**Phase 3**	
200	5	3	0.105	1.48	4.42	0.091	4.48

For the Hohmann (300 km altitude) and half-Hohmann (200 km) manoeuvres in Phase 3, an average for the resultant delta-V and time requirements is made between the two cases. At 300 km, there is a 25 m radial position difference that needs to be cancelled - therefore, the orbit of one of the satellites needs to be raised from 300 km to 300.025 km. This will require around 0.014 m/s of delta-V and a time of 0.754 h. At 200 km, the elliptical orbit has a perigee 1 km lower than the circular radius, so 199 km. To recircularise, 0.296 m/s of delta-V is needed and a time of 0.737 h. Taking averages, it is estimated that for Phase 3 non-phase-shift manoeuvres, 0.155 m/s of delta-V and a time of 0.746 h is needed per manoeuvre.

To calculate the final delta-V requirement for formation maintenance manoeuvres, the delta-V per manoeuvre per phase and the number of manoeuvres per phase is needed. For Phase 2, the required delta-V is 0.056 m/s (phase shift) per manoeuvre. For Phase 3, this is $0.091 + 0.155 = 0.246$ m/s per manoeuvre. According to table 3.4, there are 85 formation maintenance manoeuvres in Phase 2, and 98 in Phase 3. This results in a total required delta-V of 28.93 m/s. However, all these manoeuvres need to be performed by only one of the satieties. Assuming that the role of orbit maintenance is alternated between the two, half of this value is taken for the budget, so 14.465 m/s.

8.2.3 Collision Avoidance Quantification between SCATTER Satellites

The SCATTER satellites will spend almost all the mission time flying in a formation, relatively close together. This results in a non-negligible collision risk between the satellites, in case one of them becomes non-operational or due to uncertainties in its attitude and/or orbital position knowledge. As explained in section 3.7.1, the simulated collision probability between the two satellites when one fails is $p = 4.9 \cdot 10^{-6}$ for one measurement cycle (science + power mode). During such a cycle, the satellites undertake an average of two orientation flips, one that has the effect of bringing them together, and one that makes them grow apart. As only the bringing-together flips is the critical case, then the above-mentioned collision probability is indeed per measurement cycle. The measurement cycles in Phase 1 of the mission are not taken into consideration, though, as during that phase no attitude flips occur. Therefore, there are $255 + 98 = 353$ cycles to be considered. This leads to a collision probability between the two satellites for the whole duration of the mission of $b_{mission} = 1 - (1 - p)^{353} = 1.728 \cdot 10^{-3}$.

If it is assumed that the rate of collision over time is a constant λ, the collision probability over a certain time can be written as $b = 1 - e^{-\lambda t}$, where t is the time over which the probability is calculated in years. λ can be calculated from the equation $b_{mission} = 1 - e^{-\lambda \cdot 2.3}$. Then, assuming a critical probability for collision avoidance manoeuvre of $b_{critical} = 10^{-4}$, the time between manoeuvres t_{man} can be calculating from the equation $b_{critical} = 1 - e^{-\lambda t_{man}}$ and is 0.133 years. This is equivalent to 7.52 manoeuvres per year, or a total of 17.3 manoeuvres.

A collision avoidance manoeuvre between the satellites consists of a Hohmann manoeuvre upwards or downwards, depending on which is the satellite doing the manoeuvre. The altitude change is assumed to be around 1 km,

the maximum radial position difference between the satellites during all science phases. Such a manoeuvre would require around 0.6 m/s of delta-V, and since it is desirable to return to the original orbit, this number is doubled. Therefore, in total 20.76 m/s of delta-V is needed for the mission for this type of collision avoidance. However, only one of the satellites needs to perform such a manoeuvre at a time, so the budget per satellite becomes 10.38 m/s.

8.2.4 Collision Avoidance Quantification from Other Space Objects

Due to the high amount of space objects in low-Earth orbit, a certain amount of delta-V needs to be reserved for collision avoidance manoeuvres. It is found that for a typical manoeuvre, between 0.03 and 0.1 m/s delta-V is needed [47][13]. Therefore, a conservative estimate of 0.1 m/s per manoeuvre is taken. Most debris is found at altitudes above 400 km [48], so the sizing will be mostly done with regard to Phase 1. A debris-avoidance manoeuvre would consist of a slight orbit-lowering manoeuvre. This would not significantly affect the measurements during Phase 1, as the altitude step is much higher (around 10 km). Therefore, another manoeuvre to return to the initial orbit is not needed. The satellites of the European Space Agency require normally more than one collision avoidance manoeuvre per satellite per year[1]. For further analysis, it is assumed that two collision avoidance manoeuvres are needed per year. However, this was the case in 2019, when the ESA estimate was published. As debris is expected to increase over time, this number needs to be corrected for this effect.

One source states that there were around 20 000 space objects larger than 10 cm in LEO, with the expected maximum in the period 2030 - 2040 to be around 24 000 objects [48]. It is assumed that collision avoidance manoeuvres need to be performed when the probability of collision exceeds 10^{-4}. If it is assumed that the collision probability of the satellite with one piece of debris is p, the collision probability with a population of $a_1 = 20\,000$ space objects is $1-(1-p)^{a_1}$. As it was assumed earlier that two manoeuvres are needed per year, it can be said that the collision probability with the a_1 population is 10^{-4} over 0.5 years. Therefore, if the probability p is defined over 0.5 years, the following equation can be written: $1-(1-p)^{a_1} = 10^{-4}$, from which p can be calculated to be around $5 \cdot 10^{-9}$. The collision probability of the $a_2 = 24\,000$ population can then be calculated as $b_1 = 1-(1-p)^{a_2} = 1.2 \cdot 10^{-4}$ over 6 months. If a constant rate of collision λ from the a_2 population over time is assumed, the collision probability over a certain time can be written as $b = 1-e^{-\lambda t}$, where t is the time over which the probability is calculated. Considering the b_1 probability over 0.5 years, the following equation can be written: $b_1 = 1-e^{-\lambda \cdot 0.5}$, from which λ can be calculated to be $2.4 \cdot 10^{-4}\,\text{year}^{-1}$. Finally, the time between collision avoidance manoeuvres can be calculated from the equation $b_2 = 1-e^{-\lambda t} = 10^{-4}$, ending up being $t = 0.417$ years, or having to do 2.4 collision avoidance manoeuvres per year.

However, the above-mentioned population does not take into account the launch of the so-called mega-constellations, that contain tens of thousands of satellites. Multiple companies like SpaceX and OneWeb [1] have such plans, which would drastically increase the number of objects in LEO by the 2030s. Another model for future space object population also does not take into account this drastic increase [49], making finding an accurate estimate difficult. Therefore, a contingency factor of 10 is taken on the number of manoeuvres per year, to take into account the increase in encounter probability. This raises the number of manoeuvres per year to 24. For a maximum expected mission lifetime of 2.3 years, this equates to around 55.2 manoeuvres. With a maximum of 0.1 m/s of delta-V required per manoeuvre, a final budget of 5.52 m/s per satellite is obtained. As it will be seen in the next subsection, the extra delta-V that will be added due to a 25% contingency margin is around 34 m/s, over six times as currently estimated for the collision avoidance with space objects. Therefore, this shows that there is plenty of margin in case the space object population increases.

8.2.5 SCATTER Delta-V Budget Results

Summing up all the sources of delta-V budget, a subtotal of 137 m/s is obtained. Taking a 25% contingency margin on top, a total of 171.24 m/s per satellite is obtained. Assuming a dry mass of the satellite of 16.62 kg and an I_{sp} of 220 s, 1.37 kg of fuel are needed. However, the tanks will be filled up to their maximum capacity of 1.6 kg, which in the end will provide a delta-V capability of 198.3 m/s.

8.3 Orbital Control Subsystem Overview

The OCS consists of two EPSS C2 propulsion units from Nanoavionics[2]. Their specifications are included in table 8.3. An image of one EPSS C2 unit is shown in figure 8.4. Multiple monopropellant propellant unit options were considered, and this was chosen as it has the biggest datasheet, and it also satisfies the requirements. Furthermore, having two units instead of one helps with the integration of the spacecraft, as these can be put on a diagonal, and still allow other components to be placed next to them. In contrast, having put a single propulsion unit on the centre would have effectively made the surrounding space unusable for standard COTS.

[1] https://www.esa.int/Safety_Security/Space_Debris/Automating_collision_avoidance

[2] https://satsearch.co/products/nanoavionics-propulsion-system-epss-c2

Table 8.3: Specifications of EPSS C2 propulsion unit.

Parameter	Value	Parameter	Value
Envelope size	100 × 100 × 200 mm^3	Thrust at BOL	1 N
Propulsion type	Monopropellant	Thrust at EOL	0.25 N
Propellant	ADN blend (LMP-103S)	Propellant mass flow at BOL	0.5 g/s
Dry mass	1.8 kg	Propellant mass flow at EOL	0.12 g/s
Wet mass	2.6 kg	Average specific impulse	220 s
Propellant mass	0.8 kg	Maximum total impulse	>1700 Ns
Data interface	CAN / UART / RS422	Operating temperature	10 °C to 40 °C
Heater & valve operating voltage	12 V	Survival temperature	−30 °C to 60 °C
Telemetry Logic Voltage	3.3 V	Idle power consumption (telemetry)	0.3 W
Tank pressurisation type	Blow-down	Catalytic bead heater power	2 W to 8 W
BOL pressure	25.0 bar(a)	Propellant tank heater power	<12.7 W
EOL pressure	5.5 bar(a)	Maximum peak power	<21 W
No. of thrusters	1	Radiation tolerance of electronics (unshielded)	20 kRad

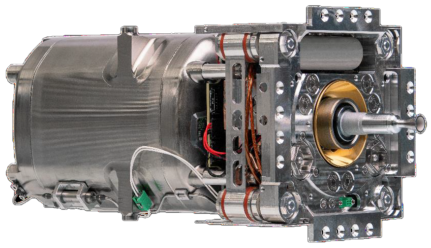

Figure 8.4: The EPSS C2 monopropellant propulsion unit[3].

8.3.1 Orbital Control Subsystem Thrust Plume Analysis

Due to the placement of the solar arrays also behind the spacecraft, the effect of the thrust plume needs to be analysed, such that no significant damage is done to the solar panels. The datasheet of the EPSS C2 unit provides a map of the thrust plume density and temperature as a function of polar coordinates from the centreline of the exit of the nozzle. The graphs are included in figure 8.5a and figure 8.5b.

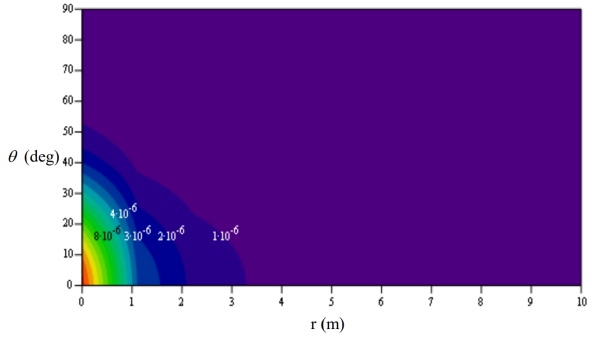

(a) 1 N HPGP thruster exhaust plume density field [kg/m^3] in polar coordinates. Reproduced from the EPSS C2 datasheet [4].

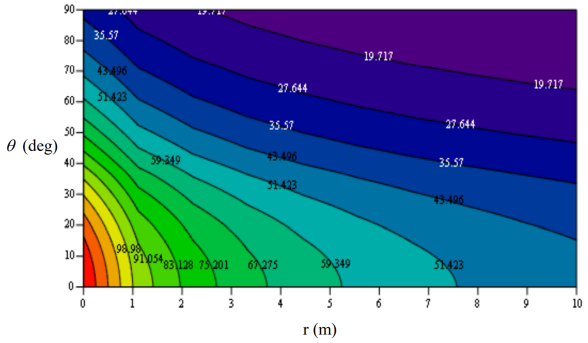

(b) 1 N HPGP thruster exhaust plume temperature field [K] in polar coordinates. Reproduced from the EPSS C2 datasheet [4].

The most critical case is the one shown in red in figure 8.6. This is the point where the panel is hit at the shallowest angle by the exhaust plume. At higher angles, the plume characteristics decrease drastically. The polar coordinates of this most significant point have been calculated to be 375.44 mm and 28.432° from the centreline of the exhaust nozzle. Using this position and the maps included above, the following plume parameters can be estimated at the point of contact: density is between $5 \cdot 10^{-6}$ and $6 \cdot 10^{-6}$ kg/m^3 and temperature is around 100 K. The value of the temperature is well below the maximum operational value of the solar panel, and thus does not affect the analysis.

In order to calculate the pressure that is exerted on the solar panels, the velocity of the exhaust plume is needed. This can be calculated using equation 8.3. Here v_e is the exhaust velocity, T is the thrust force, A_e is the exhaust area at the exit of the nozzle, p_e is the exit pressure and $\dot{m}$ is the mass flow of the propellant.

[3] https://satsearch.co/products/nanoavionics-propulsion-system-epss-c2
[4] https://satsearch.co/products/nanoavionics-propulsion-system-epss-c2

$$v_e = \frac{T - A_e p_e}{\dot{m}} \tag{8.3}$$

The most extreme case is assumed for a conservative estimate, which consists of a thrust force of 1 N and mass flow of 0.5 g/s, which were also used when generating the temperature and density fields of the plumes. The exit area of the nozzle was calculated from the technical drawing in the datasheet, and a value of 63.617 mm^2 was obtained. To calculate the exit pressure, the chamber pressure p_c and the chamber-to-exit pressure ration p_e/p_c are needed. The chamber pressure is assumed to be the value used also for the plume maps, i.e. $p_c = 15$ bar. Furthermore, the expansion ratio of the nozzle is known to be $\varepsilon = 100{:}1$[5]. In the datasheet, it is mentioned that the specific heat ratio is $\gamma = 1.23$. Lastly, using equation 8.4 and equation 8.5, the needed p_e/p_c ratio can be obtained through root finding. Using this method, it was obtained that $p_e/p_c = 0.00057064$, which leads to $p_e = 855.963$ Pa. Having now all the needed parameters for the exhaust velocity, it is calculated to be $v_e = 1891.1$ m/s.

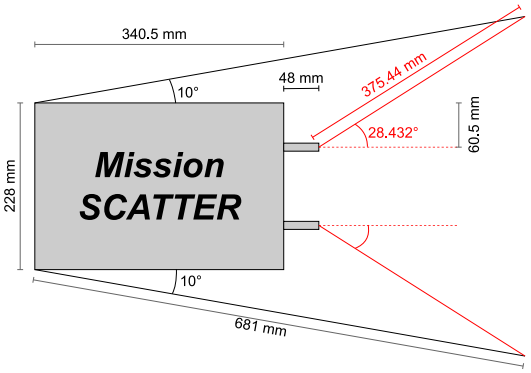

Figure 8.6: Diagram showing the geometry of the satellite (side view) used to calculate the distance and angle of the exhaust plume. The most significant direction is shown in red, alongside its length and angle, used to calculate the plume parameters from the maps included before.

The pressure that is exerted on the panel by the plume can now be calculated using equation 8.6, where p_{sp} is the pressure applied on the end of the solar panel, p is the momentum of the incoming plume, A is the reference solar panel area, m is the control mass of the plume, V is the velocity of the incoming plume, assumed to remain constant to the same value as v_e, ρ is the plume density and $i = 18.432°$ is the incidence angle of the plume on the solar panel. This formula was derived assuming a fully specular deflection, which is a conservative estimate, as it is the maximum value the pressure can attain. Using the values derived before, a maximum pressure of $p_{sp} = 13.569$ Pa.

$$\varepsilon = \frac{\Gamma(\gamma)}{\sqrt{\frac{2\gamma}{\gamma-1} \cdot \left(\frac{p_e}{p_c}\right)^{2/\gamma} \cdot \left[1 - \left(\frac{p_e}{p_c}\right)^{\frac{\gamma-1}{\gamma}}\right]}} \tag{8.4}$$

$$\Gamma(\gamma) = \sqrt{\gamma \cdot \left(\frac{1+\gamma}{2}\right)^{\frac{1+\gamma}{1-\gamma}}} \tag{8.5}$$

$$p_{sp} = \frac{\Delta p}{A \cdot dt} = \frac{2mV \sin i}{A \cdot dt} = 2\rho V^2 \sin i \tag{8.6}$$

The moment that will be exerted on the solar panels can now be calculated. For the long solar array, only the panel that is further back will be affected by the plume. Taking a very conservative assumption of having the maximum pressure applied over the whole area of this solar panel, a force of $F_{plume} = p_{sp} \cdot A_{sp} = 13.569 \cdot 0.3405 \cdot 0.288 = 1.053$ N is exerted. Taking again a very conservative assumption that the application point of the force is at the most back point on the solar array, a maximum moment of $M = F_{plume} \cdot l_{2sp} = 1.053 \cdot 2 \cdot 0.3405 = 0.717$ Nm appears at the front of the solar array. This moment is also transmitted to the front deployable hinge mechanism, which needs to sustain it. However, as not enough information is available on the hinge mechanics, which will most probably be custom-made, it needs to be further analysed in a future design iteration.

To calculate the maximum axial stress that appears in the solar array, the thickness and the second moment of area of the panel is needed. The thickness of the backplate is $t = 1.6$ mm and thus the second moment of area is $I = \frac{1}{12} \cdot 0.228 \cdot 0.0016^3 = 7.7824 \cdot 10^{-11}$ m^4. The maximum axial stress experienced by the backplate is therefore $\sigma = \frac{Mt}{2I} = 7.37$ MPa. As the yield strength of the backplate material (FR-4) is between 65 and 70 MPa[6], it can be seen that the maximum stress that can appear is almost 10 times lower than the yield limit; therefore, the solar array is considered to not be affected mechanically by the thrust plume in a critical way.

According to the datasheet, the thrust plume contains 50% H_2O, 23% N_2, 16% H_2, 6% CO and 5% CO_2 as volume fractions. As N_2 and CO_2 are usually inert gasses, they are not expected to affect the solar panels significantly. The solar panel material is FR-4, which is flame retardant and also has a very low water absorption; therefore, H_2O will also not pose a significant threat to the solar arrays. However, more analysis is recommended to be done regarding the chemical influence of the thrust plume, especially for the reactive H_2 and CO compounds.

[5] https://www.ecaps.space/products-1n.php

[6] https://www.google.com/url?sa=t&rct=j&q=&esrc=s&source=web&cd=&ved=2ahUKEwja1anukKr4AhXJm_OHHRHvD64QFnoECAYQAQ&url=https%3A%2F%2Fpdf4pro.com%2Fcdn%2Fg-10-fr-4-g-11-glass-epoxy-dielectric-corp-4d23a7.pdf&usg=AOvVaw1VZYl4wDnf-AZDUOF9ypmb

8.3.2 Orbital Control Subsystem Power Analysis

The power numbers in table 8.3 were estimated from the data available in the EPSS C2 datasheet. The idle and peak power numbers are referenced directly, the catalytic bed power is assumed to be the same as the engine firing power usage (and conservatively assumed to be 8 W for further analysis), and thus the maximum power that can go to the propellant tank heaters is $21 - 0.3 - 0.8 = 12.7$ W.

In order to size the energy needs of the OCS system, the case in which the most power is used: longest burn time (during Hohmann transfers in Phase 1), when the satellite is in a noon-midnight polar orbit. The longest (total) burn time for a Hohmann transfer in Phase 1 is 94.2 s, as explained in section 8.2. During the noon-midnight polar orbit, the propellant tank gets to a temperature as low as $-20\,^{\circ}$C according to figure 7.3 and needs to be heated up to the minimum operational temperature of $10\,^{\circ}$C.

Furthermore, the catalytic bed needs to be heated up for 30 minutes before firing. Therefore, the catalytic bed needs to be turned on for the duration of the burn and 30 minutes beforehand; the required energy is $8 \cdot (94.2 \cdot 1.2 + 30 \cdot 60) = 15\,304.32$ J per propulsion unit, where a 20% margin was applied to the burn time.

To calculate the required heat to heat up the propellant tank, the specific heat of the propellant is needed. For this, the composition of the LMP-103S from [50] is used, alongside the specific heats of all components. These are included in table 8.4, as well as the final specific heat of the propellant. The mass of the propellant per tank is 0.8 kg, as mentioned in table 8.3.

Table 8.4: Composition of the LMP-103S propellant and the specific heats of itself and its constituents. The fractions are taken from [50].

Component	ADN	Water	Methanol	Ammonia	Total
Fraction	0.63	0.14	0.184	0.046	1.0
Specific heat [J/kg·K]	1770[7]	4187[8]	2530[9]	4744[10]	2385.02

The last values needed to calculate the required heat are the mass and the specific heat of the tank. As these values are not available from the manufacturer, estimates will be used. The material of the tank is assumed to be the aluminium alloy AL7075-T6, a material often used in the aerospace industry. Its specific heat is 946 J/kgK [51]. To estimate the mass of the tank, a sizing method from [12] is used. First, the size of the tank was estimated from the technical drawing in the datasheet: a cylinder with the length of 240.52 mm and radius of 57.5 mm. This resulted in a tank volume of approximatively 2.5 L. Using a statistical formula from [12] for diaphragm propellant tanks, a tank mass of approximatively 0.59 kg was obtained.

The total energy needed to heat up the propellant tank could then be computed as the sum of the products of mass, specific heat and change in temperature for both the propellant and the tank itself. The temperature needs to be increased from -20 to $10\,^{\circ}$C, so for a range of 30 K. Using the previously computed values, the total required propellant tank heat is $0.8 \cdot 2385.02 \cdot 30 + 0.59 \cdot 946 \cdot 30 \approx 73\,980$ J. A 5% margin is applied to take into account other minor components, which bring the estimate to 77 678.75 J.

This leads to the total energy needed by the propulsion system for a Hohmann transfer in Phase 1, which is $15304.32 + 77678.75 = 92\,983.07$ J per unit, or 185 966.14 J for the whole subsystem. Due to how EPS calculates the needed peak power for sizing the batteries, this value needs to be normalised to the assumed burn time (113.04 s including margin), leading to a value of 1645.1 W equivalent peak power. To be noted that this value is to be used by EPS only for battery capacity sizing purposes, as the actual peak power of the propulsion subsystem will never exceed $21 \cdot 2 = 42$ W, as stated in the datasheet.

8.3.3 Orbital Control Subsystem Cost Analysis

The price of one EPSS C2 is around €230 000[11] without including fuelling and integration costs. The LMP-103S was not found for purchase online, so the pricing for a comparative green monopropellant fuel (AF-M315E) is used. For a package of 10 lb or 4.54 kg, the price is \$5925 or €5601.25 at the conversion rate of 13$^{\text{th}}$ of June 2022. Therefore, to fill up one EPSS C2 tank with 0.8 kg of propellant, it would cost around €987. This results in a subtotal of €230 987 per unit. Taking a 25% margin for integration and handling, a total of €288 733.75 per unit is obtained, or €577 467.5 per satellite.

8.3.4 Minimum Total Impulse Burst Analysis

In order to satisfy the minimum total impulse burst requirement REQ-OCS-05, an analysis on the smallest required delta-V burn is needed. Currently, the shortest burn is required for one of the two Hohmann transfer burns for the beginning of Phase 3 (at 300 km altitude), which requires $0.0145/2 = 0.007\,25$ m/s delta-V. For a conservative estimate, the propellant usage will be calculated at the end of life of the propulsion system, when after the burn

[7] https://www.sciencedirect.com/science/article/pii/S2214914718300187

[8] https://www.engineeringtoolbox.com/water-thermal-properties-d_162.html

[9] https://www.engineeringtoolbox.com/methanol-methyl-alcohol-properties-CH3OH-d_2031.html

[10] https://www.engineeringtoolbox.com/ammonia-d_1413.html

[11] Armando Rojas, email message to Andrei Pârvulescu, 30th of May 2022

the mass of the satellite will just be its dry mass $m_{dry} = 16.7\,\text{kg}$. Such a burn would require 0.056 g of propellant. The mass flow at BOL is 0.12 g/s per propulsion unit, or 0.24 g/s per satellite. This results in a burn time of 0.233 s, The thrust at that point would 0.25 N per thruster, or 0.5 N in total. This results in a minimum total impulse burst of 0.1166 Ns per satellite, or 58.3 mNs per engine.

8.3.5 Orbital Control Subsystem Sensitivity Analysis

For the sensitivity analysis of the OCS, the influence of I_{sp} on needed fuel and of the number of revolutions spent in the transfer orbit of the phase shift in Phase 3 on the delta-V and time budgets is analysed. In figure 8.7, the first item is visualised. As it can be seen, the I_{sp} can decrease to as low as 190 s and still have enough propellant. For the second item, the visualisation is in figure 8.8. The delta-V requirement decreases drastically until 3 revolutions, after which the effect is not that high, mostly getting time penalty. Therefore, 3 revolutions are proved to be the optimal number for that particular manoeuvre. These two items are considered to be the most important parameters to be varied at the moment. It is recommended though to do other sensitivity analysis also for other parameters, such as the influence of changing the thrust level, the altitude step in phase 1, the number of measurements done between consecutive burns in Phases 2 and 3 etc.

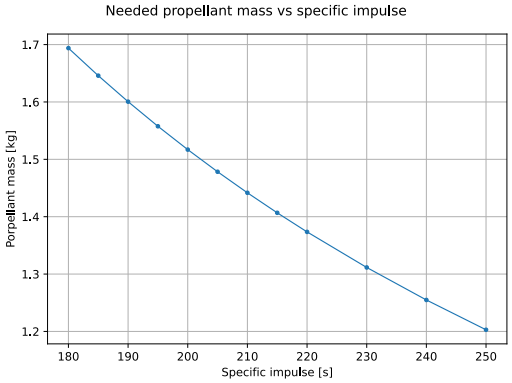

Figure 8.7: Plot of the needed propellant graphs as a function of the specific impulse.

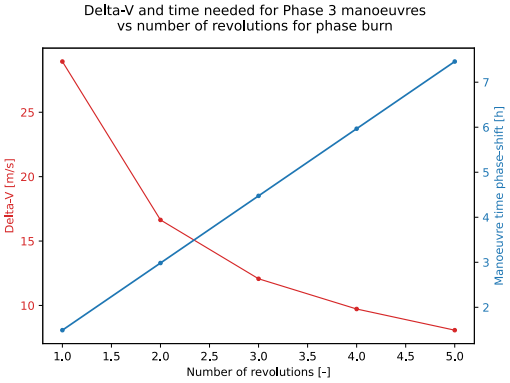

Figure 8.8: Plot of the delta-V required for Phase 3 burns and of the phase shift manoeuvre in Phase 3, as a function of the number of revolutions spent in the transfer orbit of the phase shift.

8.4 Orbit Control Subsystem Requirements Verification

The verification of the Orbit Control Subsystem by compliance with requirements is given below:

REQ-OCS-01: - this requirement is verified through the analysis of the thermal response of the engine propulsion unit. The thermal simulation as shown in figure 7.3 has already been made for at least 3 m/s of continuous burn, and the temperature remains within the operational range of the EPSS C2. Therefore, the requirement is considered satisfied.

REQ-OCS-02: - this requirement is verified through inspection of the EPSS C2 engine [12], which has 1500 start-stop sequences, as shown in table 8.3;

REQ-OCS-03: - this requirement is verified through analysis performed in figure 3.5, which yields 0.83 kg of fuel used for such a manoeuvre. As the OCS has 1.6 kg of fuel, this requirement is satisfied;

REQ-OCS-04: - this requirement is verified through the analysis performed in section 8.3.4, which yields a minimum total impulse burst of 58.3 mNs. Thus, the requirement is satisfied;

REQ-OCS-05: - this requirement is verified through inspection of the CoM of SCATTER, which is given in chapter 13. The offset computed is 0.23 mm, which satisfies the requirement;

REQ-OCS-06: - this requirement is verified through an analysis performed in section 8.3.1, which yields a maximum stress applied on the panels of 7.37 MPa, which is 8 times lower than the yield strength of their material. Therefore, the requirement is satisfied;

REQ-OCS-12: - this requirement is verified through analysis of the ΔV budget which is performed in section 8.2, which yields 1.37 kg of needed fuel, that is less than the available 1.6 kg available. Therefore, the requirement is satisfied;

8.4.1 OCS Concluding Remarks

Based on the results of this chapter, it is concluded that the propulsion subsystem can be integrated into the spacecraft, while satisfying all requirements. It is recommended to perform more detailed analysis and simulations

[12] https://satsearch.co/products/nanoavionics-propulsion-system-epss-c2

for the delta-V budgets, as well as thermal simulations, due to the sensitivity of the system to its operational temperature range. The number of collision avoidance with debris should be updated throughout the whole design process with as up-to-date as possible space object population numbers, as these will certainly increase significantly until launch. As these will increase, so will the delta-V budget; however, the closer to a finished design, the smaller the margin that will be needed, thus the overall being expected to remain at a constant level.

Furthermore, it is recommended to also perform more sensitivity analyses, to capture the influence of changing multiple parameters of the mission or of the OCS. Lastly, the thrust plume shall be investigated using an in-house built simulation, for better parameter control. On top of that, the chemical effect of the plume should be investigated, especially that of the more reactive components, that could degrade the solar panels.

9. Attitude Determination & Control Subsystem

This chapter focuses on the detailed design of the satellite Attitude Determination and Control Subsystem (ADCS). Section 9.1 first shows the subsystem requirements for ADCS. This is followed by the overview of the ADCS design, which is explained in section 9.2. The control characteristics of the subsystem will be displayed in section 9.3. Thereafter, section 9.4 gives a list of simulation results representing the operation of ADCS. The sensitivity analysis is also performed in this section. The model used for simulation will then be verified and validated in section 9.5. Finally, the requirements compliance check as well as the concluding remarks will be presented in section 9.6.

9.1 ADCS Subsystem Requirements

Table 9.1: Subsystem requirements.

ID	Description	Parent Requirement	Rationale
REQ-ADC-01	The ADCS shall finish de-tumbling within 2 days after separation	REQ-SYS-F-08	De-tumbling needs to be done within a time range to minimize energy consumption and thus limit battery size. The time is derived from the satellite with similar mission objective[52]
REQ-ADC-02	The ADCS shall be able to orient the space element with a magnitude of at least 90° along the x-axis with respect to the body axis frame, within a time of 180 seconds	REQ-SYS-P-09	Same as the parent requirement
REQ-ADC-03	The ADCS shall be able to orient the space element with a magnitude of at least 90° along the y-axis with respect to the body axis frame, within a time of 180 seconds	REQ-SYS-P-22	Same as the parent requirement
REQ-ADC-04	The ADCS shall be able to orient the space element with a magnitude of at least 90° along the z-axis with respect to the body axis frame, within a time of 180 seconds	REQ-SYS-P-23	Same as the parent requirement
REQ-ADC-05	The ADCS shall be able to maintain the attitude of the space element in the x-axis with respect to the body axis frame with an accuracy of at least 5° for the duration of at least one orbital revolution	REQ-SYS-P-08	Same as the parent requirement
REQ-ADC-06	The ADCS shall be able to maintain the attitude of the space element in the y-axis with respect to the body axis frame with an accuracy of at least 5° for the duration of at least one orbital revolution	REQ-SYS-P-20	Same as the parent requirement
REQ-ADC-07	The ADCS shall be able to maintain the attitude of the space element in the z-axis with respect to the body axis frame with an accuracy of at least 5° for the duration of at least one orbital revolution	REQ-SYS-P-21	Same as the parent requirement
REQ-ADC-08	The satellites shall carry an attitude sensor with an average accuracy of 1° for the inertial attitude.	REQ-U-16	Same as the parent requirement
REQ-ADC-09	The ADCS shall provide a maximum torque of at least 0.000 081 Nm	REQ-SYS-F-21	Derived based on the torque needed to rotate the satellite 90° around z-aixs in 180 seconds $T = \frac{4I_{zz}\cdot\theta}{s^2} = 0.000054Nm$ and the margin factor 1.5
REQ-ADC-10	The reaction wheels shall have a maximum momentum storage of at least 0.014 Nms	REQ-SYS-F-21	Derived based on the momentum needed to counteract periodical external disturbances $h = \frac{T_D P}{4\sqrt{2}}$ and the margin factor, where worst-case disturbance T_D is derived based on an estimation of aerodynamic drag disturbance in chapter 4

9.2 ADCS Design Overview

The design of the ADCS consists of two parts: attitude determination sensors and attitude control actuators. This section will discuss the detailed design of these two groups of components, including the types, numbers and positions of the selected sensors and actuators as well as the properties of each product.

Firstly, attitude control actuators are of two types: external and internal. External control actuators including thrusters and magnetorquers are mandatory for attitude control and the de-saturation of reaction wheel momentum. Due to the fact that requirement REQ-U-15 does not allow the use of thrusters, a magnetorquer board containing three magnetorquers to achieve control in three directions was chosen. However, the control results of the magnetorquers can be affected by magnetic field strength significantly, and therefore may not reach the accuracy required to perform scientific measurement [53]. In order to perform fine attitude control four reaction wheels, with one for redundancy, were chosen.

For the attitude determination sensors, two magnetometers with one for redundancy were selected. They can measure the magnetic field strength, while magnetorquers are used as attitude control actuators [54]. Moreover, Sun sensors were also applied for more accurate attitude determination, since the use of star sensors is discarded for the high power consumption and the larger volume which increases the difficulty of integration and deployment[53]. Table 9.2 gives the key properties of the selected magnetorquer board, which combines two torque rods and one air coil torquer and has flight heritage since 2013. Table 9.3 displays the properties of reaction wheels chosen from ROCKETLAB. They are widely used in the University of Toronto SpaceFlight Lab's GNB series of spacecraft[1]. Finally, table 9.4 introduces the key parameters of the selected Sun sensors and magnetometers. FSS100 is a kind of Sun sensors designed by TensorTech with a small size and a design lifetime of 3 years[2]. NSS-411, which has been used on a number of constellations with a total of over 100 delivered, is another type of Sun sensor chosen with a larger volume but can provide more accurate determination results. Finally, the used magnetometers which

[1] https://www.utias-sfl.net/,retrievedon14-06-2022

[2] https://tensortech.com.tw/sun-sensor/,retrievedon14-06-2022

have flight heritage since 2014 are shown. Calibrations can be performed for further increase of the accuracy of the magnetometers.

In addition to that, ADCS is also responsible for measuring the angular velocity of the satellite by the gyroscopes. Since there were two IMUs chosen as the payload and can be provided enough power by EPS, additional gyroscopes will not be necessary. ADCS can use the gyroscopes in the IMUs to determine the angular velocity of the satellite. The properties of the selected IMUs are considered in payload design, which will be discussed in chapter 11.

Table 9.2: Selected magnetorquer properties.

Product	Mass [kg]	Power Consumption [W]	Cost [€]	Nominal Dipole Moment [Am^2]	Temperature Range [°C]
ISIS iMTQ[3]	0.196	0.175	9750	0.2	−40 to 70

Table 9.3: Selected reaction wheels properties.

Product	Mass [kg]	Power Consumption [W]	Cost [€]	Torque [Nm]	Momentum storage [Nms]	Temperature Range [°C]
RL-RW-0.03[4]	0.185	0.1 to 1.8	25671	0.002	0.004	−40 to 70

Table 9.4: Selected sensors properties.

Product	Mass [kg]	Power Consumption [W]	Cost [€]	Accuracy	Temperature Range [°C]
FSS100[5]	0.004	0.001 65 to 0.0066	9523	0.5°	−20 to 60
NFSS-411[6]	0.035	0.015 to 0.15	11429	0.1°	−25 to 70
NSS Magnetometer[7]	0.085	0.75	14285	16 nT	−25 to 70

The numbers and positions of each type of sensor and actuator are illustrated in figure 9.1. For simplification, four reaction wheels were integrated as a configuration such that three of them have rotational axes aligned with the satellite's rotational axes. One magnetorquer board and two magnetometers should be put separately to prevent their magnetic field from affecting each other. However, due to the fact that one of the magnetometers is always turned off, it is still reasonable to put two magnetometers together.

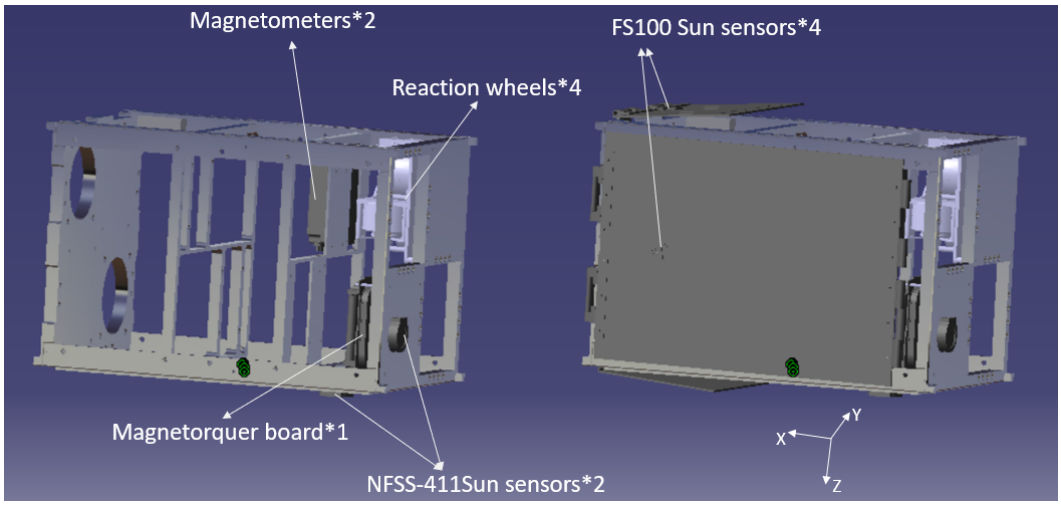

Figure 9.1: ADCS components integration positions.

Theoretically, six Sun sensors should be mounted on six surfaces of the satellite to ensure sufficient field of view. However, due to the requirements REQ-PL-04 and REQ-PL-14 which are explained in more detail in chapter 11, Sun sensors can not be mounted on the satellite surfaces with GNSS and mass spectrometer to ensure their proper functioning. Moreover, the two mainADCS solar arrays fully cover two satellite surfaces, making them impossible to be assembled with Sun sensors. Therefore, for six satellite surfaces, only two of them can be mounted with Sun sensors, which leads to a very limited field of view. However, four additional solar panel mounted Sun sensors can

[3] https://www.isispace.nl/product/isis-magnetorquer-board/,retrievedon14-06-2022
[4] https://www.rocketlabusa.com/space-systems/satellite-components/reaction-wheels/,retrievedon14-06-2022
[5] https://tensortech.com.tw/sun-sensor/,retrievedon14-06-2022
[6] https://www.cubesatshop.com/product/digital-fine-sun-sensor/,retrievedon14-06-2022
[7] https://www.cubesatshop.com/product/nss-magnetometer/,retrievedon14-06-2022

be selected to widen the field of view. Finally, the design of Sun sensors ends up with four solar panel mounted Sun sensors (FSS100) and two satellite surface mounted Sun sensors (NFSS-41).

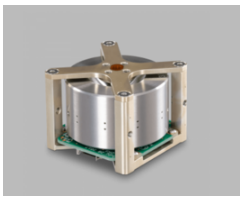

(a) RL-RW-0.03 reaction wheels.

(b) ISIS iMTQ magnetorquer board.

(c) NSS magnetometer.

(d) FSS100 Sun sensor.

(e) NFSS-411 Sun sensor.

Figure 9.2: Selected ADCS components.

9.3 SCATTER Stability and Control Characteristics

As discussed in section 9.2, the origin of actuator torque varies in different modes. More specifically, magnetorquers can provide a coarse attitude control result with the B-dot algorithm which is mainly used in the de-tumbling mode. Meanwhile, reaction wheels are responsible for controlling the attitude more accurately with a PD controller during science mode.

The operation procedure of ADCS can be seen in figure 9.3. The sensors measure the absolute and relative attitudes which are influenced by the external environment. The measurements with noise will be sent to C&DH for further filtering. It was decided to use an Extended Kalman Filter (EKF) to reduce the effect of measurement noise[55]. C&DH will then give the commanded value of torque to the actuators based on either B-dot control or PD control. Finally, the actuators provide actuator torque to control the attitude of the satellite.

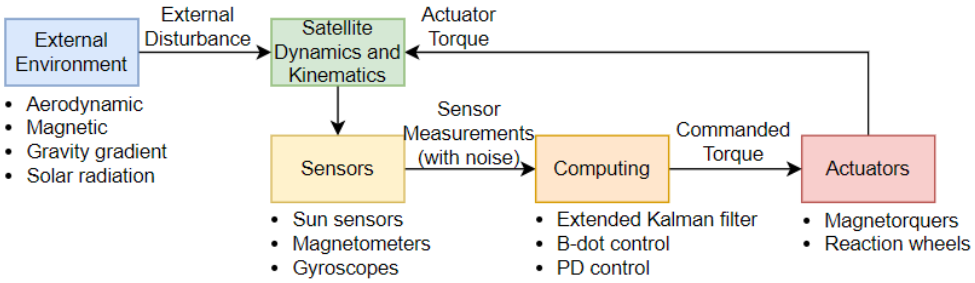

Figure 9.3: ADCS operation scheme.

B-dot control and PD control can be expanded in more detail, as shown in figure 9.4 and figure 9.5. For B-dot control, the angular velocity measured by IMUs and magnetic field measured by magnetometers are considered as input. After implementing EKF on the raw measurement data, the commanded dipole moment can be derived based on the pre-designed B-dot control gain. However, as discussed in section 9.2, the selected magnetorquer board can only provide a maximum of $0.2\,\mathrm{Am}^2$ dipole moment, which will limit the output magnetorquer torque. Moreover, the output magnetorquer torque is highly dependent on the actual magnetic field, which differs in orbit altitude and inclination. For the PD control, the situation is more complex. The Euler angle generated from magnetic field measured by magnetometers and/or Sun vector measured by Sun sensors will firstly have to be transformed to quaternion form, which aims to prevent singularity formation at large Euler angles[56]. Then through EKF, the quaternion error can be computed by comparing the desired attitude and filtered attitude. PD Control gain is designed to generate the commanded reaction wheel torque based on the given quaternion error. However, the actual torque generated by the reaction wheels is limited by the maximum torque and maximum momentum storage of the selected product.

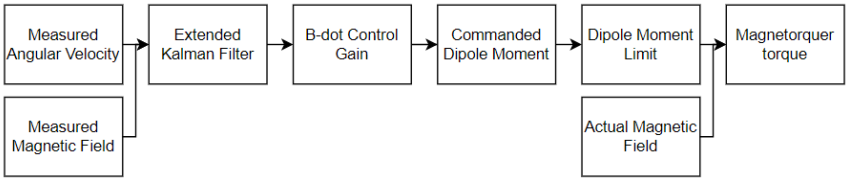

Figure 9.4: ADCS B-dot control scheme.

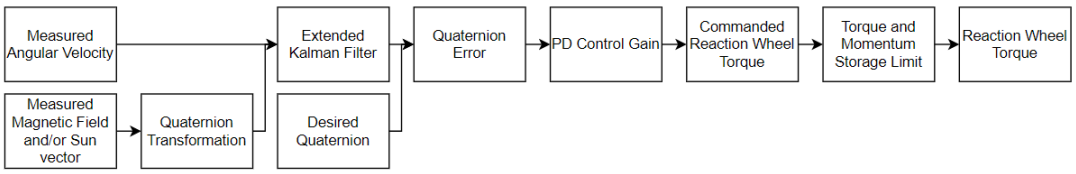

Figure 9.5: ADCS PD control scheme.

One aspect that is a point of interest is the de-saturation of the reaction wheels. Reaction wheels cannot decrease their angular velocity by themselves since that will transfer the momentum to the spacecraft and thus change the attitude of the spacecraft. Instead, an external torque should be applied to help de-saturate the reaction wheels [57]. This is done by a magnetorquer board integrated in SCATTER, since no use of thrusters is allowed.

9.4 ADCS Performance Analysis

This section aims to evaluate the performance of the designed ADCS based on an in-house simulation tool built following [56]. Due to the high viability of ADCS testing on the ground, SIMULINK was chosen as the platform of the ADCS simulation because it can be connected with external products easily. Section 9.4.1 first describes the model used for simulation. Then, the de-tumbling, satellite rotation manoeuvre and attitude determination and control accuracy will be simulated with the results shown in section 9.4.2, section 9.4.3, and section 9.4.4 separately. Finally, the sensitivity analysis will be performed in section 9.4.5.

9.4.1 Model Description

The SIMULINK tool is built using figure 9.6. Firstly, SCATTER's designed Kepler orbit parameters will be addressed as the inputs of the whole simulation procedure. Based on the J2 propagation model and Julian date model, the satellite external environment can be simulated including solar radiation, magnetic field, gravity gradient and aerodynamic forces. These are done in figure 9.7. Afterwards, the spacecraft dynamics and kinetics model will be simulated. The transformation between the quaternion vectors, the Direction Cosine Matrix (DCM) and the Euler angles will also be performed. Finally, the B-dot and PD controller will be simulated in the following figure 9.9 and figure 9.10. The sensor measurement errors are modeled based on the accuracy given in section 9.2 or measurement noise matrix which was addressed in [56]. The SIMULINK installed EKF block is used to simulate the filter process of the sensor measurements with given state functions and measurement functions. The equations used in the simulation tool are based on [56].

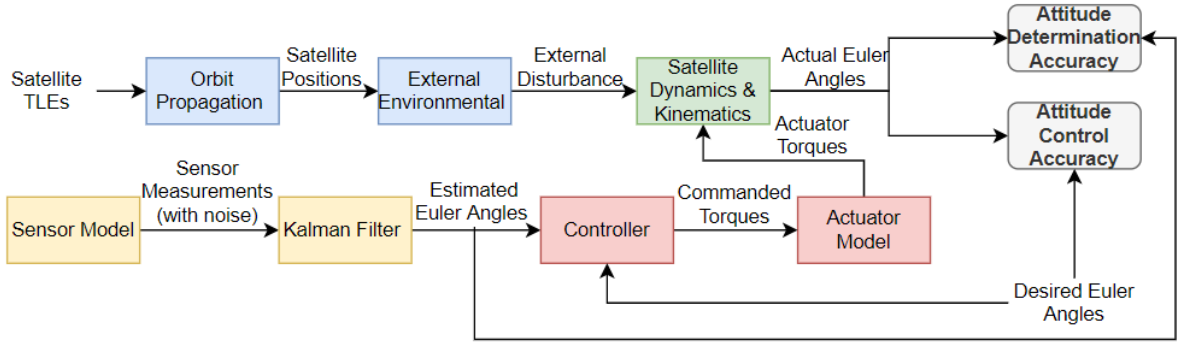

Figure 9.6: SIMULINK tool building scheme.

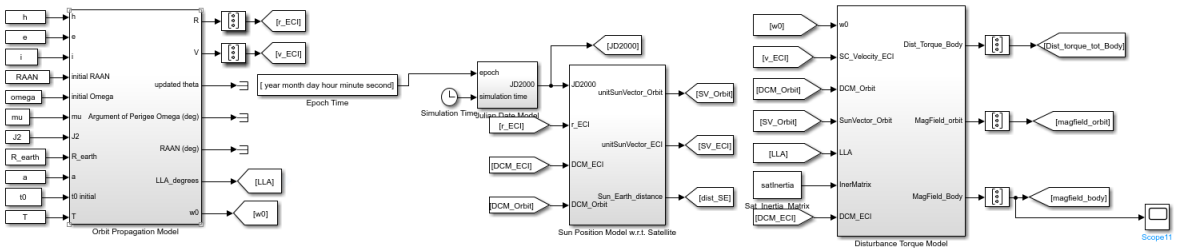

Figure 9.7: Satellite external environment SIMULINK model.

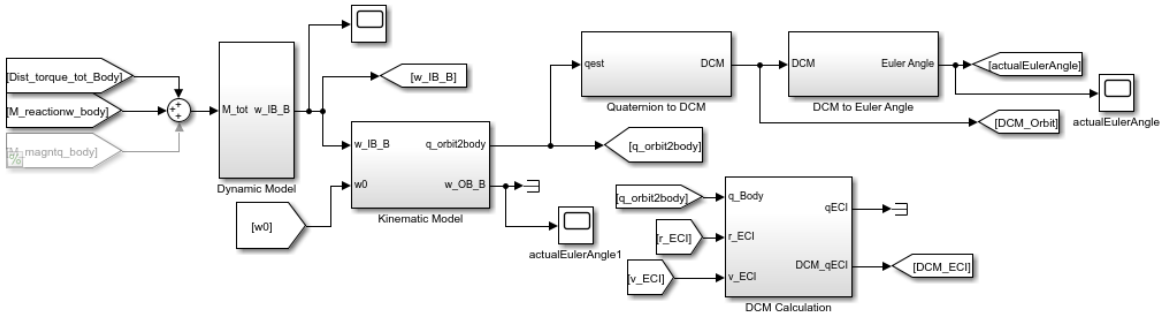

Figure 9.8: Satellite dynamics and kinetics SIMULINK model.

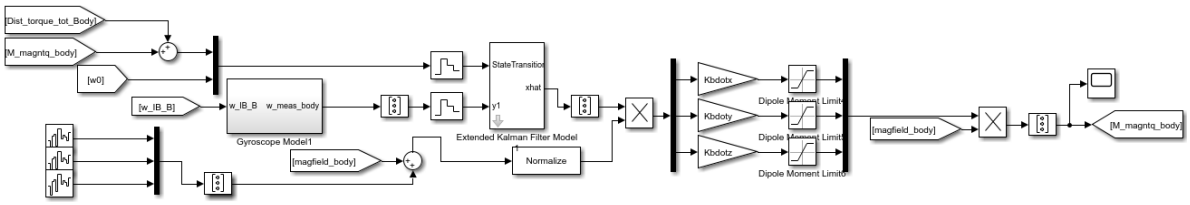

Figure 9.9: Satellite B-dot control SIMULINK model.

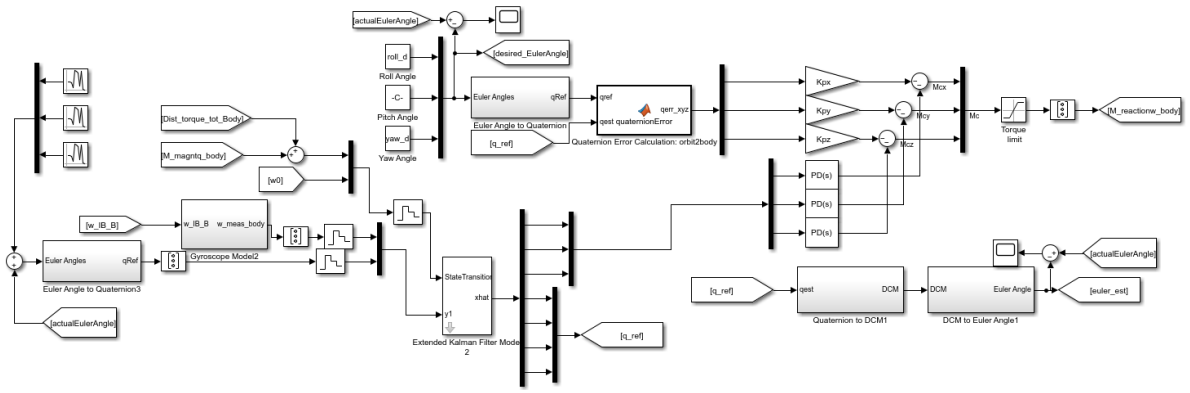

Figure 9.10: Satellite PD control SIMULINK model.

9.4.2 De-tumbling Simulation Result

Firstly, a simulation of the de-tumbling phase will be performed with the key initial parameters shown in the following table 9.5. Here, it is assumed that the body frame of the satellite is aligned with the orbital frame at the initial state. Also, the angular velocity here refers to the angular velocity of the orbital frame with respect to the body frame and the value was taken from the selected launch vehicle properties [18]. The simulation results are shown in figure 9.11. It can be found that with the pre-designed gain, the ADCS can decrease the angular velocity of the spacecraft down to 0.01 rad/s in 6 hours (including a 1.5 margin factor) with the influence of the magnetometer and gyroscope noise being considered and filtered by EKF.

Table 9.5: Key parameters used to perform de-tumbling simulation.

Initial angular velocity [rad/s]	Gain	Sampling frequency [Hz]
[0.08727; 0.08727; 0.08727]	$[I_{ss}e^4; I_{yy}e^3; I_{zz}e^4]$	1

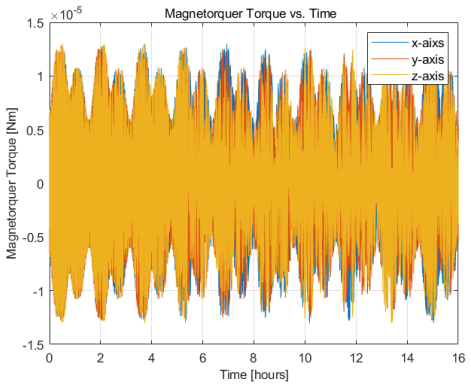

(a) Magnetorquer torque generated in body frame.

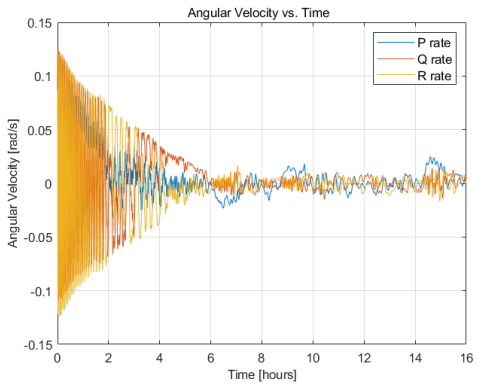

(b) Angular velocity variation with time.

Figure 9.11: Simulation results for B-dot de-tumbling.

9.4.3 Rotation Simulation Result

Another key requirement for ADCS is that the subsystem shall rotate the satellite with a magnitude of 90° in 180 seconds.. Through the SIMULINK tool described above and using the key simulation parameters presented in table 9.6, the simulation result is obtained and shown in figure 9.12. The rotation results depend heavily on the gain chosen. However, even though significant overshoot and oscillation can be found in the given rotation simulation result, it can still reach a relatively stable state in around 100 seconds with the effect of sensor errors and Extended Kalman Filter.

Table 9.6: Key parameters used to perform accuracy simulation.

Gain	Sampling frequency [Hz]
P: 1.5; D: 1; K: 1.2	1

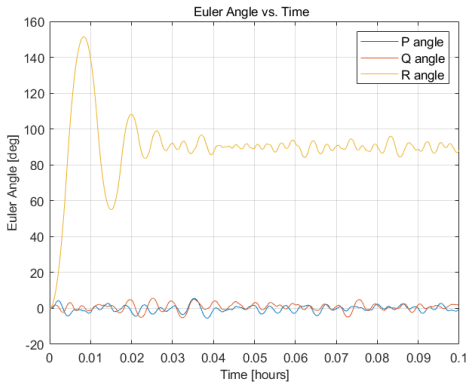

Figure 9.12: 90° rotation simulation.

9.4.4 Accuracy Simulation Result

Finally, it is necessary to simulate the determination and control accuracy of the subsystem. A reaction wheel-based PD controller should be used in this simulation since it is responsible for fine attitude control. As for the use of attitude determination sensors, there are two different cases: sunlight and eclipse periods. In the sunlight period, the Sun vector may be measured by the selected two types of Sun sensors. However during eclipse, SCATTER can only use magnetometers as absolute attitude determination sensors, which leads to a relatively low attitude determination accuracy. Moreover, the angular velocity measured by IMUs is also necessary as an input of the simulation. From the product properties shown in section 9.2 and an estimation of the magnetometer accuracy based on [12], the ADCS accuracy can be simulated in the different situations. The key parameters used in the following simulations are summarised in table 9.6. Also, Extended Kalman Filter block installed in SIMULINK is used to perform filtering for the noisy measurements from magnetometers, Sun sensors and IMUs. The simulation results based on Sun sensors measurements are shown in figure 9.13 and figure 9.14 while those with the use of magnetometers are shown in figure 9.15. Moreover, table 9.7 summarises the simulation results of the designed ADCS subsystems. The average attitude determination and control accuracy per orbit is estimated based on the chosen orbit and field of view of the Sun sensors. It can be found that even though the attitude determination error with the use of magnetometers is slightly above 1°, the orbital average value is well below the 1° requirement.

Table 9.7: ADCS simulation results summary - Root Mean Squared error.

	Attitude Determination Accuracy[deg]	**Attitude Control Accuracy[deg]**
Surface Mounted Sun Sensors	[0.2136, 0.1898, 0.1898]	[0.1725, 0.9907, 0.1426]
Solar Panel Mounted Sun Sensors	[0.4360, 0.4254, 0.4256]	[0.2791, 1.0373, 0.2800]
Magnetometers	[1.0447, 1.0413, 1.0413]	[0.5138, 1.1158, 1.0121]
Orbital Avearge	[0.6128, 0.4407, 0.6011]	[0.3410, 1.0751, 0.5316]

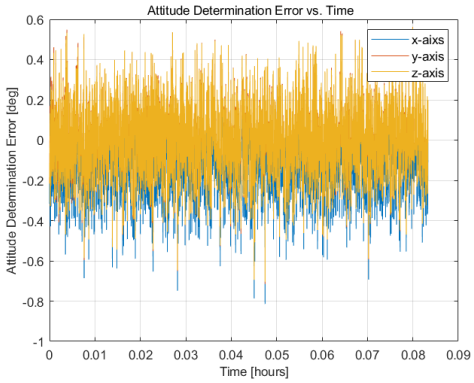

(a) Attitude determination accuracy.

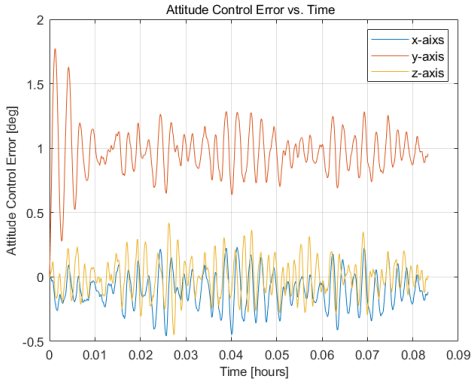

(b) Attitude control accuracy.

Figure 9.13: Accuracy simulation results with the use of surface mounted Sun sensors and reaction wheels.

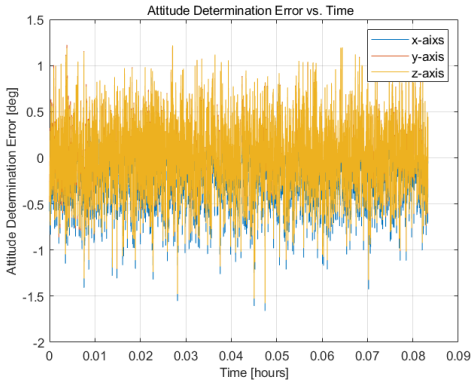

(a) Attitude determination accuracy.

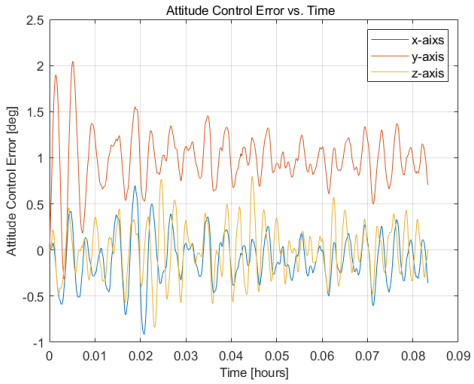

(b) Attitude control accuracy.

Figure 9.14: Accuracy simulation results with the use of Solar panel mounted Sun sensors and reaction wheels.

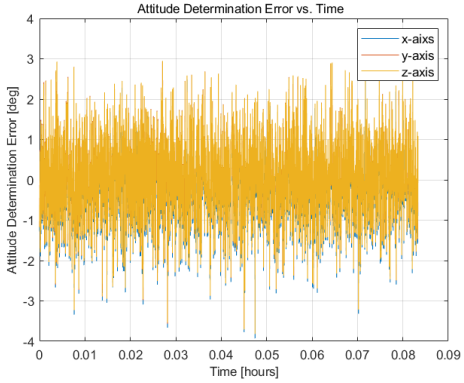

(a) Attitude determination accuracy

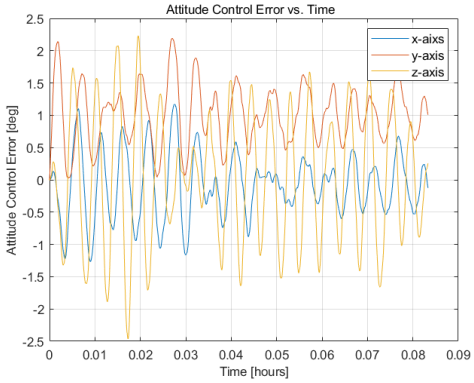

(b) Attitude control accuracy

Figure 9.15: Accuracy simulation results with the use of magnetorquers and reaction wheels

9.4.5 Sensitivity Analysis

This section presents the sensitivity analysis to check the design of the ADCS. Firstly, the simulation of the sensitivity analysis of the attitude determination and control accuracy has been performed in table 9.7, where different sensors with different accuracy levels were used as simulation inputs. Therefore, it was decided to analyse the performance of B-dot algorithm with different initial angular velocities as shown in figure 9.17. The variation of the de-tumbling time with respect to the initial angular velocity is shown in figure 9.16. According to chapter 5, the time needed for de-tumbling with an initial angular velocity of 9 deg/s is still acceptable.

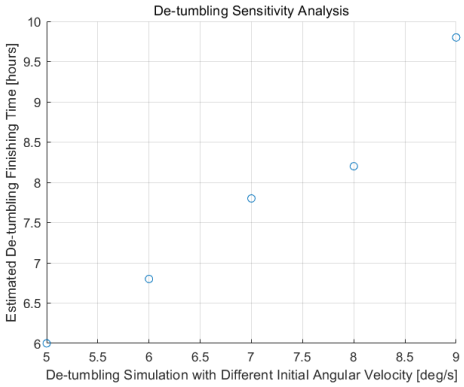

Figure 9.16: De-tumbling sensitivity analysis simulation results.

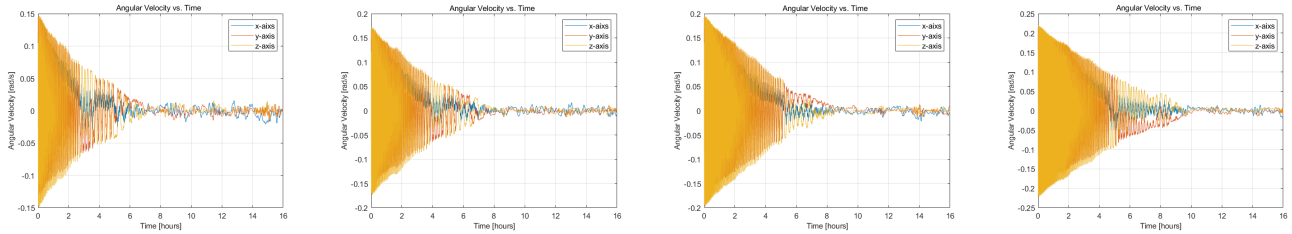

(a) De-tumbling simulation with the initial angular velocity of 6 deg/s.

(b) De-tumbling simulation with the initial angular velocity of 7 deg/s.

(c) De-tumbling simulation with the initial angular velocity of 8 deg/s.

(d) De-tumbling simulation with the initial angular velocity of 9 deg/s.

Figure 9.17: De-tumbling simulation with different initial angular velocity.

9.5 Attitude Control Software Verification & Validation

The SIMULINK tool used to size and analyse the ADCS subsystem has been verified using the AstoSIM software 6 degree-of-freedom implementation and B-dot algorithm shown in section 3.8.1. As AstroSIM does not simulate attitude determination accuracy of spacecraft, only the attitude pointing algorithms are verified in this subsection. For this analysis, the magnetorquer de-tumbling of the SCATTER satellites was simulated using both the SIMULINK tool and AstroSIM. The following simulation inputs were used:

Table 9.8: Simulink tool verification with AstroSIM de-tumbling simulation inputs.

Parameter Name	Value	Parameter Name	Value	Parameter Name	Value
RAAN	0 °	Semi-major axis	6978 km	Initial Angular Velocity	(0.1, 0.07, -0.11) rad/s
Inclination	97 °	Eccentricity	0	Ascending Node	0 rad
Satellite Attitude in E-frame	(0, 0, 0) °	Satellite Moments of Inertia	(0.16, 0.265, 0.282) kgm^2	Satellite Rotation in E-frame	(0, 0, 0) °

The results of the simulations for the SIMULINK tool verification are given in figure 9.19 and figure 9.18.

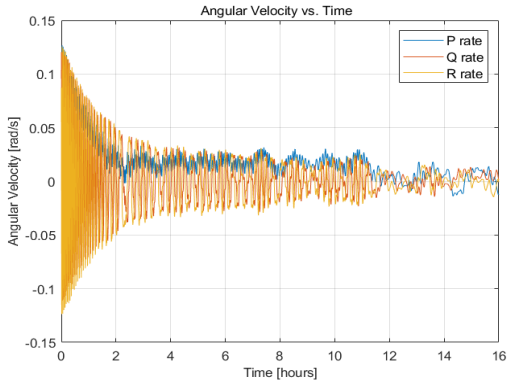

Figure 9.18: SCATTER de-tumbling simulation using the SimuLink tool.

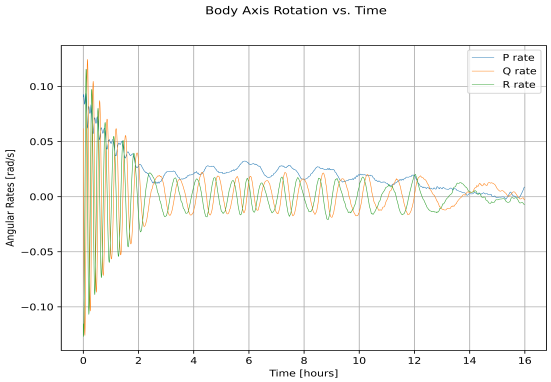

Figure 9.19: SCATTER de-tumbling simulation using AstroSIM.

As it can be seen in the figures, SIMULINK and AstroSIM produce very similar de-tumbling figures. The maximum angular rates simulated by both are 0.148 rad/s (SIMULINK) and 0.1477 (AstroSIM), while full de-tumbling occurs for both simulations in around 12 hours. The pointing accuracy error due to disturbance torques is also similar for both softwares. For SIMULINK, the error is $\mp 0.025 rad/s$, while for AstroSIM it is $\mp 0.0236 rad/s$. All differences in results can be explained by the differences in the algorithms used by the two codes. While SIMULINK models the sensor measurement noise on top of the pointing accuracy, AstroSIM assumes it is negligible. Furthermore, the chaotic nature of the B-dot algorithm itself contributes to the discrepancies. However, given that the parameters of interest of the simulations (maximum angular rate, de-tumbling time and pointing accuracy) are strongly correlated, the SIMULINK tool is considered verified.

As for the validation of SIMULINK tool, QSat gives an attitude determination accuracy of 0.23° with the use of Sun sensors while an actual attitude determination accuracy of 1.32° is reached with the use of magnetometers as absolute attitude determination sensors[58]. Considering that QSat uses a relatively cheap magnetometer with a price of around €200 while SCATTER uses magnetometers with a price of €14285, the SIMULINK tool can be considered validated by comparing with the results shown in table 9.7.

9.6 ADCS Requirements Verification

The verification of the Attitude Determination and Control Subsystem by compliance with requirements is given below:

REQ-ADCS-01: - this requirement is verified through analysis of the satellite de-tumbling, performed in section 9.4.2, which results in a time of de-tumbling of 6 hours, thus satisfying the requirement;

REQ-ADCS-02: - this requirement is verified through analysis of the chosen reaction wheel 90° actuation, performed in section 9.4.3, which results in a time of rotation of 100 seconds, thus satisfying the requirement;

REQ-ADCS-03: - this requirement is verified through analysis of the chosen reaction wheel 90° actuation, performed in section 9.4.3, which results in a time of rotation of 100 seconds, thus satisfying the requirement;

REQ-ADCS-04: - this requirement is verified through analysis of the chosen reaction wheel 90° actuation, performed in section 9.4.3, which results in a time of rotation of 100 seconds, thus satisfying the requirement;

REQ-ADCS-05: - verified through the analysis in table 9.7. The control accuracy remains between $\mp 5°$;

REQ-ADCS-06: - verified through the analysis in table 9.7. The control accuracy remains between $\mp 5°$;

REQ-ADCS-07: - verified through the analysis in table 9.7. The control accuracy remains between $\mp 5°$;

REQ-ADCS-08: - verified through the analysis in table 9.7. The average determination error is below 1°;

REQ-ADCS-09: - verified through inspection of the RW-0.03 reaction wheel [8], which has a maximum torque of 0.002 Nm, that satisfies the requirement;

REQ-ADCS-10: - verified through inspection of the RW-0.03 reaction wheel, which has a maximum momentum storage of 0.04 Nms. This satisfies the requirement.

9.6.1 ADCS Concluding Remarks

In order to improve the design for further iterations, it is recommended that a more complex simulation tool is built with the dynamics and kinematics of reaction wheels taken into consideration. Moreover, the model of reaction wheels should also consider the effect of current. As for the design of ADCS, according to the simulation results of [58], a linearised Kalman Filter which presents a higher accuracy during eclipse period can be applied. In addition to that, the sensors calibration needs to be investigated in the next design phases.

[8] `https://satsearch.co/products/sinclair-interplanetary-rw-0-03`

10. Telemetry, Tracking & Command Subsystem Design

The telemetry, tracking & command (TT&C) system is a crucial part of the satellite architecture as it is the only point of contact between the ground and space segments of the mission. The design of this subsystem was made per satellite. This chapter aims to report the design of this subsystem first, by defining the subsystem requirements in section 10.1. Following this, section 10.2 describes the system architecture and the connection between the ground and space segments is then assessed with the help of a link budget analysis in section 10.3. A sensitivity analysis was conducted as explained in section 10.3.3 and the subsystem requirements were verified and validated in section 10.4.

10.1 Telemetry, Tracking & Command Subsystem Requirements

The requirements for this subsystem are given below in section 10.1.

Table 10.1: Subsystem requirements.

ID	Description	Parent Requirement	Rationale
REQ-TTC-01	The telecommunications shall have a bit error rate (BER) no more than 10^{-5}.	REQ-SYS-F-13 and -14	Derived from allowed short-term error performance for satellites as stipulated by the International Telecommunications Union (ITU) [1].
REQ-TTC-02	The antenna shall have an unobstructed field of view in the nadir direction for at least 120°.	REQ-SYS-F-13 and -14	Derived from typical patch antenna fields of view [15].
REQ-TTC-03	The telecommunication shall be in an ITU certified S-band frequency.	C-LEGAL-01	The S-band radio frequency is reserved for Near Earth Missions and its use must be certified by ITU.
~~REQ-TTC-04~~	~~The subsystem hardware shall occupy an internal volume of less than 1000 cm^3.~~	~~REQ-SYS-D-07~~	Struck out as volume is a tradeable parameter, and not a requirement.
~~REQ-TTC-05~~	~~The system shall be operational in the temperature range of −20 °C to 50 °C.~~	~~REQ-SYS-D-07~~	Struck out as it was moved to chapter 7
REQ-TTC-06	The antenna shall be placed on the surface of the satellite such that the multipath effects are reduced.	REQ-SYS-F-14	Integration of the components with the spacecraft must allow for telecommands to be received clearly from the ground station.
REQ-TTC-07	The satellite shall have a minimum available link margin of 3 dB for effective ground communication.	REQ-SYS-P-18	Derived as requirement to close the link budget such that the communication paths between the satellite and ground station can be established [12].
REQ-TTC-08	The satellite shall operate without communication with the ground station for at least 3 days.	REQ-M-02	Directly follows from parent requirement, thus same rationale.
REQ-TTC-09	The subsystem components shall have a minumum lifetime of 3 years.	REQ-M-02	The mission is required to operate in less than 3 years.
REQ-TTC-10	The communicated data shall be secured with encryption so as to prevent purposeful external interference and influence.	REQ-SYS-F-13 and -14	Derived as security measure to prevent hacking.
REQ-TTC-11	The link budgets shall be calculated for a weather availability of 95%.	REQ-SYS-F-13	Derived from availability parameters from other comparable missions.
REQ-TTC-12	The telecommunication system shall be capable of simultaneously handling telemetry, and telecommands.	REQ-SYS-F-13 and -14	Derived from availability parameters from other comparable missions.
REQ-TTC-13	The telecommunication system shall support a downlink data rate of at least 150 kbps.	REQ-SYS-F-13	Derived from initial data rate estimates as well as a statistical analysis of COTS products available for CubeSat telecommunication systems in S-band.
REQ-TTC-14	The telecommunication system shall support an uplink data rate of at least 15 kbps.	REQ-SYS-F-14	Derived from initial data rate estimates and a statistical analysis of comparable missions in the S-band.

10.2 Telemetry, Tracking & Command Subsystem Architecture

With the requirements of the subsystem established it was important to begin defining the system architecture. This section aims to do that by defining the ground station along with the communication band, the modulation and coding scheme chosen for the system and finally, explaining the flow of telemetry and commands throughout the whole system with the help of a communication flow diagram.

10.2.1 Ground Station Selection

Before the ground station for the mission was selected, the radio frequency bands of the downlink and uplink had to be selected. Out of the various frequency bands, the most suitable band was chosen through reasoning based on the associated link properties and by observing comparable missions.

SCATTER is a scientific mission conducted to record atmospheric properties, for the most part, as scalar measurements without taking any images. Thus, it requires a relatively low data rate for transmission. This is supported by looking at the composition of the mission-specific scientific data produced. As such, the satellite could be designed to communicate in a lower radio frequency range as it does not require a high bandwidth. Higher frequency bands such as Ku-, K- and Ka-bands are more suitable for the high data rates required from deep space missions.

Out of the remaining frequencies commonly used by CubeSat missions, the UHF-band and lower were discarded due to the overcrowding of those spectra by the many satellites and services that have been using them. The next lowest frequency band was the S-band which was sufficiently capable of handling the data rate requirements for the mission and chosen for this mission. This was because, on average, the data rate facilitated by this band is 540 kbps in altitude range around 400 km [59]. This was true to the final estimated mission data rate of 615 kbps.

Amongst the options for ground stations, it was possible to either build one for the sake of the mission or to buy the services of an already licensed one [32]. The main aspects to consider for this were the flexibility of scheduling, manpower required for operations, licensing for frequency use and the costs that would go into either option.

While it is advantageous to build a ground station for its flexible scheduling, buying the services of a ground station was chosen for the associated conveniences. It would not be necessary to get licensing for the ground station as that would already have been done by the station and similarly, the service provider would also have the responsibility of supplying the manpower required for it. Even though there would be less flexibility in the scheduling, the full services can be bought for a subscription fee and they can usually be reserved two to three days in advance which would sufficiently make up for the reduction in schedule flexibility. [32]

Out of the available ground stations that are capable of providing uplink as well as downlink services in the S-band, the one at the Vienna University of Technology was selected as a reference for the purpose of this mission's design. This ground station is equipped with two S-band antennas for the uplink and downlink communications of which the parabolic antenna for the downlink is illustrated in figure 10.1. For the uplink, a Yagi-Uda antenna was used. It is located at the university's Institute of Astronomy and is affordable for other universities. It has been functioning since 2003 and maintained a connection reliability of 93%. Additionally, its geographic proximity to the base of this project in Delft, Netherlands allows for an ease of logistical operations. These factors made the ground station in Vienna, Austria to be a mission-comparable choice based on whose properties the design and link budget calculations were carried out. [60]

Figure 10.1: Parabolic antenna at Vienna University of Technology for downlink in S-band [60].

10.2.2 Modulation & Coding Scheme

The modulation and coding schemes for the mission were decided based on the BER requirement given in section 10.1. Due to the nature of the scientific mission and the high-accuracy BER requirement for the downlink and uplink, a modulation and coding form that is best suitable for achieving this requirement needed to be chosen.

For modulation, phase-shift keying methods were chosen over frequency- and amplitude-shift keying due to their better performance in terms of spectral efficiency and energy stored per bit. The basic forms to consider were binary phase shift keying (BPSK) and quadrature phase shift keying (QPSK) where BPSK encodes one bit of information per transmitted symbol and QPSK encodes two bits per symbol. Higher number of bits per symbol would reduce the required bandwidth for data transmission but they also introduce phase-noise induced errors and so were not considered. However, as can be seen in figure 10.2, BPSK and QPSK both perform the same in terms of the required the energy per bit to noise power spectral density ratio Eb/N0 necessary for maintaining a given BER. Eb/N0 is also referred to as the SNR per bit as it gives the signal-to-noise ratio (SNR) per bit which is a value independent of the bandwidth.

Higher data rates such as for the downlink require a higher bandwidth for transmission and so, since QPSK can encode two bits per symbol for transmission as opposed to the BPSK method's one bit per symbol, QPSK requires half the bandwidth as BPSK for the same data rate. Thus, QPSK was chosen as the modulation method for the downlink which has a higher data rate.

On the other hand, the uplink is a lower data rate and is capable of working with the lower phase-noise induced errors of BPSK modulation while still being able to efficiently transmit data in the available bandwidth. As such, it was decided that the uplink signal would be modulated using this BPSK method.

[2] `https://en.wikipedia.org/wiki/Eb/N0`, Retrieved 13-06-2022

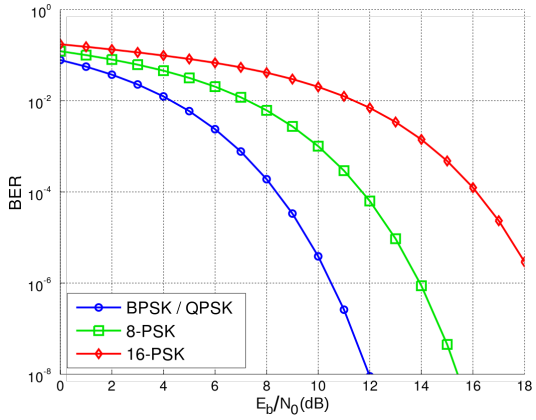

Figure 10.2: Bit error rate vs. signal-to-noise ratio graph per type of phase-shift keying modulation [2].

For the downlink, QPSK with a 6/7 forward error coding (FEC) rate was selected as the coding scheme. This means that for every six bits of information, there will be one redundant bit added to the data to make up for errors that may be produced in the data as it travels to the receiver. There is also an extra block of code that is sent with the signal which allows for any errors in the data to be detected and corrected at the receiver without having to re-transmit the data. This reduces the minimum signal-to-noise ratio which needs to be achieved in order to maintain a low BER.

For the uplink, an uncoded BPSK scheme was used as this is typical of satellite missions due to the less restrictive requirements placed on the uplink signal [12]. Both of these modulation and coding schemes allow for the data to have a BER of less than 10^{-5}, satisfying REQ-TTC-01 [12].

10.2.3 Space Segment Components Selection

The selection of transceiver and antenna components was driven by the design needs of maximizing data rates as well as minimizing the BER, transmission power and the required bandwidth. Additionally, as the CubeSat structure of the SCATTER mission's satellites allows for the use COTS products, the components of this subsystem would also be readily available COTS products in order to reduce the time and costs required for designing custom products.

For the CubeSat mission, it was decided to choose a non-deployable antenna such as a patch antenna in order to avoid introducing a point of failure related to deployment mechanisms. A fixed patch antenna which takes up little volume and surface area on the satellite is suitable for the compact shape of the CubeSat structure. These factors combined with how the communications would be conducted in the S-band, lead to the choice of a lightweight S-band patch antenna made by ISISpace as see in figure 10.4 being used as the antenna on the CubeSat.

Amongst the considered transceivers that could fulfil the established data rates and power constraints were the Endurosat S-band Transceiver I, the Satlab SRS-3, the Rakon NewSpace S-band Transceiver and the IQ Spacecom XLink-S. One of the main constraining factors was the modulation scheme. The transceivers such as Endurosat's and Satlab's could not be configured for QPSK and BPSK. So, the choice was to be made between Rakon's and IQ Spacecom's transceivers. IQ Spacecom's XLink-S was found to have a TRL of 7 whereas Rakon's NewSpace S-band Transceiver was newer and lacking in a proven reliability. As such the IQ Spacecom XLink-S in figure 10.3 was chosen as transceiver for this mission.

Figure 10.3: Commercial off-the-shelf transceiver: IQ Spacecom XLink-S.

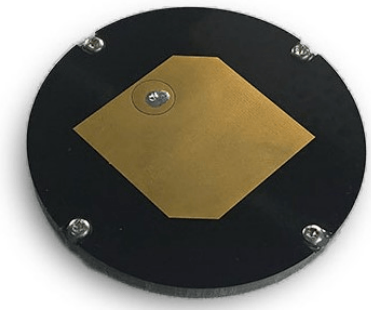

Figure 10.4: Commercial off-the-shelf S-band patch antenna from ISISpace.

Figure 10.5: Commercial off-the-shelf products chosen for the TT&C design.

The properties such as mass, power and dimensions of these products are summarised in table 10.2. Two of each product will be placed on the satellite for redundancy as statistical analyses show that a large proportion of CubeSat mission failures are associated with the failure of the communications system [61].

Table 10.2: Summary of TT&C components' properties per satellite.

Property	Transceiver	Antenna
Product	IQ Spacecom XLink-S[3]	ISIS S-band patch antenna[4]
Quantity [-]	2	2
Mass per unit [g]	200	50
Dimensions [mm]	$90 \times 65 \times 25.3$	$80 \times 80 \times 5$
Power [W]	<12 W (Tx + Rx)	N/A
Cost per unit [€]	10,000	2,150

The ISISpace S-band patch antenna has a gain of 6.5 dBic and a half power beam width of 100° with a transmission power of 2 W. The XLink-S transceiver can be configured for BPSK, QPSK as well as OQPSK modulation schemes. It supports a transmission frequency band of 2.200 GHz to 2.290 GHz and a receiving frequency band of 2.025 GHz to 2.110 GHz. However, as it is configured for separate transmitting and receiving antennas, the connection between the antenna and transceiver would need to be fitted with a diplexer so that the patch antenna can transmit telemetry from the transceiver while also receiving telecommands from the ground station. It is capable of supporting downlink data rates of between 500 kbps and 100 Mbps, although it is highly unlikely that the mission will require such high data rates. It also supports uplink data rates of 56 kbps which fulfils the requirements given in section 10.1.

10.2.4 Telemetry, Tracking & Command Subsystem Communication Flow Diagram

The flow of communication of the entire satellite system along with its link to the ground station is given in figure 10.6. This flow is split between the space and ground segments of the mission. The space segment, which consists of two satellites, has the same flow of information. Although only one satellite is depicted in the diagram, this flow can be considered to be duplicated for the second satellite as well.

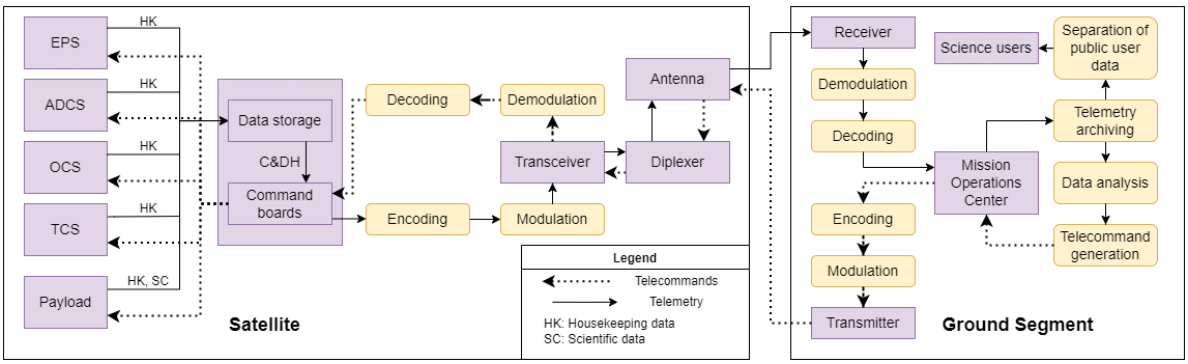

Figure 10.6: Communication flow diagram between a satellite and the ground segment.

First, the housekeeping data is collected from the EPS, ADCS, OCS and TCS while the scientific data is collected from the payload consisting of the IMU, the GNSS and the mass spectrometer. The types of information delivered in housekeeping and scientific data per subsystem is summarised below.

- **EPS:** Housekeeping data obtained from the PDU (system level voltage and temperature values), the PCU (system level current and power values) and the batteries (cell voltage, current and power values).
- **ADCS:** Housekeeping data obtained from the magnetorquer (component temperature and current values), the magnetometer (magnetic field direction's vector components), the Sun sensor (Sun direction's vector components) and the reaction wheels (system angular velocity).
- **OCS:** Housekeeping data obtained from the thruster consisting of temperature and pressure sensors as well as the main actuators.
- **TCS:** Housekeeping data obtained from the extra temperature sensors.
- **Payload:** Scientific as well as housekeeping data obtained from the mass spectrometer, the GNSS (satellite positional and velocity data as well as the dual-frequency code and carrier phase observations) and the IMU (change in satellite velocity and angles).

All of these data types are sent to the ground station except for the ADCS magnetometer which only relays its information to the on-board computer but not the ground as reasoned in chapter 9. This telemetry is relayed to the C&DH system to be stored until it needs to be transmitted to the ground station.

Once the data needs to be transmitted, it can be encoded. This includes encryption and also be forward error coding for the downlink as discussed in section 10.2.2. An advanced encryption standard (AES) algorithm would

[2] `https://www.itu.int/dms_pubrec/itu-r/rec/s/R-REC-S.2099-0-201612-I!!PDF-E.pdf` Retrieved 09-06-2022
[3] `https://www.iq-spacecom.com/products/xlink-s`, Retrieved 15-06-2022
[4] `https://www.isispace.nl/product/s-band-patch-antenna/`, Retrieved 15-06-2022

be preferred for use during encryption as it would be suitable for both encrypting and decrypting using a single application-specific integrated circuit (AISC) which is currently one of the most secure options for encryption methods. This is due to the how difficult it is to reverse-engineer its circuit pathway, making the encryption key nearly impossible to crack. There are a wide variety of low power (< 0.2 W) consuming AISCs available on the market which could be selected in the future designs[5]. However, these could not be selected for the current design due to time constraints on the project.

Following this, the signal is modulated using the QPSK modulation scheme as discussed in section 10.2.2 after which it is sent to the transceiver where the appropriate signal high power amplifications are applied. Telemetry is then sent to a diplexer (which allows the same antenna to be used for both transmitting and receiving) and the telemetry data is transmitted to the ground station.

Once it is received and the appropriate low noise amplification is applied, the data is demodulated, decoded for the FEC and decrypted, it is sent to the mission operations center which is where "all satellite commanding is generated, ground station control is managed, and satellite telemetry is archived" [32]. Through this center, the telemetry is archived and the data can be analysed in a virtual science operations center where the involved experts can analyse the data from anywhere in the world. A science operations center was chosen to be virtual rather than a physical one with highly secure servers because the mission data was not going to be confidential and so did not need such a high level of security. [32]

While some of the archived telemetry that is not related to the commanding of the mission could be separated and made publicly available to science users, the telemetry data as a whole would still be analysed by the science experts who could co-ordinate with the mission operations center to generate telecommands to be transmitted back to the satellite.

The telecommands would once again be encoded, modulated, amplified and sent by the transmitter to the satellite where the data is also demodulated and decoded, and then sent to the OBC of the C&DH system which would redistribute those commands to the various listed subsystems.

10.3 Telemetry, Tracking & Command Link Budget Analysis

The connection between the ground station and the satellite consists of a radio frequency signal. As this signal travels from between the ground station and the satellite, it experiences gains in its signal power from the antennas and losses from the transmitter, propagation and the receiver. These gains and losses are assessed in a link budget analysis to ensure that the communication link can be established without the signal being too weak to be detected by the receiver.

10.3.1 Link Budget Factors

While the antenna gains for the ground station and the satellite were known from product specifications, the various losses were estimated using available literature and calculations. The link budget was designed for the limiting case during nominal operations wherein the satellite is at its lowest altitude where transmissions must still occur (200 km) and therefore, the required data rate is highest. The telemetry data must be collected, stored and then transmitted during the time when the ground station is in contact.

$$L_s = -10 \log \frac{m}{k(1+\rho)} \qquad (10.1) \qquad L_p = -12 \left(\frac{e}{\theta}\right)^2 \qquad (10.2) \qquad L_{FS} = -20 \log \frac{4\pi S f}{c} \qquad (10.3)$$

The spectral efficiency associated with the FEC method could be calculated using equation 10.1. For the pointing loss L_p, only the ground station antennas were considered as the fixed patch antenna's pointing offset could be considered as negligible. Then, the pointing loss could be calculated using equation 10.2 where e is a pointing offset while θ is the beamwidth of the ground station antenna for the uplink or downlink. The free space loss could also be calculated using equation 10.3 wherein S is the distance between the ground station and the satellite, f is the signal frequency of the link and c is the speed of light. [15]

$$\frac{E_b}{N_0}[dB] = P_t + G_t - L_e - L_a - L_{FS} - L_p - L_{tl} - L_{rl} + \frac{G}{T_s} + 228.6 - 10 \log R_d \qquad (10.4)$$

Finally, the Eb/N0 could be calculated using equation 10.4. Here, the transmitter power P_t, transmitter gain G_t and the figure of merit (G/T_s) were given by the equipment specifications while the losses could be estimated and the data rate R_d could be calculated based on the on-board telemetry production as estimated in table 12.2 in chapter 12.

10.3.2 Link Budget Analysis Results & Discussion

Using the formulas given in section 10.3.1, the link budget could be calculated. Its associated factors are summarised in table 10.3.

[5] `https://www.raytheon.com/capabilities/products/space_encryption` Retrieved 15-06-2022

Table 10.3: Link budget calculation for SCATTER mission.

Parameter	Uplink	Downlink
Frequency f [GHz]	2.03	2.23
Transmitter Power P_t [dBW]	17	3
Transmit Line Loss L_{tl} [dB]	-2.5	-2
Spectral Efficieny L_s [dB]	-	-1.9
Antenna Gain G_t [dBi]	25	6.5
EIRP [dBW]	**39.38**	**7.5**
Distance S [km]	1146.7	1146.7
Atmospheric attenuation L_a [dB]	-0.04	-0.04
Free space loss L_{FS} [dB]	-159.8	-160.6
Pointing Loss L_p [dB]	-0.12	-0.03
Receive Line Loss L_{rl} [dB]	-2	-2.5
Figure of merit (G/Ts) [dB]	-18.55	13.3
Data rate R_d [kbps]	12	615
Predicted (Eb/N0) [dB]	**46.82**	**26.5**
Required (Eb/N0) [dB]	9.6	4.4
Margin [dB]	**37.22**	**22.10**

The downlink will be established at a frequency of 2.03 GHz while the uplink is at a frequency of 2.23 GHz. As the transceiver is capable of a full-duplex configuration, the transmitting and receiving of telemetry and telecommands respectively can be conducted at the same time. The transmit and receive line losses, L_{tl} and L_{rl}, were estimated based on similar small satellite missions and the cabling present in them. The atmospheric losses were also estimated based on the frequency of the transmission and the corresponding losses due to atmospheric gases. [12]

The spectral efficiency is applicable only to the downlink which is forward error coded with a code rate k of 6/7 whereas the uplink is uncoded. Assuming a roll-off factor ρ of 0.5 and knowing that QPSK modulation uses 2 bits per symbol (m), the spectral efficiency could be calculated using equation 10.1 to be -1.9 dB.

The free space loss was calculated assuming an altitude of 200 km and a minimum elevation of 5° necessary in order for the satellite to establish contact with the ground station. Using these two values, the direct distance between the satellite and ground station S could be calculated using trigonometric properties. Then, with the frequency known, the free space loss could be calculated per uplink or downlink using equation 10.3.

Using the AstroSIM 6DoF software described in section 3.8.1 to estimate the number of ground passes per day and the time they take, it was found that the total time when ground station contact can be established in a day was 19.87 minutes. During this time, the telemetry data that needed to be transmitted on average was the volume that was collected over the course of the day. This storage of data in a single day was calculated from the values in table 12.2. Multiplying this produced data with a safety factor of 1.25 for the addition of redundant bits as well as coding blocks gives 91.65 MB of data that needs to be transmitted over 19.87 minutes. This leads to a downlink data rate of 615 kbps. The uplink data rate was estimated from comparable missions which gave a data rate of 9.6 kbps [60]. This was then multiplied with a margin of 1.25 in order to get the uplink data rate of 12 kbps.

Finally, the Eb/N0 could be calculated as in equation 10.4 to get an uplink margin of 37.22 dB and a downlink margin of 22.10 dB. Both of these margins are well above the required 3 dB margin needed for the link to close and be able to transmit all data in the uplink and downlink. The large margins are also not unexpected as the data rates are being carried in the S-band.

These margins imply that the receivers receive a strong signal in the uplink and downlink which means that the system may have a rather robust design. This is confirmed with the help of the following sensitivity analysis.

10.3.3 Sensitivity Analysis: Telemetry, Tracking & Command

In order to check the robustness of the designed system, a sensitivity analysis was conducted on the parameters that have the highest influence on the design. The ground contact time's sensitivity was analysed as well as that of the distance between the ground station and satellite. The effect of these changes on the link margins will be checked to see whether the satellite connection can still be established with the ground station upon varying them.

Change in distance between Ground station and Satellite

The sensitivity of the distance between the satellite and ground station was also analysed. This is because it influences the free space losses which are the largest contributors to the signal losses in both the uplink and downlink. The change was incremented by 200 km as, at an elevation of 5°, this corresponds to a change in altitude of approximately 50 km when going from 200 km to 150 km.

Table 10.4: Effect of changing the ground station-satellite distance, with a fixed uplink and downlink data rate of 12 kbps and 615 kbps.

Change in distance [km]	-200	0	200	400	600	800
Uplink free space loss [dB]	-158.1	-159.8	-161.1	-162.4	-163.4	-164.4
Downlink free space loss [dB]	-158.9	-160.6	-162.0	-163.2	-164.2	-165.2
Uplink margin [dB]	38.9	37.2	35.8	34.6	33.6	32.6
Downlink margin [dB]	23.7	22.1	20.7	19.5	18.4	17.5

As is evident from table 10.4, the link margins still close with the various changes in distance. The design of the system does not need to be changed which means that it is quite robust.

Change in Ground Contact Time

The ground contact time's sensitivity was analysed. This influences the downlink data rate requirement which, in turn, has a large influence on the design as it is the limiting case out of the downlink and uplink data rates.

Table 10.5: Effect of changing the ground contact time, at an altitude of 200 km.

Change in contact time [minutes]	-4	-2	0	2	4
Downlink data rate required [kbps]	770	684	615	559	512
Downlink margin [dB]	21.1	21.6	22.1	22.5	22.9

Upon observing the results of the sensitivity analysis in table 10.5, it was concluded that the link margins still close even with the changes in ground coverage time. The sensitivity of the system is low and so it was concluded that it is a robust design in this aspect as well.

In a more extreme case such as when data is stored on board for 3 days, increasing the data rate by 3 times results in a required data rate of 1.845 Mbps. Using this value, the downlink link margin only reduces to 17.3 dB. This is a positive value more than 3 dB, which means the data can still be transmitted.

10.4 Telemetry, Tracking and Command Subsystem Requirements Verification

The verification of TT&C by compliance with requirements is given below:

REQ-TTC-01: - this requirement is verified through inspection, by choosing QPSK as a modulation scheme for downlink, in section 10.2.2, which reduces the BER to the order of magnitude of 10^{-5} according to [12];

REQ-TTC-02: - this requirement is verified through inspection of the SCATTER satellites. As the patch antennas are placed 84.6 mm away from the small, 1U x 2U solar panels, they have a 173 ° field of view, which satisfies the requirement;

REQ-TTC-03: - this requirement is verified through inspection of the chosen frequencies of 2.2 GHz for downlink and 2.1 GHz for uplink given in section 10.2.3. These frequencies satisfy the requirement;

REQ-TTC-06: - this requirement shall be verified through ground-based testing of the TT&C set-up after qualification models are built, where multi-path effects shall be simulated;

REQ-TTC-07: - this requirement is verified through an analysis of the link budget of the satellite-ground station communication in section 10.3.2

REQ-TTC-08: - this requirement is verified through an analysis of the storage capacity of the satellites and the collected data rate. As shown in table 12.2, in 3 days, 234.5 Mb of data are recorded, while the storage capacity available is 475 Mb as given by section 12.2.1, and therefore the requirement is satisfied;

REQ-TTC-09: - this requirement shall be verified through inspection of the TT&C ISIS Space Patch antenna, in further stages of the design, when Non-Disclosure Agreements are signed to get a full set of specifications [6];

REQ-TTC-10: - this requirement shall be verified through ground-based demonstration of the encryption scheme chosen in future stages of the design;

REQ-TTC-11: - this requirement is verified through analysis of the link budget performed in table 10.3, where an atmospheric attenuation of -0.04 dB was chosen based on [12] and a weather availability of 95 %. Therefore, the requirement is satisfied;

REQ-TTC-12: - this requirement is verified through inspection of the ISIS-Space patch antenna [7] and the IQ Spacecom XLink-S transceiver [8]. As both products are capable of handling telecommands and telemetry, the requirement is satisfied;

REQ-TTC-13: - this requirement is verified through inspection of the ISIS-Space patch antenna [9], which is able to support 500 kbps of downlink data rate according to section 10.2.3. Therefore, the requirement is satisfied;

REQ-TTC-14: - this requirement is verified through inspection of the ISIS-Space patch antenna [10], which is able to support 56 kbps of uplink data rate according to section 10.2.3. Therefore, the requirement is satisfied;

[6] https://www.isispace.nl/product/s-band-patch-antenna/
[7] https://www.isispace.nl/product/s-band-patch-antenna/
[8] https://catalog.orbitaltransports.com/xlink-s-s-band-transceiver-sdr/
[9] https://www.isispace.nl/product/s-band-patch-antenna/
[10] https://www.isispace.nl/product/s-band-patch-antenna/

10.4.1 Telemetry, Tracking & Command Concluding Remarks

This chapter conducted an initial detailed design of the telecommunications system on the mission satellites. Once the system components were chosen and the link budget was analysed, it was deemed that using their parameters, the communication link between the satellite and ground station could be established in both directions with an uplink link margin of 37.22 dB and a downlink link margin of 22.10 dB. This system was designed for an altitude of 200 km as this is where the requirement for the data transfer in the downlink was the most constraining.

In order for future iterations of the design to be improved, some aspects that could be further looked into are the integration of encryption modules into the subsystem and the effect of Doppler shift of the signal on the communication link. Doppler shift involves the slight increase in the frequency of the signal as the satellite approaches the ground station and the reduction in frequency as it moves away. This variation could be simulated and its impact on the design must be analysed. Additionally, due to time constraints on the project, an encryption product could not be chosen for the design. However to secure the connection between the ground station and the satellite, an AISC and an encryption scheme such as AES could be chosen for future iterations of the design.

11. Payload Subsystem Design

The payload of the SCATTER satellites consists of 5 instruments. Each satellite carries 2 mass spectrometers, 2 Inertial Measurement Units (IMU's) and a Global Navigation Satellite System (GNSS) receiver. In this chapter, the selection of these components will be discussed. Subsystem requirements related to these instruments is presented in section 11.1. The selection of the components is then described in section 11.2. In section 11.3, the compliance with the subsystem requirements is verified.

11.1 Payload Subsystem Requirements

The subsystem requirements for the payload are listed in table 11.1. They are to be verified in section 11.3.

Table 11.1: Payload subsystem requirements.

ID	Description	Parent Requirement	Rationale
REQ-PL-01	The IMU shall measure gyroscope data with a maximum bias instability of $2\,^\circ\,\mathrm{h}^{-1}$.	REQ-SYS-F-20	This value was calculated to be the maximum to achieve the required attitude determination accuracy for the ADCS.
REQ-PL-02	The IMU shall measure gyroscope data with a maximum angular random walk of $0.15\,^\circ/\sqrt{\mathrm{h}}$.	REQ-SYS-F-20	This value was calculated to be the maximum to achieve the required attitude determination accuracy for the ADCS.
REQ-PL-03	The GNSS receiver shall provide position accuracy of at least 0.1 m.	REQ-SYS-P-07	Derived from the performance requirements.
REQ-PL-04	The GNSS antenna shall have an unobstructed view in the Zenith axis in all flight orientations.	REQ-SYS-P-07	Derived from the performance requirements, as obstructing objects degrade the signal quality and thus introduce errors into the measurements.
REQ-PL-05	The mass spectrometer shall measure the atmospheric temperature with an absolute error of at most 60 K.	REQ-SYS-P-10	Derived from the performance requirements.
REQ-PL-06	The mass spectrometer shall measure the atmospheric temperature with a frequency of at least 0.1 Hz.	REQ-SYS-P-11	Derived from the performance requirements.
REQ-PL-07	The mass spectrometer shall measure the helium particle concentration with an absolute error of at most $10^{11}\,\mathrm{m}^{-3}$.	REQ-SYS-P-12	Derived from the performance requirements.
REQ-PL-08	The mass spectrometer shall measure the helium concentration with a frequency of at least 0.1 Hz.	REQ-SYS-P-13	Derived from the performance requirements.
REQ-PL-09	The mass spectrometer shall measure the atomic oxygen particle concentration with an absolute error of at most $10^{10}\,\mathrm{m}^{-3}$.	REQ-SYS-P-14	Derived from the performance requirements.
REQ-PL-10	The mass spectrometer shall measure the oxygen particle concentration with a frequency of at least 0.1 Hz.	REQ-SYS-P-15	Derived from the performance requirements.
REQ-PL-11	The IMU shall measure its non-gravitational acceleration with an accuracy of at least $2 \cdot 10^{-7}\,\mathrm{m}^2\,\mathrm{s}^{-1}$.	REQ-SYS-P-16	Derived from the performance requirements.
REQ-PL-11	The IMU shall measure accelerations with a frequency of at least 0.1 Hz.	REQ-SYS-P-17	Derived from the performance requirements
REQ-PL-12	The GNSS receiver shall provide positioning measurements with a frequency of at least 0.1 Hz.	REQ-SYS-P-17	Derived from needs as described in project description.
REQ-PL-13	The mass spectrometer shall have a ram intake in flight direction of at least one flight orientation with a FoV of at least 10°.	REQ-SYS-P-08, -10, -12, -14, -20, and -21	The mass spectrometer needs an air intake to measure atomic oxygen and helium concentrations. The FoV should be at least twice the size of the pointing accuracy provided by the ADCS.
REQ-PL-14	The mass spectrometer surface is not available for sun sensors to be mounted on.	-	Derived from the QB50 Interface Control Document [23].

11.2 Payload Analysis

In this section, the payload instrument selection process will be described. This will be followed up by a sensitivity analysis and ends with some concluding remarks that can be made regarding recommendations.

11.2.1 Mass Spectrometer Selection

In the preliminary design, it was determined that a time-of-flight mass spectrometer was the most suitable type of mass spectrometer for the SCATTER mission. During the past decade, 3 different mass spectrometers of this type have been flown in CubeSAT missions, and one of these mass spectrometers was selected for the SCATTER mission. The selection process is described in this subsection.

The first mass spectrometer to be considered was the Ion and Neutral Mass Spectrometer (INMS) from the Mullard Space Science Laboratory. This INMS was used for the QB50 mission, where 13 CubeSATs were launched in 2016 and 2017 with the INMS. Subsequently, it was used on the SOAR mission in 2021 and is selected as payload for the CIRCE satellites, which are scheduled to be launched near the end of 2022. The instrument can analyze a mass range including 14 Da to 32 Da [63], but it can be adapted to include helium particles, which have a mass of 4 Da. It does so with a mass resolution of

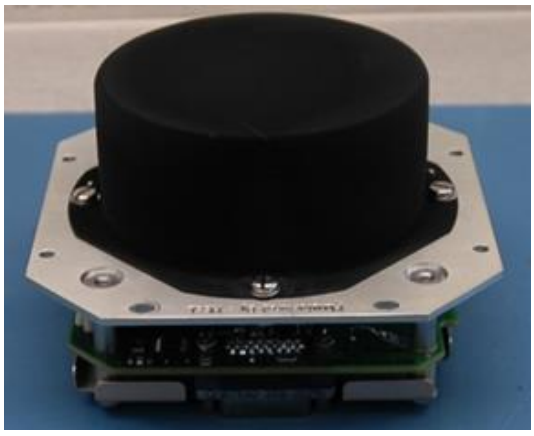

Figure 11.1: Image of the QB50 INMS [62].

7 m/Δm, which is sufficient to reliably measure the atmospheric temperature[1].

The second mass spectrometer is the Wind Ion Neutral Composition Suite (WINCS) developed by the NRL. This instrument was used for the CADRE satellite launched in 2016 and contains multiple instruments, among which a neutral mass spectrometer. This instrument can measure a wide mass range of 1 Da to 56 Da with a mass resolution of 18 m/Δm [64].

The final instrument is the INMS from the Goddard Space Flight Center, payload on the ExoCube in 2015 and the Dellingr in 2017. Its mass range is 1 Da to 40 Da and its mass resolution is 12 m/Δm [65].

Ultimately, the QB50 INMS was selected for the SCATTER mission. The WINCS suite was eliminated as its sampling interval is 41 seconds, which is considerably larger than the sampling interval required. And even though the ExoCube INMS performs better, its power consumption is twice as high. This made integration with the EPS difficult, as the sensitivity analysis in chapter 5 concludes that the duty cycle is highly sensitive to power consumption. Furthermore, the performance, which is worse, is still likely to be sufficient, as was stated before.

However, a remark needs to be made regarding the reliability of the selected instrument. Of the 13 QB50 mass spectrometers, data was accumulated with only 1 satellite. The other satellites failed for unknown reasons, though it can be argued that those satellites failed due to poor testing and quality control [63], but this cannot be stated with any certainty. This means that the fact that the INMS was flown on 13 satellites cannot be seen as a proof of high reliability on its own. It is known from the SOAR satellite that the INMS itself started malfunctioning shortly after launch[2]. Therefore, it was decided to mount 2 mass spectrometers on each of the SCATTER satellites for redundancy. On top of that, it is expected that the reliability will improve somewhat before the launch, as the INMS is to be launched on the CIRCE mission as mentioned before, and possibly more missions thereafter.

The QB50 INMS can be seen in figure 11.1. As mentioned before, two of these mass spectrometers are mounted on each of the satellites on the +x surface, so that it has a ram intake for one of the flight orientations. Only one mass spectrometer runs at a time, as the second is included for redundancy. The mass spectrometer is only turned on when the satellite is in science mode while the +x surface is facing the incoming air. When the satellite is in science mode but in a different orientation, the mass spectrometer is turned off. All relevant details of the mass spectrometer units can be found in table 11.2. The cost listed in the table is the development cost for a single component. As explained earlier, it may be necessary to change the instrument so that it can measure helium particles as well, but this is not expected to be a radical change and additional costs for this are thus likely to be low.

Table 11.2: Details of the mass spectrometer [23][66].

Component	Size [mm]	Mass [kg]	Power Consumption [W]	Cost [€]	Sampling frequency [Hz]	FoV [rad]	Particle Number Density Error [cm^{-3}]
QB50 INMS	$98 \times 98 \times 64$	0.2	0.88	100,000	0.1	0.279×0.035	$\sqrt{N} + 0.7$

11.2.2 Inertial Measurement Unit Selection

The primary use of the IMU is that of measuring non-gravitational accelerations, as defined by requirement REQ-PL-11. As use of an IMU over a dedicated accelerometer was chosen, it was decided that the IMU provides gyroscopic data to the ADCS. However, no COTS IMU's exist that can meet the accuracy required as defined by REQ-PL-11. Still, it was deemed useful to include an IMU as accelerations increase up to a point where the IMU is capable of measuring the accelerations once the satellites descend closer to the earth. Because of this, there was a strong incentive to select an IMU that provides an accuracy that is as high as possible, so that this point can be reached earlier during the mission.

Table 11.3: Selection of suitable accelerometers or IMU's. Some of these sensors are flight proven in space missions and some are radiation hardened, but that does not apply to all of these sensors.

Model	Size [mm]	Mass [g]	Power Consumption [W]	Acceleration Bias Noise [µg]	Angular Bias Instability [$° h^{-1}$]	Angular Random Walk [$°/\sqrt{h}$]
Safran STIM377H [3]	$45 \times 39 \times 22$	55	1.5	40	0.3	0.15
Parker Lord 3DM-CX5-IMU [4]	$38 \times 24 \times 10$	8	0.3	40	8	0.3
SBG Pulse-40 [5]	$30 \times 28 \times 14$	12	0.3	6	0.8	0.08
Vector-Nav Vn-100 [6]	$36 \times 33 \times 9$	15	0.22	40	7	N/A
Vector-Nav Vn-110 [7]	$56 \times 56 \times 23$	12	2	10	1	N/A
Epson M-G362 [8]	$24 \times 24 \times 10$	7	0.2	100	3	0.15
Epson M-G370 [9]	$24 \times 24 \times 10$	10	0.1	12	0.8	0.06
Analog Devices ADIS 16485 [10]	$47 \times 47 \times 14$	N/A	N/A	32	6.25	0.3

[1] Dhiren Kataria, email message to Jort Roelofs, 10th of May, 2022.

[2] Christian Siemes, personal communication with Jort Roelofs, 7th of June 2022

The IMU's considered in the selection can be found in table 11.3. From the IMU's considered in the selection, the Pulse-40 from SBG Systems, pictured in figure 11.2, was selected as it provides the highest accuracy in measuring accelerations. With the given sensitivity, the IMU can measure the non-gravitational accelerations starting at an altitude of 180 km until reentry, according to the simulations performed in chapter 3. However, the relative accelerations between the two satellites will remain below the given accuracy for the entirety of the mission.

As the Pulse-40 IMU is not space-grade, extensive testing will be required to ensure that the component has sufficient reliability. Furthermore, it was decided to have two IMU's on board for redundancy. This has the additional effect that the accuracy of the acceleration measurements can improve, as certain factors that introduce noise to the data are eliminated. Examples of these factors are distance in placement between the IMU and the CoM and movement of the CoM over the course of the mission.

Figure 11.2: Image of the Pulse-40 IMU[11].

The IMU's are mounted inside the structure next to the fuel tanks where they are located close to the CoM. Both are expected to run continuously over the entire mission as they provide gyroscopic data to the ADCS. The sampling frequency of the IMU's is 100 Hz, which is the lowest possible frequency for these IMU's. This is also the attitude determination frequency of the ADCS, as can be read in chapter 9. The scientific data that is to be sent to the ground is then compressed by the on-board to provide measurements every 0.1 Hz, as a higher sampling frequency is not needed for scientific analysis and puts a large strain on the transmission bandwidth provided by the TT&C subsystem. In table 11.4, the properties of the IMU can be found. Table 11.5 contains the performance properties of the IMU.

Table 11.4: Details of the IMU [11].

Component	Size [mm]	Mass [kg]	Power Consumption [W]	Cost [€]	Sampling frequency [Hz]
SBG Systems Pulse-40	$30 \times 28 \times 13.3$	0.012	0.3	23,000	0.1

11.2.3 GNSS Receiver Selection

The GNSS receiver provides the satellite with orbit determination. Furthermore, it is valuable for the scientific goal of the mission by measuring the drift between the two satellites. For this, there is a requirement on the position accuracy, namely REQ-PL-03. This level of accuracy can generally be achieved, as long as a dual-frequency receiver is used. Therefore, selection of GNSS receivers is only done on receivers with multi-frequency capabilities. Furthermore, post-processing of the raw GNSS data is necessary, as on-board positioning relies on the broadcast GNSS position and clock data that has an equivalent accuracy of only 1 m, which is an order of magnitude larger than the desired position accuracy of 0.1 m.

Table 11.5: Performance of the IMU[12].

Parameter	Gyroscope	Accelerometer
Measurement Range	$\pm 490\,^\circ\,s^{-1}$	± 40 g
Random walk	$0.08\,^\circ/\sqrt{h}$	$0.02\,m/s/\sqrt{h}$
Bias instability	$0.8\,^\circ\,h^{-1}$	6 µg

Precise Orbit Determination

A key factor in achieving the required position accuracy is Precise Orbit Determination (POD). In the past, this has successfully been applied to large satellites with custom-made GNSS receivers and recently efforts have been made to apply this to satellites with COTS receivers.

Although the GRACE-FO satellites were fitted with custom-made GNSS receivers, a sensitivity analysis performed on the GPS data of these satellites can provide a reasonable indication on whether the required accuracy can be achieved [67]. From the paper, a number of observations can be made. First, a reasonable improvement in accuracy can be seen when the sampling interval decreases from 120 s to 60 s, but this improvement is only marginal when considering a step between 20 s to 10 s. Therefore, a sampling interval of 10 s as set by the requirements is deemed

[3] https://www.sensonor.com/products/inertial-measurement-units/stim377h/, retrieved on 20/06/2022.
[4] https://www.microstrain.com/inertial-sensors/3dm-cx5-10, retrieved on 20/06/2022.
[5] https://www.sbg-systems.com/products/pulse-imu-sensor/#pulse-40, retrieved on 20/06/2022.
[6] https://www.vectornav.com/products/detail/vn-100, retrieved on 20/06/2022.
[7] https://www.vectornav.com/products/detail/vn-110, retrieved on 20/06/2022.
[8] https://www.texim-europe.com/promotion/777/m-g362%20datasheet_prelim_te.pdf, retrieved on 20/06/2022.
[9] https://global.epson.com/products_and_drivers/sensing_system/imu/g370/, retrieved on 20/06/2022.
[10] https://www.analog.com/en/products/adis16485.html, retrieved on 20/06/2022.
[11] https://www.sbg-systems.com/wp-content/uploads/Pulse-40_IMU-Leaflet.pdf, retrieved on 09-06-2022.

sufficient and decreasing this even more will not have a significant effect. Furthermore, it was found that with the aforementioned sampling interval, sufficient accuracy can be achieved with a duty cycle as low as 20 %.

Analysis of the CASSIOPE satellite also provides valuable insight [68]. The CASSIOPE satellite has 4 COTS GNSS receivers on board for an attitude determination experiment, but its orbit determination is done with data from one receiver only. With POD, the orbit of the CASSIOPE satellite can generally be calculated with a 10 cm 3D RMS error after continuously one orbit with a sampling interval of 1 s. This is significantly lower than what is suggested by the aforementioned sensitivity analysis on the GRACE-FO satellites, but this can for the most part be explained by poor signal quality, as the GNSS antenna's on the CASSIOPE satellite were mounted at the edge of the top panel where it was affected by a large amount of distortions and multipath errors. If a choke ring had been used for the GNSS antennas, the quality of the signal would have increased by a reasonable amount.

From the presented cases, it is clear that with the use of dual-frequency GNSS and POD, a positioning accuracy of better than 10 cm can be achieved.

GNSS receiver selection

The accuracy that can be achieved with POD is also directly related to the performance of the GNSS receiver itself. The Pumpkinspace GNSS Receiver Module is expected to achieve good performance. It is based on the Novatel OEM719 receiver, which was also used on the SOAR mission [66]. Furthermore, it is a successor of the receivers used on the CASSIOPE, namely the NovAtel OEM4-G2L [68].

The receiver module, presented in figure 11.3, is located inside the structure, close to the -z surface. As stated before, a sampling interval of 10 s was found to be more than sufficient. The selected receiver has 555 channels to track satellites and has capabilities for multi-frequency and multi-constellation measurements. The selected Pumpkinspace board however is only limited to GPS on the L1 and L2 frequencies. More details of the GNSS receiver can be found in table 11.6. The module is expected to run constantly, also in non-science modes. This ensures that the highest possible position accuracy is achieved.

Because the GNSS receiver is critical to the mission, it was considered to include a second receiver for redundancy. This was discarded for a number of reasons. First, the selected receiver is space-grade, flight proven, and is therefore expected to operate in the space environment. Second, the CASSIOPE has multiple predecessor receivers on board, and these have proven to be reliable [68]. Of the four receivers, one receiver malfunctioned after 5 years, after which a spare receiver was activated. The remaining receivers are functioning properly at the time of writing, which is close to 9 years after launch. This is more than enough for the SCATTER mission, which is expected to be shorter than 3 years. Furthermore, the receivers for the CASSIOPE mission are operating in a harsher environment, as the apogee of the satellite is located at an altitude of 1400 km where the radiation is much stronger compared to what is expected for the SCATTER mission. Therefore, a single GNSS receiver was considered sufficient.

Table 11.6: Details of the GNSS receiver[13].

Component	Size [mm]	Mass [kg]	Power Consumption [W]	Cost [€]	Sampling frequency [Hz]	Real-time position accuracy [m]
Pumpkinspace GPS Receiver Module	$96 \times 90 \times 18.1$	0.109	1.5	20,000	0.1	1.2

GNSS Antenna Selection

For GNSS, 2 types of antennas are generally used: patch and helix antennas. However, helix antennas were not considered for this selection. The reasons for this are the same as the reasons why patch antennas were selected over helix antennas for the TT&C subsystem, primarily due to the volume and requirement to deploy the antenna. Therefore, selection of GNSS antennas was done with patch antennas only.

$$SNR[dB] = P_{GPS} + G_{ant} + G_{LNA} - L_{FS} - L_{ax} - L_{LNA} + N \tag{11.1}$$

$$N[dBW] = 10 \log kT_E B \tag{11.2}$$

The position accuracy for a GNSS receiver is directly related to the signal quality. Therefore, it is desired to maximize the potential Signal-to-Noise Ratio (SNR). An antenna was selected that provides the highest SNR, as can be calculated with equation 11.1. GPS satellites transmit their signals with approximately 500 W including gain. G_{ant}, G_{LNA}, L_{ax}, and L_{LNA} are the antenna gain, low-noise-amplifier gain, axial ratio loss, and low-noise-amplifier loss, which are all antenna properties and allow selection of an antenna. L_{FS} was calculated with equation 10.3, where a scenario was with the highest possible free space loss that can be expected during the mission. This is in an orbit at 150 km where the GPS satellite is located at an elevation of 0° for the antenna, equivalent to the satellite being at the horizon. The receiver noise can be calculated with section 11.2.3 where k is Boltzmann's constant and T_E is the effective noise temperature of the receiver. The effective noise temperature is dependent on multiple variable such as sky noise, antenna noise temperature, and more, but is assumed to be

constant for every antenna as 513 K [69]. Finally, B is the antenna bandwidth, which is also different for each antenna.

Figure 11.3: Image of the Pumpkinspace GPS Receiver Module[14].

Figure 11.4: Image of the Tallysman TW3882E Dual-band GNSS antenna[15].

As antenna, the Tallysman TW3882E was selected. It is presented in figure 11.4. Due to its strong low-noise-amplifier, it provides the highest SNR. Its low axial ratio makes it also suitable for the need for high quality measurements, as it ensures there is little variation between signals coming in from different directions. The calculated SNR can be found in table 11.8. The details of the antenna are listed in table 11.7. To provide high accuracy measurements, the antenna is located at the center of the -z surface. By placing it at the centre, the chance of multipath errors is minimized. Furthermore, it is given a wide FoV to maximize the quality of the measurements, as only a panel slightly reduces its FoV.

Table 11.7: Details of the GNSS antenna[16].

Component	**Size [mm]**	**Mass [kg]**	**Power Consumption [W]**	**Cost [€]**
Tallysman TW3882E	60⌀ × 16.2	0.07	Included in receiver consumption	250

Table 11.8: Link budget for the GNSS antenna.

Parameter	**GPS L1**	**GPS L2**
Frequency f [GHz]	1.57542	1.22760
Bandwidth B [MHz]	1559 – 1606	1191 – 1255
Transmitter Power P_t [dBW]	26.9897	26.9897
Distance S [km]	25743.3	25743.3
Free space loss L_{FS} [dB]	-184.609	-182.442
Antenna gain G_t [dBic]	4.5	4
Axial ratio loss L_{ax} [dB]	-1	-1.5
Receiver noise loss N [dBW]	124.777	123.436
Low noise amplifier gain G_{LNA} [dB]	35	35
Low noise amplifier loss L_{LNA} [dB]	-2.5	-2.5
SNR [dB]	**3.1577**	**2.9837**

11.2.4 Sensitivity Analysis

As 2 identical mass spectrometers are mounted on each spacecraft, each mass spectrometer could be tuned to a specific mass region and increase its resolution within that region. However, due to the limited availability of data on present-day space mass spectrometers and due to the highly specialized nature of the application of mass spectrometers in space flight, it cannot be said with certainty how much this affects the resolution and the subsequent accuracy of particle and temperature measurements. Furthermore, the power consumption of the payload segment would increase significantly, which affects the mission negatively. For example, time spent in science mode would be reduced by 34 % in phase 3.

Another aspect worth investigating is the choice of a single-frequency GNSS receiver. Research indicates that modern POD methods could approach or even achieve a 10 cm RMS accuracy on single-frequency GNSS [70][71]. However, it may require a high sampling frequency and high duty cycle, which could increase stress on multiple subsystems such as C&DH and TT&C. This increases the risk of mission failure which is not desirable. Therefore, it is still desired to use a dual-frequency GNSS receiver.

[14] `https://www.pumpkinspace.com/store/p58/GNSS_Receiver_Module_%28GPSRM_1%29_Kit.html`, retrieved on 13-06-2022.
[15] `https://www.tallysman.com/product/tw3882e-embedded-dual-band-gnss-antenna/`, retrieved on 10-06-2022.

11.3 Payload Subsystem Requirements Verification

The verification of the Payload Subsystem by compliance with requirements is given below:

REQ-PL-01: - this requirement is verified through inspection of the datasheet of the Pulse 40 IMU [17], which states that the gyroscope has a bias instability of $0.8\,^{\circ}\,\mathrm{h}^{-1}$. Therefore, it is satisfied;

REQ-PL-02: - this requirement is verified through inspection of the datasheet of the Pulse 40 IMU [17], which states that gyroscope has a bias instability of $0.08\,^{\circ}/\sqrt{\mathrm{h}}$. Therefore, it is satisfied;

REQ-PL-03: - this requirement shall be verified in future stages of the design through ground-based qualification testing of the GPSRM 1 GPS Receiver Module [18].;

REQ-PL-04: - this requirement is verified through inspection of the SCATTER external layout shown in section 13.1. As shown, the GPS patch antenna is placed 119 mm away from the -X axis edge of the satellite, which yields a field of view of 172.6° in the -Z axis (Zenith). Therefore, the requirement is satisfied;

REQ-PL-05: - this requirement shall be verified through ground-based testing of the QB50 INMS [23], in conditions similar to those imposed by the mission;

REQ-PL-06: - this requirement shall be verified through ground-based testing of the QB50 INMS [23], in conditions similar to those imposed by the mission;

REQ-PL-07: - this requirement shall be verified through ground-based testing of the QB50 INMS [23], in conditions similar to those imposed by the mission;

REQ-PL-08: - this requirement shall be verified through ground-based testing of the QB50 INMS [23], in conditions similar to those imposed by the mission;

REQ-PL-09: - this requirement shall be verified through ground-based testing of the QB50 INMS [23], in conditions similar to those imposed by the mission;

REQ-PL-10: - this requirement shall be verified through ground-based testing of the QB50 INMS [23], in conditions similar to those imposed by the mission;

REQ-PL-11: - this requirement is verified through inspection of the Pulse 40 IMU [17]. As shown, the bias instability of the accelerometer is $6\,\mu\mathrm{g} \approx 6 \cdot 10^{-5}\,\mathrm{m^2\,s^{-1}}$, which does not satisfy the requirement;

REQ-PL-12: - this requirement shall be verified in future stages of the design through ground-based qualification testing of the GPSRM 1 GPS Receiver Module [18];

REQ-PL-13: - this requirement shall be verified through ground-based testing of the QB50 Mass Spectrometer [23], in conditions similar to those imposed by the mission;

REQ-PL-14: - this requirement is verified through inspection of the external layout of SCATTER, which is outlined in section 13.1. As shown, the mass spectrometers lie together on a $100\,\mathrm{mm} \times 100\,\mathrm{mm}$ face of the satellite, without any solar panels or sensors mounted on the same surface. Therefore the requirement is satisfied;

11.3.1 Payload Subsystem Concluding Remarks

As mentioned before, the reliability of the mass spectrometer could be low to an extent that it significantly decreases the value of data accumulated by the mission. That is why a second mass spectrometer was integrated for redundancy. The CIRCE satellites that will be launched are expected to provide more information on this. One possible outcome could be that their reliability is sufficiently high that a second mass spectrometer would be unnecessary. In that case, the space could be used for another payload instrument. One example of these is a wind sensor as proposed for the CASPA-ADM mission [72].

Another aspect to consider is the GNSS receiver which uses GPS by default. Compatibility with other constellations such as GLONASS and Galileo could also be provided by the board manufacturer. Due to current geo-politics GLONASS may not be a good choice, but Galileo is an attractive alternative as it is guaranteed by the EU to be available for civilian use, in contrast to GPS. Further research should determine whether Galileo provides more benefits compared to GPS. Using multi-constellation capabilities with both GPS and Galileo is also an alternative.

Finally, during the design process, the usage of a choke ring for the GNSS antenna was not considered. A choke ring could prevent multipath errors and subsequently increase the quality of measurements. Therefore, further investigation is required in the application of a choke ring.

[17] `https://www.sbg-systems.com/products/pulse-imu-sensor/`, retrieved on 09-06-2022.

[18] `https://www.pumpkinspace.com/store/p58/GNSS_Receiver_Module_%28GPSRM_1%29_Kit.html`, retrieved on 13-06-2022.

12. Command & Data Handling Subsystem Design

The final subsystem which must be analysed on a detailed design scale is the Command & Data Handling (C&DH) subsystem. The C&DH subsystem is responsible for ensuring that the scientific and housekeeping measurements conducted by the spacecraft are correctly processed, stored and transmitted by the TT&C antenna when within range of a ground station. Furthermore, the C&DH subsystem is also responsible for commanding the various individual subsystems of the spacecraft during the different flight phases based on the commands received from the ground. The design of this subsystem therefore requires a detailed understanding of the inputs and outputs of every component on the spacecraft, and of how the flow of information between these components can be done efficiently while minimizing single points of failure. This chapter is structured similarly as chapter 4 to chapter 11: first the subsystem requirements are clearly described, as well as a justification for their inclusion and the parent system requirement in section 12.1. Next, section 12.2 explains the detailed design of the C&DH subsystem, including an analysis of the computing power, memory storage and interfacing required. This information is visualized with a data handling block diagram at the end of the section. Finally, subsystem verification and validation is conducted in section 12.3, including a compliance matrix.

12.1 Command & Data Handling Subsystem Requirements

In this section, the C&DH subsystem requirements are presented in Table 12.1. These (in combination with the specifications of the other subsystems which require command and data handling) will drive the detailed design process which will take place in the subsequent sections of this chapter.

Table 12.1: Requirements for the C&DH subsystem.

ID	Description	Parent Requirement	Rationale
REQ-CDH-01	~~The C&DH subsystem shall have a mass of at most, 0.3 kg~~	REQ-SYS-D-03	This requirement is struck out as this is an issue for the mass budgeting on a system level. Therefore, a requirement here would just constrain the design.
REQ-CDH-02	~~The C&DH subsystem shall have a volume of at most 0.5U~~	EQ-SYS-D-07	This requirement is struck out as this is an issue for the size budgeting on a system level. Therefore, a requirement here would just constrain the design.
REQ-CDH-03	~~The C&DH subsystem shall consume a power of at most 1 W~~	REQ-EPS-03	This is a power budget issue, and not a requirement. The EPS will be sized according to the sum of the subsystems power usage
REQ-CDH-04	The C&DH subsystem shall store all the needed scientific data for the duration of at least 3 days	REQ-SYS-F-12, REQ-SYS-P-19	The system needs to function without communications for 3 days, which includes storing all the data that appears in the meantime.
REQ-CDH-05	The C&DH subsystem shall store all the needed housekeeping data for the duration of at least 3 days.	REQ-SYS-F-12, REQ-SYS-P-19	The system needs to function without communications for 3 days, which includes storing all the data that appears in the meantime.
REQ-CDH-06	~~The C&DH subsystem shall have a throughput of at least 4000 KIPS~~	REQ-SYS-F-31	No analysis on this topic will be made during this design phase.
REQ-CDH-07	The C&DH subsystem components shall have a mission lifetime of at least three years	REQ-M-22	The mission lifetime is required to be less than 3 years, hence the C&DH subsystem components should respect this.
REQ-CDH-08	The C&DH shall interface with all external sensors and actuators onboard	REQ-SYS-F-31,	Derived from the requirement that all subsystems and payload need to be connected via the onboard computer.
REQ-CDH-09	The C&DH shall provide reconfiguration capabilities for components with single points of failure, in case a malfunction is detected	REQ-M-22	In case of software failures, the C&DH system should be able to receive updates from the ground station to reconfigure its code
REQ-CDH-10	~~The C&DH subsystem shall be operational in a temperature range of −25 to 65 C~~	REQ-M-14	Requirement has been moved to TCS requirements
REQ-CHD-11	~~The On-Board Computer shall have two independent memory storage units to store all scientific measurements prior to transmission~~		Removed due to a lack of parent requirements

12.2 Command & Data Handling Subsystem Overview

With the subsystem requirements of the C&DH outlined in detail, the design of the subsystem may now be completed. This is done by first the data rates passing through each subsystem to the on-board computer. The handling of the measured scientific and housekeeping data will ultimately drive the sizing of the required memory on-board. Once this analysis is completed, the selection of the OBC may take place. This will mainly be done through an analysis of available OBC products for European CubeSat missions. Following from this, the placement of software watchdogs is briefly discussed and the communications interfacing between the various subsystems is analysed, to build the complete C&DH architecture. The data handling block diagram summarizes all the information into a clear visual representation.

12.2.1 Analysis of the Data Handling Functionality of the C&DH Subsystem - Sizing of the Required Memory

The data handling functionality of the C&DH is vital to ensuring that the measured data from the scientific instruments and other subsystems can be stored until it can be relayed to the ground station for further post-processing. Furthermore, in the event that only a fraction of the sampled data is relayed to the ground, then the C&DH must first process the data such that only the necessary information is stored while the other data is either forwarded to another subsystem for command, or discarded altogether. These elements will drive the required storage space and the required data processing algorithms. In order to get a detailed overview of both these design aspects, an analysis into each subsystem requiring data handling must be done. This is completed in the enumerated list below.

- **Payload - Mass Spectrometer**: The mass spectrometer is one of the primary pieces of equipment generating scientific data. When operational, the mass spectrometer can be commanded to produce either housekeeping or scientific data packets. These data packets will always consist of 1392 bits, and the rate at which these packets are generated is a choice made by the user (which in this case, was conducted in Chapter 11) based on the quality of the scientific information which is to be sent to the ground. This was found to be 0.1 Hz. No information measured here will play a role in the commanding of the spacecraft, therefore, the unedited sampled data can be directly stored until sent to ground.
- **Payload - GNSS**: The GNSS receiver is another large contributor to the generation of scientific data, as it provides detailed positional and velocity information of each satellite. The data packet of the GNSS receiver is 800 bits, and once again, based on the information provided in Chapter 11, the sampling frequency of this instrument is 0.1 Hz.[1] No data here needs to be used for command, so the unedited data can be preserved and stored.
- **Payload - IMU**: The IMU is the final scientific instrument which forms the payload of the spacecraft. Its response data packets are of 328 bits, which contain information such as the change in velocity and angle in all three axes.[2] The information obtained from the IMU is important for the pointing accuracy of the ADCS subsystem, therefore an initial sample frequency of 100 Hz is selected. However, such high sample rate does not need to be sent to the ground. Therefore, due to its large packet size, from this data only 0.1 Hz will be used stored for transmission to ground. Therefore, a sampling software will need to be included in the OBC.
- **ADCS - Magnetorquer**: While the magnetorquer does produce housekeeping telemetry on the temperature and the current, based on the analysis made on Chapter 9, this information only needs to be relayed to the OBC and not sent to the ground station directly.[3]
- **ADCS - Magnetometer**: The magnetometer returns key information on the spacecraft attitude in the form of the three vector components of the magnetic field direction.[4] As there is no information available on the size of each response packet, it is assumed that each of these components are of a single point floating point precision (as six to nine digits of accuracy is sufficient for many telemetry outputs, and this assumption will be carried through for many components), which is of a size of 32 bits. Three components therefore leads to a total packet size of 96 bits. For complete attitude determination, this measurement must be sampled at 100 Hz as described in chapter 9. However, not all of this data will be transmitted to the ground, as a much lower sampling rate will also allow for sufficient post-processing. Instead, only 1 Hz will be sent. Thus, similarly to the IMU, a sampling software will be required for this data as well on-board the OBC.
- **ADCS - Sun Sensor**: The Sun Sensor data handling follows the exact same procedure as the magnetometer; however, here the vector is a three-dimensional Sun Vector rather than magnetic field.[5]
- **ADCS - Reaction Wheels**: The reaction wheel data handling follows the same procedure as the preceding two components; however, here only one angular velocity value is returned, so the packet size is 32-bit rather than 96-bit per measurement.
- **OCS - Thruster**: The thrusters have a number of key telemetry features that must be monitored to ensure its proper health. This mainly includes telemetry from the temperature and pressure sensors in key locations of the thruster system, as well as the status of the main actuators.[6] There are ten sensors monitoring temperature and pressure, and 11 actuators, each producing a telemetry 32-bit value. In total, this leads to a packet size of 672 bits. The sampling frequency was selected to be 1 Hz, as discussed in Chapter 8.
- **EPS - PDU**: As explained in Chapter 5, the PDU is responsible for ensuring that the power stored by the batteries and the power generated by the solar arrays is properly sent to all the other subsystems within the spacecraft. To ensure that this power distributed properly, the voltage regulators must be monitored. There are 4 voltage regulators, each with a 32-bit data value (assumed).[7] Additionally, the temperature of the main

[1] http://www.pumpkininc.com/space/datasheet/710-00908-D_DS_GPSRM_1.pdf
[2] https://support.sbg-systems.com/sc/imu/latest/user-manual/digital-interfaces
[3] https://www.isispace.nl/product/isis-magnetorquer-board/
[4] https://www.newspacesystems.com/wp-content/uploads/2021/10/NewSpace-Magnetometer_20211018_2020_10e.pdf
[5] https://www.newspacesystems.com/wp-content/uploads/2021/10/NewSpace-Sun-Sensor_20211018_2020-10e.pdf
[6] https://satsearch.co/products/nanoavionics-propulsion-system-epss-c2
[7] https://www.isispace.nl/wp-content/uploads/2019/12/ISIS-iMEPSv2-DS-00001-iEPS_Datasheet_v0.2-.pdf

computer of the PDU is also monitored to prevent overheating. Therefore, the total packet size is 160 bits and, based on the results from Chapter 5, and a sampling rate of 1 Hz is found to be sufficient for the ground station.

- **EPS - PCU**: Very similarly to the PDU, the PCU ensures that the outputted power which is distributed through the PDU to the other subsystems is of the appropriate current and power values.[8] This must be measured across each channel, of which there are 16 per PCU (four regulators per PCU/PDU, and four channels per regulator, as explained in Chapter 5. Therefore, the packet size for the PCU is 1024 bits (32 data points multiplied by 32), and similarly to the PDU, the sampling rate is 1 Hz.
- **EPS - Battery Unit**: The battery unit telemetry monitors the health of the cells themselves. There are four cells per battery unit, and each cell's voltage, current and power is measured.[9] Therefore, the packet size for each battery unit is 288 bits (9 data points multiplied by 32) and conforming with the other EPS telemetry points, the sample frequency is 1 Hz.
- **Temperature Sensors**: Asides from the integrated temperature measurements which are included in the response data packets of other subsystems, there are a number of dedicated temperature sensors to monitor the health of the CubeSat in critical areas (particularly the solar panels and battery packs). The temperature readings are assumed to be 32 bits each, and the number of readings corresponds to the number of temperature sensors, as described in section 7.3.1. Furthermore, to the gradual nature of temperature fluctuations, a sample frequency of 1 Hz is sufficient.

The results from the above analysis can be summarized in table 12.2. Included in the table is also the number of each component which is expected to be active at the same instance in time. Furthermore, each component is characterized as either scientific or housekeeping data; however, both data types will be stored in the same location in solid-state memory. At the bottom of the table, the total expected data rate to be passed on through the OBC and into solid-state memory is indicated to be 7.16 kbps. Based on REQ-CDH-04 and REQ-CDH-05, there must be enough space to store both the housekeeping data for a duration of at least three days. Therefore, assuming that throughout this duration these components will continue to relay this information at the aforementioned data rate, the total amount of memory that must be stored 1875778 kilobits, or equivalently, 234 Megabytes. Taking a safety factor of two into consideration due to the uncertainty with the assumed packet size for many telemetry points and the potential for storing on-board post-processed data (see section 13.5), the total amount of memory to size for in the spacecraft is 468 Megabytes. This amount of memory can be easily stored in standard microSD or SD cards, therefore this is well within the available design space. Depending on the selection of On-Board computer, this memory storage can be internal to the computer or mounted as an external connection in the C&DH subsystem. This decision will be made following the selection of the OBC.

Table 12.2: Telemetry data rate for all key subsystems in the spacecraft design.

Component	Parent Subsystem	Quantity	Type of Data	Packet Size [bits]	Sample Frequency [Hz]	Data Rate [bps]
Mass Spectrometer	Payload	1	Scientific	1392	0.1	139.2
Inertial Measurement Unit	Payload	2	Scientific	328	0.1	65.6
GNSS Receiver	Payload	1	Scientific	800	0.1	80
Magnetorquer	ADCS	1	Housekeeping	0	0	0
Magnetometer	ADCS	2	Housekeeping	96	1	192
Sun Sensor	ADCS	6	Housekeeping	96	1	576
Reaction Wheels	ADCS	4	Housekeeping	32	1	128
Thrusters	OCS	2	Housekeeping	1024	1	2048
PDU	EPS	2	Housekeeping	160	1	320
PCU	EPS	2	Housekeeping	672	1	1344
BCU	EPS	4	Housekeeping	288	1	1152
Temperature Sensors	TCS	35	Housekeeping	32	1	1120
Total		**62**		**4920**		**7164.8**

12.2.2 OBC Selection

Following the analysis of the data rates for the memory storage components and the TT&C subsystem, the next step is to select the components for the OBC, and to decide the placement of any software and hardware watchdogs throughout the C&DH system. The selection of the OBC requires an in-depth analysis of the required clock speed, the instruction throughput of the microcontroller in the OBC, available rapid memory and other detailed analysis of the exact hardware. As much of this information is protected by non-disclosure agreements of the suppliers themselves, such an analysis is outside the scope of this design stage. As a result, a more empirical approach is taken based on available OBCs for European CubeSat missions. Within Europe, there are a number of primary suppliers for OBCs: namely Endurosat, GOMSpace, Nanoavionics and IsisSpace. While the OBC provided by

[8] https://www.isispace.nl/wp-content/uploads/2019/12/ISIS-iMEPSv2-DS-00001-iEPS_Datasheet_v0.2-.pdf
[9] https://www.isispace.nl/wp-content/uploads/2019/12/ISIS-iMEPSv2-DS-00001-iEPS_Datasheet_v0.2-.pdf

each supplier does have subtle differences, many key elements do remain the same. In each of the OBC (apart from the GOMSpace product), the main computing unit is a 32-bit processor provided by ARM, with a clock speed of 400 MHz.[10][11][12][13] With regard to code storage, all of them vary from 512 kB to 3 MB. Finally, each of them have a mass of about 100 g, a power consumption of at most 1 W and dimensions of 100 mm in width, 100 mm in length and 10 mm in height. Because these key features are universal across all commercial products for OBCs dedicated to CubeSat missions, and because the number of components which require data handling in this system (62) conforms with other CubeSat missions, it can be concluded that any of these products should be sufficient for the task at hand. As a result of this, comparison of these products is based upon the available documentation for detailed design and the variety of available communication interfaces with other subsystems in the spacecraft. When performing a comparison based on these factors, the product of NanoAvionics (officially called the SatBus 3C2) became an attractive option due to the availability of detailed documentation of the product which is available for free access. Furthermore, while this will become evident only in the following subsection, there is a high demand for interfaces with I2C and UART communication protocols, especially for ADCS, EPS and payload components. The SatBus 3C2 has 4 I2C and 3 UART interfaces, which is more than the Endurosat equivalent, which only has 2 I2C interfaces and 3 UART interfaces.[14][15] The other products do not have this information freely available. Therefore, it was concluded that the SatBus 3C2 is the most suitable OBC for this satellite design. An image of the OBC, as well as the key specifications and available interfaces are provided in table 12.3 and figure 12.1, respectively. It is important to note that as the solid state memory available with the OBC is 4 GB, there is more than enough room available for the storage of the required housekeeping and scientific data as described in section 12.2.1.

Table 12.3: Key specifications of the Nanoavionics SatBus 3C2[16].

Parameter	Value	Unit
Name	SatBus3C2	-
Manufacturer	NanoAvionics	-
Mass	62	g
Dimensions [width, length, height]	95.50 x 90.17 x 6.57	mm
Processor	ARM Cortex M7, 400 MHz	-
Code Memory	3	MB
Solid Drive Memory (for Housekeeping & Scientific Data Storage	4	GB
Total allowed radiation exposure	20	krad
UART Interfaces	3	-
I2C Interfaces	3	-
CAN Interfaces	2	-
SPI Interfaces	3	-
RS-485 Interfaces	0	-

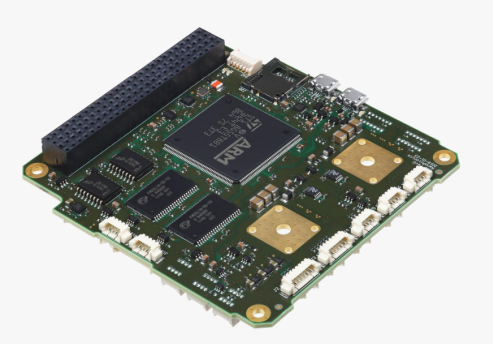

Figure 12.1: NanoAvionics SatBus 3C2 OBC - Chosen OBC for this spacecraft design (Courtesy of NanoAvionics[17]).

12.2.3 Communication Interfacing and Generation of C&DH architecture

The analysis of the data rates and the selection of the OBC allows for the construction of the C&DH architecture to take place. The generation of a C&DH architecture depends primarily on ensuring that the OBC can provide the required communications protocols to the other subsystems, and making sure that there are sufficient redundancies in the communications system in case there is a failure in an electrical component. With that in mind, the data handling block diagram which shows the data travelling from the subsystems and the OBC (and vice versa), and the protocols which are used for communication are shown in figure 12.2. As it can be seen, due to the high number of subsystems and components which require command and/or data handling, the OBC alone could not satisfy all the required interfaces. Therefore, a custom daughterboard is needed to be added as part of the main processing element of the spacecraft in order to provide all required communication. More information regarding the exact nature of this board will be provided in the next subsection. The decision to place certain subsystem communications on the OBC while others on the daughter board was aimed at maximizing the potential redundancy in case either the OBC or the daughter board fails. For example, for both the EPS and the OCS subsystems, all components are connected to both the on-board computer and the daughterboard via a CAN and I2C connection, respectively. As a result, if there is a communication breakdown between the OBC and these components, then the daughterboard can communicate directly to these components for redundancy. In the case

[10] https://nanoavionics.com/cubesat-components/cubesat-on-board-computer-main-bus-unit-satbus-3c2/
[11] https://www.endurosat.com/cubesat-store/cubesat-obc/onboard-computer-obc/#modifications
[12] https://www.isispace.nl/product/on-board-computer/
[13] https://gomspace.com/shop/subsystems/command-and-data-handling/nanomind-a3200.aspx
[14] https://nanoavionics.com/cubesat-components/cubesat-on-board-computer-main-bus-unit-satbus-3c2/
[15] https://www.endurosat.com/cubesat-store/cubesat-obc/onboard-computer-obc/#modifications
[16] https://nanoavionics.com/cubesat-components/cubesat-on-board-computer-main-bus-unit-satbus-3c2/
[17] https://nanoavionics.com/cubesat-components/

of TT&C, the primary antenna is connected to the OBC while the other is connected to the daughterboard. Finally, for the ADCS and the Payload subsystem components, they were split in two groups such that in case of communication failure of one of the boards, then there is still a possibility for partial functionality so that the mission objectives can be partially fulfilled. An overview of the components which one board can control in case of failure in the other is shown in table 12.4. With this reliability ensured, the architecture of the C&DH is complete.

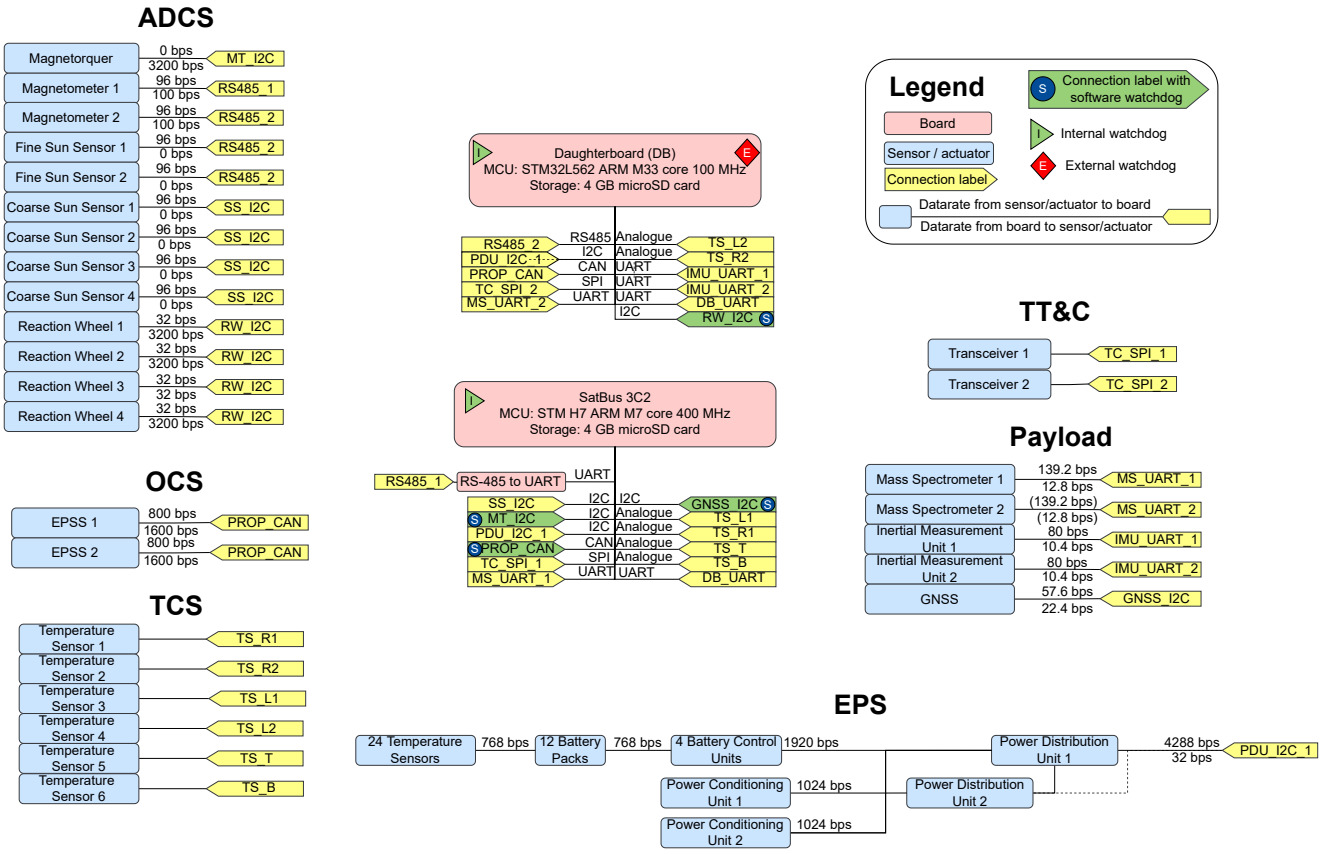

Figure 12.2: Data handling block diagram for project SCATTER.

Table 12.4: Components which can be controlled individually by the OBC and the daughterboard if the other one fails.

Only OBC	Only daughterboard
One Magnetometer	One Magnetometer
Four Coarse Sun Sensors	Two IMUs
Magnetorquer	Four Reaction Wheels
GNSS	One Mass Spectrometer
One Mass Spectrometer	Transceiver
Transceiver	EPS Subsystem
EPS Subsystem	OCS Subsystem
OCS Subsystem	

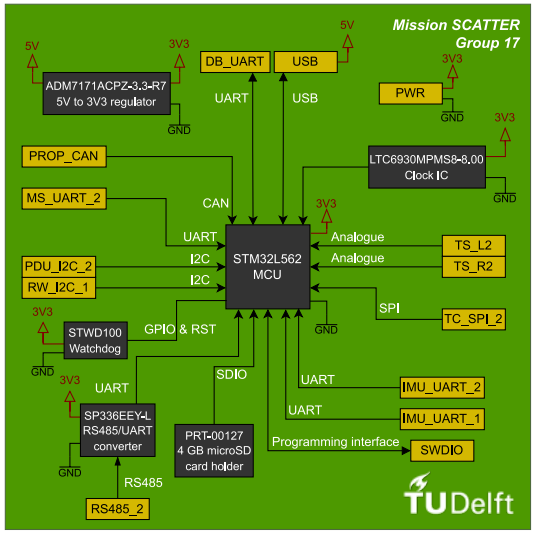

Figure 12.3: Simplified schematics of the custom-designed daughterboard. The principal components / ICs are represented in dark grey, the connection points in golden, the power voltage connections with red arrows and the voltage level (3V3, 5V), the grounding connections with GND and the in-board connections with black arrows, on which the connection protocol is indicated with white text.

12.2.4 Description of the daughterboard

As was described in the previous subsection, the necessity for a custom daughterboard appeared due to a need to provide the required amount of communication interfaces, and was also beneficial to provide additional reliability in case the communication to a component happens to unexpectedly fail. This subsection provides more detail about the exact design that the daughterboard requires in order to fulfil the interfacing. Due to being a custom-made board, it will require a great amount of space-proofing and testing. A simplified schematic of the daughterboard is included in figure 12.3.

The main component of the daughterboard is the MCU, which is an STM32L562 microcontroller[18]. It was chosen to have the same STM32 architecture as the OBC, but with a lower performance and thus lower power consumption. During nominal operations, most of the data processing and operations will be done on the OBC MCU; therefore, the MCU of the daughterboard does not need to be as powerful, having a frequency of 110 MHz. This MCU has all the connections needed for interfacing with the remaining sensors, actuators, storage and other communications. Of these, the ones that are used are outlined in table 12.5.

Table 12.5: Daughterboard external connections, their description and communications protocol where applicable.

Connection ID	Description	Protocol to MCU
`PDU_I2C_2`	Connection from the second PDU of EPS	I2C
`RW_I2C_1`	Connection from the four reaction wheels group of ADCS	I2C
`TC_SPI_2`	Connection from the second transceiver of TT&C	SPI
`IMU_UART_1`	Connection from the first IMU of payload	UART
`IMU_UART_2`	Connection from the second IMU of payload	UART
`MS_UART_2`	Connection from the second mass spectrometer of payload	UART
`DB_UART`	Connection between the daughterboard and the OBC. All collected data by the DB MCU will be relayed through this connection.	UART
`RS485_2`	Connection from the two fine sun sensors and the second magnetometer. RS485 can be implemented in a master-slave configuration, which allows having multiple slaves connected to the same dataline. The MCU contains a driver for RS485 communication on its UART lines; however, the voltage levels of the signal are not according to the RS485 standard. Therefore, a converter is needed.	UART
`PROP_CAN`	CAN bus connection between the two propulsion units and the MCU. CAN-bus does not operate on a master-slave configuration, but on a preference-based hierarchy. Therefore, multiple components can be connected without assigning specific roles.	CAN
`TS_L2`	Connection from the L2 solar panel temperature sensor. Because it is analogue, the data will be transformed to digital using the internal ADC (analogue-to-digital converter) of the MCU.	Analogue
`TS_R2`	Connection from the R2 solar panel temperature sensor. Same situation as `TS_L2`	Analogue
`SWDIO`	Programming interface for the MCU. Using an SWDIO connector, the MCU code can be changed to the required software. The same line can be used for diagnostics and testing. This interface is not used during in-space operations.	SWDIO
`USB`	Communications and power interface. A standard micro-USB or USB-C connector can be used with this line, reading / writing data, reprogramming the MCU and providing 5 V of power when plugged in. This interface is not used during in-space operations.	USB
`PWR`	3.3 V power connection from EPS. The only source of power of the board while in-orbit.	None

Furthermore, the components / integrated circuits (ICs) used in the daughterboard are summarised in table 12.6. All the components shown in table 12.6 are recommended components, and can be changed with other ICs that perform the same function. They have all been chosen such that they can operate in the temperature range of $-40\,°C$ to $85\,°C$.

Table 12.6: Daughterboard components, recommended ICs, their description and connections to the MCU where applicable.

Component	Possible IC	Description	Connection to MCU
External watchdog	STWD100[19]	The external watchdog timer acts as another barrier against software errors that might freeze the MCU, besides the internal one.	GPIO & RST
MicroSD cardholder	PRT-00127[20]	Interface where a 4 GB microSD card will be placed and used for storage.	SDIO
External clock IC	LTC6930M PMS8-8.00[21]	This IC provides the MCU with an external cock signal that is usually more accurate than the internal clock of the MCU and thus improves its performance. It replaces the required external crystal oscillator, which requires a more complicated interface.	Reserved pin on MCU
RS485 to UART converter	SP336EEY-L[22]	This converter is needed to translate the 3.3 V unipolar signals from the MCU UART to the bipolar RS485 standard	UART
5 V to 3.3 V regulator	ADM7171A CPZ-3.3-R7[23]	This IC regulates the input voltage from the USB (5 V) to the nominal voltage of the board (3.3 V). It is only used with the USB connection and thus is non-operative in-orbit.	None

[18] `https://nl.mouser.com/datasheet/2/389/dm00532745-1799456.pdf`

12.2.5 Watchdog placement

The final element of the C&DH subsystem which has not yet been addressed is the placement of watchdogs in case of a software time-out. In the data handling block diagram, MCU watchdogs are denoted as "internal" with an "I", and "external" with an "E". The STM32 MCUs used in both the OBC and the daughterboard have an internal watchdog timer included in the package[24][25]. However, especially in missions on which manual maintenance cannot be made and the application is critical, such an unmanned space mission, it is good practice to have an additional external watchdog timer[26], in case the whole MCU package fails.

For the chosen OBC, no information is made available regarding an external watchdog timer. As no further data could be obtained from the manufacturer at this stage of the design, it is recommended in future stages to investigate with the manufacturer this problem. For the daughterboard, as shown in the previous subsection, an STWD100 series external watchdog timer is recommended for the design, which will reset the MCU in case of a failure. It receives a periodic signal from the MCU which resets its timer. If it does not receive this signal for a long period of time, it will reset the MCU using the RST pin.

Besides the MCU watchdogs, it was decided to also include software watchdogs for the components that are single points of failure; i.e., there are no redundant back-ups for them. The only ones connected to the OBC are the magnetorquer and the GNSS. The only ones connected to the daughterboard are the four reaction wheels. The propulsion units are connected to both through the CAN bus. A software watchdog will work in the following way: when the sensor / actuator no longer communicates with the MCU, it will reset the sensor / actuator using one of the available GPIO pins, which will be connected to the RST pin of each of them. As the OBC has four GPIO pins and two output pins available, it will be used to watchdog the magnetorquer, the GNSS and the two propulsion units. The daughterboard will watchdog the four reaction wheels.

12.2.6 Sensitivity Analysis

Firstly, the sampling frequency of all subsystems can be varied and its effect on the required memory quantified. Secondly, the flexibility of the C&DH architecture can be analysed, by changing some of the subsystem interfaces.

In figure 12.4, the required storage with scaling the sampling rate of all subsystems is shown. The scale of the x-axis is logarithmic. It can be seen that the limit of 4 GB of available storage is reached for a scaling factor of around 8.5. In figure 12.5, the required storage as a function of payload sampling rate is shown. The 4 GB limit is reached for around 43.45 Hz. However, raising the payload sampling frequency from the original 0.1 Hz to 10 Hz does not affect the storage in a critical way, only raising the requirement to around 1.27 GB. Therefore, it is recommended to increase the payload sampling rate to 10 Hz, while retaining the other component's original sampling rates, as their data is not as valuable. This amount of data can still be sent by the TT&C subsystem, as the link budget still closes well above the required margin, as said in section 10.3.3.

Regarding the connections, the OBC currently has most interfaces such as I2C, UART and its analogue-to-digital converters occupied. However, there are still two SPI connections open. This means that if any components change their communications protocol to SPI, there is a great chance that a direct connection to the OBC is possible. However, is any of the other communications protocols need to be used, these new connections would need to be added to the custom daughterboard. This proves however the flexibility of the design solutions by the inclusion of a custom daughterboard, being able to account for multiple variations in interface choices.

[19] https://www.st.com/content/ccc/resource/technical/document/datasheet/06/6a/b3/83/9a/c7/4f/22/CD00176077.pdf/files/CD00176077.pdf/jcr:content/translations/en.CD00176077.pdf

[20] https://www.digikey.nl/en/products/detail/sparkfun-electronics/PRT-00127/14671643?s=N4IgTCBcDaIAoCUAqBaADGgjGA7CAugL5A

[21] https://www.analog.com/media/en/technical-documentation/data-sheets/6930fe.pdf

[22] https://assets.maxlinear.com/web/documents/sipex/datasheets/sp336e.pdf

[23] https://www.analog.com/media/en/technical-documentation/data-sheets/adm7171.pdf

[24] https://www.st.com/resource/en/datasheet/stm32h743vi.pdf

[25] https://nl.mouser.com/datasheet/2/389/dm00532745-1799456.pdf

[26] https://resources.altium.com/p/pcb-design-tips-should-you-include-an-external-watchdog-timer-wdt-in-your-board-design

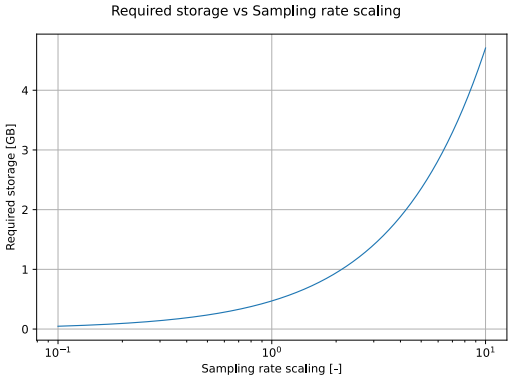

Figure 12.4: Variation of the required storage of C&DH as a function of scaling all components sampling rates with regard to their originals. The x-axis is in logarithmic scale.

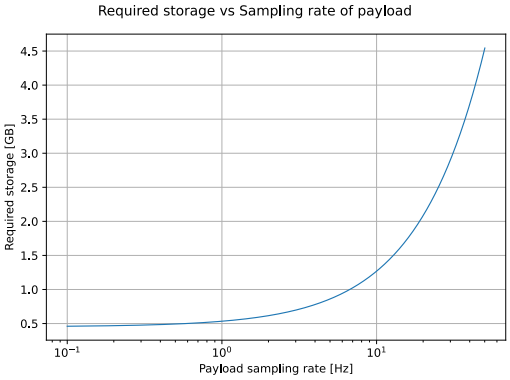

Figure 12.5: Variation of the required storage of C&DH as a function of payload sampling rate. The x-axis is in logarithmic scale. The original payload sampling rate is 0.1 Hz.

12.3 Command & Data Handling Subsystem Requirements Verification

The verification of the C&DH Subsystem by compliance with requirements is given below:

REQ-CDH-04: - this requirement is verified through analysis of the sizing of the on-board data storage components. The total on board memory capacity is 468 Megabytes, which is twice the amount of the total measured data for housekeeping and scientific data over three days. Therefore, the requirement is satisfied;

REQ-CDH-05: - this requirement is verified through analysis of the sizing of the on-board data storage components. The total on board memory capacity is 468 Megabytes, which is twice the amount of the total measured data for housekeeping and scientific data over three days. Therefore, the requirement is satisfied;

REQ-CDH-07: - this requirement is partially verified through inspection of the datasheet of the NanoAvionics SatBus 3C2.[27] Based on that information, the total radiation allowed radiation exposure is 20 krad. Based on information from NASA, the expected radiation exposure for low earth orbiting satellites ranges is 5500 krad on average.[28] As such, the expected lifetime based on radiation is 3.63 years, and thus the required for the OBC is satisfied. However, allowed radiation exposure and the resulting expected lifetime for the custom daughterboard is unknown and therefore shall be verified through extensive radiation testing.

REQ-CDH-08: - this requirement is verified through analyses of the communication interfaces of all sensors and actuators on-board and through the generation of the data handling block diagram (see section 12.2.3 and figure 12.2) which allows for communication between the OBC and these sensors and actuators. Therefore, this requirement is satisfied;

REQ-CDH-09: - this requirement is verified through the analysis of watchdog placements, as discussed in section 12.2.5. Every critical component has the ability to be reset in case of a lack in response due to watchdog timers, and incorrect readings can be detected on ground post-processing and corrections can be applied using uploaded commands. Therefore, this requirement is satisfied;

12.3.1 Concluding Remarks

As a final element to the design of the C&DH subsystem, some concluding remarks are highlighted here, as well as some recommendations for future development stages. The first conclusion to draw is that extensive environmental testing is required for the custom daughterboard of the C&DH subsystem. Based on the high number of components that require data handling, the need for a daughterboard is inevitable and the highly specific interfacing requirements means that a custom board is needed. While there is reasonable confidence in the estimated lifetime of the commercial off-the-shelf OBC, there is significant uncertainty in a custom board and its lifetime with radiation exposure. Multiple daughterboards would need to be manufactured and tested in order to meet the reliability requirements of space-grade components. The effect of such an action should be taken into account in the cost budget in future design iterations. The second conclusion which can be drawn pertains to the possibility of multi-master multi-slave configurations for communication. Currently, the redundancy strategy for the C&DH subsystem is to split key subsystems into two groups which are interfaced separately to the OBC and daughterboard. This allows for partial functionality in case of failure; however, many components communicate with I2C which in theory results in the possibility for these components to be able to talk to both the OBC and daughterboard simultaneously. Such a possibility would allow for increased redundancy, but more analysis is required as such a strategy is not commonly used in practice.

[27] https://nanoavionics.com/cubesat-components/cubesat-on-board-computer-main-bus-unit-satbus-3c2/
[28] https://llis.nasa.gov/lesson/824

13. SCATTER System Detailed Design & Integration

This chapter covers the integration and interfacing of all the subsystems outlined in chapters 4 to 12 into the spacecraft bus of the SCATTER satellites, as well as the integration of the bus with the Vega-C launcher [10]. Section 13.1 begins the chapter with an overview of the external layout of the system, and reasoning for sensor placement, while in section 13.2, a detailed overview of the internal placement of subsystems is given. Then, in section 13.3, the trade-able parameters of each subsystem in the context of integration are given. In section 13.4 and section 13.5 the hardware and software diagrams of the SCATTER system are presented, showing the interfaces between subsystems. Finally, section 13.6 discusses the integration of the SCATTER satellites with the Vega-C.

13.1 Detailed External Layout

The SCATTER space element consists of two satellites, as shown in section 1.2, which need to communicate with two external elements: a GNSS network (the GPS constellation) and the ground station described in chapter 10. Several subsystems of the space element, therefore, require specific pointing and fields of view. These requirements are summarized below and the external layout derived from them is explained. Figure 13.1 shows this layout, in the body frame (B-frame) of the satellite. The components requiring external placement on the spacecraft bus body are given below.

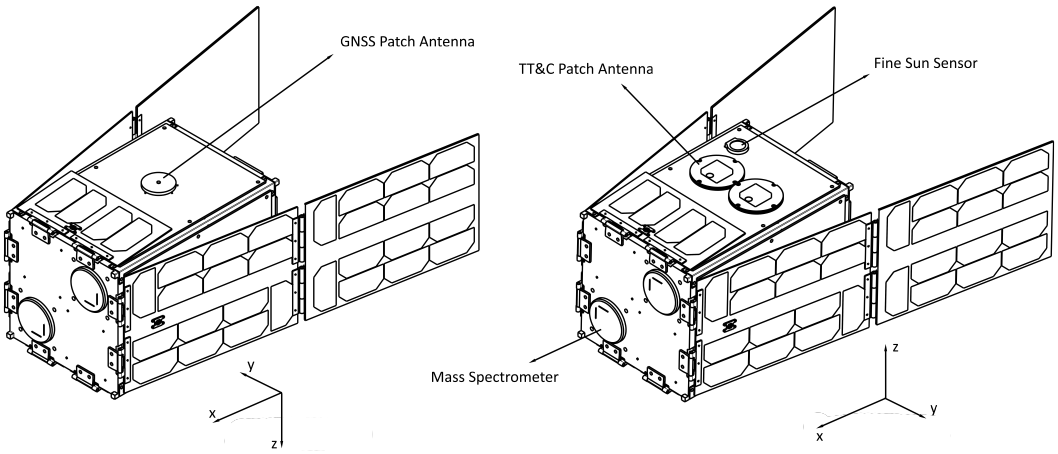

Figure 13.1: Sketch of the external layout of SCATTER in top view (left) and bottom view (right).

1. **The GNSS receiver** is part of the Payload subsystem. It requires pointing to the GPS network, situated in the -Z (zenith) direction, as per REQ-PL-04 in chapter 11. Furthermore, it requires a field of view as large as possible in order to connect to a large number of GPS satellites in the network (8 to 10). Consequently, it must be placed as far away as possible from surface edges, in order to minimise multi-pass effects which could affect the accuracy required by REQ-PL-03. The positioning requirement of this component has been satisfied by placing the patch antenna linking to it on the -Z face of the satellites, as depicted in figure 13.1, on the left. This orientation is maintained in all operational modes requiring orbit determination (science mode, power mode, safe mode). Next, because the multi-pass effect was not quantified at this stage of the design, as it requires extensive analysis and testing of the radio wave patterns emitted from and to the patch antenna of the receiver, a decision was made to position the GPS antenna such that it maximises the distance from all edges, while not interfering with any other subsystems or the bus frame. The projection of the small solar panel onto the -Z face is also considered an edge in this reasoning. Figure 13.2 shows the placement of this antenna. The internal subsystems were placed to allow for a margin of change of this position after more extensive analysis is performed in later design stages;

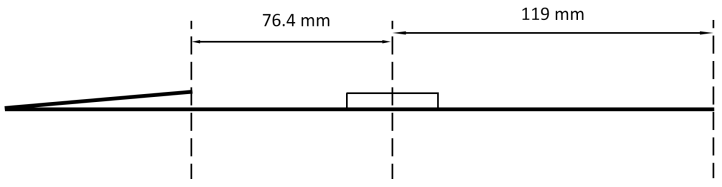

Figure 13.2: Sketch of the GNNS patch antenna placement on the SCATTER satellite surface.

2. **The mass spectrometers** are part of the Payload subsystem and require pointing towards the incoming gas flow of the particles, along the satellite velocity vector. Furthermore, they require a pointing accuracy in this direction of at least 10° according to REQ-PL-13. Finally, they require a flat plane surface, unobstructed by solar panels or other sensors, as per the requirements outlined in [23]. To satisfy these requirements, the mass spectrometers were placed on the +X plane of the satellites, which shall be perpendicular to the incoming velocity vector for at least one of the satellites at any given point in time during science mode. On top of this, no other sensors or solar panels were placed on this surface;
3. **The TT&C patch antennas** are part of the TT&C subsystem and require pointing towards the +Z (nadir) direction and a field of view of at least 120°, as per REQ-TTC-02 and REQ-TTC-07. Furthermore, it requires placement on a flat plane, as per REQ-TTC-06. To satisfy these requirements, they were placed on the +Z face of the spacecraft bus, at a position such that to maximise the distance from all edges, while maintaining the required field of view, while not interfering with other subsystems. This is shown in figure 13.3;

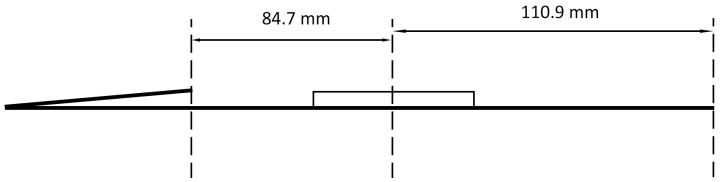

Figure 13.3: Sketch of the TT&C patch antenna placement on the SCATTER satellite surface.

4. **The sun sensors** are 6 in number and part of the ADCS and are described in chapter 9. They require a surface placement and a field of view of as high as possible to satisfy REQ-ADCS-02 to REQ-ADCS-07. To satisfy these requirements 4 solar panel-mounted sun sensors were chosen, and mounted on the small and long solar panels, as described in section 9.2. Furthermore, two fine sun sensors were mounted on the flat +Z and -X faces, to provide increase the over-all field of view and accuracy. A sun sensor was not added to the -Z face, as to not interfere with the accuracy of the GNSS receiver data;
5. **Thrusters** - these components are 2 in number, and part of the OCS, described in chapter 8. The main requirement of concern with them lies in the offset in the ZY plane of the thrust vector produced by them. To solve this, they were placed symmetrically w.r.t. the X-axis on the -X face;

13.2 Detailed Internal Layout

With the external placement of components on the SCATTER satellites decided based on the mission needs and the given requirements, an internal layout of the subsystems was developed to meet these requirements. In the development of this layout the following aspects were weighted: **subsystem compatibility**, **symmetry**, **reduction of cabling** and **ease of assembly**. System compatibility implies any placement requirements that some components may have, while symmetry is added to ensure the satellites have minimal off-diagonal moments of inertia, which is desired for attitude control. Reduction of cabling is wanted for mass efficiency as well as to reduce cabling losses. Finally, ease of assembly would ensure elements can be connected to the frame in assembly and that no custom tools are needed. The chosen layout is given in figure 13.4:

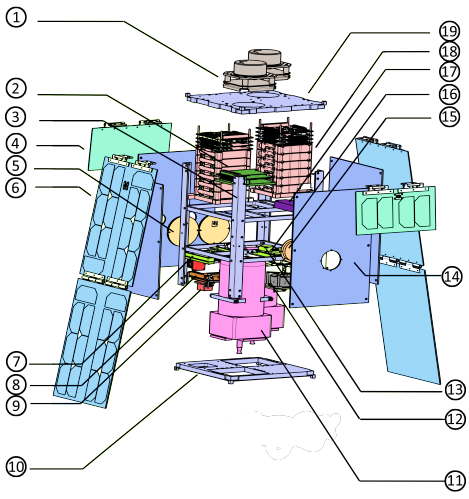

Figure 13.4: Exploded view of one SCATTER satellite and its main subsystems. Numbers are explained in section 13.2.

The components outlined in the figure above are the following:

1. **The Mass Spectrometers** - these components are part of the Payload subsystem, and are placed on the +X face panel of the system, in order to measure the particle number densities and temperature of the incoming gas flow, during the mission. They come as a pair for redundancy purposes as outlined in chapter 11. They were placed symmetrically w.r.t the X-axis, in the ZY-plane to ensure symmetry to the satellites;
2. **The Main Flight Computer** - this component is part of the C&DH subsystem, and it is connected to all other electronic components in the system. As it is not an element requiring special placement, it was fitted such that all other constraining components have their mounting requirements satisfied. However, as it is one singular component, it introduces asymmetry w.r.t the X-axis, and therefore was placed as close as possible to the ZY-plane center, in order to minimise it;
3. **The Rails** - 4 rails are part of the structures subsystem. Their purpose is to ensure structural stability for all subsystems, and interface mechanically with the CubeSat deployer of the Vega-C launcher [10];
4. **The Small Solar Panels** - 2 of these panels are used to increase the sensitivity to energy accommodation coefficient of the satellite, as outlined in chapter 4, as well as provide extra power to the EPS in power mode, propulsion mode and safe mode. They are placed symmetrically w.r.t. the X-axis, as to not introduce an aerodynamic moment during science mode, in a low-drag configuration;
5. **The TT&C Patch Antennas** - these components are part of the TT&C subsystem come in a number of 2 for redundancy purposes. They are placed on the +Z face panel of the satellites for reasons outlined in section 13.1;
6. **The Large Solar Panels** - these components are part of the EPS and come in a number of 2. They have two main functions in the system: provide the majority of the power needed for nominal operations, and provide the largest contribution to energy accommodation coefficient as outlined in chapter 5 and chapter 4. They are placed symmetrically w.r.t. the X-axis in order to not induce an aerodynamic moment in the low-drag configuration of the science mode;
7. **The TT&C Transceiver** - this component is part of the TT&C subsystem and its main function is to transmit and receive signals from the ground station. It is placed close to the +Z face of the satellite, behind the patch antenna. This is to reduce the cable length between the transceiver and antennas, as well as to balance the components placed on the opposite side w.r.t. the XY plane;
8. **The Magnetorquer** - this component is part of the ADCS, and its main function is to de-tumble the satellites after deployment, as well as dump momentum stored in the reaction wheels during the mission lifetime. It is placed on top of the bottom blukhead, close to the +Z face panel of the satellite, to act as a counterweight to the reaction wheels, which are placed on the opposite side w.r.t. the X-axis. It is also placed at a significant distance from other electronic components as to not produce interfering magnetic fields on them;
9. **The Fine Sun Sensors** - these components are part of the ADCS, and come in a number of 6. 4 of these sensors are solar-panel-mounted sensors, while 2 of them are body-mounted, and have a higher accuracy. Their main function is to determine the attitude of the spacecraft during daytime, by measuring the sun direction. They are placed on each available face of the satellites to maximise the over-all attitude determination field of view of the ADCS.
10. **The Bottom Bulkhead** - this component is part of the Structures subsystem and its main functions are to provide structural integrity to the other subsystems, as well as act as a heat sink to the engines. Its placement is dictated by CubeSat standards [15];
11. **The Engines** - these components are part of the OCS, and come in a number of 2. Their primary function is to provide orbit control to the spacecraft, and are placed symmetrically w.r.t. the X-axis for two reasons. Firstly, to minimise the off-diagonal moments of inertia, and secondly, to provide a combined thrust vector acting close to the CoM of the satellite, and thus minimise thrust-induced moments;
12. **The Reaction Wheels** - these components are part of the ADCS, and come in a number of 4 (3 needed and 1 for redundancy). Their main function is to change the attitude of the satellites in the science mode, power mode and transmission mode, as well as when performing maneuvers. They are placed on the bottom bulkhead, close to the -Z face panel, to act as a counterweight to the magnetorquer and TT&C receiver;
13. **The GNSS Receiver** - this component is part of the Payload subsystem, and its main function is to receive position and velocity data from the chosen GNSS network. It is placed next to the -Z face panel, on top of the reaction wheels, to reduce cabling length between it and the GNSS patch antenna, as well as act as a counter-weight to the TT&C receiver;
14. **The Face Panels** - these components are part of the Structures subsystem, and come in a number of 4. Their main function is to provide structural support to externally-mounted components and shield the inner components from the external environment.
15. **The GNSS Patch Antenna** - this component is part of the Payload subsystem, and its main function is to receive GNSS signals from the GNSS network. It is placed according to the reasoning explained in section 13.1;
16. **The Inertial Measurement Units (IMU)** - these components are placed on top of the reaction wheels and magnetorquer, symmetrically opposite w.r.t. the CoM of the satellite, in the ZY plane. Their main function is to measure the angular and translational accelerations of the satellites for attitude and orbit determination;
17. **The Magnetometers** - these components are part of the ADCS, and come in a number of 2. Their main

function is to measure the magnetic field of Earth in order to aid with satellite de-tumbling and general attitude determination. They are placed next to the -Z face panel, on top of the GNSS receiver and Inertial Measurement Unit, to act as counterweights to the TT&C receiver;

18. **The Battery Packs** - these components are part of the EPS, and come in a number of 12, in 2 x 6 packets. Their main function is to store the power collected by the solar panels during eclipse, as well as provide power for the de-tumbling phase, when the solar panels are not deployed;
19. **The Top Bulkhead** - this component is part of the Structures subsystem and its main function is to provide structural support to all other subsystems, and especially to the mass spectrometers. It is placed according to CubeSat standards [15];
20. **The Thermal Blankets (not shown)** - these components are part of the TCS subsystem and it is placed on the +Z and -Z face panels of the satellites. Their main function is to regulate the temperature of all subsystems;
21. **Others (not shown)** - other components which do not play a major impact into the design integration due to their small size and versatility include: temperature sensors, radiators, cables, etc... . In later stages of the design these shall be taken into consideration individually.

13.3 Detailed Design Budgets

This section aims to give a detailed budget allocation to each subsystem. In table 13.1, the cost, mass, dimensions, peak power, idle power and production property for each subsystem will be shown. This will be used later for verification and validation by comparing with the preliminary design budgets in section 2.5 and statistical resources.

Table 13.1: Detailed design budget allocation for single satellite.

Subsystem	**Component**	**Cost** $[EUR]$	**Mass** $[kg]$	**Dimensions for Single Component** $[mm^3]$	**Peak Power** $[W]$	**Idle Power** $[W]$	**Production**
Structure	Bulkheads (4 no.)	12262.00	2.729	224x224x18.5	0.000	0.000	Customised
	Panels (4 no.)	9112.00	2.028	303.2x207x3	0.000	0.000	Customised
	Rails (4 no.)	1779.00	0.396	18x18x340.5	0.000	0.000	Customised
	Counterweight	7.00	0.230	18x18x42	0.000	0.000	Customised
	Subsystem	23,160.00	5.383	-	0.000	0.000	Customised
TCS	-	66,153.25	0.330	-	0.000	0.000	Customised
OCS	Engines with propellant(2 no.)	577,467.50	5.200	200x100x100	42.000	0.600	Off-shelf
ADCS	Magnetorquer	9,750.00	0.196	95.9x90.1x17	1.200	0.175	Off-shelf
	Surface mounted Sun sensor (2 no.)	22,378.00	0.002	34x40x20	0.300	0.080	Off-shelf
	Solar panel mounted Sun sensor (4 no.)	38,092.00	0.070	20x10x5.7	0.026	0.007	Off-shelf
	Reaction wheels (4 no.)	100,688.00	0.740	50x50x40	7.200	1.200	Off-shelf
	Magnetometers (2 no.)	27,972.00	0.170	96x43x17	0.750	0.750	Off-shelf
	Subsystem	198,880.00	1.178	-	8.726	2.432	Off-shelf
EPS	Small solar panels (2 no.)	11,160.00	0.240	10x113.5x227	-	-	Customised
	Large solar arrays (2 no.)	78,120.00	1.120	10x681x227	-	-	Customised
	Battery Packs	39,600.00	2.212	80x80x135	-	-	Off-shelf
	PCU (2 no.)	4,000.00	0.116	80x80x20	2.118	0.132	Off-shelf
	PDU (2 no.)	4,000.00	0.115	80x80x18	-	0.132	Off-shelf
	BCU (4 no.)	8,000.00	1.008	80x80x19	-	0.195	Off-shelf
	Subsystem	144,880.00	4.811	170x10x10	-	0.393	-
TTC	Patch Antenna (2 no.)	4,300.00	0.100	80x80x5	-	-	Off-shelf
	Transceiver (2 no.)	20,000.00	0.400	90x65x25.3	-	-	Off-shelf
	Cables	3,645.00	0.100	-	-	-	Off-shelf
	Subsystem	27,945.00	0.600	-	12.000	1.000	Off-shelf
CDH	Main flight computer	18,364.21	0.124	95.5x90.17x6.57	-	1.000	Off-shelf
Payload	Mass spectrometer (2 no.)	200,000.00	0.400	98x98x64	0.880	0.000	Off-shelf
	GNSS receiver	19,965.00	0.109	96x90x18.1	0.000	1.500	Off-shelf
	GNSS patch antenna	250.00	0.070	61.2x61.2x16.2	1.500	0.000	Off-shelf
	IMU (2 no.)	46,000.00	0.024	30x28x14	0.600	0.600	Off-shelf
	Total	266,215.00	0.603	-	2.980	2.100	Off-shelf
Total	System	1,323,064.96	18.229	-	-	7.524	-

As it can be seen in the table above, the largest contributors to each of the budgets are the engines in terms of cost (€577000), mass (5.2 kg) and peak power (42 W). This is due to the high reliability required for the engines, as they represent a single-point-of-failure to the SCATTER system, in the case one or both of them malfunction. As the engines concentrate most of the system's weight into one diagonal, which could increase the momentum needed to be provided by ADCS actuators in certain orientations. To counter this effect, the 12 battery packs used by the EPS are added in the opposite diagonal, which yields the inertia tensor shown in equation 13.1, for the entire system:

$$\mathbf{I} = \begin{bmatrix} 0.16 & -0.008 & 0.001 \\ -0.008 & 0.265 & -0.006 \\ 0.001 & -0.006 & 0.282 \end{bmatrix} [kgm^2] \tag{13.1}$$

Based on the negligible off-diagonal components of the inertia tensor, it is concluded that the structure is symmetric, and efficient angular-momentum-wise.

13.4 Hardware Block Diagram

The hardware block diagram as shown in figure 13.5 illustrates how the components connected with each other and provides an overview of the whole system.

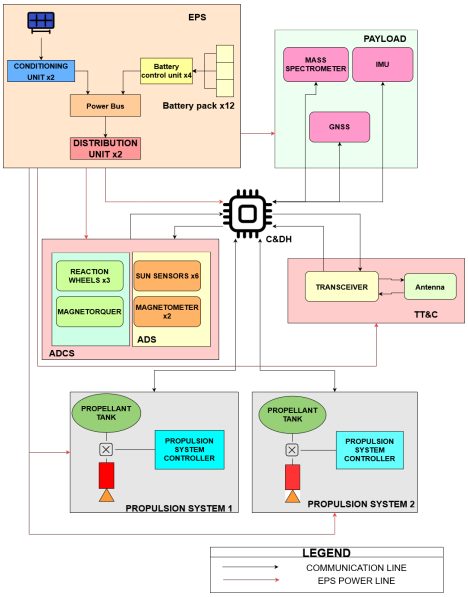

Figure 13.5: Hardware block diagram for the spacecraft of SCATTER mission.

13.5 Software Block Diagram

The software block diagram is a means to illustrate the algorithms which are to be used by the C&DH subsystem of the spacecraft, and the resulting subsystems which are interfaced to each piece of software. This will become beneficial in later stages of the development of the C&DH subsystem in which the OBC is to be programmed for the actual spacecraft.

In figure 13.6, the green rectangles denote the external subsystems which require commanding. The blue elements are the internal algorithms which the OBC requires in order to allow for the required data processing and command. As can clearly seen in the software block diagram, the OBC is directly connected to all components which are required for attitude determination and control, as well as orbit control. This allows for the corrective torques and rotational rates for attitude control to be determined automatically. For the payload data specifically, the processing of the data is done on the ground. However, certain measured data which is needed for this scientific data processing on ground must first be compressed on board in order to prevent an unnecessarily large data rate being sent which could overload the TT&C subsystem.

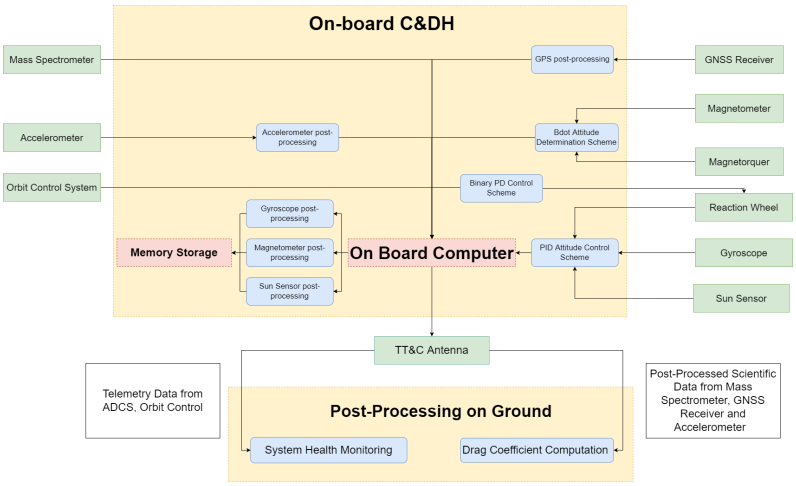

Figure 13.6: Software block diagram for the spacecraft of the SCATTER mission.

With this in mind, the individual algorithms which correspond to the C&DH subsystem are discussed. With this assembly of software, the spacecraft would be able to perform all required science operations as needed.

The accelerometer post-processing software compresses the data obtained which is useful for deriving the translational acceleration caused by the drag force acting on the spacecraft. This, in turn, is useful for the drag coefficient computation. Acceleration information is measured as part of the IMU itself which is simultaneously also measuring the gyroscopic information. Given that the gyroscopic information must be sampled at 100Hz for ADCS control accuracy, the acceleration information is also sampled at 100Hz. This sampling frequency is well above what is needed for the drag coefficient computation, therefore, it was necessary for the data be compressed to a sample rate of 0.1Hz which corresponds to the sampling rate of the other payload.

The GPS post-processing software is mainly required for the sorting of information which is obtained by the

receiver itself. The GPS receiver has the option of obtained real-time clock information for drift correction of the OBC clock. In other instances, positional and velocity information is received. While all this information is key, the clock correction is information which does not need to be directly sent back down to the ground, while the other positioning information should be returned. This sorting is done through the post-processing of the data.

The sun sensor, magnetometer and gyroscope post-processing follows from a similar logic as the accelerometer: a high sampling frequency is required for the ADCS to meet the positioning accuracy which is needed for the mission. However, such high sampling frequency is not required to be returned to the ground in order to monitor the health of the ADCS subsystem. Therefore, the data is compressed to 1Hz in the post-processing of the information prior to it being stored in memory.

The binary partial differential control scheme is a software that uses the distance between satellites and the relative velocity in order to generate an error function. Depending on the sign of the error function, the software then decides whether to rotate the satellites accordingly to reduce the drift distance or not.

The bdot attitude determination scheme makes use of the magnetic field changes of the earth as measured by the magnetometer and is then used to determine the required control torque in order to decrease the angular velocity and maintain a certain attitude.

The proportional-integral-differential control scheme makes use of the cross product between the current orientation vector of the spacecraft and the desired orientation vector in order to create an error function which in turn can then be used towards to determine a required control torque for the reaction wheels

13.6 Vega-C Launcher Integration

One final system-level aspect to consider for the design of the SCATTER satellites is the integration into the CubeSat deployer and consequently, the Vega-C fairing. As mentioned in section 3.4, the chosen CubeSat deployer is the Tyvak 12U deployer [19]. This is a heritage deployer for 2U x 2U x 3U standard CubeSats, which is compatible with the chosen launcher. A sketch of the internal structure of the deployer, and how the SCATTER satellite fits inside, is given in figure 13.7 and figure 13.8. table 13.2 shows the margins between the satellite and the maximum allowed dimensions.

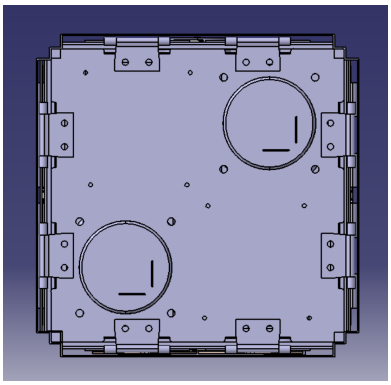

Figure 13.7: Front view of SCATTER as fitted in the Tvyak 12U deployer [19].

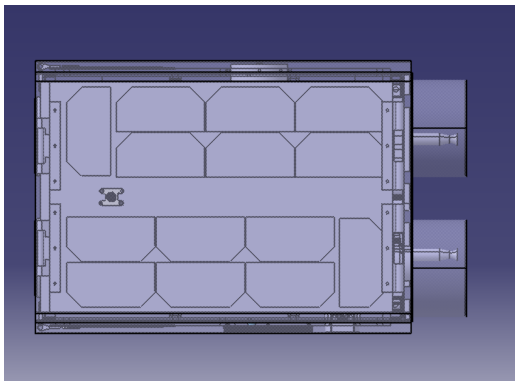

Figure 13.8: Side view of SCATTER as fitted in the Tvyak 12U deployer [19].

Table 13.2: Spatial margins of SCATTER inside the chosen CubeSat deployer.

SCATTER CubeSat Deployer Margins				
GNSS Antenna Margin	**TT&C Antenna Margin**	**ODCS Thruster Margin**	**Mass Spectrometer Margin**	**Solar Panels**
3 mm	3 mm	7.5 mm	0.5 mm	1.88 mm

13.7 System Integration Concluding Remarks

In this chapter, the integration of the subsystems of SCATTER into the satellite bus was outlined, together with the over-all integration of the satellites inside the CubeSat deployer and Vega-C launcher. With the existing internal layout, symmetry has been achieved for the satellites, by placing even numbers of most components on different sides of the x-axis, which has minimized the off-diagonal moments of inertia to a negligible amount below $\mathrm{kg\,m^2}$. This aspect has also added redundancy in subsystems, namely Payload through the mass spectrometers and accelerometers and EPS through the internal battery packs.

14. Design Verification and Validation Procedures Overview

This chapter covers the system-level verification and validation procedures performed on the SCATTER design. Firstly, in section 14.1, the system-level requirements are either verified through analysis / inspection, or a verification procedure is proposed if testing, demonstration or extensive analysis is needed to verify them. Next, in section 14.2, the trade-able quantities of the detailed design, namely mass, cost and power for each subsystem are compared against the preliminary design values outlined in chapter 2, as well as against statistical percentages from similar missions. Finally, all subsystem and system-level compliance matrices for the design are presented in section 14.3 and section 14.4.

14.1 System Requirement Verification

In this section, the detailed design of SCATTER is verified against all system-level requirements for compliance. The user requirements are not verified, as they are not written in a "VALID" format. Instead, as these requirements are parented to system-level requirements, compliance is ensured by verifying the latter. As most system-level requirements are linked to sets of subsystem-level ones, the verification of the latter is used to prove compliance with the former. If a requirement could not be verified with existing information available at this stage of the project, a brief verification procedure is proposed. The verification overview of the functional requirements of SCATTER is given below:

REQ-SYS-F-02: - this requirement is verified with a structural static analysis in chapter 6, through the verification of REQ-SM-01 and REQ-SM-02;

REQ-SYS-F-03: - this requirement is verified with a structural dynamic analysis in chapter 6, through the verification of REQ-SM-03, REQ-SM-04, REQ-SM-05, REQ-SM-06, REQ-SM-07, REQ-SM-09, REQ-SM-10 and REQ-SM-11;

REQ-SYS-F-04: - this requirement is verified with a modal dynamic analysis and inspection in chapter 6, through the verification of REQ-SM-04, REQ-SM-05, REQ-SM-06, REQ-SM-07, REQ-SM-09, REQ-SM-10, REQ-SM-11, REQ-SM-13 and REQ-SM-14;

REQ-SYS-F-05: - this requirement is verified with a modal dynamic analysis in chapter 6, through the verification of REQ-SM-12, REQ-SM-13, REQ-SM-14, REQ-SM-15 and REQ-SM-16;

REQ-SYS-F-07: - this requirement is verified through inspection of the SCATTER satellite dimensions in chapter 13. As the satellite is 224 mm x 224 mm by 334.2 mm, it fits inside the deployer of Vega-C [10];

REQ-SYS-F-08: - this requirement is verified through analysis in the mission profile analysis in figure 3.4 and through the functional breakdown structure in section 2.1;

REQ-SYS-F-12: - this requirement is verified through analysis in chapter 12 and chapter 10, through requirements REQ-CDH-04 and REQ-TTC-08;

REQ-SYS-F-13: - this requirement is verified through analysis in table 10.3 in chapter 10;

REQ-SYS-F-14: - this requirement is verified through analysis in table 10.3 in chapter 10;

REQ-SYS-F-16: - this requirement is verified through the thermal analysis performed in chapter 7 on the subsystems of SCATTER;

REQ-SYS-F-17: - this requirement shall verified through ground-based testing of each subsystem of SCATTER in near-vacuum conditions. Off-the-shelf components which have already been qualification-tested for the pressure ranges of the requirement shall not be tested;

REQ-SYS-F-18: - this requirement shall verified through ground-based testing of each subsystem of SCATTER in similar radiation conditions. Off-the-shelf components which have already been qualification-tested for the radiation ranges of the requirement shall not be tested. Radiation shielding shall be added to vulnerable components;

REQ-SYS-F-19: - this requirement shall verified through more extensive analysis of each subsystem of SCATTER in a standard model of Earth's magnetic field such as IGRF [1]. Off-the-shelf components which have already been qualification-tested for these magnetic field conditions shall not be analysed;

REQ-SYS-F-20: - this requirement is verified in section 9.2 through the analysis of the chosen attitude determination sensors (sun sensors and gyroscopes);

REQ-SYS-F-21: - this requirement is verified in section 9.2 through the analysis of the chosen attitude control actuators: the selected reaction wheels and the magnetorquer;

REQ-SYS-F-22: - this requirement is verified in section 9.2 through the analysis of the GPS receiver and accelerometers of the SCATTER satellites, in chapter 11;

REQ-SYS-F-23: - this requirement is verified in chapter 8, through the analysis of the engines chosen for the SCATTER satellites;

REQ-SYS-F-24: - this requirement is verified in chapter 3, where the mission allocates time for the satellites to operate in "Science Mode", where they change their orientations, and chapter 9, where reaction wheels are designed to rotate the satellite 90° in pitch and yaw to change the projected surface area of the satellites with respect to the incoming gas flow;

REQ-SYS-F-27: - this requirement shall be verified in the subsystem prototyping phase as well as in the qualification phase, through ground-based testing of all electrical components at their nominal current and voltage ranges;

REQ-SYS-F-29: - this requirement is verified through the inspection of the functional flow diagram and functional breakdown structure in section 2.1 and section 2.1, where the "Separation" and "De-tumbling" phases are defined;

REQ-SYS-F-30: - this requirement is verified through the addition of 12 battery packs in the Electrical Power Subsystem design, which supply the satellites with power before solar panel deployment as described in chapter 5;

REQ-SYS-F-31: - this requirement is verified through the analysis of the data handling block diagram shown in chapter 12, in figure 12.3;

The verification overview of the performance requirements of SCATTER is given below:

REQ-SYS-P-02: - this requirement is verified by the thermal analysis performed in chapter 7, through REQ-TCS-02 to REQ-TCS-16;

REQ-SYS-P-03: - this requirement shall be verified through ground-based testing of the subsystems in the temperature, radiation and pressure conditions resembling those experienced at the mentioned altitudes;

REQ-SYS-P-04: - this requirement shall be verified through ground-based testing of the subsystems under the pressure range of 10 Pa to 105 Pa;

REQ-SYS-P-05: - this requirement is verified through the dynamic load and modal analyses performed in chapter 6 for loads of 10 g amplitudes applied in all body axes;

[1] `https://www.ngdc.noaa.gov/geomag/models.shtml`

REQ-SYS-P-07: - this requirement shall be verified through ground-based testing of the GPS receiver chosen in chapter 11 for the Payload Subsystem;

REQ-SYS-P-08: - this requirement is verified using the Simulink tool developed and described in section 9.4, which provides determination and pointing accuracy estimations for the chosen ADCS components;

REQ-SYS-P-09: - this requirement is verified using AstroSIM in section 9.6, by a numerical analysis of the satellite responses to reaction wheel actuation;

REQ-SYS-P-10: - this requirement shall be verified through ground-based qualification testing of the QB50 INMS (mass spectrometer) proposed in chapter 11, in conditions similar to those experienced in the mission;

REQ-SYS-P-11: - this requirement shall be verified through ground-based qualification testing of the QB50 INMS (mass spectrometer) proposed in chapter 11, in conditions similar to those experienced in the mission;

REQ-SYS-P-12: - this requirement shall be verified through ground-based qualification testing of the QB50 INMS (mass spectrometer) proposed in chapter 11, in conditions similar to those experienced in the mission;

REQ-SYS-P-13: - this requirement shall be verified through ground-based qualification testing of the QB50 INMS (mass spectrometer) proposed in chapter 11, in conditions similar to those experienced in the mission;

REQ-SYS-P-14: - this requirement shall be verified through ground-based qualification testing of the QB50 INMS (mass spectrometer) proposed in chapter 11, in conditions similar to those experienced in the mission;

REQ-SYS-P-15: - this requirement shall be verified through ground-based qualification testing of the QB50 INMS (mass spectrometer) proposed in chapter 11, in conditions similar to those experienced in the mission;

REQ-SYS-P-16: - this requirement shall be verified through ground-based qualification testing of the GPSRM 1 GPS receiver proposed in chapter 11, to determine its accuracy after post-processing;

REQ-SYS-P-17: - this requirement shall be verified through ground-based qualification testing of the GPSRM 1 GPS receiver proposed in chapter 11, to determine its frequency of measurement with post-processing;

REQ-SYS-P-18: - this requirement is verified through a link budget analysis of the signal-to-noise ratio of the TT&C subsystem, shown in table 10.3, in chapter 10;

REQ-SYS-P-19: - this requirement is verified through an analysis of the data rates produced by all subsystems, shown in table 12.2, in chapter 12, as well as the chosen memory size for the subsystem, outlined in the same chapter;

REQ-SYS-P-20: - this requirement is verified using the Simulink tool developed and described in section 9.4, which provides determination and pointing accuracy estimations for the chosen ADCS components;

REQ-SYS-P-21: - this requirement is verified using the Simulink tool developed and described in section 9.4, which provides determination and pointing accuracy estimations for the chosen ADCS components;

REQ-SYS-P-22: - this requirement is verified using AstroSIM in section 9.6, by a numerical analysis of the satellite responses to reaction wheel actuation;

REQ-SYS-P-23: - this requirement is verified using AstroSIM in section 9.6, by a numerical analysis of the satellite responses to reaction wheel actuation;

REQ-SYS-P-24: - this requirement is through inspection of the C&DH subsystem in chapter 12 where a memory of 439 Megabytes is selected;

REQ-SYS-P-25: - this requirement is through the analysis performed in the chapter 12 and chapter 10, on REQ-TTC-08;

The verification overview of the design requirements of SCATTER is given below:

REQ-SYS-D-01: - this requirement is verified through the same procedures as outlined for **REQ-SYS-F-05**;

REQ-SYS-D-02: - this is verified through inspection of the current SCATTER design, and by what margins it fits into the chosen CubeSat deployer, as shown in chapter 13;

REQ-SYS-D-03: - this requirement is verified through an analysis of the mass budget of each subsystem of the SCATTER satellites which yielded an estimation of the total mass of the system as shown in chapter 13

REQ-SYS-D-06: - this requirement is verified through an analysis of the shape of the SCATTER satellites, performed in chapter 4, through verifying REQ-AER-03;

REQ-SYS-D-07: - this requirement is verified through an analysis of the shape of the current SCATTER satellite design, and how it fits into the chosen CubeSat deployer, in chapter 13;

REQ-SYS-D-08: - this requirement is verified through an analysis of the shape of the current SCATTER satellite design, and how it fits into the chosen CubeSat deployer, in chapter 13;

REQ-SYS-D-09: - this requirement is verified through an analysis of the shape of the current SCATTER satellite design, and how it fits into the chosen CubeSat deployer, in chapter 13;

The verification overview of the legal constraints of SCATTER is given below:

C-LEGAL-01: - this requirement shall be verified by inspection of the mission profile and the TT&C subsystem in the qualification phase of the SCATTER design;

C-LEGAL-02: - this requirement shall be verified by inspection of the entire system and mission in the qualification phase of the SCATTER design;

C-LEGAL-03: - this requirement shall be verified by inspection of the entire system and mission in the qualification phase of the SCATTER design;

C-LEGAL-04: - this requirement shall be verified by inspection of the entire system and mission in the qualification phase of the SCATTER design;

C-LEGAL-05: - this requirement shall be verified by inspection of the entire system and mission in the qualification phase of the SCATTER design;

C-LEGAL-06: - this requirement shall be verified by inspection of the entire system and mission in the qualification phase of the SCATTER design;

C-LEGAL-07: - this requirement shall be verified by inspection of the entire system and mission in the qualification phase of the SCATTER design;

C-LEGAL-08: - this requirement shall be verified through a planning with contingencies of the launch phase of the mission shown in blocks 1.1 to 1.5 in the functional breakdown structure in section 2.1;

C-LEGAL-09: - this requirement shall be verified through a planning with contingencies of the launch phase of the mission shown in blocks 1.1 to 1.5 in the functional breakdown structure in section 2.1;

The verification overview of the resource constraints of SCATTER is given below:

C-RES-01 - this requirement is verified in chapter 13, through an analysis of the estimated costs of each subsystem shown in chapter 13, coming either from the publicly-available prices of the chosen components, or through statistical estimations;

C-RES-02: - this requirement is verified through the analysis of the development plan following this phase of the project (the detailed design phase), shown in chapter 16;

C-RES-05: - this requirement is verified through the manufacturing and production plan proposed in chapter 15;

C-RES-06: - this requirement shall be verified through inspection of the insurance policies taken in the development of the system;

The verification overview of the safety constraints of SCATTER is given below:

C-SAFE-05: - this requirement is verified through the analysis performed on the collision avoidance strategies in section 3.7;
C-SAFE-06: - this requirement is verified through the aerodynamic DSMC-SIM analysis performed in section 17.4;

The verification overview of the sustainability constraints of SCATTER is given below:

C-SUS-01: - this requirement is verified through the materials chosen for each component outlined in chapter 6, chapter 15, chapter 13;
C-SUS-02: - this requirement is verified through the analysis performed on the collision avoidance strategies in section 3.7;

This concludes the verification of the SCATTER design at this phase of the project. In section 14.2, the validation of this design is outlined based on the evolution of the system's budgets.

14.2 Detailed Design Validation

In this section, an overview of the differences between the preliminary and detailed designs of SCATTER is given, as well as a comparison with similar missions. This is done with the purpose of validating the current design and the decision made in the 4^{th} phase of the project. Firstly, changes in the satellite shape are addressed, and the effects they have on the mission performance are explained. Then, the evolution of trade-able parameters in the design (mass, cost and power) is given for each subsystem, together with a comparison with the aforementioned similar missions.

The shapes of the preliminary and detailed designs of SCATTER are given in figure 14.1 and figure 14.2:

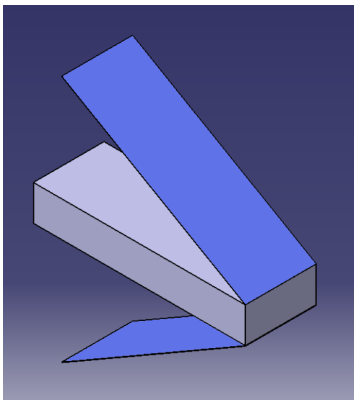

Figure 14.1: Sketch of the preliminary design of SCATTER.

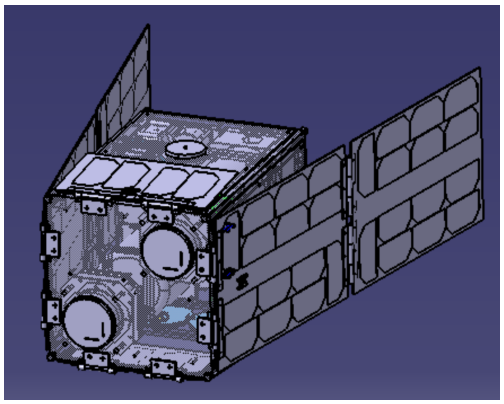

Figure 14.2: Sketch of the detailed design of SCATTER.

As it can be seen in the figures, several changes have been made between the preliminary and detailed design in terms of shape. The first major difference is the CubeSat body shape change. As mentioned in Section 2.4, the SCATTER preliminary design was a 1U x 2U x 6U CubeSat, whereas the detailed design consists of a 2U x 2U x 3U satellite. The initial choice to use a non-standard CubeSat shape was performed for reasons related to aerodynamics. As the drag sensitivity to energy accommodation coefficient $\Delta C_D\alpha$ is dependent on the ratio of ratios between the normal and tangential surface areas of the shape in the low and high-drag configurations as per REQ-SYS-D-05. Therefore, the initial shape was chosen to be slender, which would reduce the needed solar panel surface area to achieve the ΔC_{D_α} required by REQ-AER-01. The shift to a standard 12U (volume) CubeSat shape was performed due to launcher integration reasons. With the Vega-C launcher selected for the mission, no CubeSat deployer could be found that satisfied the size requirements of the launch manual [10]. To satisfy the aerodynamic sensitivity requirement, two additional 2U x 1U panels were added on the remaining flat faces of the satellites, at the cost of an increased design complexity. However, by choosing off-the-shelf deployable solar panels as explained in chapter 5, the complexity problem is mitigated. Next, the mass, cost and power budgets of the subsystems of SCATTER are compared, firstly between the preliminary and detailed design, and then with the DANDE mission [2]. These comparisons are shown in table 14.1 and table 14.2. For the preliminary design subsystem budgets, statistical data from literature [12] was used, while the detailed design used information available on the chosen supplier sites.

[2] `https://directory.eoportal.org/web/eoportal/satellite-missions/d/dande`

Table 14.1: Preliminary design vs. detailed design budgets.

Source	Detailed Design			Preliminary Design			Deviation		
Subsystem	**Cost [EUR]**	**Mass [kg]**	**Average Power [W]**	**Cost [EUR]**	**Mass [kg]**	**Average Power [W]**	**Cost [%]**	**Mass [%]**	**Average Power [%]**
Structures	€23,160.00	5.383	0.000	€14,700.00	3.170	0.000	57.55%	69.81%	-
TCS	€64,934.30	0.400	0.000	€51,957.89	0.790	0.000	24.97%	-49.37%	-
OCS	€577,467.50	5.200	0.610	€129,000.00	3.960	1.328	347.65%	31.31%	-54.07%
ADCS	€198,880.00	1.178	3.300	€293,250.00	1.580	1.328	-32.18%	-25.44%	148.49%
EPS	€144,880.00	4.810	0.393	€223,600.00	3.170	1.992	-35.21%	51.74%	-80.28%
TT&C	€27,945.00	0.600	1.170	€20,000.00	0.790	2.656	39.73%	-24.05%	-55.95%
CD&H	€18,364.21	0.124	1.000	€6,650.00	0.790	2.656	176.15%	-84.30%	-62.35%
Payload	€266,215.00	0.603	2.540	€300,000.00	1.580	2.656	-11.26%	-61.84%	-4.37%
Total	€1,323,064.96	18.228	9.013	€1,039,157.89	15.830	12.616	27.20%	15.15%	-28.56%

As it can be seen in the table, several significant deviations occur between the two designs for all the trade-able parameters. These are discussed in the following paragraphs.

The estimated cost of the detailed design has risen by 27% in comparison to the preliminary design, which occurs for several reasons. The biggest contributing factor is the OCS subsystem, which suffered an increase of 350%, from €129000 to €577000. This occurred primarily due to the choice of having two engines on the satellites. Such a choice was made to ensure spatial efficiency inside the satellite, which has a volume of 2U x 2U x 3U. As all off-the-shelf engines commercially available for CubeSats were sized to be 1U x 1U wide, and REQ-OCS-05 requires that the thrust vector must have a maximum offset of 0.697 mm from the CoM in the ZY plane, placing two engines diagonally proved to be the best option. The other reason for this cost is the high reliability of the engines, which was needed to mitigate the one-engine-inn-operative scenario, for which no other design contingency was found. Finally, the structures subsystem also increased in cost by 60% from the initial estimates, which is due to the amount of custom-built components needed. Such components require qualification and acceptance testing to be flown on the Vega-C rocket [10], and therefore added additional cost.

The estimated mass of the detailed design has risen, much like the cost, by 15.15%. The OCS has the highest contribution to this difference. This is again due to the decision to add two engines for spatial efficiency reasons, which adds 1.24 kg extra to the overall mass. Furthermore, the structure of the satellites has increased in mass significantly, to 5.4 kg versus the estimated 3.17 kg in the preliminary design. Such a difference is attributed to the custom structural components used in SCATTER design, which are thicker than those used in standard CubeSats [15]. This design choice was made to account with a safety margin for the launch loads experienced by payloads of the Vega-C launcher [10]. Furthermore, additional support frames are added for the two engines of the OCS and battery packs of the EPS, to maximise the minimum natural frequencies of the satellites. The final significant contribution is that of the EPS internal battery packs, which are needed to provide power to the satellites during science mode. This mode can last up to 3 days at the beginning of Phase II of the mission, where formation flying becomes the primary method of reducing altitude, according to section 3.5.

The estimated power of the detailed design has suffered an opposite trend to the cost and mass, as it has decreased by 29%. This difference is due to the contribution of 4 subsystems: EPS, OCS, TT&C and C&DH. For OCS, the initial over-estimation of the power is due to the specific design of the engines. The idle power of the engines is only due to telemetry, as no heater is required, as shown in chapter 8. For TT&C, the choice of a patch antenna explains the low power requirement, while for the remaining subsystems, the difference can be attributed to statistical error from the SMAD [12].

As for the comparison between the SCATTER detailed design and similar mission, here DANDE, which is also aiming to improve the understanding of the satellite drag environment, is used [52]. This specific mission was chosen as it has a similar set of payload sensors: 6 accelerometers, 1 mass spectrometer and 1 GPS receiver. On the other hand, it uses aero-braking to lower its orbit, while SCATTER uses a combination of thrusters and aero-braking. Table 14.2 gives an overview of the mass and power fraction taken by each subsystem in SCATTER and DANDE. It should be noted that DANDE included cabling mass in their mass estimations, which is something that could not be estimated for SCATTER at this stage of the design. Therefore it was ommited from the DANDE budget as well, which results in the total mass fraction for this mission to be 90.42%. The significant deviations will be discussed in the following paragraphs.

Table 14.2: Detailed design budgets vs. DANDE design budgets [3].

Source	Detailed Design Fraction		DANDE Budget Fraction			Deviation		
Subsystem	**Mass [%]**	**Average Power [%]**	**Cost [%]**	**Mass [%]**	**Average Power [%]**	**Cost [%]**	**Mass [%]**	**Average Power [%]**
Structures	29.53%	0.00%	-	44.89%	0.00%	-	-34.21%	0.00%
TCS	1.81%	0.00%	-	1.55%	0.00%	-	16.66%	0.00%
ODCS	28.53%	6.77%	-	2.33%	0.00%	-	1125.50%	-
ADCS	6.46%	36.61%	-	13.70%	6.44%	-	-52.81%	468.39%
EPS	26.39%	4.36%	-	18.86%	7.36%	-	39.95%	-40.77%
TT&C	3.29%	12.98%	-	3.72%	10.92%	-	-11.62%	18.87%
C&DH	0.68%	11.10%	-	1.01%	15.34%	-	-32.56%	-27.66%
Payload	3.31%	28.18%	-	4.36%	59.94%	-	-24.21%	-52.99%
Total	100.00%	100.00%	-	90.42%	100.00%	-	10.60%	0.00%

As it can be seen in the table above, several differences can be distinguished between the DANDE and SCATTER budgets, for multiple subsystems. The structures subsystem of SCATTER is 34 % lighter than that of DANDE. This can be explained by the usage of a CubeSat structure which maximizes the used space for the former, while the latter has a ball-like custom structure, which is less spatially efficient. The TCS subsystem, on the other hand, is 17 % heavier on SCATTER than DANDE. Such a difference can be explained by the vastly-different shapes of the satellites. Since SCATTER has deployable panels, these require heat sinks, as to not overheat, while the sphere-like shape of DANDE is more thermally-efficient. The OCS subsystem shows the largest differences in terms of power and mass between the two designs, for the reasons mentioned in the previous paragraph. As SCATTER contains two engines, it is 10 times heavier and requires power, while DANDE only needs a radar beacon to determine its position. For ADCS, SCATTER has a much larger mass and power as well, as it contains 6 sun sensors, 1 magnetorquer, 4 reaction wheels, 2 magnetometers, and 2 IMUs, while DANDE only uses 2 magnetometers for attitude determination and 2 torque rods for control. The EPS of SCATTER is 40 % higher in mass and 41 % lower in average power required. This is most likely due to the large number of batteries used by SCATTER to allow for at least 2 days of continuous science time. While the TT&C and C&DH show small deviations (much like TCS) which can be attributed to minor design differences, the payload subsystem of SCATTER shows a significant reduction in both mass and average power used. This can be explained by the higher number of 6 accelerometers used by DANDE, in comparison to the 2 used by SCATTER.

In conclusion, as all differences in the budgets of SCATTER and DANDE are either small, or explainable by different design choices, the SCATTER design is considered valid. In section 14.3, the requirement compliance matrices of SCATTER are shown.

14.3 Subsystem-Level Design Compliance Matrices

This section covers the compliance matrices of the SCATTER design at a subsystem level. For each requirement, a colour is assigned. A colour of **green** signifies that the requirement is verified using an analysis with existing information. On the other hand, **yellow** implies that the requirement is not verifiable at this stage of the design, either due to the need for testing, or due to insufficient analysis. If this is the case, a verification procedure is proposed. Finally, **red** signifies that the requirement was analysed with existing information, and it is not verified. In the tables below, the compliance matrices for all subsystems of SCATTER are shown:

Table 14.3: Compliance matrix of aerodynamic requirements.

Aerodynamics Requirements Compliance Matrix					
Requirement ID	**Verified?**	**Requirement ID**	**Verified?**	**Requirement ID**	**Verified?**
REQ-AER-01		REQ-AER-03		REQ-AER-04	

Table 14.4: Compliance matrix of EPS requirements.

EPS Requirements Compliance Matrix					
Requirement ID	**Verified?**	**Requirement ID**	**Verified?**	**Requirement ID**	**Verified?**
REQ-EPS-01		REQ-EPS-10		REQ-EPS-20	
REQ-EPS-02		REQ-EPS-11		REQ-EPS-23	
REQ-EPS-03		REQ-EPS-12		REQ-EPS-24	
REQ-EPS-04		REQ-EPS-15		REQ-EPS-26	
REQ-EPS-05		REQ-EPS-16		-	-
REQ-EPS-07		REQ-EPS-17		-	-

Table 14.5: Compliance matrix of Structure subsystem requirements.

Structures Subsystem Requirements Compliance Matrix					
Requirement ID	**Verified?**	**Requirement ID**	**Verified?**	**Requirement ID**	**Verified?**
REQ-SM-01		REQ-SM-07		REQ-SM-14	
REQ-SM-02		REQ-SM-09		REQ-SM-15	
REQ-SM-03		REQ-SM-10		REQ-SM-16	
REQ-SM-04		REQ-SM-11		REQ-SM-17	
REQ-SM-05		REQ-SM-12		REQ-SM-18	
REQ-SM-06		REQ-SM-13		REQ-SM-19	

Table 14.6: Compliance matrix of Thermal Control subsystem requirements.

Thermal Control Subsystem Requirements Compliance Matrix					
Requirement ID	**Verified?**	**Requirement ID**	**Verified?**	**Requirement ID**	**Verified?**
REQ-TCS-02		REQ-TCS-08		REQ-TCS-13	
REQ-TCS-04		REQ-TCS-09		REQ-TCS-14	
REQ-TCS-05		REQ-TCS-10		REQ-TCS-15	
REQ-TCS-06		REQ-TCS-11		REQ-TCS-16	
REQ-TCS-07		REQ-TCS-12		-	-

Table 14.7: Compliance matrix of Orbital Control subsystem requirements.

Orbital Control Subsystem Requirements Compliance Matrix					
Requirement ID	**Verified?**	**Requirement ID**	**Verified?**	**Requirement ID**	**Verified?**
REQ-OCS-01		REQ-OCS-04		REQ-OCS-012	
REQ-OCS-02		REQ-OCS-05		-	-
REQ-OCS-03		REQ-OCS-06		-	-

Table 14.8: Compliance matrix of ADCS requirements.

ADCS Requirements Compliance Matrix					
Requirement ID	**Verified?**	**Requirement ID**	**Verified?**	**Requirement ID**	**Verified?**
REQ-ADCS-01		REQ-ADCS-05		REQ-ADCS-09	
REQ-ADCS-02		REQ-ADCS-06		REQ-ADCS-010	
REQ-ADCS-03		REQ-ADCS-07		-	-
REQ-ADCS-04		REQ-ADCS-08		-	-

Table 14.9: Compliance matrix of TT&C requirements.

TT&C Requirements Compliance Matrix					
Requirement ID	**Verified?**	**Requirement ID**	**Verified?**	**Requirement ID**	**Verified?**
REQ-TTC-01		REQ-TTC-07		REQ-TTC-11	
REQ-TTC-02		REQ-TTC-08		REQ-TTC-12	
REQ-TTC-03		REQ-TTC-09		REQ-TTC-13	
REQ-TTC-06		REQ-TTC-10		REQ-TTC-14	

Table 14.10: Compliance matrix of Payload subsystem requirements.

Payload Subsystem Requirements Compliance Matrix					
Requirement ID	**Verified?**	**Requirement ID**	**Verified?**	**Requirement ID**	**Verified?**
REQ-PL-01		REQ-PL-06		REQ-PL-11	
REQ-PL-02		REQ-PL-07		REQ-PL-12	
REQ-PL-03		REQ-PL-08		REQ-PL-13	
REQ-PL-04		REQ-PL-09		REQ-PL-14	
REQ-PL-05		REQ-PL-10		-	-

Table 14.11: Compliance matrix of C&DH requirements.

C&DH Subsystem Requirements Compliance Matrix					
Requirement ID	**Verified?**	**Requirement ID**	**Verified?**	**Requirement ID**	**Verified?**
REQ-CDH-04		REQ-CDH-07		REQ-CDH-09	
REQ-CDH-05		REQ-CDH-08		-	-

14.4 System-Level Design Compliance Matrices

This section covers the compliance matrices of the SCATTER design at a system level. For each requirement, one of three colours is assigned, with the meanings explained in section 14.3. In the tables below, the compliance matrices for the system requirements and constraints of SCATTER are shown:

Table 14.12: Compliance matrix of mission requirements.

Mission Requirements Compliance Matrix					
Requirement ID	**Verified?**	**Requirement ID**	**Verified?**	**Requirement ID**	**Verified?**
REQ-M-01		REQ-M-09		REQ-M-18	
REQ-M-02		REQ-M-10		REQ-M-19	
REQ-M-03		REQ-M-11		REQ-M-20	
REQ-M-04		REQ-M-13		REQ-M-21	
REQ-M-05		REQ-M-14		REQ-M-22	
REQ-M-06		REQ-M-15		REQ-M-23	
REQ-M-07		REQ-M-16		-	-
REQ-M-08		REQ-M-17		-	-

Table 14.13: Compliance matrix of system functional requirements.

Functional Requirements Compliance Matrix					
Requirement ID	**Verified?**	**Requirement ID**	**Verified?**	**Requirement ID**	**Verified?**
REQ-F-02		REQ-F-14		REQ-F-23	
REQ-F-03		REQ-F-16		REQ-F-24	
REQ-F-04		REQ-F-17		REQ-F-27	
REQ-F-05		REQ-F-18		REQ-F-29	
REQ-F-07		REQ-F-19		REQ-F-30	
REQ-F-08		REQ-F-20		REQ-F-31	
REQ-F-12		REQ-F-21		-	-
REQ-F-13		REQ-F-22		-	-

Table 14.14: Compliance matrix of system performance requirements.

Performance Requirements Compliance Matrix					
Requirement ID	**Verified?**	**Requirement ID**	**Verified?**	**Requirement ID**	**Verified?**
REQ-P-02		REQ-P-11		REQ-P-19	
REQ-P-03		REQ-P-12		REQ-P-20	
REQ-P-04		REQ-P-13		REQ-P-21	
REQ-P-05		REQ-P-14		REQ-P-22	
REQ-P-07		REQ-P-15		REQ-P-23	
REQ-P-08		REQ-P-16		REQ-P-24	
REQ-P-09		REQ-P-17		REQ-P-25	
REQ-P-10		REQ-P-18		-	-

Table 14.15: Compliance matrix of design requirements.

Design Requirements Compliance Matrix					
Requirement ID	**Verified?**	**Requirement ID**	**Verified?**	**Requirement ID**	**Verified?**
REQ-D-01		REQ-D-06		REQ-D-09	
REQ-D-02		REQ-D-07		-	-
REQ-D-03		REQ-D-08		-	-

Table 14.16: Compliance matrix of constraints.

Constraints Compliance Matrix					
Requirement ID	**Verified?**	**Requirement ID**	**Verified?**	**Requirement ID**	**Verified?**
C-LEGAL-01		C-LEGAL-07		C-RES-06	
C-LEGAL-02		C-LEGAL-08		C-SAFE-05	
C-LEGAL-03		C-LEGAL-09		C-SAFE-06	
C-LEGAL-04		C-RES-01		C-SUS-01	
C-LEGAL-05		C-RES-02		C-SUS-02	
C-LEGAL-06		C-RES-05			

14.5 Design Verification and Validation Concluding Remarks

Based on the verification and validation procedures performed in this chapter, the SCATTER detailed design satisfies almost all requirements that could be verified. The exception to this are only REQ-M-16 ("The mission shall use an accelerometer to measure the translational acceleration of phase III") and REQ-PL-11 ("The IMU shall measure accelerations with a frequency of at least 0.1 Hz"), which are both related to the usage of an accelerometer to measure the drag coefficient in Phase III of the mission. This requirement was not satisfied due to the insufficient accuracy of the chosen IMU. It is recommended to perform further research into non-commercial IMUs used in similar missions, to find a more accurate one, or alternatively, use a data-processing scheme with multiple IMUs to increase the existing measuring accuracy, much like the DANDE mission [52].

15. Manufacturing, Assembly & Testing Plans

Following the detailed design laid out in the previous chapters, this chapter presents the plans for the manufacturing, assembly and testing of the spacecraft. Section 15.1 deals with the purchase of COTS components and the manufacturing of the structure. Next, section 15.2 describes the procedure of combining all subsystems. This chapter concludes with a description of the required testing in section 15.3. A summary of these processes is depicted in figure 15.1.

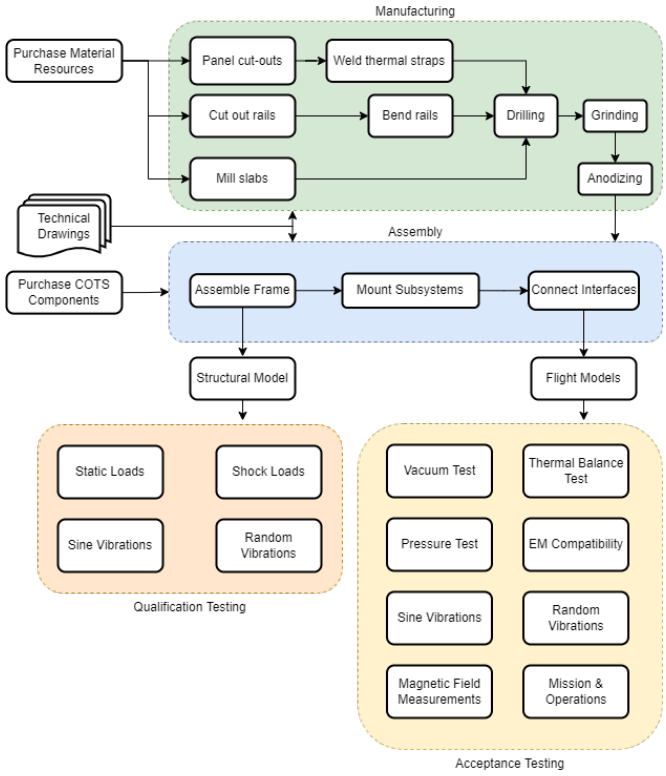

Figure 15.1: Manufacturing, Assembly & Testing Flow Diagram.

15.1 Manufacturing

By respecting the request to consider COTS components, the majority of the subsystems can be readily purchased from commercial providers. These decisions significantly lowered the overall price, as these space-grade components do not require any additional funds for development, resources or individual testing. To satisfy C-RES-05, back-up suppliers for all COTS have been considered, as demonstrated in table 15.1.

Table 15.1: COTS components and their suppliers.

Products	Primary supplier	Back-up supplier
PCUs, PDUs	ISISpace	GOMspace [1]
Batteries, BCUs	ISISpace	GOMspace [2]
Propulsion unit	NanoAvionics	Aerojet Rocketdyne [3]
Magnetorquers	ISIS	Naonoavionics [4]
Reaction wheels	ROCKETLAB	CUBESPACE [5]
Surface mounted Sun sensors	NSS	SOLARMEMS [6]
Solar panel mounted Sun sensors	Tensor Tech	SOLARMEMS [7]
Magnetometer	NSS	AAC CLYDE SPACE [8]
Transceiver	IQ Spacecom	Rakon [9]
Patch Antenna	ISISpace	Endurosat [10]
Mass spectrometer	Mullard Space Science Laboratory	Goddard Space Flight Center [65]
IMU	SBG Systems	Epson [11]
GNSS Receiver	Pumpkinspace	GOMspace [12]
GNSS antenna	Tallysman	NovAtel [13]
OBC	NanoAvionics SatBus 3C2	ISIS On Board Computer
Kapton films	Dunmore Corporation	Sheldahl, Aerospace Fabrication Materials LLC
Paints	Dunmore Corporation	AZ technology

Solar panels

As explained in chapter 4 and chapter 5, the solar arrays used on the SCATTER satellites all deploy at an angle of 10° for aerodynamic reasons. This non-standard angle requires the use of custom solar panel hinges. The dimensions of the main arrays also require them to fold 180° into two 6U faces. COTS solutions for this already exist[14], but these solutions do not have the required 10° hinge to connect to the body. Currently, two options are available: the first is to contact a company such as EnduroSat or GOMspace, and request a quote for a modified version of their offerings meeting the requirements of the SCATTER mission, and the second is to opt for a completely custom solution, as offered by Pumpkin[15].

C&DH Daughterboard

As presented in chapter 12, a custom design for a daughterboard is laid out. While the actual manufacturing of such a component is rather inexpensive, extensive testing will add a significant cost. This would include shock, radiation, thermal and vacuum testing.

Thermal Coats

For the thermal system, passive components such as insulating films are customised for the shape of the spacecraft. The paint is directly applied to the panel and does not require any special accommodations.

Structures Subsystem

As presented in chapter 6, a custom structural frame was designed to fit the subsystems in the most optimal way. Therefore, in contrast with the other COTS subsystems, material resources have to purchased, and actual manufacturing has to be taken into account. Table 15.2 present estimates on the bulk material that needs to be purchased. The respective bulk cost estimates are based upon a price per kilogram. Once the aluminium is bought in the form of sheets and slabs, several manufacturing processes are required to obtain the final end product. The expected processes are listed here, with a short description of their nature and need [73].

Table 15.2: Raw material breakdown.

Component	Mass [kg]	Raw Material	Cost [€] [16]
Bulkheads	6.527	Al 6061-T6	16.35
Panels	2.041	Al 6061-T6	5.11
Rails	0.428	Al 6061-T6	1.07
Counterweight	0.230	Tungsten	6.62
Structure	9.226	/	29.15

- Punching/Laser cutting/Abrasive water jet cutting: these processes are candidates for making the cut-outs in the thin body panels. All methods obtain sufficient accuracies and can be used for small series of products. In case of laser cutting, extra considerations need to be made, as the reflectivity and high thermal conductivity of aluminium might introduce adverse effects.
- Face milling: this process would be used to machine the bulkheads from full slabs of aluminium. This process is sufficiently accurate to create the more complex corner geometries.
- Drilling: to allow for a proper assembly of the frame, a large amount of holes needs to be drilled in every part.
- Grinding: processes such as milling and drilling can leave rough edges for which a finishing treatment is needed.
- Bending: the corner rails are single curved elements with small bending radii. These elements could be fabricated on a press brake.
- Welding: to attach the thermal strap and the counterweight, welding could be considered. The aluminium alloy 6061-T6 is easy to weld, although one must be careful not to compromise its heat treatment. Other joining options for the counterweight might be needed depending on the exact welding method, as tungsten has a very high melting point

[1] https://gomspace.com/shop/subsystems/power/default.aspx, retrieved on 15/06/2022
[2] https://gomspace.com/shop/subsystems/power/default.aspx, retrieved on 15/06/2022
[3] https://satsearch.co/products/aerojet-rocketdyne-holdings-inc-mps-130
[4] https://nanoavionics.com/cubesat-components/cubesat-magnetorquer-satbus-mtq/
[5] https://satsearch.co/products/cubespace-cube-wheel-large
[6] https://www.cubesatshop.com/product/ssoc-d60-2-axis-digital-sun-sensor/
[7] https://www.cubesatshop.com/product/nanossoc-d60-digital-sun-sensor/
[8] https://www.aac-clyde.space/what-we-do/space-products-components/adcs/mag-3
[9] https://www.rakon.com/products/system-solutions/s-band-transceivers, Retrieved on 15-06-2022
[10] https://www.endurosat.com/cubesat-store/cubesat-antennas/s-band-antenna-commercial/, Retrieved on 15-06-2022
[11] https://global.epson.com/products_and_drivers/sensing_system/imu/g370/, retrieved on 15th June, 2022.
[12] https://gomspace.com/shop/subsystems/attitude-orbit-control-systems/gps-kit.aspx, retrieved on 15th June, 2022.
[13] https://hexagondownloads.blob.core.windows.net/public/Antcom/Pdfs/Product%20Sheets/PS_G5Ant-3XMXX.pdf, retrieved on 15th June, 2022.
[14] https://gomspace.com/shop/subsystems/power/nanopower-tsp.aspx, retrieved 15/06/2022
[15] https://www.pumpkinspace.com/store/p166/Custom_PMDSAS_panel%2C_deployable%2C_per_cell.html, retrieved 15/06/2022
[16] https://www.metalary.com/

- Anodizing: to obtain a structure that is fully space-grade, a hard anodizing coat of type III can be applied to prevent outgassing [74]. Adhering to the regulations of the European Cooperation for Space Standardization (ECSS) [75], one should aim at achieving a Total Mass Loss (TML) and a Collected Volatile Condensable Material (CVCM) smaller than 1 % and 0.1 % respectively.

To obtain a cost estimate for the structure, a top-down approach was taken, as the mere addition of bulk material and manufacturing cost would be a large underestimate. An average cost per CubeSat unit was calculated to be €1,450 per unit [17]. For 12 units, this gives a lower bound of €17,400. To adjust for its custom nature and low production series, the raw material costs and a 15 % testing fraction were added [12]. Finally, an anodizing cost of €260 per piece was assumed, resulting in a total frame cost of €23,160[18]. Individual component costs are estimated using their weight fraction.

15.2 Assembly

Using the internal and external lay-outs presented in chapter 13 supplemented with detailed technical drawings from the respective CAD models, all subsystem components can be put together. The first step requires to assembly the structural frames, of which one is needed as a Development Model (DM) . Next, the subsystems need to be mounted in their required locations, for the reasons presented in chapter 13. Finally, all subsystems need to be interfaced by physically and functionally combining all components [76]. This includes checking electrical signals, software/hardware connections, fields of view and deployment envelopes [76]. Once this is all completed, an actual Flight Model (FM) can be constructed.

15.3 Testing

When the DM is assembled, the testing procedures can start, as depicted in figure 15.1. Qualification testing is to be performed upon the DM, more specifically on a Structural Model (SM) , as the spacecraft frame is fully custom. COTS components are for now assumed to have been through qualification testing, unless otherwise specified by the supplier. To perform these tests, the appropriate safety factors need to be taken into account, as requested by Arianespace [33]. Loads encountered during qualification testing are not expected to occur during launch, thus passing these tests provides confidence that the model will survive the launch. One must keep in mind that these tests might damage the DM in case of an insufficient design, thereby perhaps requiring multiple DMs.

The FMs constructed during assembly, of which there are at least two, are the actual spacecraft to be flown and require testing before they are accepted for flight on the launch vehicle. Acceptance testing also involves safety factors, but lower than those for qualification testing, as the FMs are not supposed to be damaged [33]. Several testing procedures exist, of which some of them apply to both qualification and acceptance [76]. The ones mentioned in figure 15.1 are listed below, with a short elaboration:

- Static Loads (Q): the SM will be subjected to launch accelerations with qualification safety factors as specified in the launcher manual [33].
- Shock Loads (Q): the SM will be subjected to shock loads on a shaker device with qualification safety factors as specified in the launcher manual [33].
- Sine Vibrations (Q, A): the SM and FM will be subjected to sine vibrations on a shaker device with qualification and acceptance safety factors as specified in the launcher manual [33].
- Random Vibrations (Q, A): the SM and FM will be subjected to random vibrations on a shaker device with qualification and acceptance safety factors as specified in the launcher manual [33].
- Vacuum Test (A): the FM will be subjected to the most stringent vacuum conditions accounted during the mission by using a thermal vacuum chamber [19].
- Pressure Test (A): Fuel tanks will be subjected to three cycles of 150 % design pressure for at least 5 min. While doing so, all joints will be checked for leakages [76].
- Thermal Balance Test (A): the FM will be subjected to the mission thermal environment by using a thermal vacuum chamber [20].
- Electromagnetic compatibility (A): All electronic components will be tested for electromagnetic interferences from internal and external sources. Antennas will be tested for the required downlinks and uplinks.
- Magnetic Field Measurements (A): Magnetically-sensitive items such as magnetometers are to be tested for interference of magnetic fields induced in metallic structures [76].
- Mission & Operations (A): a simulated mission will be run via a communication link with the mission operation centre to verify ground-to-space interfaces, mission operations sequences and spacecraft data handling.

[17] https://www.isispace.nl/product-category/cubesat-structures/
[18] https://www.nyccnc.com/how-to-outsource-anodizing/
[19] https://www.esa.int/Enabling_Support/Space_Engineering_Technology/Test_centre/Phenix_Thermal_Vacuum_Chamber
[20] https://www.esa.int/Enabling_Support/Space_Engineering_Technology/Test_centre/Phenix_Thermal_Vacuum_Chamber

16. Project Design & Development Logic

This chapter focuses on the future work after phase IV. Section 16.1 shows the work flow diagram specifically for post-DSE activities. In addition to that, the cost breakdown structure mainly focusing on post-DSE activities is presented in figure 16.1.

16.1 Future Workflow Diagram

Figure 16.2 shows a high-level work flow diagram for the future of the project. It depicts the workflow for future, more in-depth analyses, ordering of parts, as well as qualification testing, acceptance testing, and launcher integration.

16.2 Cost Breakdown Structure

After finalising the manufacturing, assembly, testing plan as well as the post-project activities identification, the cost breakdown structure can be derived. figure 16.1 gives an overview of the costs during the overall spacecraft development, production and operation procedure. The general format of this cost breakdown structure is from [77]. In the cost breakdown structure, there are a total of four different phases, where research phase is mainly accomplished by a group of ten people in ten weeks. Therefore, the costs estimation of this phase is based on a €40 hourly rate assumption. However, due to the fact that overtime working is common in the group and each person is allocated two roles, an estimation of €0.544M is given. The production costs, which are derived from the detailed design given by subsystem engineers and [12], take part in the main part of the total costs. [12] also supports the highly-estimated operation costs. As for the disposal cost, extra system planning analysis should be done in the case that debris mitigation needs to be performed, caused by insufficient burn-up. This leads to a total of €5.504M for each satellite. However, due to the fact there are a total of two satellites, a rough estimation of €11M can be drawn.

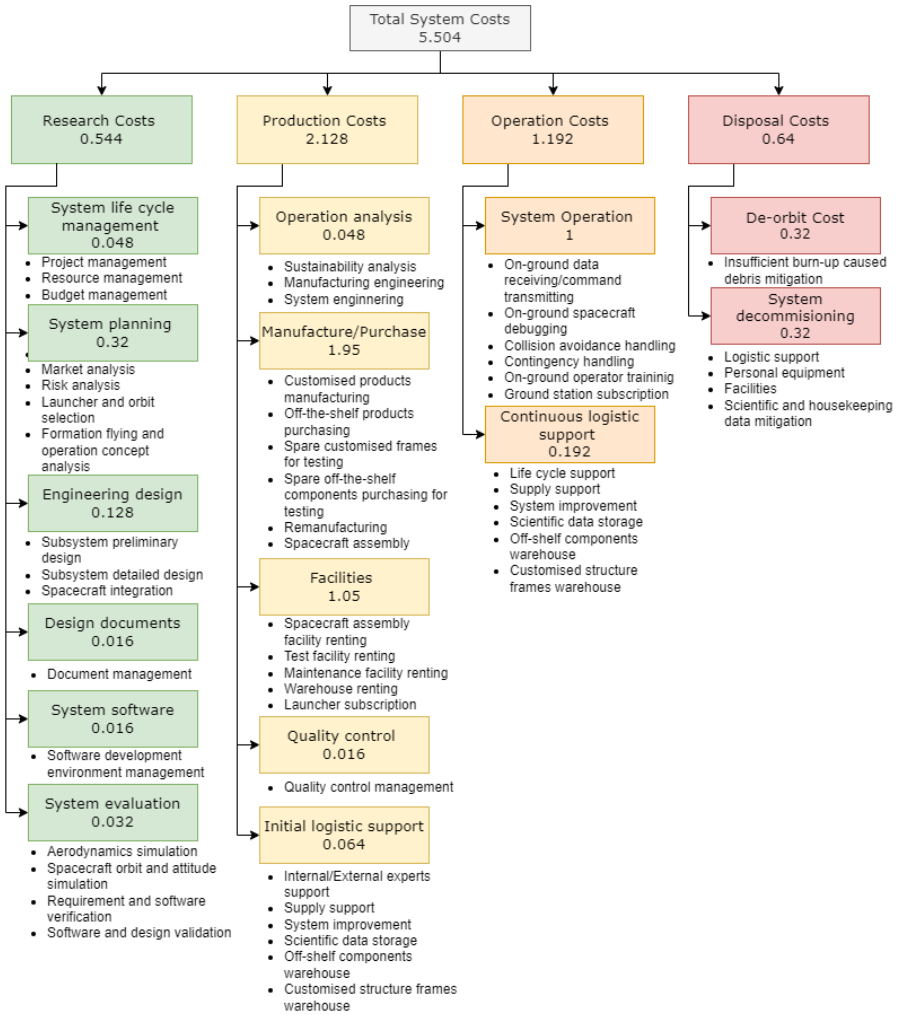

Figure 16.1: Cost breakdown structure.

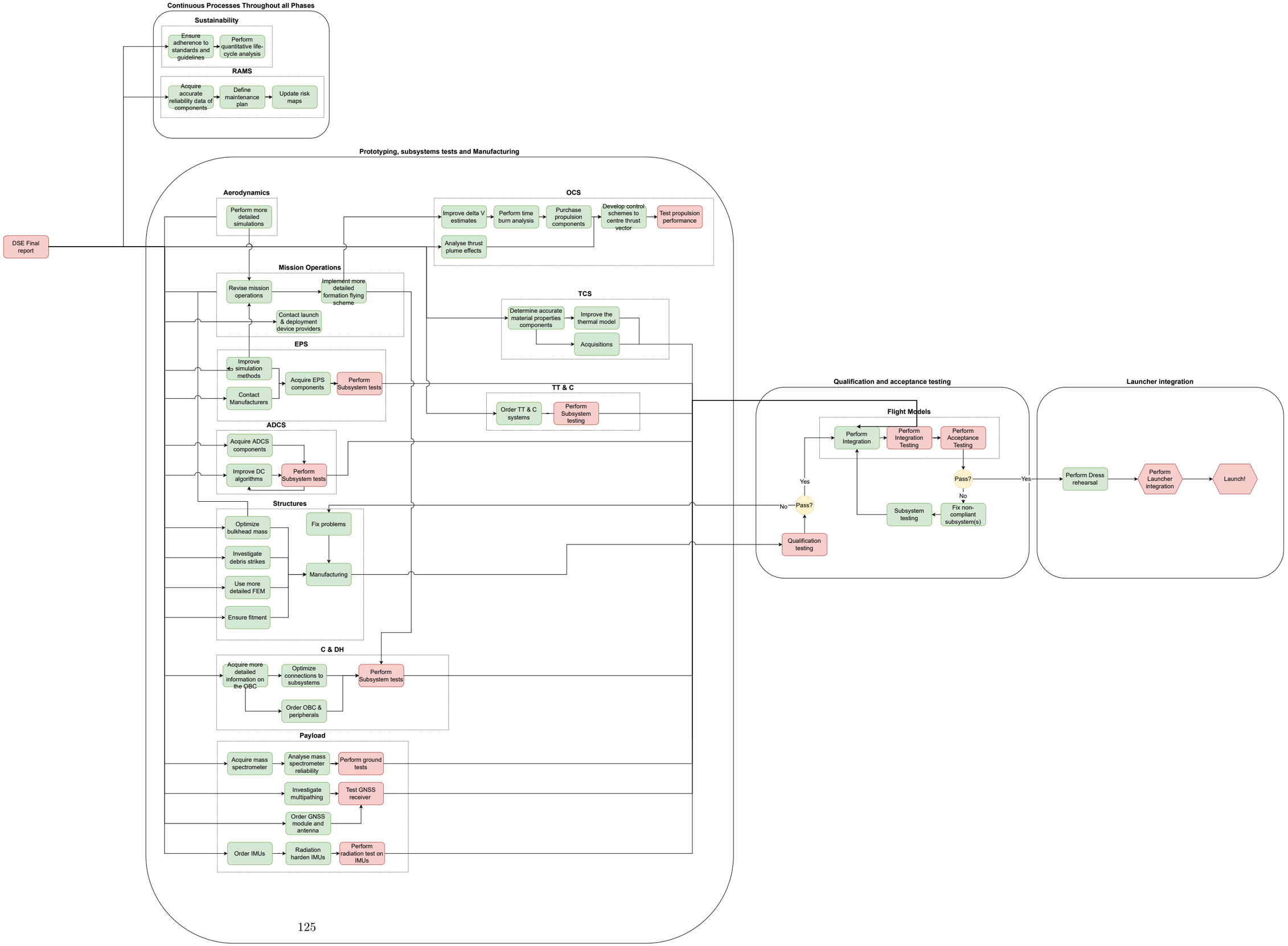

Figure 16.2: Future Workflow breakdown.

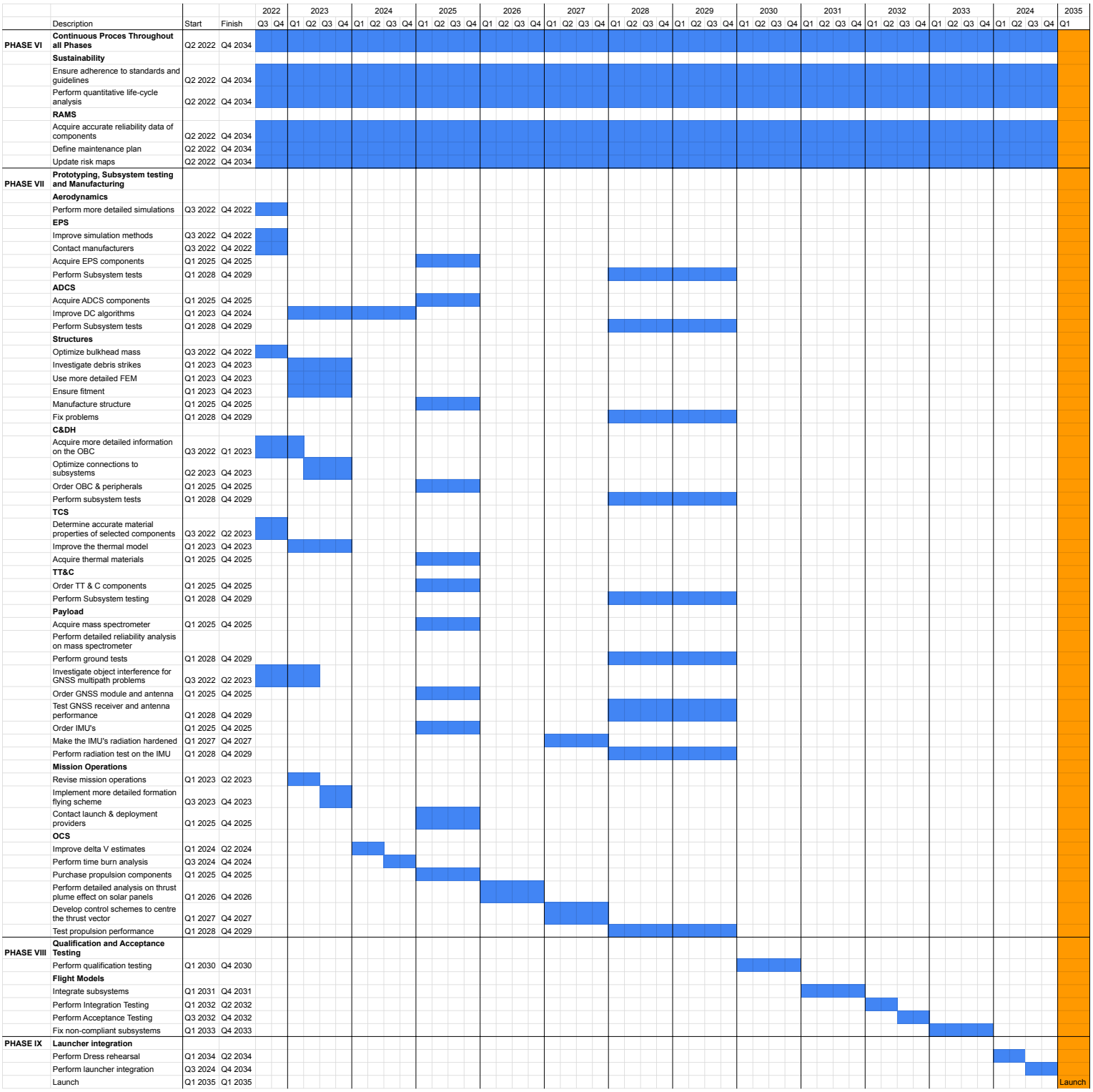

	Description	Start	Finish
PHASE VI	**Continuous Proces Throughout all Phases**	Q2 2022	Q4 2034
	Sustainability		
	Ensure adherence to standards and guidelines	Q2 2022	Q4 2034
	Perform quantitative life-cycle analysis	Q2 2022	Q4 2034
	RAMS		
	Acquire accurate reliability data of components	Q2 2022	Q4 2034
	Define maintenance plan	Q2 2022	Q4 2034
	Update risk maps	Q2 2022	Q4 2034
PHASE VII	**Prototyping, Subsystem testing and Manufacturing**		
	Aerodynamics		
	Perform more detailed simulations	Q3 2022	Q4 2022
	EPS		
	Improve simulation methods	Q3 2022	Q4 2022
	Contact manufacturers	Q3 2022	Q4 2022
	Acquire EPS components	Q1 2025	Q4 2025
	Perform Subsystem tests	Q1 2028	Q4 2029
	ADCS		
	Acquire ADCS components	Q1 2025	Q4 2025
	Improve DC algorithms	Q1 2023	Q4 2024
	Perform Subsystem tests	Q1 2028	Q4 2029
	Structures		
	Optimize bulkhead mass	Q3 2022	Q4 2022
	Investigate debris strikes	Q1 2023	Q4 2023
	Use more detailed FEM	Q1 2023	Q4 2023
	Ensure fitment	Q1 2023	Q4 2023
	Manufacture structure	Q1 2025	Q4 2025
	Fix problems	Q1 2028	Q4 2029
	C&DH		
	Acquire more detailed information on the OBC	Q3 2022	Q1 2023
	Optimize connections to subsystems	Q2 2023	Q4 2023
	Order OBC & peripherals	Q1 2025	Q4 2025
	Perform subsystem tests	Q1 2028	Q4 2029
	TCS		
	Determine accurate material properties of selected components	Q3 2022	Q2 2023
	Improve the thermal model	Q1 2023	Q4 2023
	Acquire thermal materials	Q1 2025	Q4 2025
	TT&C		
	Order TT & C components	Q1 2025	Q4 2025
	Perform Subsystem testing	Q1 2028	Q4 2029
	Payload		
	Acquire mass spectrometer	Q1 2025	Q4 2025
	Perform detailed reliability analysis on mass spectrometer		
	Perform ground tests	Q1 2028	Q4 2029
	Investigate object interference for GNSS multipath problems	Q3 2022	Q2 2023
	Order GNSS module and antenna	Q1 2025	Q4 2025
	Test GNSS receiver and antenna performance	Q1 2028	Q4 2029
	Order IMU's	Q1 2025	Q4 2025
	Make the IMU's radiation hardened	Q1 2027	Q4 2027
	Perform radiation test on the IMU	Q1 2028	Q4 2029
	Mission Operations		
	Revise mission operations	Q1 2023	Q2 2023
	Implement more detailed formation flying scheme	Q3 2023	Q4 2023
	Contact launch & deployment providers	Q1 2025	Q4 2025
	OCS		
	Improve delta V estimates	Q1 2024	Q2 2024
	Perform time burn analysis	Q3 2024	Q4 2024
	Purchase propulsion components	Q1 2025	Q4 2025
	Perform detailed analysis on thrust plume effect on solar panels	Q1 2026	Q4 2026
	Develop control schemes to centre the thrust vector	Q1 2027	Q4 2027
	Test propulsion performance	Q1 2028	Q4 2029
PHASE VIII	**Qualification and Acceptance Testing**		
	Perform qualification testing	Q1 2030	Q4 2030
	Flight Models		
	Integrate subsystems	Q1 2031	Q4 2031
	Perform Integration Testing	Q1 2032	Q2 2032
	Perform Acceptance Testing	Q3 2032	Q4 2032
	Fix non-compliant subsystems	Q1 2033	Q4 2033
PHASE IX	**Launcher integration**		
	Perform Dress rehearsal	Q1 2034	Q2 2034
	Perform launcher integration	Q3 2024	Q4 2034
	Launch	Q1 2035	Q1 2035

17. Sustainable Development

This chapter concerns the development of a sustainability strategy for this mission. First, the current rules and state of sustainability in the space sector is discussed in section 17.1, then the Life Cycle Assessment method (LCA) is described in section 17.2. Finally, section 17.3 presents the sustainable development strategy by applying LCA.

17.1 Current Guidelines on Sustainability in the Space Sector

There are currently no binding commitments for sustainability in the aerospace sector. However, there are several guidelines, such as guideline 27 of the UN Committee on the Peaceful Uses of Outer Space (UN COPUOS). It requires states and organizations to "promote the development of technologies that minimize the environmental impact of manufacturing and launching space assets and that maximize the use of renewable resources and the reusability or repurposing of space assets to enhance the longterm sustainability of those activities"[1]. This will be the goal of this sustainable development strategy.

In the European Union, where this space mission is developed, there are also non-space related regulations that need to be followed such as:

- RoHS directive restricting the use of certain hazardous substances like lead or mercury in electrical equipment. [2]
- REACH (EC 1907/2006), the European Commission Regulation aiming to "improve the protection of human health and the environment through the better and earlier identification of the intrinsic properties of chemical substances" which mainly affects propellants and manufacturing chemicals. [3]

Furthermore, there are several ISO standards for space activities including:

- ISO 16164:2015 - Disposal of satellites operating in or crossing Low Earth Orbit[4]
- ISO/TR 16158:2021 Space systems — Avoiding collisions among orbiting objects [5]
- ISO 24113:2019 Space systems — Space debris mitigation requirements [6]

17.2 Life Cycle Assessment

Figure 17.1: Life cycle assessment [7].

In its Clean Space Initiative, ESA determined the life cycle assessment (LCA) approach as a powerful method to assess the environmental impact of the space sector [78]. ISO standards 14040 and 14044 [8] define LCA as a "cradle-to-grave" evaluation, determining the environmental impact, inputs and outputs of each step in a product's life cycle. Use of this method eliminates burden shifting, where one process is made more sustainable by shifting the environmental impact to another process [78]. According to ESA's ecodesign assessment, the 5 steps in a space mission life cycle are design, production, launch, operations and disposal as shown in figure 17.1. The following ecological indicators are considered at each life cycle stage and are the recommended ecological impact factors of ESA [79]. Given that enough data is available for each design choice and selection, these indicators can be used to quantify the total impact of a certain option. This allows to include sustainability as a criterion in each trade-off and to guide the design making with respect to sustainability. These indicators are:

- Air acidification
- Climate change
- Water eutrophication
- Ionising radiation
- Ozone depletion
- Photochemical oxidation
- Resource depletion
- Toxicity water/human
- Water consumption
- Mass disposed in space
- Mass disposed in ocean

[1] https://blogs.esa.int/cleanspace/2017/03/10/clean-space-the-un-and-the-sustainability-of-space-activities/, Retrieved 29-04-2022
[2] https://ec.europa.eu/environment/topics/waste-and-recycling/rohs-directive_de, Retrieved 29-04-2022
[3] https://ec.europa.eu/environment/chemicals/reach/reach_en.htm, Retrieved 29-04-2022
[4] https://www.iso.org/standard/55741.html, Retrieved 29-04-2022
[5] https://www.iso.org/standard/81695.html, Retrieved 29-04-2022
[6] https://www.iso.org/standard/72383.html, Retrieved 29-04-2022
[8] https://www.iso.org/standard/37456.html, Retrieved 29-04-2022

17.3 Sustainable Development Strategy

Applying LCA to this mission results in the sustainable development plan produced in figure 17.2. Steps I-V correspond to the mission life cycle phases described in figure 17.1 and given below each phase are the main factors that need to be considered during each phase by the team in both trade-offs and mission planning.

Subsections 17.3.1, 17.3.2 and 17.3.3 group these factors into 3 main segments to be considered and provide more detail into which indicators are affected and the main contributors of that segment. Also, each segment includes potential solutions for these problems that can be kept in mind during trade-offs and mission planning. The office work by the team and all related impacts have already been considered in the organizational approach to sustainability.

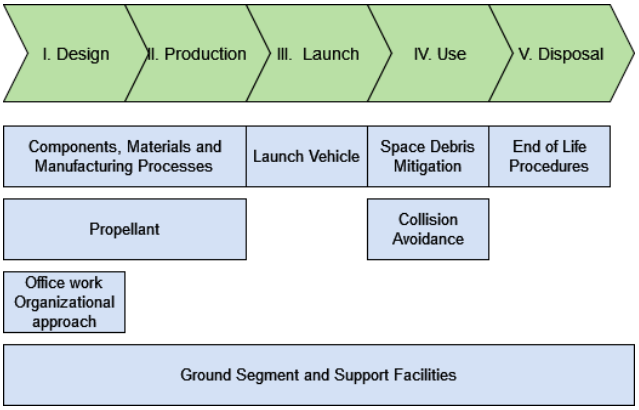

Figure 17.2: Sustainable development plan.

17.3.1 Components, Materials and Manufacturing Processes

Spacecraft are unique products and are produced in low quantities which implies a low ecological impact, there are however several resource intensive processes, special or rare materials and toxic substances used. The use of Germanium in photovoltaic panels is one of the main contributors to global warming in this category. Next to that, silver, gold and Germanium contribute to metal resource depletion. Heavy metals such as platinum or rhodium affect humans and water toxicity. Space-grade thermoplastics such as PTFE used in cable harnesses contribute largely to ozone depletion and global warming in production. Surface treatments using chemical baths are producing high toxicity, but can be partly mitigated using the European REACH regulation described earlier [78]. The key steps for reducing these issues are recycling of materials, novel sustainable materials and mass and volume reduction due to technology evolution.

17.3.2 Launch Vehicle and Propellant

Propellants typically make up to 85% of space mission mass, including the launcher, hence their impact is large. Hydrazine and xenon are both conventional spacecraft propellants and heavily used but highly toxic and are now regulated by REACH. The launch vehicle itself has a large effect on air acidification and ozone layer depletion caused by emissions in high altitudes[79]. "Green" non-toxic propellants are being researched and slowly implemented into the space sector which can replace conventional propellants [80]. Furthermore, reusable launchers can be selected and the environmental profile of each launcher should be considered at launcher selection. Lastly, sharing a launcher with other missions is an effective way to reduce ecological impact and cost.

17.3.3 End Of Life Procedures and Debris Mitigation

Space debris and collisions are increasing, threatening current missions and future space access. According to ESA, The biggest contributor to the space debris problem are explosions in orbit, caused by leftover energy, fuel and batteries onboard spacecraft.[9]. Furthermore, defunct satellites, fairings and parts from launch vehicles are left behind in orbit. To reduce these impacts several actions are effective, such as minimizing launch vehicle shedding and release of materials during operations (complying with ISO 24113:2019), releasing fuel and energy at EOL to prevent explosions and performing collision avoidance manoeuvres (complying with ISO/TR 16158:2021). Lastly, an important part is proper disposal of the mission at EOL, either into a graveyard-orbit or by re-entry (complying with ISO 16164:201).

17.4 Sustainability Assessment

With the sustainability guidelines and strategy established, the mission could be assessed at both a system and subsystem level based on the cradle-to-grave LCA. At system level, results were grouped in 4 segments: components, materials and manufacturing processes; launch vehicle and propellant; ground segment and office work; end of life procedures and debris mitigation. Components, materials and manufacturing effects are largely analysed on a subsystem level as that is where they have the greatest environmental impact. Finally, the future impact of SCATTER on sustainability in the space sector will be elaborated on.

17.4.1 System Level

Components, materials and manufacturing processes. For the manufacture and assembly of the satellites on a system level, COTS products were used wherever possible. This would mean that fewer resources are spent

[9] `https://www.esa.int/Safety_Security/Space_Debris/The_current_state_of_space_debris`, Retrieved 29-04-2022

on testing and developing the system, making the system economically sustainable. Additionally, the use of mass-produced products allows for a more sustainable use of resources with the help of efficient manufacturing methods used in industry. A more detailed analysis of materials and manufacturing is done at the subsystem level in section 17.4.2.

Launch vehicle and propellant. The launch segment contributes heavily to the environmental impact of the space mission. The Vega-C launcher was chosen, wherein the satellites will be launched into orbit via ride-sharing as a secondary payload along with other small satellites, which allows reducing the environmental impact per payload. Furthermore, a European launcher was selected to minimise transportation and logistical distances. Finally, Vega-E is recommended as a future option with a new green propellant upper stage and the use of additive manufacturing for waste reduction. For the spacecraft propellant, the green monopropellant LMP-103S, which is approved by REACH [81], was chosen and is elaborated on in section 17.4.2.

Ground segment and office work In design and production phases, the office work can have a relevant role on sustainability. Organisationally, this was carried out by the members of the team by using sustainable modes of transport, making sure to switch off the lights and electrical appliances when they were not in use etc. In the ground segment, only one ground station, dedicated for establishing contact with the satellite, is used. As mentioned in section 10.2.1, a single station in Vienna was chosen as the reference ground station for this design. As such, there is no need for additional resources to be spent on the maintenance of multiple stations which would have consumed more energy, funds, data processing power and manpower. Additionally, this ITU licensed station is shared with other missions and efficiently allocates resources for the general purpose of contacting satellites in orbit [60].

End of life procedures and debris mitigation. A satellite collision avoidance strategy has been developed in section 3.7, accounting to satellite-debris and satellite-satellite collision risks (complying with ISO/TR 16158:2021). To comply with ISO standard 16164:201 and the user requirements, the satellites will burn-up in the atmosphere at EOL. The estimated time to re-entry of 2.271 years falls well short of the recommended 25 years to re-entry, given in ISO 16164:201. Launch vehicle shedding and release of materials during operations (complying with ISO 24113:2019) proved to be difficult to assess and could not be evaluated at this stage.

The "Design for Demise" approach presented by ESA, is used to ensure a complete burn up of the satellites upon re-entry and reduce the probability of debris injury to humans to less than 1 in 10000[10]. Heavier elements, such as the tungsten counterweight and large metals parts like reaction wheels and propellant tanks, are more likely to survive the re-entry process. Section 17.4.1 shows re-entry simulations performed at 100 km using the DSMC simulation. Although both satellites are starting re-entry in high drag orientation, they are expected to start rotating during re-entry. Therefore, figure 17.3a and figure 17.3b show the temperature distribution at 100 km in high drag and low drag orientation, respectively. Based off of initial simulations, an approximate temperature of 2000 K to 7000 K is expected near the surface, depending on orientation. At these temperatures, the majority of the components will disintegrate and burn up. To ensure a complete burn up of the tungsten counterweight and the reaction wheels, it is recommended to conduct further analysis using tools such as DRAMA (Debris Risk Assessment and Mitigation Analysis).

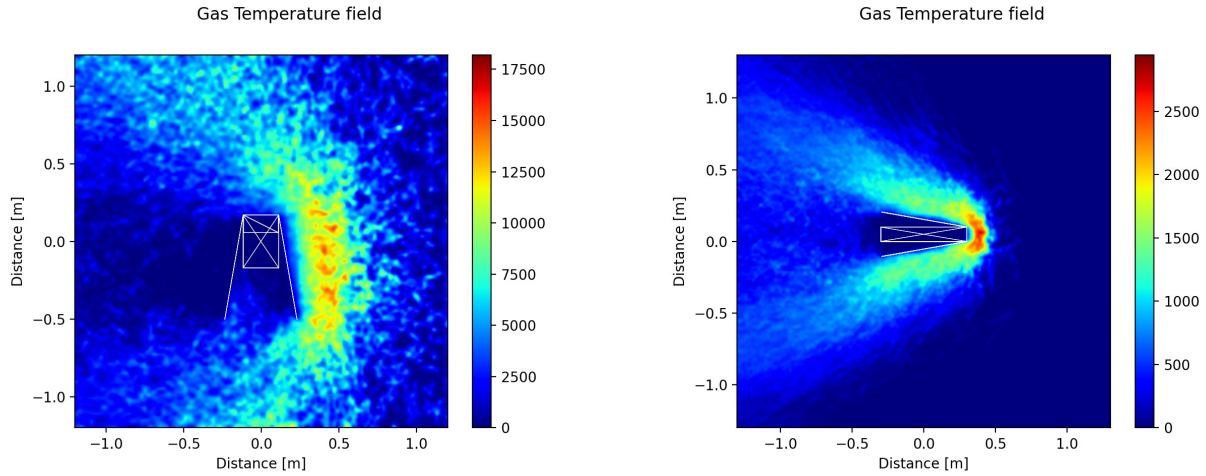

(a) Satellite in high drag orientation.

(b) Satellite in low drag orientation.

Figure 17.3: Re-entry simulation of SCATTER at 100 km using DSMC-SIM.

[10] `https://www.esa.int/Safety_Security/Clean_Space/Space_debris_feel_the_burn`, Retrieved 15-06-2022

17.4.2 Subsystem Level

Each subsystem that has been designed consists of several components and materials, which have undergone differing manufacturing procedures before they were delivered to be assembled with the satellite. These aspects are assessed below per subsystem. Their assessment will be largely focused on the design and production phases, as the following phases of launch, use and disposal are phases in which they do not produce a large environmental impact.

Electrical Power System

The main parts of the EPS are the solar arrays made of photovoltaic cells and the lithium-ion batteries. The chosen solar cells are indium-gallium phosphide/gallium arsenide/germanium on germanium substrate. The production of solar cells and batteries are amongst the major contributors to the overall ecological impact of SCATTER. The extraction of gold, silver and germanium contributes to metal depletion and involves unsustainable mining practices. Toxicity to humans and water, ozone depletion and acidification are additional consequences [82]. Production processes and surface treatments used, such as for the germanium wafer, are resource heavy and have large global warming potential. The use of recycled germanium, gold and silver and more efficient industrial processes can help resolve these issues [78]. However, recycling of lithium-ion batteries is complicated and not yet established in industry.

Printed Circuit Boards

Almost all subsystems include the use of electronics and therefore printed circuit boards (PCB). Composite materials like FR4, which is a glass-reinforced epoxy laminate material, are commonly used for circuit boards. In conventional PCB manufacturing, electricity and chemicals have high impacts on global warming [83]. Furthermore, heavy metals such as silver are used as conductive material. PET or paper is proposed as alternative for PCB substrates. In addition, additive manufacturing can decrease the material consumption in PCB manufacturing, in comparison with subtractive manufacturing.

Orbital Control System

When assessing the various options available for use as a monopropellant for the OCS, hydrazine was seen to be the type most often used in spaceflight due to its many advantages, such as the high specific impulse it provides. However, according to REACH, hydrazine is a toxic propellant which is highly carcinogenic. So, the European Chemicals Agency (ECHA) added it to the Substances of Very High Concern (SVHC) list in June 2011. The use of this substance also runs the risk of being banned in the European Union in the future years. In order to avoid the use of this toxic propellant, the propellant selection process focused on sustainability as a key factor. As a result, the green propellant known as LMP-103S was used for the design of this subsystem which complies with REACH (EC 1907/2006). It is a high performance propellant with a 32% better average lifetime performance than hydrazine. So, for example, a smaller tank could be needed for the satellite to provide the same delta-V as hydrazine. The material handling and transportation is simpler, due to how much safer it is to handle, and cost-effective. All these factors reduce the ecological impact in the design and production phases, as well as the life-cycle phase when it is in use. [81]

Structures

The structures subsystem largely consists of an aluminium alloy structure making up the frame of the satellite bus. The machining of Aluminium 6061T6 from a slab for the frame produces waste material along with the ADCS and housing structures for all of the subsystems. In order to reduce waste in the production phase, additive manufacturing methods will be adopted. This alloy has a melting point of 582 °C to 652 °C (table 6.3) which is far below that of the temperatures reached during re-entry (2000 K to 7000 K), thus guaranteeing that the frame will burn up on re-entry.

However, tungsten was continued to be used as the counterweight in the structure even though its melting point is 1960 K[11]. This was because the alternative materials of similar density included radioactive elements and other elements, such as gold and platinum. However, the use of gold would contribute to the depletion of rare metals and the use of platinum would be supporting platinum mining, a process which is harmful to the environment as it increases water toxicity. In order to avoid shifting the burden of the ecological impact of this counterweight from the disposal phase to the production phase, it was decided that the tungsten counterweight would remain. As a supplemental measure, it is recommended that simulation tools such as DRAMA be used for a better analysis of this component's burn up.

Thermal Control System

The products used in the thermal control system have an ecological impact mostly in the design and production phase but not in the use phase of the life cycle due to it being a passive system. The main products used were the Kapton film which is a non-hazardous polyimide[12], making use of low energy intensive production methods[13]. The production of hard anodised aluminium also does not create toxic by-products. It is not an extremely energy

[11] https://material-properties.org/tungsten-density-strength-hardness-melting-point/, Retrieved on 15-06-2022

[12] https://cns1.rc.fas.harvard.edu/safety/pdf/Kapton%20Polyimide%20Etchant.pdf, Retrieved 15-06-2022

[13] https://patentimages.storage.googleapis.com/0e/7e/fe/ec790b93d7be71/US20140058060A1.pdf, Retrieved 15-06-2022

intensive process and does not emit volatile organic compounds[14]. For the following design phases, the paints chosen for this subsystem will be products that are supplied by companies which adhere to the rules and guidelines meant to reduce toxicity in paints and a similar adherence to the rules and guidelines will be implemented for the Kapton films used.

17.4.3 Future effect of SCATTER on Sustainability

SCATTER's aim to improve GSI modelling means that the orbit prediction of tracked objects in space would potentially be improved by decreasing the uncertainty in said predictions. Current uncertainties in orbit propagation lead to a large positional uncertainty field around a satellite or debris object. Anytime another space object comes close enough and the probability of collision is above a certain threshold, the probability needs to be reassessed and if needed, spacecraft need to perform collision avoidance manoeuvres.

With an improved orbit prediction model, this could lead to a reduction in collision warnings issued, for a constant number of space objects. This would reduce the resources needed to assess every one of these warnings for the next action to be carried out. Furthermore, more satellites can safely pass each other within a smaller distance from each other and so, a larger number of satellites can also be accommodated in dense orbits around the Earth. This is also crucial due to the expected increase in satellite constellations launched and growth of the space industry, as explained in section 1.4. This could eventually lead to cleaner, more sustainable use of orbits around the Earth.

[14] `https://www.greenspec.co.uk/building-design/aluminium-production-environmental-impact/`, Retrieved 15-06-2022

18. Risk Analysis and RAMS characteristics

This chapter aims to summarise the technical risks associated with the mission and the mitigation measures to be taken in order to give it the highest chance of success. Finally, the system's reliability, availability, maintainability and safety will be assessed to ensure the satellite's engineering integrity.

18.1 Risk Analysis

The risk analysis consists of two key steps: risk assessment and risk management. Risk assessment identifies the potential risks which can occur throughout the scope of the project. It also assesses how likely these are to occur and how severe the resulting consequence would be should they take place. This is directly addressed in section 18.1.1. Depending on the likelihood and consequence, risk management of varying degrees must take place in order to mitigate the adverse effects of the risks. This is extensively discussed in section 18.1.2.

18.1.1 Risk Assessment

The assessment of the risks in terms of likeliness and consequence are derived mainly from experiences of the members in other engineering projects, as well as examples from industry, literature and other space missions. For the likelihood of event, the scores are as follows [9]:

- Very low (1) - less than 1% probability of occurrence.
- Low (2) - 1% to 30% probability of occurrence.
- Moderate (3) - 30% to 50% occurrence.
- High (4) - 50% to 70% probability of occurrence.
- Very high (5) - 70% probability of occurrence.

The consequence of the event can be divided into different categories as well[9]:

- Negligible (1) - Inconvenience or non-operational impact.
- Marginal (2) - Degradation of secondary mission objectives or small reduction in technical performance.
- Significant (3) - Mission objectives still achieved, but the time and performance are affected to some extent.
- Critical (4) - Mission success is questionable and/or reduction in technical performance.
- Catastrophic (5) - Mission failure or significant non-achievement of performance.

Thus, the risk score is then simply calculated by multiplying the likelihood and consequence of each risk. The likelihood and the consequence of new risks and justification is provided in table 18.1. RISK-MP-02, RISK-AERO-01,02,03,04 flow from the midterm report for which the risk score was updated with the current design. The other risks are new risks introduced with the detailed design.

Table 18.1: Subsystem technical risks, their likelihood, consequences, risk scores and drivers. The likelihood and consequence scores are defined as mentioned earlier in the text. The risk score is calculated as the product of the likelihood and consequence scores.

ID	Technical Risk description	Likelihood	Consequence	Risk score	Risk drivers
RISK-ADCS-04	ADCS fails to de-saturate the reaction wheels	1	5	5	ADCS actuator reliability, faulty control scheme (Magnetorquer failure)
RISK-MP-02	Solar cycle is drastically different from predicted	3	4	12	Solar cycle unpredictability
RISK-TCS-03	Temperature of propellant tanks might fall outside the operational range	5	3	15	
RISK-TCS-04	Temperature of TT&C might fall outside the operational range	3	3	9	
RISK-TCS-05	Solar panel mounted sun sensors might fall outside the operational temperature range	2	3	6	Selected sun sensors have a small operational range
RISK-PROP-05	The thrust plume might damage the external components of the spacecraft	2	3	6	Thruster plume, lack of analysis/information
RISK-AERO-01	Aerodynamic drag is higher than expected during phase 3	2	3	6	Modelling uncertainty
RISK-AERO-02	Aerodynamic drag is lower than expected during phase 2	2	3	6	Modelling uncertainty
RISK-AERO-03	The drag coefficient is not as sensitive as expected	2	4	8	Modelling uncertainty
RISK-AERO-04	During measurements phases of phase 3, the satellites drift apart faster than expected	2	2	3	Modelling uncertainty
RISK-AERO-05	During measurements phases of phase 1, the satellites drift apart slower than expected	2	3	9	Modelling uncertainty

RISK-ADCS-04: ADCS fails to de-saturate the reaction wheels

The reaction wheels can only spin up to a certain rotational speed, after which they need to be de-saturated by dumping the angular momentum into Earth's magnetic field using the magnetorquer. The likelihood of is very low, as the magnetorquer is a simple component with minimal moving parts and high lifetime [84]. The consequence is catastrophic as the momentum cannot be dumped without tumbling the satellite or more importantly maintain the attitude required for scientific measurements, thus leading to mission failure.

RISK-TCS-03: Temperature of propellant tanks might fall outside the operational range

The propulsion system has a narrow operational temperature range of 283 K to 313 K. The likelihood is very high because the temperature drops below 283 K during the eclipse, as seen in section 7.3.2. The consequence is significant because the performance of the propulsion system reduces considerably.

RISK-TCS-04: Temperature of TT&C might fall outside the operational range

As discussed in section 7.3.2, the temperature of TT&C is quite close to the operational limit and thus needs to be monitored in future design phases as there are uncertainties in the thermal model due to the simplifications made. The consequence of it is significant, as the module cannot be operated and the spacecraft has to wait for the temperature to go back up.

RISK-TCS-05: Solar panel mounted sun sensors might fall outside the operational temperature range

The operational range of the solar panel is not provided also with no additional information on the sun sensors. It is not known with certainty if the sun sensors can survive the extreme temperature swings of the solar panel. However, the likelihood is low because the solar panels mounted sun sensors come integrated with the solar panels and are generally made for those conditions. The consequence is significant because there are still some sun sensors on the body panel which are well within the operational range, thus this risk will only cause some problems in the performance of the mission.

RISK-PROP-05: The thrust plume might damage the external components of the spacecraft

Since the solar panels are longer in comparison to the length of the body, it will be in the path of the thruster's plume. The likelihood of the damage is low, since the maximum stress experienced by the panel is well below the yield limit, as discussed in section 8.3.1. The consequence is significant, as it can damage the solar panels by imparting additional moment on the hinges or by thermally damaging the cells, thus reducing the power generating capabilities of the spacecraft.

RISK-AERO-05: During measurement phases of phase 1, the satellite drift apart slower than expected

During the phase 1 of the mission, due to the low atmospheric density, the difference in drag experienced by the two spacecrafts might be lower than what is expected due to modelling uncertainties. The likelihood is low because this risk is mainly driven by the modelling uncertainty during the design phase and extensive aerodynamic simulations have been performed to reduce the uncertainty as discussed in section 4.2.2. The consequence is significant because if the two satellites drift apart slowly, the spacecrafts may not be able to make accurate measurements in the allocated time for the science mode.

The likelihood of RISK-MP-02 increased to medium from low because a solar cycle can be predicted with confidence only when the mission is a few years into a solar cycle [1]. The likelihood of RISK-AERO-01,02,03,04 reduced to low from medium because extensive simulations were performed in this design phase as discussed in section 4.2.2.

In order to have the detailed design report independent of the midterm and baseline report, the previously derived risks are included below for reference:

- RISK-TECH-01: Collision between SCATTER satellites
- RISK-TECH-02: Collision with other (working) satellites
- RISK-TECH-03: Collision with trackable space debris
- RISK-TECH-04: Collision with untrackable space debris
- RISK-TECH-05: Fatal failure of launch vehicle
- RISK-TECH-06: Incorrect orbital insertion of the launch vehicle
- RISK-TECH-07: Loss of communication with ground due to attitude
- RISK-TECH-08: Non-functional ground station
- RISK-TECH-10: Higher load and/or vibrations experienced during launch than specified by the launch provider
- RISK-TECH-11: Improper de-orbiting
- RISK-TECH-12: High solar activity affecting the mission timeline and resources
- RISK-TECH-13: Parts not manufactured in accordance with the design
- RISK-TECH-14: Satellite is lightly damaged during assembly
- RISK-TECH-15: Satellite suffers significant damage during assembly
- RISK-TECH-16: Connections not properly made during assembly

[1] `https://solarscience.msfc.nasa.gov/predict.shtml`, Retrieved on 14-06-2022

- RISK-TECH-17: Contamination of sensitive instruments
- RISK-TECH-18: Interfaces not defined correctly during design
- RISK-TECH-19: Satellite is electrically damaged during testing
- RISK-TECH-20: Satellite is mechanically damaged during testing
- RISK-TECH-21: Negligence in changing from testing to operational configuration
- RISK-TECH-22: Mechanical and electrical connections separate during transport
- RISK-TECH-23: Satellite significantly damaged during transportation
- RISK-TECH-24: Satellite damaged during integration with the launch vehicle
- RISK-TECH-25: Satellite improperly integrated with the launch vehicle
- RISK-PL-01 Failure of instrument due to lack of radiation hardening
- RISK-PL-02 Accelerometer drift becomes too significant for inertial measurements in phase 3
- RISK-PL-03 One of the mass spectrometers malfunctions
- RISK-ADCS-01 Satellite fails to de-tumble after deployment
- RISK-ADCS-02 Magnetic components of the ADCS and TT&C subsystems influence each other intra- and inter-satellite unpredictably
- RISK-ADCS-03 Failure to determine attitude in eclipse
- RISK-TTC-01 Failure of transceiver component of TT&C subsystem
- RISK-MP-01 No launch opportunity available for preferred orbit during launch window
- RISK-MP-03 During measurements phase, the drift between the satellites can increase past 500 km
- RISK-PROP-01 Electro-mechanical components such as valves and heaters fail during operation
- RISK-PROP-02 Engine characteristics such as thrust or specific impulse are different from expected
- RISK-PROP-03 Piping connection for fluids comes loose during operations
- RISK-PROP-04 Chemical damage to people that handle propellants during assembly and testing
- RISK-EPS-01 Solar panels not deploying
- RISK-EPS-02 Battery cell malfunctions during operation
- RISK-EPS-03 Solar cell malfunctions during operation
- RISK-AERO-01 Aerodynamic drag is higher than expected during phase 3
- RISK-AERO-02 Aerodynamic drag is lower than expected during phase 2
- RISK-AERO-03 The drag coefficient is not as sensitive as expected
- RISK-AERO-04 During measurements phases of phase 3, the satellites drift apart faster than expected
- RISK-STR-01 Satellite frame does not survive the launch loads
- RISK-STR-02 Satellite structure is lightly deformed during launch
- RISK-STR-03 Satellite fails to deploy after launch

Results

The likelihood of occurrence, the significance of the consequences as well as the risk scores of the subsystem technical risks are summarized in the risk map given in figure 18.1. Using the results of this section, the risks which provide the greatest threat to the mission can be determined. From the new risks introduced, only RISK-TCS-03 which needs to be assessed and mitigated. Mitigation strategy for RISK-TECH-01,04,05,19,21, RISK-PL-01, RISK-TTC-01, RISK-MP-02 was performed already in the midterm and baseline report.

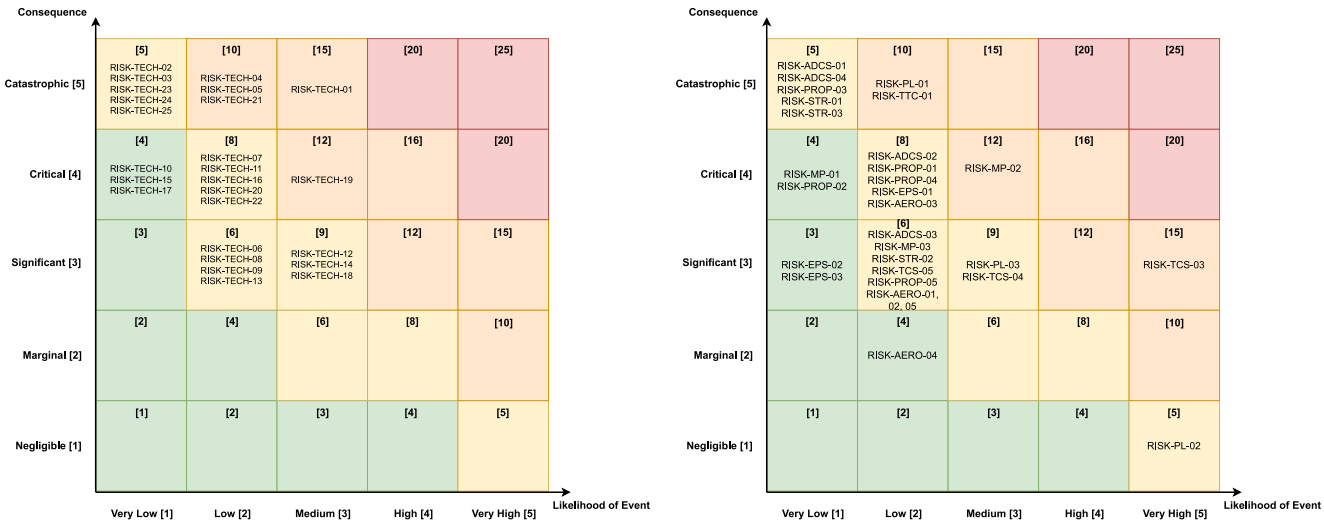

(a) Technical risk map.

(b) Subsystem risk map.

Figure 18.1: Risk map for proposed mission. Cells coloured with green represent a low risk, with yellow a moderate risk, with orange a high risk, and with red a very high risk. Formatted according to [9].

18.1.2 Risk Mitigation

Risks identified above as high (orange) and very high (red) are unacceptable for the continuation of the mission and need to be mitigated in order to decrease their consequences and/or likelihoods. These actionable steps are explained in the following paragraphs for the specific risks that will be changed. The risks in the green areas are non-critical and need not be monitored. The risks in the yellow areas are to be monitored such that they do not increase and become problematic (orange or red).

RISK-TCS-03: Temperature of propellant tanks might fall outside the operational range The likelihood of this event is very high because it is known with assurance that this scenario occurs. Therefore, only the consequence of the risk can be altered to bring the risk score lower. The consequence of the risk is reduced to negligible from significant by the presence of active heaters in the propulsion system. They will be used to heat up the tanks and the catalytic bed before the burn and maintain the optimal temperature during the burn.

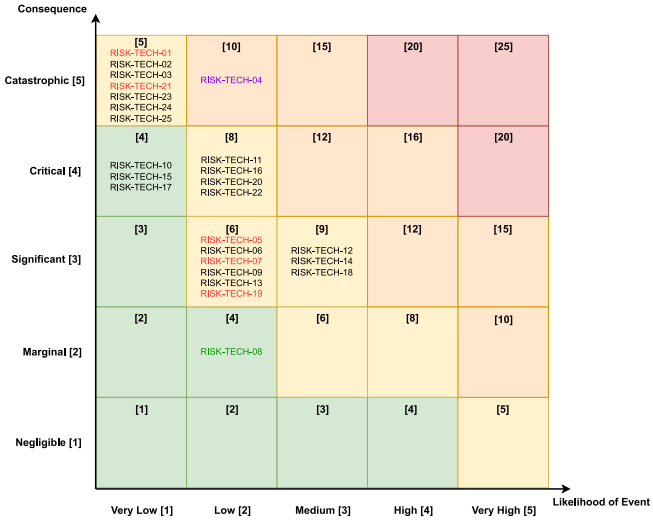

(a) Updated technical risk map for proposed mission with mitigation strategies implemented, from the midterm and baseline report. Red text shows the mitigated risks.

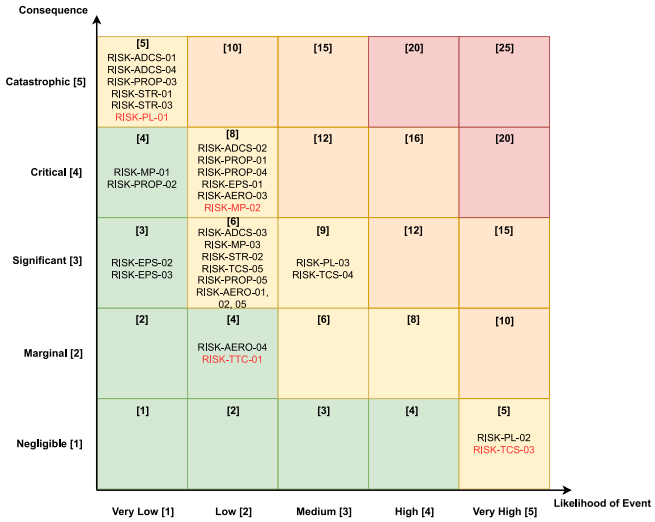

(b) Updated technical risk map.

Figure 18.2: Updated risks map post mitigation for proposed mission with mitigation strategies implemented, from the midterm and baseline report. Red text shows the mitigated risks. Green text shows the risks that had their likelihood and/or consequence modified by the mitigation of another risk. Purple text represent high risks for which no practical mitigation strategy has been found. Cells coloured with green represent a low risk, with yellow a moderate risk, with orange a high risk, and with red a very high risk. Formatted according to [9].

Furthermore, few risks worth monitoring after mitigation are listed below:

RISK-TECH-01: Collision between SCATTER satellites:

The likelihood of this risk was reduced to very low in the mitigation steps during the baseline report. Even though the risk score reduced, the consequence is still catastrophic, and therefore it should be monitored carefully. The collision avoidance analysis shall be performed with scrutiny in every phase of the design and continually update it.

RISK-TECH-04: Collision with untrackable debris

There was no proper mitigation found in the previous reports for this risk. In the detailed phase as well, the risk continues to be a subject of concern. Mitigation such as debris shielding could be used. But more analysis needs to be performed on the probability of collisions with this class of debris such that the likelihood of it decreases.

18.2 Reliability, Availability, Maintainability & Safety Characteristics

In order to maintain the engineering integrity while designing and integrating this complex set of systems, it is important to analyse and assure the reliability, availability, maintainability and safety of the final product's systems. This method will be carried out in this section to uphold the design's engineering integrity.

18.2.1 Reliability

Reliability is the probability that the spacecraft will function without failure over a specified amount of time where the failure is the inability to carry out the mission. The failure of a group of systems normally follows a bathtub curve, where the failure rate is high in the beginning of the mission (called the infant mortality) due to poor design, manufacturing errors, insufficient analysis [85]. Afterwards, the failure rate declines and stays constant for a considerable amount of time and classified as random failures. After this phase, the failure rate again increases due to the wear on the components. The reliability of the spacecraft would be modelled using the random failures. Even though most CubeSats failed during the infancy stage, the majority of them were launched by universities

which lacked proper resources, experience, analysis, testing, etc. It is assumed that with proper analysis and testing in the subsequent phases, the random failures would be a more likely scenario of mission failure. Also, the COTS components are space grade materials and thus the likelihood of failure is more due to integration rather than component failure. The random failures follow the Weibull distribution given by equation 18.1 [12][86]:

$$R = e^{-(\frac{t}{\theta})^{\beta}} \tag{18.1}$$

where β is the shape parameter θ is the scale parameter. The values of the parameters were calculated for 1584 Earth orbiting satellites launched between 1990 and 2008 in table 18.2[86].

Table 18.2: Weibull subsystems reliability parameter estimates[86].

Components	β	θ**[years]**	**No. of units**	**Arrangement**
Reaction wheel	0.7182	3831	4	3 in Series, 1 parallel
Thruster/Fuel	0.3375	6206945	2	Series
OBC	1.465	408	1	
Mechanisms/Structure/Thermal	0.356	21308746	1	
Payload	0.8874	7983	2	Parallel
Battery	0.746	7733	12	3 series, 4 parallel
EPS module	0.5021	169272	1	
Solar array	0.4035	1965868	2.5	Parallel
TT&C	0.3939	400982	2	Parallel

Furthermore, the table also documents the number of units of each component in the spacecraft and the arrangement of series or parallel. Then the reliability of the system is given by equation 18.2 and equation 18.3 for series and parallel combination respectively.

$$R_s = \Pi_{i=1}^{n} R_i \tag{18.2}$$

$$R_s = 1 - \Pi_{i=1}^{n} (1 - R_i) \tag{18.3}$$

As explained in section 11.2.1, the most of the mission carrying the QB50 INMS mass spectrometer failed due to unknown reasons. Due to the lack of reliable data available on the mass spectrometer, a safety factor of 2 is applied on the payload reliability calculated using the parameters. The resulting reliability of each subsystem after three years is shown in table 18.3:

Table 18.3: Reliability of subsystems after combinations at three years.

Components	**Reliability**	**Component**	**Reliability**
Reaction wheels	0.999897602	EPS module	0.9958942
Thruster/Fuel	0.985335806	Solar array	0.9999799
OBC	0.999251481	TT&C	0.9999093
Mechanisms/Structure/Thermal	0.996368394	Payload	0.749543348

The final reliability of the whole spacecraft is calculated by assuming that all these subsystems are in series combination and a failure of one would lead to mission failure. Therefore, the reliability of the system after three years is **0.7321 or 73.21%**. Although this reliability of the spacecraft is low, further research advancement on the mass spectrometers, as well the upcoming CIRCE satellites would provide better estimates on it would improve this figure. The reliability of the spacecraft with lifetime is shown below in figure 18.3.

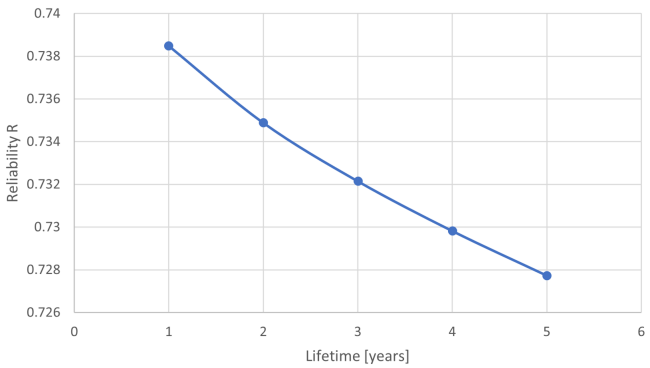

Figure 18.3: Reliability of the spacecraft vs lifetime in years.

18.2.2 Availability

Availability of a system is defined as the probability that a system would be available for operational service during its lifetime, given by section 18.2.2[87].

$$Availability = \frac{Uptime}{Total\_time} = \frac{Uptime}{Downtime + Uptime}$$

The uptime here is defined as the time spent performing scientific measurements in science mode. The downtime is defined as the time spent to recharge the batteries, perform orbital burns, downlink the data, and solve errors. This strongly relates the availability to the duty cycle of the spacecraft. Since it is known to an extent what the downtime of the spacecraft is, the availability can be derived as follows:

$$A = 1 - U = 1 - \frac{Downtime}{Total\_time} \tag{18.4}$$

As discussed in section 3.5, the maximum lifetime of the mission is expected to be around 2.3 years. The approximate downtime of the spacecraft is given in table 18.4 with values calculated from sections 3.5, 3.6.4 to 3.6.6, 5.2.2 and 10.3.2

Table 18.4: Downtime of the spacecraft in modes other than science mode.

Downtime activity	Downlink	Power mode	Burn time	Launch separation	De-tumbling	System startup
Time [s]	1007400	10454400	15181	6300	21600	86400

The total downtime therefore is 11 591 281 s. A safety factor of 1.1 is further applied for downtime due to errors in the spacecraft, which may require ground station support. By using equation 18.4

$$A = 1 - \frac{1.1 \cdot 11591281}{2.3 \cdot 365 \cdot 24 \cdot 3600} = 0.84$$

the availability of a single spacecraft is 84% of the total mission lifetime.

18.2.3 Maintainability

It is impossible to do physical maintenance of the spacecraft, therefore, the only maintenance that could be done on the spacecraft is through software updates. The system should be implemented such that the onboard computer can revert to the old software version in case of errors in the new version. On the ground station, there would be at least two engineers available at all times during the downlink, and one engineer working in shifts to monitor the spacecraft every day.

18.2.4 Safety

According to [87], safety analysis consists of three aspects: personal protection, equipment protection and environmental protection. The environmental safety is greatly discussed in chapter 17. For the personal safety, the proper safety equipment such as gloves, safety goggles must be used while working on the assembly of the spacecraft. The propellant used on board is a green propellant which can be transported on commercial aircraft[81]. For equipment safety, all personal must wear static electric discharge bands to prevent electrostatic damage to components. The components must be handled in the clean room to avoid contamination from foreign particles.

19. Conclusion & Recommendations

As a final element to this report and the phase four design stage, finally some conclusions and recommendations are highlighted for the design of the subsystems, the design of the system and the mission alike. These will help shape the future development stages of the project and the areas of focus for any teams that choose to continue refining the design itself. This chapter is structured as follows: first the subsystem level and integration conclusions are discussed extensively in section 19.1. Following from this, some conclusions regarding the mission overview and planning are discussed in section 19.2. Finally, based on the message conveyed in the aforementioned sections, some final remarks can be drawn in section 19.3.

19.1 Subsystem Level Conclusions

Throughout a significant portion of the report, the design of each individual subsystem in the SCATTER spacecraft was extensively explained. However, for each there are a number of areas of further research which can be explored in later stages of the design procedure. These are presented in the enumerated list below:

- **Structural Design:** Beginning with the structural analysis of the design, through detailed analysis with ANSYS, it can be concluded with reasonable confidence that the satellite structural design can withstand the static and dynamic loads which can be expected during flight. However, in future stages of the design, it is recommended that qualification testing is performed on the structure for fatigue testing and stress concentrations in individual components, as during scientific operations the spacecraft can be expected to rotate frequently. In addition to this, it is recommended to continue future iterations on the front and end bulkheads by machining an isogrid in them to reduce the weight.
- **Aerodynamic Design:** For the aerodynamic design of the spacecraft, it can also be concluded that the utilization of shallow angles for GSI sensitivity has proven itself to be an effective and novel solution, which should be examined in future projects which seek to observe the aerodynamic impacts that are caused by thermospheric drag. It is also recommended to simulate how the extrusions from other subsystems such as the thruster and the payload can impact the aerodynamic performance of the spacecraft. Furthermore, while it can be concluded that any change in drag coefficient can be observed from the GNSS receiver data, currently the accelerometer cannot observe this drag coefficient difference due to a high bias instability.
- **Payload Design:** For the payload subsystem design, it is recommended to develop a custom accelerometer with a bias instability of less than 0.1 µg such that this instrument can also observe the change in drag coefficient in orbits where GNSS information is unavailable (typically at low altitudes0. As it pertains to the other instruments in the payload, the mass spectrometer does not currently satisfy the required mission reliability due to a lack of information and previous mission failures. Therefore, further advancements in this technology are recommended, which is a reasonable assumption for a launch period of 2035.
- **Thermal Control Design:** The thermal control subsystem manages to regulate the equilibrium temperature for all subsystems; however, for certain components such as the TT&C and the mass spectrometer, there is a potential risk that in extreme conditions can run over the operational temperature. Therefore, it is recommended to explore a better placement for these subsystems or to consider a better means of thermal shielding for these components.
- **Orbit Control Subsystem:** Based on the conducted analysis, it can be concluded that there is sufficient delta-V budget for transitioning manoeuvres between phases and for collision avoidance. Furthermore, while the cost of the thrusters were significantly more expensive than required, this was an inevitability in order to ensure sufficient reliability on the overall mission. However, more analysis must be performed on the impacts that the plume has on the degradation of the neighbouring solar arrays.
- **Command and Data Handling:** The C&DH subsystem has been proven to provide the sufficient number of communication interfaces and memory storage in order to guarantee that all telemetry and scientific information can be measured and stored for a period of three days. To ensure a higher fidelity C&DH subsystem, multi-master multi-slave configurations should be explored so that the OBC and daughterboard can both communicate to more subsystems redundantly. Furthermore, increased testing should be done for the daughterboards in order to ensure that all C&DH components are spacegrade.
- **Attitude Determination and Control:** The ADCS subsystem design is proven to detumble and maintain attitudes as stipulated in the requirements. Investigation into the impact of the reaction wheel configuration should be considered.
- **Telemetry, Tracking and Command:** Following the link budget calculations, it was concluded that connections with the ground station could be easily established. With a predicted signal-to-noise ratio per bit (Eb/N0) that is larger than the required Eb/N0 by significantly more than 3 dB (37.2 dB and 22.1 dB respectively), the downlink and uplink data rates for this mission can be supported with a sufficient level of clear signal strength to be received by the other end. However, this does not take the effect of Doppler shift into account while the satellite passes by the ground station. So, it is recommended that further analysis be conducted into the effect

of the slightly shifting frequency of the signal due to Doppler shift and that additionally, appropriate encryption schemes can be researched for the mission.

- **System Integration:** Based on the analysis performed in chapter 13, the SCATTER satellites seem to be spatially efficient based on the chosen layout, with room to space only for cabling and house-keeping small-sized instruments such as temperature sensors. As several components create strong magnetic fields in order to function, such as the magnetorquer, an analysis must be made on the interference they might have with other electrical components. Externally-mounted antennas, while placed in their intuitively the best position, must be analysed for multi-pass effects to determine their signal noise and accuracy in the case of the GNSS receiver. Finally, a mock-up is recommended to be built and checked that it properly slides into the chosen CubeSat deployer.

19.2 Mission Wide Conclusions

With the engineering elements discussed, some conclusions and recommendations may now be discussed for the planning of the overall mission itself. Based on the numerical analysis performed, it can be said with certainty that the mission lifetime will take place between 1.8 and 2.3 years. As the science mode duration is limited to a maximum of 3 days, the recorded acceleration in the first phase of the mission appears to be the critical point for GNSS measurement accuracy, and therefore more analysis needs to be performed in order to estimate the error in drag coefficient measurement. The numerical analysis performed also showed that the duration of phase 3 and the orbital decay of the satellite is highly sensitive to the launching conditions and the events which take place in phase 1 and phase 2. Therefore, to quantify the uncertainty which results from this phase sensitivity, it is recommended to perform a Monte-Carlo analysis on the possible outcomes of phase 3 depending on the possible combinations of launch and science conditions. This is to be conducted in later stages of the mission development.

19.3 Final Remarks

Based on the subsystem, system and mission level conclusions drawn from the above, it can be said with a reasonable confidence that the user requirements which were stipulated at the beginning of the project can be satisfied, especially in the first two scientific phases of the mission. Due to the aerodynamic design which has proven to be sensitive to GSI at different orbital accelerations, the variation in drag is significant enough to be measured by the GNSS constellation. In the third phase of the mission, it is currently unclear as to whether the mission objectives can be completed as information from the GNSS network is unreliable at such low altitudes and the accelerometer error is too high to measure the drag differences between the two flying configurations. As a result of this, further research into higher accuracy accelerometers should be conducted for this project. In addition to the above, as the reliability of the mass spectrometer payload is currently unproven, it should be considered to launch multiple pairs of satellites to increase the probability of success of the overall mission as a whole.

Table 19.1: Task distribution of Group 17 for the Final Report.

Name	Tasks performed
Sabin	Performed the integration of the detailed subsystems into the spacecraft bus, and assembled cad file. Developed 2 PID control schemes for the Astrodynamics tool (AstroSIM): one in the 6-degree-of-freedom solver, for the reaction wheel design, which was then used to simulate all the pointing modes of the spacecraft and calculate the stored momentum, and one for the 3-degree-of-freedom solver, using differential drag to simulate formation flying. Developed a B-dot algorithm for de-tumbling simulations of the satellites, and validated it with a paper from literature, as well as verified it against the Simulink tool developed by Ziqi. Developed an algorithm coupled with AstroSIM to compute the power available for the satellites in 3D, for a satellite with a given number of arbitrary panels and cells. Validated the tool with a paper from literature. Wrote a link budget addition to AstroSIM which computes the ground pass based on a given ground station. Verified and validated every subsystem in design (and wrote all but one verification and validation sections in it). Wrote the entire verification and validation chapter for the design, and all software verification expect for the collision avoidance code and the Simulink code. Wrote the system integration chapter with the exception of the software and hardware diagrams. Coordinated the detailed design throughout the entirety of phase 4 by enforcing the systems engineering approach on every subsystem. Used the DSMC tool (DSMC-SIM) to build together with others, a full aerodynamic profile of the SCATTER design. Helped mission planning and design by simulating the entire mission profile including formation flying, lifetime estimations, de-tumbling and mode transitions. Created the Functional Breakdown Structure.
Oliver	Developed a full aerodynamic profile of the SCATTER design using DSMC-SIM, as well as SPARTA. Designed and developed the Command and Data Handling Subsystem and developed the software block diagram for system integration. Designed the interfaces of all subsystems with the on-board computer and developed the data handling block diagram. Analysed the aerodynamic design sensitivity with respect to solar panel angle, length, angle of attack, angle of side-slip and altitude. Computed the drag sensitivity to accommodation coefficient for these conditions.
Killian	Designed the Structures subsystem in parallel with system integration with Sabin. Iterated upon structural design to facilitate subsystem needs. Created and managed CAD files. Performed FEM analyses with Ansys. Ensured deployer integration. Reported on Manufacturing, Assembly and Testing procedures.
Naishadha	Designing and writing about the whole TT&C subsystem. Did the communication flow diagram. Reporting the system level and subsystem level LCA in the sustainability chapter and editing the prior sections. Market analysis work.
Andrei	Chosen OCS components and analysed them: thrust plume, power, cost etc. Did the delta-V budget, including analysis. Did the ColCalc collision probability simulation tool and partially verified it. Worked on the C&DH on the subsystem architecture, the daughterboard and the watchdogs. Worked on the Data Handling diagram.
Srujan	Worked on the thermal control subsystem: Performed analysis with ESATAN. Worked on Risk analysis and RAMS. Did the hardware block diagram
Jort	Designed and wrote about the payload. Contributed to introduction and updated market analysis. Contributed to future workflow diagram and future Gantt chart. Provided support to the team on writing in LaTeX
Oscar	Perfomed EPS design, modelled available science time and computed duty cycles. Found companies supplying the EPS components required. Designed the layout of the PDU's, and made the electric block diagram. Worked on future work flow structure.
Ziqi	Designed and wrote about the whole ADCS. Developed the simulink tool. Verified and validated simulink tool. Managed budget and wrote down budget related sections. Cost breakdown structure. Market analysis work
Daniel	Created the sustainable development plan and did an extensive life cycle assessment at system and subsystem level. Selection of orbit, launch vehicle and deployer. Integration in launcher. Developed the mission overview and timeline, including lifetime analysis. Developed the operational concept at each phase and operational modes. Implemented a PD controller to be used for formation flying. Created the functional flow diagram. Worked on general report writing and helping other sections.

Bibliography

[1] A. C. Boley and M. Byers, "Satellite mega-constellations create risks in Low Earth Orbit, the atmosphere and on Earth," *Scientific Reports*, vol. 11, no. 1, p. 10 642, Dec. 2021.

[2] V. Bernstein and M. Pilinski, "Drag Coefficient Constraints for Space Weather Observations in the Upper Thermosphere," *Space Weather*, vol. 20, no. 5, May 2022.

[3] J. T. Emmert, D. P. Drob, J. M. Picone, *et al.*, "NRLMSIS 2.0: A Whole-Atmosphere Empirical Model of Temperature and Neutral Species Densities," *Earth and Space Science*, vol. 8, no. 3, Mar. 2021.

[4] G. March, J. van den IJssel, C. Siemes, P. N. A. M. Visser, E. N. Doornbos, and M. Pilinski, "Gas-surface interactions modelling influence on satellite aerodynamics and thermosphere mass density," *Journal of Space Weather and Space Climate*, vol. 11, p. 54, Oct. 2021.

[5] D. Mostaza Prieto, B. P. Graziano, and P. C. Roberts, "Spacecraft drag modelling," *Progress in Aerospace Sciences*, vol. 64, pp. 56–65, Jan. 2014.

[6] O.Montenbruck and E.Gill, *Satellite Orbits: Models, Methods, Applications*, 1st ed. Springer, 2000, pp. 55–55.

[7] A. Lawrence, M. L. Rawls, M. Jah, *et al.*, "The case for space environmentalism," *Nature Astronomy*, vol. 6, no. 4, pp. 428–435, Apr. 2022.

[8] E. Mooij, *Project Management and Systems Engineering in the DSE*, Apr. 2022.

[9] E. Gill, *Systems Engineering and Aerospace Design - Risk Management and Concurrent Engineering*, Feb. 2022.

[10] J. Carroll, J. Gottschall, J. A. Johnson, and D. J. Kruger, *Vega User's Manual*, 2012.

[11] A. Walker, P. Mehta, and J. Koller, "Drag Coefficient Model Using the Cercignani–Lampis–Lord Gas–Surface Interaction Model," *Journal of Spacecraft and Rockets*, vol. 51, no. 5, pp. 1544–1563, Sep. 2014.

[12] D. F. Everett, J. R. Wertz, and J. J. Puschell, *Space Mission Engineering: The New SMAD*, 2nd ed., J. R. Wertz, D. F. Everett, and J. J. Puschell, Eds. Hawthorne: Microcosm Press, 2015.

[13] J. Wolfhagen, "Collision avoidance in the new space era," Ph.D. dissertation, 2020.

[14] S.-V. Anton, K. Caignie, D. Calliess, *et al.*, "SCATTER: Baseline Report," Delft University of Technology, Delft, Tech. Rep., Apr. 2022.

[15] C. Cappelletti, S. Battistini, and B. K. Malphrus, *Cubesat Handbook: From Mission Design to Operations*. Academic Press, 2021.

[16] S. Waydo, D. Henry, and M. Campbell, "CubeSat design for LEO-based Earth science missions," *IEEE Aerospace Conference Proceedings*, vol. 1, pp. 435–445, 2002.

[17] J. Emmert, "Thermospheric mass density: A review," *Advances in Space Research*, vol. 56, no. 5, pp. 773–824, Sep. 2015.

[18] R. Lagier, "VEGA C USER'S MANUAL ISSUE 0 REVISION 0," Arianespace, Tech. Rep., May 2018.

[19] V. Shah, "Tyvak 12U Deployer User Guide for Payloads and Launch Vehicles," TYAVK NANO-SATELLITE SYSTEMS INC., Tech. Rep., 2019.

[20] R. J. Suggs, "Future Solar Activity Estimates for Use in Prediction of Space Environmental Effects on Spacecraft Orbital Lifetime and Performance," Tech. Rep., 2015.

[21] J.A. Mulder, W.H.J.J. van Staveren, J.C. van der Vaart, *et al.*, *Flight Dynamics Lecture Notes*, Delft, Mar. 2013.

[22] R. M. Sharma, R. Kawari, S. Bhandari, S. Panta, R. C. Prajapati, and N. B. Adhikari, "Simulation of CubeSat Detumbling Using B-Dot Controller," in 2021, pp. 541–553.

[23] D. Kataria, R. Wicks, R. Chaudery, A. Spencer, and T. Brochant de Villiers, "QB50 INMS Science Unit Interface Control Document," Tech. Rep., Nov. 2015.

[24] N. Hładczuk, "SPARTA DSMC Simulator Manual," Tech. Rep., 2022.

[25] F. J. Alexander and A. L. Garcia, "The Direct Simulation Monte Carlo Method," *Computers in Physics*, vol. 11, no. 6, p. 588, 1997.

[26] M. Hedahl and R. Wilmoth, "Comparisons of the Maxwell and CLL gas/surface interaction models using DSMC Changing the European Debate on Climate Change-The Dahrendorf Project 2013 View project Parallel DSMC View project," Tech. Rep., 1996.

[27] R. Votel and D. Sinclair, "Comparison of Control Moment Gyros and Reaction Wheels for Small Earth-Observing Satellites," Tech. Rep.

[28] J. Fellner, G. Loeber, S. Vukson, and C. Riepenhoff, "Lithium-ion testing for spacecraft applications," *Journal of Power Sources*, vol. 119-121, pp. 911–913, Jun. 2003.

[29] T. Etchells and L. Berthoud, "Developing a Power Modelling Tool for CubeSats," in *Pre-Conference Posters Session I*, Utah: Proceedings of the Small Satellite Conference, 2019.

[30] B. Zandbergen, "AE1222-II: Aerospace Design & Systems Engineering Elements I," Delft University of Technology, Tech. Rep., 2020.

[31] Y. Nakasone, S. Yoshimoto, and T. Stolarski, *Engineering analysis with ANSYS software*, second. Oxford: Butterworth-Heinemann, 2018.

[32] NASA, "State-of-the-Art Small Spacecraft Technology," NASA, California, Tech. Rep., Oct. 2021.

[33] R. Lagier, "Small Spacecraft Mission Service VEGA-C User's Manual," Arianespace, Tech. Rep., Sep. 2020.

[34] T. Irvine, *An Introduction to Shock and Vibration Response Spectra*.

[35] Y. Chung, D. Krebs, and J. Peebles, "Estimation of Payload Random Vibration Loads for Proper Structure Design," in *19th AIAA Applied Aerodynamics Conference*, Anaheim, 2001.

[36] T.-Y. Park and H.-U. Oh, "New PCB strain-based structural design methodology for reliable and rapid evaluation of spaceborne electronics under random vibration," *International Journal of Fatigue*, vol. 146, no. 0142-1123, 2021.

[37] T. M. Sanders, "SHAKER TABLE VIBRATION TESTING OF A MICROSATELLITE," Ph.D. dissertation, MISSOURI UNIVERSITY OF SCIENCE and TECHNOLOGY, Rolla, Missouri, 2011.

[38] A. García-Pérez, A. Ravanbakhsh, F. Sorribes-Palmer, and G. Alonso, "Structural shock verification by numerical analysis of the EPD payload units on board Solar Orbiter spacecraft," *Acta Astronautica*, vol. 168, pp. 282–292, Mar. 2020.

[39] A. Andonova, N. Kafadarova, V. Videkov, and S. Andreev, "Investigation of thermal conductivity of PCB," in *2009 32nd International Spring Seminar on Electronics Technology*, IEEE, May 2009, pp. 1–5.

[40] L. Kauder, "Spacecraft Thermal Control Coatings References," NASA, Tech. Rep., Dec. 2005.

[41] D. Gilmore, *Spacecraft thermal control handbook. Volume I, Fundamental technologies*, Second. Reston: American Institute of Aeronautics and Astronautics, Inc, 2002.

[42] H. Ganti, A. P. Kailaje, A. A. Kumar, *et al.*, "Design of thermal model and implementation of thermal solutions for nano satellite," in *2017 IEEE Aerospace Conference*, IEEE, Mar. 2017, pp. 1–7.

[43] IBM space guidance center, "THERMAL CONTACT CONDUCTANCE BETWEEN METALS IN A VACUUM ENVIRONMENT," NASA, Huntsville, Alabama, Tech. Rep., Aug. 1965.

[44] NASA, "Thermal joint conductance," C. Mook, Ed., Washington: NASA, Feb. 1964.

[45] N. Pas, *AE4S20 Satellite Thermal Control, Thermal Analysis 1*, Delft, Oct. 2021.

[46] R. Noomen, *Flight and Orbital Mechanics AE2230-I. Lecture 3: Eclipse, Maneuvers*, Delft, 2021.

[47] S. C. Lee, H. D. Kim, and J. Suk, "Collision avoidance maneuver planning using GA for LEO and GEO satellite maintained in keeping area," *International Journal of Aeronautical and Space Sciences*, vol. 13, no. 4, pp. 474–483, 2012.

[48] H. G. Lewis, "Understanding long-term orbital debris population dynamics," *Journal of Space Safety Engineering*, vol. 7, no. 3, pp. 164–170, Sep. 2020.

[49] J.-C. Liou, "Risks from Orbital Debris and Space Situational Awareness," in *2nd IAA Conference on Space Situational Awareness*, Washington DC: National Aeronautics and Space Administration, 2020, pp. 1–27.

[50] M. Wilhelm, M. Negri, H. Ciezki, and S. Schlechtriem, "Preliminary tests on thermal ignition of ADN-based liquid monopropellants," *Acta Astronautica*, vol. 158, pp. 388–396, May 2019.

[51] Granta Design Limited, *CES EduPack 2019*, 2019.

[52] B. W. Young, "Design and Specification of an Attitude Control System for the DANDE Mission," Tech. Rep., 2006.

[53] J. Narkiewicz, M. Sochacki, and B. Zakrzewski, "Generic Model of a Satellite Attitude Control System," *International Journal of Aerospace Engineering*, vol. 2020, 2020.

[54] G. Juchnikowski, T. Barcinski, and J. Lisowski, "Optimal control gain for satellite detumbling using B-dot algorithm," Tech. Rep.

[55] A. Finance, C. Dufour, T. Boutéraon, *et al.*, "In-orbit attitude determination of the uvsq-sat cubesat using triad and mekf methods," *Sensors*, vol. 21, no. 21, Nov. 2021.

[56] G. Efendioğlu, "DESIGN OF KALMAN FILTER BASED ATTITUDE DETERMINATION AND CONTROL ALGORITHMS FOR A LEO SATELLITE," Ph.D. dissertation.

[57] Y. Mashtakov, S. Tkachev, and M. Ovchinnikov, "Use of external torques for desaturation of reaction wheels," *Journal of Guidance, Control, and Dynamics*, vol. 41, no. 8, pp. 1663–1674, 2018.

[58] Y. Mimasu, J. C. Van Der Ha, and T. Narumi, "Attitude determination by magnetometer and gyros during eclipse," in *AIAA/AAS Astrodynamics Specialist Conference and Exhibit*, 2008.

[59] Y. F. Wong, O. Kegege, S. H. Schaire, *et al.*, "An Optimum Space-to-Ground Communication Concept for CubeSat Platform Utilizing NASA Space Network and Near Earth Network," Tech. Rep., p. 30.

[60] A. L. Scholtz, T. U. Wien, and W. Keim, "Performance and reliability evaluation of the S-band Vienna satellite ground station," Tech. Rep., 2006.

[61] A. Alanazi and J. Straub, "Statistical Analysis of CubeSat Mission Failure," Tech. Rep.

[62] A. C. Nicholas, G. D. Attrill, K. F. Dymond, *et al.*, "Coordinated Ionospheric Reconstruction CubeSat Experiment (CIRCE) mission overview," in *CubeSats and SmallSats for Remote Sensing III*, C. D. Norton, T. S. Pagano, and S. R. Babu, Eds., SPIE, Sep. 2019, p. 13.

[63] D. Masutti, A. Denis, R. Wicks, *et al.*, *The QB50 Mission for the Investigation of the Mid-Lower Thermosphere: Preliminary Results and Lessons Learned*, 2018.

[64] A. C. Nicholas, F. A. Herrero, A. W. Stephan, and T. Finne, "WINCS on-orbit performance results," S. Fineschi and J. Fennelly, Eds., Sep. 2015, p. 960 404.

[65] M. Rodriguez, N. Paschalidis, S. Jones, *et al.*, *A Compact Ion and Neutral Mass Spectrometer for Cubesat/SmallSat Platforms*.

[66] N. Crisp, P. Roberts, S. Livadiotti, *et al.*, "In-orbit aerodynamic coefficient measurements using SOAR (Satellite for Orbital Aerodynamics Research)," *Acta Astronautica*, vol. 180, pp. 85–99, Mar. 2021.

[67] K. Wang, A. Allahvirdi-Zadeh, A. El-Mowafy, and J. N. Gross, "A Sensitivity Study of POD Using Dual-Frequency GPS for CubeSats Data Limitation and Resources," *Remote Sensing*, vol. 12, no. 13, p. 2107, Jul. 2020.

[68] O. Montenbruck, A. Hauschild, R. B. Langley, and C. Siemes, "CASSIOPE orbit and attitude determination using commercial off-the-shelf GPS receivers," *GPS Solutions*, vol. 23, no. 4, p. 114, Oct. 2019.

[69] M. Braasch and A. van Dierendonck, "GPS receiver architectures and measurements," *Proceedings of the IEEE*, vol. 87, no. 1, pp. 48–64, 1999.

[70] D. Svehla, "GPS Single-Frequency: From First cm-POD to Single Frequency GNSS-RO/R," in 2018, pp. 131–143.

[71] K. Shao, C. Wei, D. Gu, *et al.*, "Tsinghua Scientific Satellite Precise Orbit Determination Using Onboard GNSS Observations with Antenna Center Modeling," *Remote Sensing*, vol. 14, no. 10, p. 2479, May 2022.

[72] C. Siemes, S. Maddox, O. Carraz, *et al.*, "CASPA-ADM: a mission concept for observing thermospheric mass density," *CEAS Space Journal*, Jan. 2022.

[73] J. Sinke, "AE3211-II: Production of Aerospace Systems," Delft University of Technology, Tech. Rep., 2021.

[74] G. Hillard, S. Bailey, and D. Ferguson, "Anodized Aluminium as Used for Exterior Spacecraft Dielectrics," pp. 111–113, Oct. 1998.

[75] ESTEC, "Space product assurance: Thermal vacuum outgassing test for the screening of space materials," European Cooperation for Space Standardization, Noordwijk, Tech. Rep., Nov. 2008, pp. 9–10.

[76] P. Fortescue, G. Swinerd, and J. Stark, *Spacecraft Systems Engineering*, 4th ed. Chicester: John Wiley & Sons Ltd, 2011, vol. 1.

[77] J. Xu and L. Xu, "Affordability and Life-Cycle Costs Analysis," in *Integrated System Health Management*, Elsevier, 2017, pp. 433–450.

[78] T. Maury, P. Loubet, S. M. Serrano, A. Gallice, and G. Sonnemann, *Application of environmental life cycle assessment (LCA) within the space sector: A state of the art*, May 2020.

[79] A. R. Wilson, "Advanced Methods of Life Cycle Assessment for Space Systems," Tech. Rep., 2019.

[80] A. S. Gohardani, J. Stanojev, A. Demairé, *et al.*, "Green space propulsion: Opportunities and prospects," *Progress in Aerospace Sciences*, vol. 71, pp. 128–149, Nov. 2014.

[81] A. Dinardi and M. Persson, "High Performance Green Propulsion (HPGP): A Flight-Proven Capability and Cost Game-Changer for Small and Secondary Satellites," Tech. Rep.

[82] S. H. Farjana, M. A. P. Mahmud, and N. Huda, "Life Cycle Assessment of Copper–Gold– Lead–Silver–Zinc Beneficiation Process," in *Life Cycle Assessment for Sustainable Mining*, Elsevier, 2021, pp. 115–140.

[83] M. N. Nassajfar, I. Deviatkin, V. Leminen, and M. Horttanainen, "Alternative materials for printed circuit board production: An environmental perspective," *Sustainability (Switzerland)*, vol. 13, no. 21, Nov. 2021.

[84] M. Pastena and B.-B. James, *Comparison of Magnetorquer Performance*, Logan, Sep. 2010.

[85] J. Bouwmeester, A. Menicucci, and E. Gill, "Improving CubeSat reliability: Subsystem redundancy or improved testing?" *Reliability Engineering & System Safety*, vol. 220, p. 108 288, Apr. 2022.

[86] R. Bris, C. Guedes Soares, and S. Martorell, Eds., *Reliability, Risk, and Safety, Three Volume Set*. CRC Press, Aug. 2009.

[87] R. Stapelberg, *Handbook of Reliability, Availability, Maintainability and Safety in Engineering Design*. London: Springer London, 2009.

A. Functional Flow Diagram & Breakdown Structure

Functional Flow Diagram:

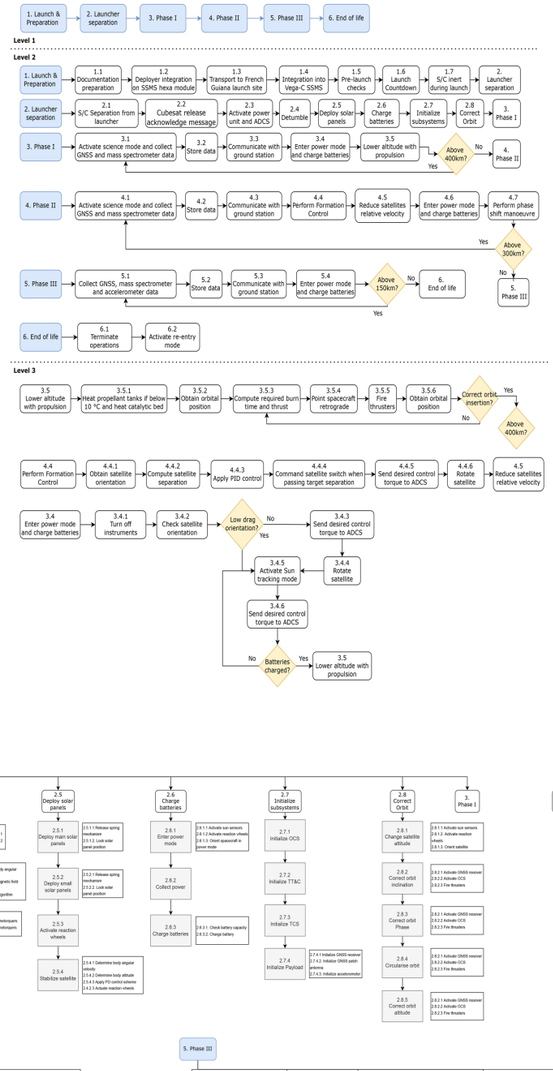

Functional Breakdown Structure:

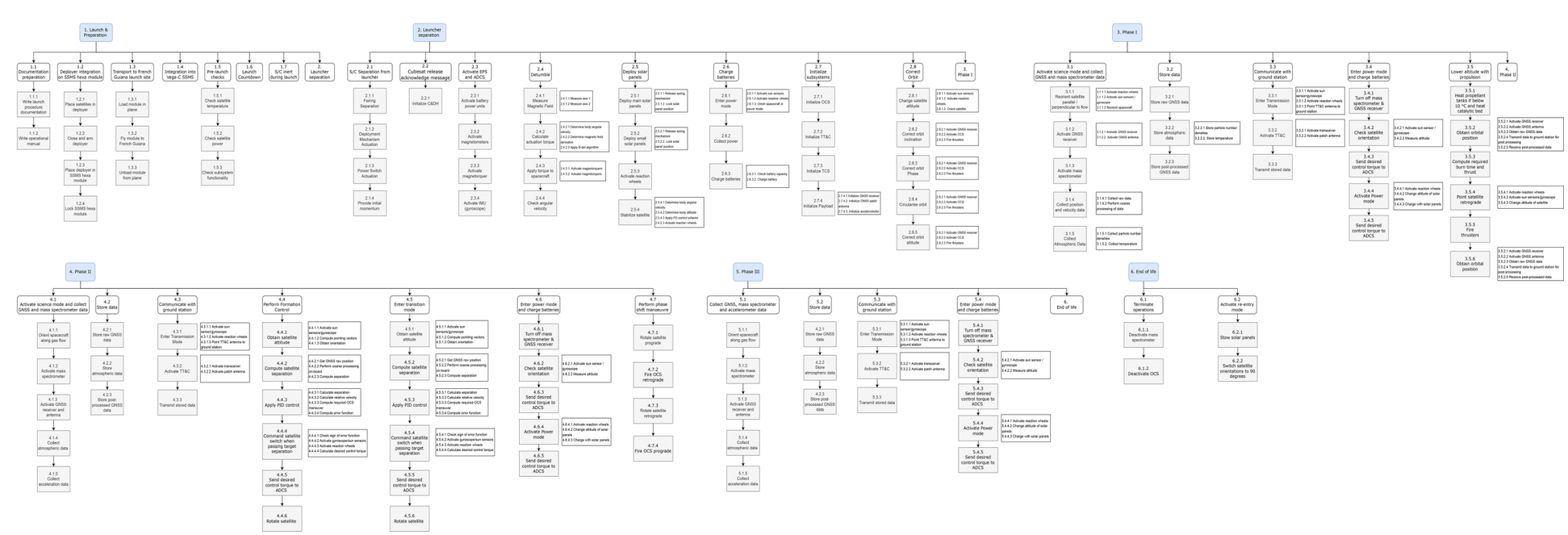

Figure A.1: Functional flow diagram and functional breakdown structure.